

Ultrafast Photoluminescence Spectroscopy of Silicon Nanocrystals

by

Glenda B. De los Reyes

A thesis submitted in partial fulfillment of the requirements for the degree of

Doctor of Philosophy

Department of Physics
University of Alberta

© Glenda B. De los Reyes, 2015

Abstract

Ultrafast carrier dynamics in silicon nanocrystals (Si NCs) is explored using time-integrated photoluminescence, time-resolved photoluminescence and pump-probe transient absorption spectroscopies. The role of surface oxygen in the optical emission dynamics of dodecyl functionalized Si NCs is explored. Significant surface oxidation results in a photoluminescence blue shift and an observation of sub-10 ns recombination lifetime. In addition, surface oxidation improves the absolute quantum yield of dodecyl functionalized Si NCs. This study also shows that surface passivation plays an important role in the emission dynamics of functionalized Si NCs. It is shown that photoluminescence in silicon nanocrystals can be tuned by changing the surface passivation alone. Tunable surface-related emissions are significantly blue shifted compared to quantum confinement predictions and exhibit a faster recombination rate similar to that for direct bandgap semiconductors. Furthermore, the photoluminescence quantum yields of these silicon nanocrystals are higher than those that exhibit quantum core state emission. On the other hand, detailed time-resolved photoluminescence studies reveal that the origin of the size-independent blue emission in dodecylamine and ammonia functionalized Si NCs originates from charge transfer states located at the silicon-silicon oxynitride interface. Time-integrated photoluminescence spectroscopy revealed that Si NCs with silicon volume filling fraction below the percolation threshold exhibit strong size-dependent emission in the infrared region. The carrier dynamics of these Si NCs are explored using pump-probe transient absorption spectroscopy with sub-picosecond resolution and time-resolved photoluminescence spectroscopy in the nanosecond and microsecond time scales. Si NC films exhibit sub-picosecond, sub-nanosecond and microsecond lifetimes attributed to carrier trapping at the oxygen-related defects, carrier recombination at the trap states and carrier recombination via the silicon core state, respectively.

The results of this study will hopefully contribute to the understanding of the role of oxygen in the optical emission properties of functionalized Si NCs. In addition, the blue emission observed in dodecylamine and ammonia functionalized Si NCs will impact applications in optoelectronic devices.

Finally, 800 nm, 65 fs laser pulses is coupled to near-field scanning optical microscopy using single mode fiber. The newly developed ultrafast NSOM is suitable for studying spatially-resolved PL emission in semiconductor nanostructures.

Preface

Some of the research conducted for this thesis forms part of an international research collaboration, led by Prof. Frank A. Hegmann of the Physics Department at the University of Alberta, with Prof. Jonthan G. C. Veinot of the Chemistry Department at the University of Alberta, Prof. Al Meldrum of the Physics Department at the University of Alberta, and Prof. Jann Linross of the ICT School at the KTH-Royal Institute of Technology. The experimental set-ups for the time-integrated PL (TIPL), nanosecond (ns) time-resolved PL (TRPL) and transient photoinduced absorption (TPA) measurements were constructed by Lyubov Titova. I helped in the characterization of those set-ups and improved some parts of the original set-ups. I constructed the μs TRPL set-up that was used in chapters 4-6. I performed all the TIPL, TRPL and TPA measurements reported in chapters 4-8. I developed the ultrafast near-field scanning optical microscopy presented in chapter 8, with the assistance from Lyubov Titova and Megan Engel.

Chapter 4 of this thesis has been published as Zhenyu Yang, Glenda B. De los Reyes, Lyubov V. Titova, Ilya Sychugov, Mita Dasog, Jan Linnros, Frank A. Hegmann, and Jonathan G. C. Veinot, "Evolution of the ultrafast photoluminescence of colloidal silicon nanocrystals with changing surface chemistry", *ACS Photonics* 2015, 2, 595-605. Zhenyu Yang and I have equal contribution on this manuscript. I was responsible for the TIPL and TRPL measurements and analysis of the results. I also helped in the manuscript composition. Zhenyu Yang was responsible for making the samples and the characterization which includes TEM, XPS, and FTIR measurements. He also helped in the manuscript composition. Lyubov Titova and Mita Dasog helped in the analysis and manuscript composition, Ilya Sychugov performed the quantum yield measurements and helped in the manuscript composition. Jan Linnros, Frank A. Hegmann, and Jonathan G.C. Veinot were the supervisory

authors and were involved with the formation of the concept and manuscript composition.

Part of the results presented in chapter 5 has been published in Mita Dasog, Glenda B. De los Reyes, Lyubov V. Titova, Frank A. Hegmann, Jonathan G.C. Veinot, "Size *vs.* surface: tuning the photoluminescence of free standing silicon nanocrystals across the visible spectrum *via* surface group", *ACS Nano* 2014, 8(9), 9636-9648. I was responsible for all the TIPL and TRPL measurements of all the samples. I also helped in the editing of the manuscript. Mita Dasog made the samples and performed the analyses of the FTIR, XRD, XPS and Raman results and wrote the manuscript. Frank A. Hegmann and Jonathan G.C. Veinot were the supervisory authors.

Chapter 6 has been submitted for publication in Glenda B. De los Reyes, Mita Dasog, Mengxing Na, Lyubov V. Titova, Jonathan G.C. Veinot, Frank A. Hegmann, "Charge transfer state emission dynamics in blue-emitting functionalized silicon nanocrystals", *Physical Chemistry Chemical Physics*, Manuscript ID CP-ART-08-2015-004819. I performed all the TIPL and TRPL measurements and the analysis of the results. I was also responsible for the manuscript composition and Lyubov Titova helped in the manuscript composition and analysis of the data. Mita Dasog made all the samples and performed the FTIR, TEM, Raman and SAED measurements of the samples. MengXing Na helped in the processing of the TRPL results. Frank A. Hegmann and Jonathan G.C. Veinot were the supervisory authors and were involved with the formation of the concept and manuscript composition.

Chapter 7 is a collaborative work between Frank A. Hegmann and Al Meldrum of the Physics Department at the University of Alberta. Al Meldrum provided all the samples that were used in the study and the μ s-TRPL measurements were conducted in his lab. I performed all the data acquisition and analysis of the results.

o *enald, and our* *abrielle*

Acknowledgments

Typically, we don't look at life in terms of how many years have passed. However, I will always treasure and remember the 6 years of my stay in the Ultrafast Nanotools lab of the University of Alberta. I will always look back at it as a challenging, and at the same time exciting, inspiring and a great learning experience. I will never forget the countless late-home-arrivals and weekend experiments that became the regular routine of my initial four years. I am very grateful and indebted to all the people who helped me to succeed during these times. I would like to express my gratitude to them for making the completion of my PhD degree a reality.

First and foremost, I thank my supervisor Dr. Frank A. Hegmann, for his guidance and unending support, and for training me how to be a scientist. I thank him for always telling me to make sure that my data makes sense so I can convince others. I am forever indebted to him for all the experimental skills I have developed under his guidance which would be valuable assets in succeeding in my future endeavors. It has been an honor to be part of his lab.

To the person I consider as my second advisor, Dr. Lyubov V. Titova. I thank her for developing the ns-TRPL and pump-probe transient absorption measurement set-ups; for the fruitful discussions to interpret my data; and also for the outside-the-lab talks, for giving me tips on parenting and where to get kids' stuff, and the list goes on.

To my collaborators outside the Hegmann Lab namely, Dr. Jonathan G. C. Veinot, Dr. Mita Dasog, and Dr. Zhenyu Kevin Yang of the Chemistry Department. I thank them for providing me all the colloidal Si NC samples and for performing and interpreting the XPS, FTIR, Raman, and XRD measurements. I give my special thanks to Dr. Mita Dasog and Dr. Zhenyu Yang for giving

me a crash course on the synthesis process of the colloidal Si NCs. My collaboration with these talented people was very productive and led to very interesting results. My chemistry knowledge has improved a lot because of their effort in teaching me the meanings and interpretations of each curve in the spectral data.

To Dr. Al Meldrum, for providing me the Si NC film samples, and for teaching and allowing me to use his lab for μ s-TRPL measurements of the Si NC films.

To the following professors: Dr. Robert Wolkow, Dr. Michael Woodside, Dr. Massimo Boninsegni, and Dr. Zubin Jacob, for their valuable lectures during my coursework that introduced me to interesting materials and helped me develop a deeper understanding of physics.

To the people who provided technical support for my experiments: Don Mullin for all the help, from the machining of the small parts for the spectrometer to designing a better way of coupling the detectors and other components to the spectrometer. His ingenious idea of how to incorporate the things we want in our system is partly responsible for my successful results. To Greg Popowich, for the maintenance of the laser coolers, for the help in setting up the ultrafast NSOM, for teaching me on how to use the NSOM and helping me with a lot of stuff in the lab from equipment maintenance to part replacement. To Dave Fortin, for making different sets of fiber coupler and for helping fix the NSOM software when it bugged down. To Paul Zimmerman, for helping me with the machining of the small components for my set-up.

I would also like to extend my gratitude to the people who performed the characterization of our colloidal Si NC samples: Wayne Moffat, Miranda Skjel and Michelle Hoyle of the analytical and instrumentation laboratory of the Chemistry Department, for their assistance with FTIR spectroscopy; the staff at the Alberta Centre for Surface Engineering and Sciences (ACSES), for their assistance in the XPS and SEM analysis; Kai Cui of National Institute of Nanotechnology (NINT) for his valuable help in TEM analysis; Greg Kaufmann, for his assistance with Raman spectroscopy.

To Megan Engel, Ketty Ng, our summer students in the lab. Megan helped me with the initial setting up of the ultrafast NSOM system while Ketty helped me a lot with the processing of the PL lifetimes.

To my former lab mates who helped me a lot during my experiments: Dr. Tyler Cocker, for giving me inputs about techniques in aligning my optics; Dr. Ayesheshim Ayesheshim, for helping me during the routine alignment of my set-up since I can't reach the middle of optics bench; Dr. Zhenyou Wang for helping me with the machining of the components for my fiber. Thank you also for the friendship that was developed.

To my current lab mates: Vedran Jelic (together with Dr. Titova), for keeping the RegA system in good working condition and for being so understanding every time I needed to turn off the lights during my experiment; special thanks to David Purschke, for helping me with the English stuff and for giving me the most needed encouragement every now and then; Peter Nguyen, for his help in the lab; Mary Alvean Narreto, for lending me her valuable time and effort in reading my thesis, helping in encoding my manuscript in latex, and for pushing me when I was about to give up.

To the support staff of the Physics Department: Sarah Derr, Linda Jacklin, Carolyn Steiborn, Sandra Hamilton and Suzette Chan, for their help with the paper works. Special thanks to Sarah Derr for always providing me information about the FGSR rules and for reminding me about the candidacy exam and thesis deadlines.

To Dr. Sharon Morsink for encouraging me to apply to Alberta Innovates Technology Futures (AITF) graduate students scholarship program. The AITF is also being acknowledged for financial support.

I would also like to extend my gratitude to the Physics Department of the College of Science, University of Santo Tomas for their financial support during the first 5 years of my study. Thanks to former dean Dr. Maribel Nonato and current dean Dr. John Donnie Ramos for allowing me to extend my study leave.

My studies won't be an easy ride without the untiring love and support of my family who never left my side especially at the lowest points where I almost gave up. To my parents, Avelina, Gregorio, Priscila, and Edilberto, and my siblings, Gredel, Gerald, and Gerlie, for their continuous prayer, love, support and undying belief in my abilities. To my husband Ronald, for his unconditional love and support all throughout my 6 years of studies. Thank you for your sacrifices and patience so I can

reach my dreams. To my angel, Gabby, thank you for always making me smile and teaching me lessons in life that I never expected to learn from a kid like you.

Above all, I would like to thank God Almighty for the gift of knowledge that helped me to complete my PhD studies, for showering me with blessings that made my stay in Edmonton a very safe and memorable journey, for guiding me through all the challenges and showing me miracles that made my faith even stronger.

Table of Contents

1	Introduction	1
2	Photoluminescence	6
2.1	Introduction	6
2.2	Interband transitions	7
2.2.1	Absorption	7
2.3	Spontaneous Emission/Radiative recombination	11
2.3.1	Non-radiative recombination	11
2.3.2	Radiative Recombination Rate	12
2.4	Photoluminescence decay time and quantum yield	13
2.5	Photoluminescence in quantum dot materials	14
3	Ultrafast photoluminescence spectroscopy	18
3.1	Time-integrated PL and steady state PL spectroscopy	18
3.2	Time-resolved Photoluminescence Spectroscopy	21
3.2.1	Time-correlated single photon counting	22
3.2.2	Microsecond-time-resolved photoluminescence spectroscopy	28
3.3	Optical pump-probe transient photoinduced absorption spectroscopy	30

4	The role of oxygen in the ultrafast photoluminescence from colloidal silicon nanocrystals	35
4.1	Introduction	35
4.2	Sample preparation and characterization	37
4.3	Experimental details	38
4.4	Results and Discussion	39
4.5	Conclusion	53
5	Effect of surface passivation on the emission dynamics of colloidal silicon nanocrystals	55
5.1	Introduction	55
5.2	Sample Preparation	56
5.3	Experimental details	57
5.4	Results and discussion	57
5.4.1	Dodecylamine functionalized silicon nanocrystals	57
5.4.2	Acetal functionalized silicon nanocrystals	61
5.4.3	TOPO functionalized Si NCs	65
5.4.4	Dodecyl functionalized Si NCs	70
5.5	Conclusions	77
6	Charge transfer state emission dynamics in functionalized silicon nanocrystals	78
6.1	Introduction	78
6.2	Sample Preparation and Characterization	80
6.3	Experimental details	82
6.4	Results and discussion	85
6.5	Conclusion	97

7	Carrier dynamics of photoexcited Si nanocrystal films with different Si filling fractions	98
7.1	Introduction	98
7.2	Sample Preparation	99
7.3	Experimental details	100
7.4	Results and Discussion	101
7.5	Conclusion	111
8	Ultrafast near-field scanning optical microscopy	112
8.1	Introduction	112
8.2	Ultrafast near-field scanning optical microscopy	114
8.2.1	Near-field scanning optical microscope	114
8.2.2	Coupling the ultrafast laser to the NSOM instrument	118
8.2.3	Ultrafast NSOM pump-probe transient absorption set-up	122
9	Summary and Recommendations	124
9.1	Summary	124
9.2	Recommendations	126
	Bibliography	128
	Appendices	146
A	Microsecond-photoluminescence lifetime of dodecyl functionalized silicon nanocrystals	146
B	Time-resolved photoluminescence of functionalized silicon nanocrystal films	148
B.1	Acetal functionalized Si NCs	148
B.2	Dodecylamine functionalized Si NCs	150
C	Thickness dependence transient absorption measurements of Si NC films with different filling fractions	152

D	Comparison of the different fitting functions	154
E	p-type GaAsBi : photoluminescence spectroscopy and AFM measurements summary	156
E.1	Photoluminescence Spectroscopy	156
E.2	Atomic Force Microscopy and Confocal Microscopy	160
F	A walk-through in using the TIPL and TRPL set-up	164
F.1	Calibrating the CCD and gratings	164
F.2	Performing TIPL spectroscopy using the CCD	168
F.3	Performing TRPL spectroscopy using the TCSPC	170
G	A walk-through in using the near-field scanning optical microscope	173
G.1	Confocal transmission mode	173
G.2	Confocal reflection mode	176
G.3	AFM Contact mode	177
G.4	NSOM transmission mode	179

List of Tables

5.1	<i>Summary of the NC diameters, TIPL maxima and TRPL lifetimes of the surface functionalized Si NCs.</i>	76
6.1	<i>Summary of the fit parameters according to Eq. 6.1 for spectrally-resolved PL dynamics of the functionalized Si NCs. The error in the lifetimes τ_1 and τ_2 is ≤ 0.02 ns. The error in the amplitude coefficients A_1 and A_2 is < 0.005. The value of the constant offset, C (not listed here), ranges from 0.001 - 0.006.</i>	87

List of Figures

2.1	<i>Schematic diagram of the processes involved in photoluminescence. The black dashed arrows indicate vibrational relaxation. E_{ph} = energy of the incident photon, E_{gap} = bandgap energy of the material, E_{PL} = energy of the emitted photon (PL).</i>	7
2.2	<i>Absorption coefficient of GaAs as a function of photon energy (Casey et al. 1975)</i>	9
2.3	<i>Interband transitions in (a) direct bandgap and (b) indirect bandgap materials.</i>	10
2.4	<i>Variation of the energy gap obtained using EMA as a function of nanocrystal diameter</i>	17
3.1	<i>(a) Schematic diagram of the experimental set-up for SSPL, TIPL and nanosecond-TRPL. (b) Photo of the experimental set-up. The TIPL and SSPL were recorded using the CCD while the nanosecond-TRPL was recorded using a single photon avalanche photodiode (SPAD) and analyzed using time-correlated single photon counting (TCSPC).</i>	19
3.2	<i>TIPL of 5.7-nm ammonia functionalized Si NCs by 400 nm pulses at excitation fluence of 2.94 mJ/cm^2. The yellow line shows the transmission spectrum of the long pass filter showing 86% transmission at 450 nm and a sharp decrease in transmission below 450 nm. The blue shaded region is the filter cut-off region.</i>	20
3.3	<i>Spectral line of mercury at 546.5 nm from fluorescent lamp for different entrance slit widths. The best spectral resolution was observed at a slit width of $100 \mu\text{m}$ with a bandwidth of $0.8 \pm 0.1 \text{ nm}$ FWHM indicated by brown arrows.</i>	21
3.4	<i>Schematic diagram of the TCSPC module for ns-TRPL measurements. Adapted with modification from Becker (2005).</i>	23
3.5	<i>The rise time of PL measured with the TCSPC setup showing a time resolution of $50 \pm 4 \text{ ps}$.</i>	24
3.6	<i>Acquisition program for the spectrally-resolved PL lifetime and detailed TRPL. The detailed TRPL records the PL lifetime per wavelength. A sample of the detailed TRPL signal is shown at the upper right window of the picture, a contour plot of the PL intensity as a function of wavelength and time after photoexcitation.</i>	26
3.7	<i>TRPL for acetal functionalized Si NCs. (a) PL intensity as a function of wavelength and time after photoexcitation. (b) Temporal evolution of the PL spectral profile. (c) Spectrally-resolved PL lifetime.</i>	27

3.8	<i>Schematic diagram of the experimental set-up for μs-TRPL measurements.</i>	28
3.9	<i>Alternate set-up for μs-PL lifetime measurements of Si NC films from Al Meldrum's lab.</i>	29
3.10	<i>Schematic diagram of the pump-probe TPA set-up.</i>	31
3.11	<i>Time evolution of the transient absorption signal obtained using the pump-probe method.</i>	32
3.12	<i>THF transmitted signal showing a 500 ± 10 fs full width of half maximum which corresponds to the time resolution of the system. The lock-in amplifier detection setting A-B was set to $20\ \mu$V.</i>	33
3.13	<i>(a) Absolute data A/B. (b) The differential data (A-B)/B as function of delay time. (c) The calibrated $-\Delta T/T_0$.</i>	34
4.1	<i>Brightfield TEM images and size distribution of ensembles dodecyl-passivated Si NCs functionalized via thermal (a-d) and photochemical (e-h) hydrosilylation approaches [Adapted from Yang, De los Reyes et al. 2015].</i>	38
4.2	<i>FTIR and XPS of dodecyl functionalized Si NCs. (a) FTIR of 5 nm hydride terminated (i), thermally-functionalized (ii), and photochemically-functionalized Si NCs (reaction time = 15 hrs (iii), 20 hrs (iv), 30 hrs (v), and 39 hrs (vi)). (b) FTIR of 3 nm dodecyl functionalized Si NCs. High-resolution XP spectra of the Si 2p spectral region for (c,d) thermally-functionalized and (e,f) photochemically-functionalized Si NCs (15 hrs reaction time). Fitting results are shown for the silicon spectrum with Si 2p_{3/2} signals. Si 2p_{1/2} components have been omitted for clarity [Adapted from Yang, De los Reyes et al. 2015].</i>	41
4.3	<i>Time-integrated PL spectra of surface functionalized SiNCs prepared using (a) thermal and (b) photochemical hydrosilylation. (c) Reaction time dependence of PL arising from photochemically-modified SiNCs (d = 5 nm) upon excitation by $\lambda = 400$ nm laser pulses at $1.62\ \text{mJ}/\text{cm}^2$ fluence. Corresponding time-resolved PL decays are shown in panels (d), (e), and (f), respectively where the red lines stretched exponential fits to the data. The inset in panel (e) shows the nanosecond lifetime PL emission at 630 nm and 690 nm for 3 nm and 5 nm SiNCs, respectively. The orange and yellow lines are the biexponential fits to the 5 nm and 3 nm Si NCs, respectively.</i>	43
4.4	<i>Time-resolved PL measured at the indicated wavelengths for 3 nm Si NCs functionalized via (a) photochemical and (b) thermal hydrosilylation. The red curve in (a) is the bi-exponential fit to the experimental data. The PL lifetime for thermal functionalized Si NCs was measured at 715 nm. The standard error for the fitted lifetimes is $\leq 1.5\%$.</i>	45
4.5	<i>Summary of time-integrated PL maxima and time-resolved PL lifetimes for surface functionalized Si NCs. The standard error for the μs-PL lifetime component is $\leq 1\mu$s while that of the ns-PL lifetime is $\leq 1.5\%$.</i>	46
4.6	<i>High-resolution XP spectra of the silicon region for purified functionalized 5 nm SiNCs after (a) 20, (b) 30, and (c) 39 hour photochemical hydrosilylation. Si 2p_{1/2} signals have been omitted for clarity [Adapted from Yang, De los Reyes et al. 2015].</i>	49
4.7	<i>XPS-derived relative oxidation of photochemically functionalized SiNCs as a function of reaction.</i>	50

4.8	(a) Maxima of time-integrated PL spectra and (b) microsecond PL lifetime components for Si NCs prepared using thermal and photochemical hydrosilylation as a function of XPS-derived relative surface oxidation. The shaded area in (a) corresponds to the relative oxidation region in which nanosecond and microsecond PL lifetimes coexist. (c) Time-integrated PL spectra for 5 nm photochemically-functionalized Si NCs with reaction times of 15 and 20 hours. The corresponding magnitude of the spectrally-resolved nanosecond PL decay contribution is also shown.	52
5.1	Characterization details of dodecylamine functionalized Si NCs. (a) Schematic representation of the functionalized Si NCs and (b) visible PL upon excitation by 365 nm from a UV lamp. XPS spectrum of (c) the Si 2p region and (d) the N 1s region. The black line in (d) is a fit to the experimental data. (e) FTIR spectra of (i) neat dodecylamine and (ii) dodecylamine functionalized Si NCs, and (f) bright field TEM image [Adapted from Dasog, De los Reyes et al. 2014].	59
5.2	(a) Time-integrated PL spectra of dodecylamine functionalized SiNCs excited by 400 nm laser pulses at 1.41 mJ/cm ² fluence. (b) TRPL decay measured at 470 nm. The red line in (b) is a bi-exponential fit to the data.	60
5.3	Characterization details of acetal functionalized Si NCs. (a) Scheme for the functionalized Si NCs, (b) visible PL upon excitation by a 365 nm UV lamp, (c) FTIR of hydride terminated Si NCs and acetal functionalized Si NCs, and (d) bright field TEM image [Adapted from Dasog, De los Reyes et al. 2014].	61
5.4	TIPL spectrum of acetal functionalized Si NCs excited by 400 nm laser pulses at an excitation fluence of 1.98 mJ/cm ² . Insets are the proposed scheme and the visible PL upon excitation by 365 nm UV lamp.	63
5.5	Detailed sub-ns TRPL of acetal functionalized Si NCs. (a) PL intensity as a function of wavelength and time after photoexcitation. (b) Temporal evolution of the PL spectral profile and (c) spectrally-resolved PL lifetime extracted from (a). (d) PL lifetimes obtained from the bi-exponential fit of the spectrally-resolved PL decays. The PL was excited by 400-nm pulses at an excitation fluence of 0.56 mJ/cm ²	64
5.6	Characterization details of TOPO functionalized Si NCs. Scheme for TOPO Si NCs functionalized for (a) 8 hours and (c) 4 weeks, while (b,d) are the corresponding visible PL upon excitation by 365 nm UV lamp. (e) FTIR of (i) neat TOPO and (ii) TOPO Si NCs functionalized for 8 hours and (f) is the corresponding bright field TEM image (Veinot Lab).	66
5.7	(a) XPS spectrum of the Si 2p region and (b) XRD analysis of the 4 weeks TOPO functionalized Si NCs (Veinot group).	67
5.8	TIPL of 8 hours (yellow line) and 4 weeks (purple line) TOPO functionalized Si NCs. The PL was excited by 400-nm pulses at an excitation fluence of 2.3 mJ/cm ²	68

5.9	<i>TRPL dynamics of TOPO functionalized Si NCs with (a) 8 hours and (b) 4 weeks reaction time. The inset in panel (a) is the μs-component of the PL lifetime of the 8-hour TOPO functionalized Si NCs measured at an emission wavelength of 600 nm. The PL lifetimes in the sub-ns time scale were measured at 590 nm for the 8-hour TOPO functionalized Si NCs and at 445 and 640 nm for the 4-week TOPO functionalized Si NCs. The red lines are bi-exponential and stretched exponential fits to the ns and μs lifetime components, respectively.</i>	69
5.10	<i>Characterization details of dodecyl functionalized Si NCs. Scheme for Si NCs functionalized in (a) air and in (c) inert atmosphere while (b, d) are the corresponding visible PL upon excitation by 365 nm UV lamp. FTIR and bright field TEM image of dodecyl Si NCs functionalized in inert atmosphere (e and g, respectively) and dodecyl Si NCs functionalized in air (f and h, respectively).</i>	71
5.11	<i>(a) TIPL of dodecyl Si NCs functionalized in air (orange line) and in inert atmosphere (black line). μs- and ns-TRPL of dodecyl Si NCs functionalized in (b) inert atmosphere and (c) air measured at 680 and 650 nm, respectively. The red lines are the stretched exponential and bi-exponential fit to the μs and ns lifetime, respectively.</i>	73
5.12	<i>Solvatochromic studies of (a) dodecylamine and (b) acetal functionalized Si NCs. The position of the PL maximum was monitored as the solvent polarity index was changed. The Si NC concentration was 0.4 mg/mL and the excitation wavelength was 350 nm.</i>	74
6.1	<i>Schemes for (a) ammonia and (c) dodecylamine functionalized Si NCs. Visible PL of (b) ammonia and (d) dodecylamine functionalized Si NCs excited by 365 nm UV lamp. TEM images of ~ 3 nm (e) ammonia and (f) dodecylamine functionalized Si NCs. Histograms of the NC size distribution showing an average diameter of (g) 3.4 ± 0.4 nm for ammonia functionalized Si NCs and (h) 3.1 ± 0.4 nm for dodecylamine functionalized Si NCs.</i>	80
6.2	<i>Electron diffraction pattern of (a) ammonia and (b) dodecylamine Si NCs.</i>	82
6.3	<i>TEM images of ~ 6 nm (a) ammonia and (b) dodecylamine functionalized Si NCs while (c) and (d) are their corresponding size distributions, respectively.</i>	83
6.4	<i>FTIR spectra of (a) ammonium bromide and ammonia functionalized Si NCs and (b) dodecylamine ligand and dodecylamine functionalized Si NCs. (c,d) are the corresponding Raman spectra of functionalized Si NCs.</i>	84
6.5	<i>Transmission spectrum of the long pass filter showing 86% transmission at 450 nm (blue broken line) and a sharp decrease below 450 nm.</i>	85
6.6	<i>TIPL of ~ 3 nm (black) and ~ 6 nm (red) (a) ammonia and (b) dodecylamine functionalized Si NCs excited by 400-nm pulses at an excitation fluence of 0.42 mJ/cm^2. The shaded area represents the cut-off region of the long pass filter. The corresponding ns-TRPL decays at 470 nm are shown in (c) and (d), respectively. The green and blue lines are the bi-exponential fits to the ~ 3 nm and ~ 6 nm Si NCs, respectively. Fit parameters are given in the text and Table 6.1.</i>	86
6.7	<i>Spectrally-resolved ns-PL dynamics of functionalized Si NCs.</i>	88

6.8	<i>Microsecond-TRPL measurements of the functionalized Si NCs at 560 nm using a fast Si photodetector. The photodetector response was measured using scattered light from the 400 nm excitation pulse.</i>	89
6.9	<i>TRPL intensity as a function of wavelength and time for ~3 nm (a) ammonia and (b) dodecylamine functionalized Si NCs. The color scale represents photon counts. (c) and (d) are the corresponding temporally-resolved PL spectra at specific times after excitation and averaged within a time window of 0.4 ns. Comparison of the SSPL (grey shaded area) and the normalized PL of (e) ammonia and (f) dodecylamine functionalized Si NCs. The blue-shaded area represents the cut-off region of the long pass filter. PL was excited by 400-nm pulses at an excitation fluences of 0.48 mJ/cm² and 0.55 mJ/cm² for ammonia and dodecylamine functionalized Si NCs, respectively.</i>	91
6.10	<i>Fluence-dependence of (a) TIPL and (b) ns-TRPL dynamics at 493 nm for ~6-nm ammonia functionalized Si NCs. Insets show the fluence-dependence of the (a) PL intensity and (b) PL lifetimes, respectively. The blue-shaded area represents the cut-off region of the long pass filter.</i>	92
6.11	<i>Normalized absorbance of different sizes of functionalized Si NCs.</i>	94
6.12	<i>Energy diagram for the CT state emission dynamics. Electrons are first photoexcited within the Si NC core and then rapidly transfer to the SiO_xN_y, creating a CT state at the interface. The CT process quenches the emission from the Si core, which is normally expected to emit red PL over μs time scales, as shown by the solid red downward arrow. Radiative recombination of the electron and hole in the CT state results in blue PL over ns time scales, as indicated by a solid blue downward arrow. (CB = conduction band; VB =valence band). The electron transfer (dashed blue arrow) and thermalization times (dashed red downward arrow) are adopted from Trojanek et al. (2006).</i>	96
7.1	<i>(a) SSPL of the Si NC films with different filling fraction excited by 405 nm cw laser at 5 mW. The arrows indicate the peaks of the PL spectra. (b) Comparison of the normalized SSPL and TIPL at different fluences for x =1.4 (ρ_{Si} = 16%).</i>	103
7.2	<i>(a) Microsecond PL decay lifetimes for different silicon volume filling fractions that follows stretched exponential behavior. The standard error is 1 μs for τ and 0.001 for β. The red curve is the fit to the data. (b) Spectrally-resolved PL lifetime and dispersion factor β as a function of emission wavelength for x = 1.4 (β = 16%). Inset: PL decay curves at different emission wavelengths.</i>	105
7.3	<i>ns-TRPL of Si NC films with different silicon filling fractions: (a) 16%, (b) 23%, and (c) 31%. The PL was excited by 400 nm laser pulses at an excitation fluence of 0.25 mJ/cm² [cw=center of the emission wavelength].</i>	108
7.4	<i>TIPL spectra of Si NC films with ρ_{Si} = 16% (x = 1.4) excited by 400 nm laser pulses at an excitation fluence of 2.0 mJ/cm². The ns- and μs-PL lifetime intensities are also shown.</i>	109

7.5	<i>Fluence dependent TRPL of Si NC film with $\rho_{Si} = 16\%$ ($x = 1.4$) in (a) sub-ns and (b) μs-time scales. The ns-TRPL is measured at emission wavelength of 750 nm while the μs-TRPL is the total PL lifetime. Also shown is the dispersion factor β as a function of pump power. Inset is the semi-log plot of the μs-PL lifetime as a function of excitation power.</i>	109
7.6	<i>Effect of Si volume filling fraction on the transient PA decay as probed by 800 nm pulses. (b) Zoom-in of the initial 15 ps of the decay. Excitation fluence is $9.2\mu\text{J}/\text{cm}^2$ and the probe fluence is $6.7\mu\text{J}/\text{cm}^2$. The error in τ is ≤ 0.8 ps while error in β is ≤ 0.004.</i>	110
8.1	<i>Schematic diagram of the high spatial resolution scanning that overcomes the diffraction limit.[Adapted from Synge 1928]</i>	115
8.2	<i>Schematic diagram of the NSOM instrument (Witec Manual 2012). The feedback laser (red line) is used to control the distance between tip and the sample.</i>	116
8.3	<i>SEM images of the cantilever tip showing (a) the pyramid tip and (b) the zoom in of the pyramid tip showing an aperture with diameter of 100 nm.</i>	117
8.4	<i>(a) NSOM transmission image of Al projection pattern and (b) corresponding variation of the count rate along the blue line of the near field transmitted image.</i>	117
8.5	<i>The experimental set-up showing the single mode fiber coupled to the NSOM system.</i>	118
8.6	<i>Schematic diagram of the experimental set-up. The 800 nm laser pulses were free-space coupled to the single mode fiber. The fiber's output pulses exhibiting a 200 fs pulse width was coupled to the NSOM system. A 20\times objective was then used to focus the excitation pulses to the hollow cantilever probe. The transmitted signal was collected by 60\times objective and sent to an APD for NSOM the transmitted image or to the spectrometer for the TIPL and TRPL measurements. A combination of polarizer and half wave-plate was used to control the power input to the fiber as well as the polarization of the input laser pulses to obtain maximum throughput.</i>	119
8.7	<i>(a) Topography of the CdSe/ZnS core-shell nanocrystals cluster drop coated on fused silica glass. (b) Ultrafast NSOM temporally-resolved PL image corresponding to the initial 5.5 ns PL lifetime. (c) Two-photon TIPL spectrum taken at the location marked by a circle on the topography image and (d) the corresponding PL lifetime decay measured at 570 nm. Inset: rise-time of the PL signal is 54 ps, which corresponds to the time resolution of the ultrafast NSOM PL set-up and TCSPC system.</i>	121
8.8	<i>Image of the cantilever probe taken after the time-resolved PL microscopy. Before coupling the excitation pulses to the NSOM, the cantilever aperture is 100 nm in diameter (Fig. 8.3(a)), but after the first scan, was damaged by the excitation pulses.</i>	122
A.1	<i>Spectrally-resolved μs-PL lifetimes of (a) 5 nm and (b) 3 nm thermally-functionalized Si NCs. The red lines are the stretched exponential fit to the data. Inset figures are the normalized PL lifetimes.</i>	147
A.2	<i>Spectrally-resolved μs-PL lifetimes of (a) 5 nm and (b) 3 nm photochemically-functionalized Si NCs. The red lines are the stretched exponential fit to the data. Inset figures are the normalized PL lifetimes.</i>	147

B.1	<i>Comparison of the emission properties of acetal functionalized Si NCs in solution and in films. (a) Time-integrated PL and (b-d) time-resolved PL of acetal functionalized Si NCs in solution (b), in films dropcoated on a quartz glass slide (c), and deposited by UV irradiation using 267 nm pulsed laser(d).</i>	149
B.2	<i>Comparison of the emission properties of dodecylamine functionalized Si NCs in solution and in films. (a) Time-integrated PL, (b) PL lifetime measured at 505 nm, and detailed TRPL of (c) solution and (d) film deposited by UV irradiation using 267 nm pulsed laser. The red curves in (b) is the bi-exponential fit to the data.</i>	151
C.1	<i>Thickness dependence transient photoinduced absorption of Si NC films with filling fractions of $\rho = 16\%$ and (b) 51%. The red curves in (a) are the stretched exponential fit to the data.</i>	153
C.2	<i>UV-Vis absorption of Si NC films with different Si volume filling fractions and thicknesses. (a) has a film thickness of $1\ \mu\text{m}$ and (b) $200\ \text{nm}$. The oscillations observed at lower energy is due to multiple beam interference.</i>	153
D.1	<i>Comparison of the different fitting functions that were tested to describe the μs-PL lifetime behavior functionalized Si NCs. (a) shows the stretched exponential, biexponential, and single exponential fits to the data. Also shown are the values for reduced R^2 and χ^2. Residual plots of the (b) stretched exponential fit, (c) bi-exponential fit, and (d) single exponential fit.</i>	155
E.1	<i>Normalized PL spectra of GaAsBi films under 400 nm and 800 nm excitation.</i>	157
E.2	<i>PL spectra under 800 nm excitation.</i>	158
E.3	<i>Summary of PL peak parameters for 800 nm (filled symbols) and 400 nm (open symbols) excitation.</i>	159
E.4	<i>Integrated PL intensity and slow decay component of THz photoconductivity decay of GaAsBi.</i>	160
E.5	<i>r2208, p-type GaAs, confocal microscopy image (left) and AFM image (right).</i>	161
E.6	<i>r2201, GaAsBi, 0.91% Bi, confocal microscopy image (left) and AFM image (right).</i>	161
E.7	<i>r2205, GaAsBi, 1.4% Bi, confocal microscopy image (left) and AFM image (right).</i>	161
E.8	<i>r2164, GaAsBi, 1.9% Bi, confocal microscopy image (left) and AFM image (right).</i>	162
E.9	<i>r2157, GaAsBi, 3.5% Bi, AFM images.</i>	162
E.10	<i>r2153, GaAsBi, 4.4% Bi, AFM images.</i>	162
E.11	<i>r2148, GaAsBi, 5.5% Bi, AFM images.</i>	163
F.1	<i>Configuring the Hardware Config tab of the SpectraSense software.</i>	165
F.2	<i>Selecting the grating to calibrate.</i>	165

F.3	<i>Acquiring the room lights spectrum.</i>	166
F.4	<i>Performing the calibration at the CCD Survey mode tab.</i>	166
F.5	<i>Setting the center wavelength for the calibration.</i>	167
F.6	<i>Extracting the calibration parameters.</i>	168
F.7	<i>Placing the calibration parameters of the grating for the TIPL and TRPL measurements.</i>	168
F.8	<i>An image of the acquisition labview program, CCD only and PicoHarp.vi, for the spectrally-resolved PL lifetime and detailed TRPL measurements.</i>	172
G.1	<i>Sample image taken from the upper objective.</i>	174
G.2	<i>Sample image taken from the lower objective.</i>	175
G.3	<i>Confocal transmission image of Al deposits.</i>	176
G.4	<i>Confocal reflection image of Al deposits.</i>	177
G.5	<i>Topography of the Al deposits obtained from the AFM contact mode scan.</i>	178
G.6	<i>The image of the Al deposits taken from the upper objective (left) and lower objective (right) at bright field.</i>	179
G.7	<i>Focused laser on the image of the Al deposits taken from the upper objective (left) and lower objective (right) at dark field.</i>	179
G.8	<i>Image of the NSOM tip at bright field (left) with the focused laser centered at its hole (right).</i>	180
G.9	<i>Image taken from the lower objective at dark field (left) with increased intensity of laser beam (right).</i>	180
G.10	<i>NSOM images of the Al deposits. The image on the left is the topography while the one on the right is the transmitted image.</i>	181

List of Abbreviations

AQY	Absolute quantum yield
BBO	Barium borate
CCD	Charge-coupled device
CT	Charge transfer
FTIR	Fourier transform infrared
NC	Nanocrystal
NSOM	Near-field scanning optical microscopy
PL	Photoluminescence
QC	Quantum confinement
QY	Quantum yield
Si NC	Silicon nanocrystal
SPAD	Single photon avalanche photodiode
SSPL	Steady-state photoluminescence
STS	Scanning tunneling spectroscopy
TCSPC	Time-correlated single photon counting
TEM	Transmission electron microscopy
TIPL	Time-integrated photoluminescence
TOPO	Trioctylphosphine oxide
TPA	Transient photoinduced absorption
XPS	X-ray photoelectron spectroscopy

XRD	X-ray diffraction
fs	femtosecond
μ s	microsecond
μ s-PL	microsecond-photoluminescence
ns	nanosecond
ns-PL	nanosecond-photoluminescence
ps	picosecond

CHAPTER 1

Introduction

Silicon nanocrystals (Si NCs) exhibit interesting properties which have potential applications in the field of optoelectronics, ultrafast data communication and data storage (Link *et al.* 2003), photovoltaic devices (Luterova *et al.* 2002,) and biological imaging (Erogbogbo *et al.* 2008). Despite these important practical devices, no clear consensus regarding the origin of optical emission from Si NCs exists (Kim *et al.* 2012, de Boer *et al.* 2010, Sung *et al.* 2007, Garcia *et al.* 2003, Wolkin *et al.* 1999, Fan *et al.* 1998, Kovalev *et al.* 1994, Kanemitsu *et al.* 1994). Bulk Si is a poor light emitter because of its indirect band gap (1.1 eV) which makes the radiative recombination dominated by non-radiative processes. Non-radiative recombination processes in bulk silicon are typically dominated by Shockley-Hall-Read recombination at mid gap states arising from defects or impurities in the crystal (Shockley *et al.* 1952, Hall 1952). In nanocrystals that are small enough to show quantum confinement (QC) effects, such defects are thermodynamically unfavorable and tend to grow out of the quantum dot (QD) (Walters 2007). Two other recombination mechanisms that contribute to the inefficiency of light emission in bulk silicon are recombination at surface defects (Wagner *et al.* 1995) and Auger recombination (Pavesi *et al.* 2004, Pavesi *et al.* 2012), in which the energy of the excited-electron is transferred to a third charge carrier. Both of these mechanisms can be more significant in Si NCs compared bulk silicon, to the extent that a single surface defect or a single extra free charge carrier can effectively quench the core state emission (Credo *et al.* 1999, Khriachtchev *et al.* 2001, Pavesi *et al.* 2003). The enhanced sensitivity to surface recombination

can be understood by noting the high surface-to-volume ratio, while the rapid Auger recombination rate in excited nanocrystals results from the large effective carrier concentration that a single carrier represents in the small nanocrystal volume.

On the other hand, visible luminescence at room temperature in different Si NC sample configurations such as Si NCs embedded in an oxide or nitride matrix (Dal Negro *et al.* 2006), in Si NC core-shell structures (Biteen *et al.* 2004) and in colloidal Si NCs with different surface passivations (Yang, de los Reyes *et al.* 2015, Lopez *et al.* 2014) has been demonstrated. Luminescence from Si nanostructures has been classified into two distinct categories: emission from the Si core due to QC (Hessel *et al.* 2011, Dohnalova *et al.* 2010) and emission from surface/interface-defect states (English *et al.* 2002, Voos *et al.* 1992). While the existence of these emissive states is generally accepted, the reported origin of the nanosecond (ns) and microsecond (μ s) photoluminescence (PL) lifetimes is not consistent. In this work, we will attempt to address these issues by exploring the ultrafast dynamics of colloidal Si NCs and Si NCs in a SiO₂ matrix. The effect of the NC size and surface passivation on the emission dynamics will be investigated using time-integrated photoluminescence (TIPL), time-resolved photoluminescence (TRPL), and pump-probe transient absorption spectroscopies.

PL spectroscopy is an optical technique used for the characterization of a variety of material properties such as optical properties and discrete electronic states (Meyers 2000). A typical PL spectroscopy set-up provides a simple, non-destructive, non-contact method capable of investigating a material's bandgap (Behren *et al.* 2000), doping/impurity levels (Xu *et al.* 1998), recombination mechanisms (Robertson 1996), and material surface quality (Gfroerer 2000). In addition, PL spectroscopy can be modified to investigate ultrafast processes in materials, such as charge carrier dynamics. TRPL spectroscopy using time-correlated single photon counting is capable of investigating fast charge carrier dynamics in the ns and sub-ns time scales (Buschmann *et al.* 2013). By measuring the time between sample excitation by a pulsed laser and the arrival of the emitted photon at the detector, this spectroscopic technique can determine charge carrier recombination lifetimes (Tessler *et al.* 1993), carrier transport (Metzger *et al.* 2005) and quantum efficiencies in materials (Kim *et al.* 2010).

Another time-resolved technique, the pump-probe transient absorption spectroscopy is capable of probing the electronic and structural changes of short-lived excited states in materials (Berera *et al.* 2009). In this method, two ultrashort pulses are used. The first pulse is the pump used to excite the sample. The second pulse is the probe used to precisely monitor the state of the system after a time delay between the pulses. By monitoring the transient absorption of the material, the evolution of the excited states as a function of the time delay over fs to ns time scales can be characterized (Wakeham *et al.* 2000).

One of the most intriguing aspects of light emission from Si NCs is the role of surface oxygen. Recent reports indicate that oxygen induces a PL red shift accompanied by an increase in PL lifetime from ns to μ s (Dohnalova *et al.* 2009, Wolkin *et al.* 1999). Contrasting this suggestion is the report that silicon-oxygen species on the NC surface induce a short-lived PL that is inconsistent with QC (Yang, de los Reyes *et al.* 2015, Kim *et al.* 2012, Tsybeskov *et al.* 1994). These results clearly show the lack of consensus on the role of oxygen on the emission dynamics of Si NCs. While this might originate from differences in sample preparation, this work studies the effect of surface oxidation on the emission properties of dodecyl functionalized Si NCs prepared using two complementary synthesis techniques. The samples were made by Johnathan Veinot's group in the Chemistry Department of the University of Alberta. We then correlated the PL emission dynamics to the amount of oxidation of dodecyl functionalized Si NCs.

Si NCs have been considered for potential light-emitting applications (Dal Negro *et al.* 2003, Cheng *et al.* 2010, Hirschman *et al.* 1996). However, emission from nanostructured Si is still considered inefficient compared to that from direct gap III-V (Harris *et al.*, 2012, Mi *et al.*, 2009) and II-VI (Dabbousi *et al.* 1997, Alivasatos 1996) semiconductor quantum dots that exhibit higher quantum yield (QY) and fast radiative recombination rates. Initial attempts in improving light emission in Si were focused on exploiting the influences of quantum confinement via particle reduction (Holmes *et al.* 2001, Vinciguerra *et al.* 2000). While this method demonstrates that PL emission in Si NCs can be tuned across the visible spectrum, a dramatic decrease in PL QY was observed as the NC size was reduced down to 2 nm (Miller *et al.* 2012, Mastronardi *et al.* 2011, Garcia *et al.* 2003). This observation was explained in terms of the significant increase in the non-radiative recombination

channels at the surface/interface of the NCs. In this study, we will investigate the effects of surface passivation on the emission dynamics in Si NCs (De los Reyes *et al.* 2015). Specifically, the origin of the PL emission will be explored and contrasted with core state emission using TIPL and TRPL spectroscopy.

Of the observed visible-range PL, blue emission from Si NC is considered the most intriguing due to the indirect bandgap of Si. Pure-blue emission is commonly reported in porous silicon (Lee *et al.* 1993, Mizuno *et al.* 1996, Koyama *et al.* 1998) but rarely observed Si NCs (only in Si NCs with diameters ≤ 1.5 nm) (Nayfeh *et al.* 2001, Rosso-Vasic *et al.* 2009, Shiohara *et al.* 2011). These observations limit the potential application of Si NCs in light emitting sources such as full color displays. In light of this, the mechanism of blue emission in dodecylamine and ammonia functionalized Si NCs that have average diameters beyond the strong confinement region (> 5 nm) will be explored (Yang, de los Reyes *et al.* 2015). Fourier transform infrared spectroscopy (FTIR), Raman spectroscopy, ns- and μ s-TRPL spectroscopy, fluence-dependent TIPL and TRPL measurements will be utilized to elucidate the origin of the blue emission.

Si NC composite films that contain mainly isolated nanocrystals are promising candidates for Si-based lasers (Pavesi *et al.* 2000), light emitting diodes (Wang *et al.* 2009), and optical memory elements (Ostraat *et al.* 2001) due to the non-radiative recombination rates and suppressed diffusion of carriers to trap states. Among other forms of Si NCs, Si NCs embedded in an amorphous SiO₂ matrix have gained considerable interest due to their PL stability with time for light emission applications and nanoelectronics applications (Wang *et al.* 2007, Hryciw *et al.* 2005, Meldrum 2004, Heitmann *et al.* 2005). However, PL emission in this material system is always affected by carrier trapping at surface or interface states. As a result, a contradicting interpretation of the observed μ s-PL lifetime component exists. Some groups attributed the μ s-PL to radiative recombination within the Si core based on temperature-dependent TRPL measurements (Dovrat *et al.* 2004, Wen *et al.* 2007). Other groups assigned it to recombination of carriers trapped on surface/interface states (Trojanek *et al.* 2006, Sykora *et al.* 2008). It is clear from those reports that a complete picture of the relaxation and recombination processes in this material system has not yet been established. To address this, the carrier dynamics in Si NC films over sub-picosecond, sub-nanosecond, and

microsecond time scales will be studied to obtain a clearer picture of the dynamics of photoexcited carriers and light emission in this material system.

Finally, 800 nm 65 fs laser pulses were coupled to a near-field scanning optical microscope (NSOM). NSOM has been widely used for PL microscopy with sub- μm resolution studies involving organic, biological (Raymond 2011, Szymanski *et al.* 2005, Lewis *et al.* 1998), and semiconductor nanostructures (Leong *et al.* 1996, Gregor *et al.* 1995, Grober *et al.* 1994). Recently, NSOM PL has also been used for direct photocurrent mapping of organic solar cells (McNeill *et al.* 2004). The newly developed ultrafast NSOM system is suitable for studying spatially-resolved PL emission in semiconductor nanostructures.

CHAPTER 2

Photoluminescence

2.1 Introduction

Luminescence is the emission of light from any substance that occurs from electronically excited states. While it can occur by a number of mechanisms, however, this thesis will focus on the emission of light after absorption of a photon, which is referred to as photoluminescence (PL). PL has become a standard non-contact method for the characterization of semiconductor properties. In addition, PL can be used to determine energy levels, concentration of impurities, defects and other fundamental properties of semiconductors (Stradling *et al.* 1990, Collins *et al.* 1957).

Typically, PL in semiconductors involves three processes, as shown in Fig. 2.1. First an electron is promoted to a higher excited state by absorption of a photon (1). This process requires that the energy of the incident photon, E_{ph} , must be higher than the bandgap, E_{gap} , of the material. After excitation, the photoexcited electron (hole) relaxes non-radiatively (vibrational relaxation) to the bottom (top) of the conduction band (valence band) (2). Finally, the electron recombines with the hole by releasing a photon that has energy lower close to the bandgap energy of the semiconductor (3). The difference in the emission and excitation energy is referred to as the *Stokes shift*.

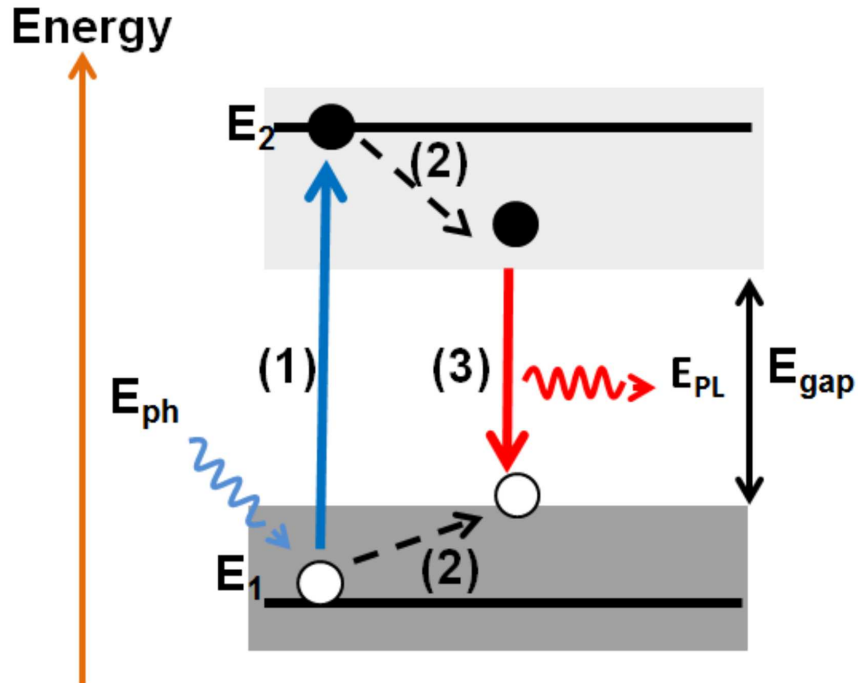


Figure 2.1: Schematic diagram of the processes involved in photoluminescence. The black dashed arrows indicate vibrational relaxation. E_{ph} = energy of the incident photon, E_{gap} = bandgap energy of the material, E_{PL} = energy of the emitted photon (PL).

2.2 Interband transitions

2.2.1 Absorption

Absorption occurs when the photon energy of the incident light is resonant with excitations in a material. The absorption of light by an optical medium can be quantified by its absorption coefficient, α . The absorption coefficient is defined as the amount of power absorbed per unit length of a medium (Fox 2004). If the beam of light is propagating in the z direction, and the intensity (optical power per unit area) at position z is $I(z)$, then the decrease in the intensity in an incremental distance dz

is given by

$$dI = -\alpha dz \times I(z) \quad (2.1)$$

Integrating Eq. (2.1) will give the intensity $I(z)$ at any distance z along the medium

$$\int_{I_0}^{I(z)} \frac{dI}{I} = \int_{z=0}^z -\alpha dz \quad (2.2)$$

$$\ln \frac{I(z)}{I_0} = -\alpha z \quad (2.3)$$

$$I(z) = I_0 e^{-\alpha z} \quad (2.4)$$

where the I_0 is the intensity at $z = 0$. The absorption coefficient can be a strong function of frequency (photon energy), so that the material may absorb one color but not another. Figure 2.2 shows the typical absorption spectrum for GaAs (Casey *et al.* 1975). Based on this graph, the optical absorption edge is located at 1.42 eV (873 nm). This indicates that only incident photons that have energies higher than 1.42 eV will be absorbed by the material. In addition, the absorption edge corresponds to the separation in energy between the bottom of the conduction band and the top of the valence band, or simply the bandgap of the material.

In a crystal, the optical absorption spectra are observed as a result of electronic transitions of the electrons from the valence band to the conduction band, as illustrated in Fig. 2.1. Applying the law of conservation of energy, Fig. 2.1 implies that $E_2 = E_1 + E_{ph}$ where E_2 is the energy of the electron at the final state, E_1 is the energy of the hole and E_{ph} is the energy of the incident photon. It is evident from the figure that the minimum energy needed to excite an electron is $E_2 - E_1 = E_{gap}$, which is the absorption threshold, as discussed above. Hence, interband transitions will occur when $E_{ph} > E_{gap}$.

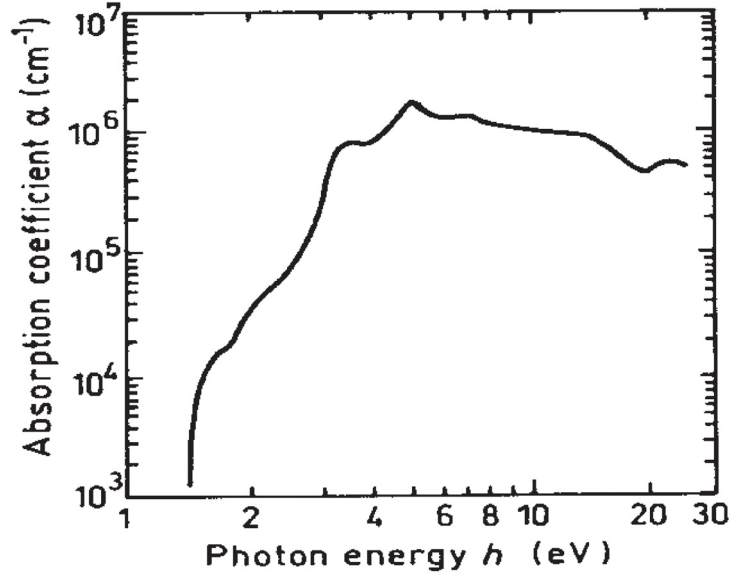


Figure 2.2: Absorption coefficient of GaAs as a function of photon energy (Casey et al. 1975)

Aside from conservation of energy, interband transition also requires that the momentum of the system must be conserved, that is

$$\vec{k}_2 - \vec{k}_1 = \vec{k}_{ph} \quad (2.5)$$

where k_1 and k_2 refer to the momentum of the hole and the electron, respectively, and k_{ph} is the momentum of the incident photon. Since the wavelength of the incident photon is much longer than the lattice constant, k_{ph} is much smaller than the reciprocal of the lattice constant, hence the photon momentum can be neglected from Eq. (2.5). This implies that in an (E,k) diagram, the transitions will be vertical.

2.2.1.1 Absorption in direct and indirect bandgap materials

A material has a direct bandgap when both the bottom of the conduction band and the top of the valence band occur at the center of the Brillouin zone where $k = 0$, as shown in Fig. 2.3(a). In

an indirect gap material, however, the bottom of the conduction band does not occur at $k = 0$ but rather at some other value of k which is usually at the zone edge or close to it (Fig. 2.3 (b)) (Kittel 2005, Fox 2004). As discussed above, absorption requires that both energy and momentum of the crystal must be conserved. It is apparent in Fig. 2.3(b) that in an indirect bandgap material, it is not possible to promote the electron to the minimum of the conduction band by absorption of a photon alone. The electron wave vector k must change significantly, either by emitting a phonon or absorbing a phonon to conserve its momentum. Conservation of energy implies that the energy of the excited electron is $E_{ph} = E_1 + E_{gap} \pm \hbar\Omega$ while conservation of momentum becomes $\hbar k_2 = \hbar k_1 \pm q$ where $\hbar\Omega$ and q is the energy and wave vector of the phonon, respectively (Fox 2004). In contrast, a direct bandgap material does not require a phonon for absorption across the bandgap.

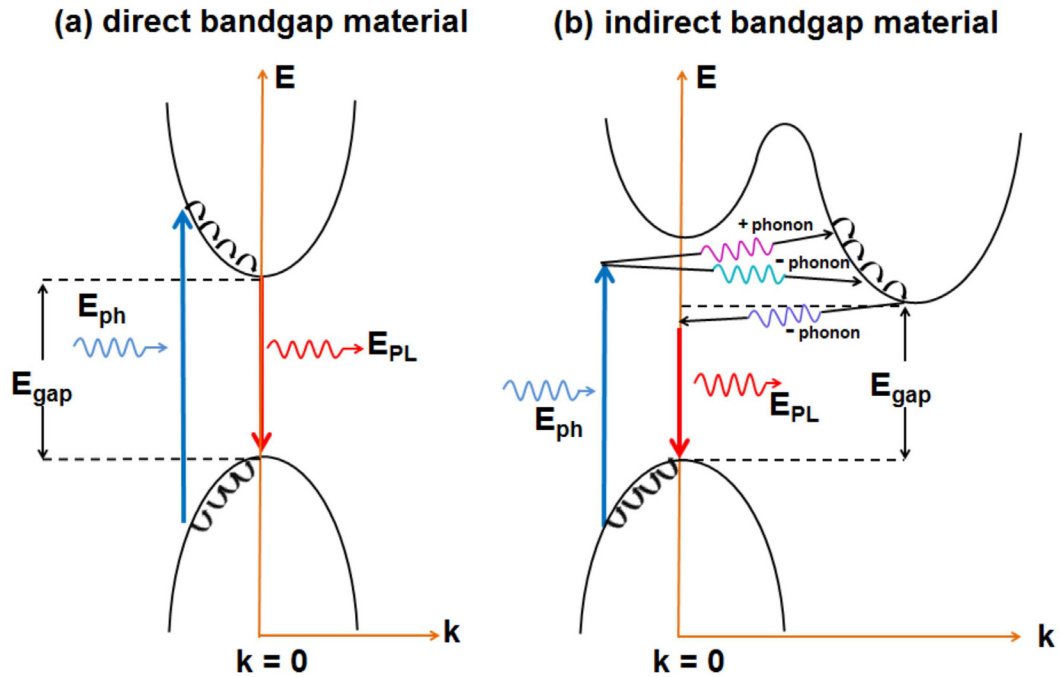


Figure 2.3: Interband transitions in (a) direct bandgap and (b) indirect bandgap materials.

As shown in Fig. 2.2, the absorption coefficient of a material strongly depends on the frequency.

For a direct gap material, the dependence of the absorption coefficient on frequency is given by $\alpha(\hbar\omega) \propto (\hbar\omega - E_g)^2$ while for indirect gap material $\alpha(\hbar\omega) \propto (\hbar\omega - E_g \mp \hbar\Omega)^2$.

2.3 Spontaneous Emission/Radiative recombination

When a semiconductor absorbs a photon, an electron-hole pair is created. The excited electron thermalizes quickly with the lattice and resides in a region at the bottom of the conduction band. Thermalization is generally achieved by phonon emission. The holes follow similar relaxation processes. The electron then recombines with the hole by emitting a photon, a process called *radiative recombination or spontaneous emission*. Since the momentum of the photon is negligible compared to the momentum of the electron, the electron and hole must have the same \mathbf{k} vector. Hence, radiative recombination is represented by a vertical arrow in a (E,k) diagram.

Radiative recombination is readily observed in direct bandgap semiconductor materials, as illustrated in Fig. 2.3(a). Emission from a direct bandgap material occurs without any phonons so that radiative lifetimes are typically within 10^{-8} to 10^{-9} s (Vivien *et al.* 2013). Hence, the luminescence efficiency is normally high. On the other hand, radiative recombination in an indirect gap material requires the participation of a phonon to conserve momentum. The requirement of emitting both a phonon and a photon makes the radiative recombination a second-order process and thereby much less probable than direct transitions in direct gap materials. This process is normally observed in the microsecond to second time scales. Hence, radiative recombination in indirect gap materials is normally weak because of the competition with faster non-radiative processes.

2.3.1 Non-radiative recombination

Radiative recombination is not the only pathway for the electron to recombine with the hole. Normally, there are several alternative pathways between the excited state and ground state which do not require emission of a photon. Auger processes, for example, could be responsible for the non-radiative recombination of electrons and holes. In Auger processes, an electron undergoes an

interband transition by giving its energy to another electron in the conduction band which is then brought to a higher level in the same band (Grundmann 2010). Auger recombination is a non-linear process that strongly depends on excitation fluence or the doping level of the material. The carrier lifetime for the Auger process is written as

$$\tau_A = \frac{1}{Cn^2} \quad (2.6)$$

where C is the Auger coefficient and n is the density of excited carriers.

Aside from Auger processes, excited electrons might also lose their energy as heat by emitting phonons, or they can transfer their energy to impurities or defects/traps. Non-radiative recombination processes could possibly dominate the radiative recombination if the former occurs on a faster time scale (Fox 2004).

2.3.2 Radiative Recombination Rate

The rate of spontaneous emission for radiative transitions between excited (level 2) and ground (level 1) states is directly dependent on the population of the excited electrons N in level 2 and the probability A that the electron in level 2 will transition to level 1 by emitting a photon. The number of emitted photons at any time t can be expressed as a rate equation given by

$$\frac{dN}{dt} = -A_{21}N \quad (2.7)$$

where A_{21} is the coefficient of transition and the subscript 2-1 indicates transition from level 2 (excited state) to level 1 (ground state). Integrating Eq. (2.7) to solve for N gives

$$\int_{N(0)}^{N(t)} \frac{dN}{N} = - \int_0^t A_{21} dt \quad (2.8)$$

$$\ln \frac{N(t)}{N(0)} = -A_{21}t \quad (2.9)$$

$$N(t) = N(0)e^{-A_{21}t} \quad (2.10)$$

$$N(t) = N(0)e^{-\frac{t}{\tau_r}} \quad (2.11)$$

Equation 2.10 shows that the number of emitted photons follows an exponential decay; hence the probability A_{21} is equal to the inverse of the characteristic time decay constant τ_r explicitly shown in Eq. (2.11). This time constant is the natural radiative lifetime of the excited state.

2.4 Photoluminescence decay time and quantum yield

In general, the behavior of the excited carriers is described by Eq. (2.7). Extending this rate equation to accommodate all de-excitation processes (radiative and non-radiative) and changing the variable A_{21} to k which is the rate of all deexcitation processes, Eq. (2.7) becomes

$$\frac{dN}{dt} = -kN + c(t) \quad (2.12)$$

where the $c(t)$ is an arbitrary function of time describing the time course of excitation (Fukuda 1999). When the excitation source is switched off at $t = 0$, integrating Eq. (2.12) will yield

$$N(t) = N(0)e^{-kt}. \quad (2.13)$$

Equations 2.11 and 2.13 imply that k is equal to $1/\tau$, where τ is the PL lifetime of the material. The de-excitation rate k is the sum of the rates of all possible recombination pathways given by

$$k = k_r + k_1 + k_2 + k_3 + \dots \quad (2.14)$$

$$\therefore k = k_r + k_{nr} \quad (2.15)$$

where k_r is the radiative recombination rate and k_{nr} is the sum of the rates of all non-radiative recombinations. In terms of the lifetime,

$$\frac{1}{\tau} = \frac{1}{\tau_r} + \frac{1}{\tau_{nr}} \quad (2.16)$$

where τ is the total lifetime, and τ_r and τ_{nr} are the lifetimes for radiative and non-radiative recombination processes, respectively. If $\tau_r \gg \tau_{nr}$ (or $\tau_r \ll \tau_{nr}$), the PL lifetime $\tau \sim \tau_r$ (or $\tau \sim \tau_{nr}$). In general, the lifetime is the time it takes for the number of excited carriers to decay to $1/e$ or 36.8% of the original population.

The luminescent efficiency or PL quantum yield (QY) is the ratio of the number of photons emitted to the number absorbed. Since both the rate constants k_r and k_{nr} both depopulate the excited states, the QY can be calculated by getting the fraction of the excited carriers that recombine radiatively. By dividing Eq. (2.7) by Eq. (2.12) with $A_{21} = \frac{1}{\tau_r}$ and $c(t) = 0$, then

$$QY = \frac{1/\tau_r}{k} \quad (2.17)$$

$$\therefore QY = \frac{k_r}{k_r + k_{nr}} \quad (2.18)$$

2.5 Photoluminescence in quantum dot materials

Quantum dots (QD) are tiny particles or nanocrystals (NC) of semiconducting material with diameters in the range of 2-10 nm (Ekimov *et al.* 1981). QDs display unique electronic properties, intermediate between those of bulk semiconductors and discrete molecules (Collier *et al.* 1998, Ashoori *et al.* 1996, Kastner *et al.* 1993). QDs have zero-dimensional properties with quantized energy levels for all directions of motion. Assuming that an infinite barrier is present in all directions, the energy level of a rectangular dot with dimensions d_x, d_y, d_z is given by

$$E(n_x, n_y, n_z) = \frac{\hbar^2 \pi^2}{2m^*} \left(\frac{n_x^2}{d_x^2} + \frac{n_y^2}{d_y^2} + \frac{n_z^2}{d_z^2} \right) \quad (2.19)$$

where n_x, n_y, n_z specify the quantized levels in each direction, \hbar is the reduced Planck constant, and m^* is the effective mass of the particle .

Generally, as the size of the crystal decreases, the difference in energy between the highest point in the valence band and the lowest point in the conduction band increases. Due to their small size, the electrons in QDs are confined in a small space (quantum box). When the radii of the semiconductor nanocrystals are smaller than the exciton Bohr radius (average distance between the electron in the conduction band and the hole in the valence band), there is quantization of the energy levels according to Pauli's exclusion principle (Bawendi *et al.* 1990, Reimann *et al.* 2002).

The quantum size effects become significant when at least one of the dimensions of a structure is comparable to the de Broglie wavelength, $\lambda_{dB} \equiv h/p$ (Fox 2004). The limit to quantum confinement can be obtained by visiting the Heisenberg uncertainty principle. According to this principle, the position and momentum of a particle cannot be simultaneously measured with high accuracy. If a particle is confined to a region Δx along the x axis, then an uncertainty in its momentum p will be observed, given by

$$\Delta p_x \sim \frac{\hbar}{\Delta x} \quad (2.20)$$

If the particle is free to move, the confinement in the x direction will give it an additional kinetic energy equal to the confinement energy, E_{QC}

$$E_{QC} = \frac{\Delta p_x^2}{2m} \sim \frac{\hbar^2}{2m(\Delta x)^2} \quad (2.21)$$

This confinement energy is significant only if it is comparable to or greater than the particle's kinetic energy as a result of thermal motion, that is

$$E_{QC} \sim \frac{\hbar^2}{2m(\Delta x)^2} > \frac{1}{2}k_bT \quad (2.22)$$

From this it implies that quantum confinement effects will only be observed when

$$x_{QC} \leq \sqrt{\frac{\hbar^2}{2mk_bT}} \quad (2.23)$$

where k_b is Boltzmann's constant, and T is the temperature in Kelvin.

The most apparent effect of miniaturization of the material is in the absorption onset and in the luminescence. More energy is needed to excite the dot compared to bulk material, and concurrently, more energy is released when the crystal returns to its ground state, resulting in a PL shift from red to blue. As a result of this phenomenon, quantum dots can emit any color of light from the same material simply by changing the dot size. Additionally, because the size of the quantum dot can be controlled during synthesis, emission from these nanostructured materials can be easily tuned (Yoffe 2001). The size dependence of the optical properties in nanocrystals is a consequence of quantum confinement effects.

Different theoretical modelling has been reported to simulate the PL emission from quantum dots. Some of the commonly used approximation methods are effective mass approximation theory (EMA) (Brus 1999), empirical tight binding (Niquet *et al.* 2000), empirical pseudopotential method (Franceschetti *et al.* 2000), Wetzell-Kramers-Brillouin approximation (Loockwood *et al.* 2006), to name a few. Among these approximation methods, EMA is widely used. In this method, electrons e and holes h are confined in a small space. For a 'spherical dot' of radius R_0 in the strong confinement limit such that $R_0 \ll a_x$ (where a_x is the Bohr radius), e and h have no excitonic bound state. Also, Coulomb interaction between e and h can be significant and should be accounted for. The total energy becomes,

$$E = E_{gap} + \frac{\hbar^2 \pi^2}{2m_e^* R_0^2} + \frac{\hbar^2 \pi^2}{2m_h^* R_0^2} - 1.786 \frac{e^2}{\epsilon R_0} \quad (2.24)$$

where E_{gap} is described in section 2.1. The second and third terms are the quantum confinement energies of e and h (Eq. 2.21) and the fourth term is the Coulomb interaction term where e is the elementary charge and ϵ is the bulk optical dielectric constant or relative permittivity. Comparing the latter term with the exciton Rydberg energy $R_y^* = \frac{e^2}{2\epsilon R_0}$ and that for the strong confinement limit, $R_0 \ll a_x$, it shows that the Coulomb interaction cannot be simply ignored in small quantum dots (Gaponenko 2003) such as in the case of semiconductor nanocrystals. Eq. (2.24) can be simplified by using the reduced mass μ ,

$$\mu = \left(\frac{1}{m_e^*} + \frac{1}{m_h^*} \right)^{-1} \quad (2.25)$$

$$\therefore E = E_{gap} + \frac{\hbar^2 \pi^2}{2\mu R_0^2} - 1.786 \frac{e^2}{\epsilon R_0} \quad (2.26)$$

This equation is known as the *effective mass approximation* (EMA) normally used for estimating optical emission energy in nanostructures.

In case of Si, the bulk exciton Bohr radius is 4.9 nm (Beard *et al.* 2007, Lockwood 1994) which indicates that a strong confinement is observed for $R_0 < 4.9$ nm. All the samples we studied in this thesis are within the strong confinement regime. Using Eq. (2.26), the emission in Si NCs as a function of NC size (assuming the emission is due to QC only) is plotted in Fig. 3.4, using $\epsilon=11.68$, $m_e^* = 0.19m_o$ and $m_h^* = 0.286m_o$ where m_o is the free electron rest mass (Hessel *et al.* 2011).

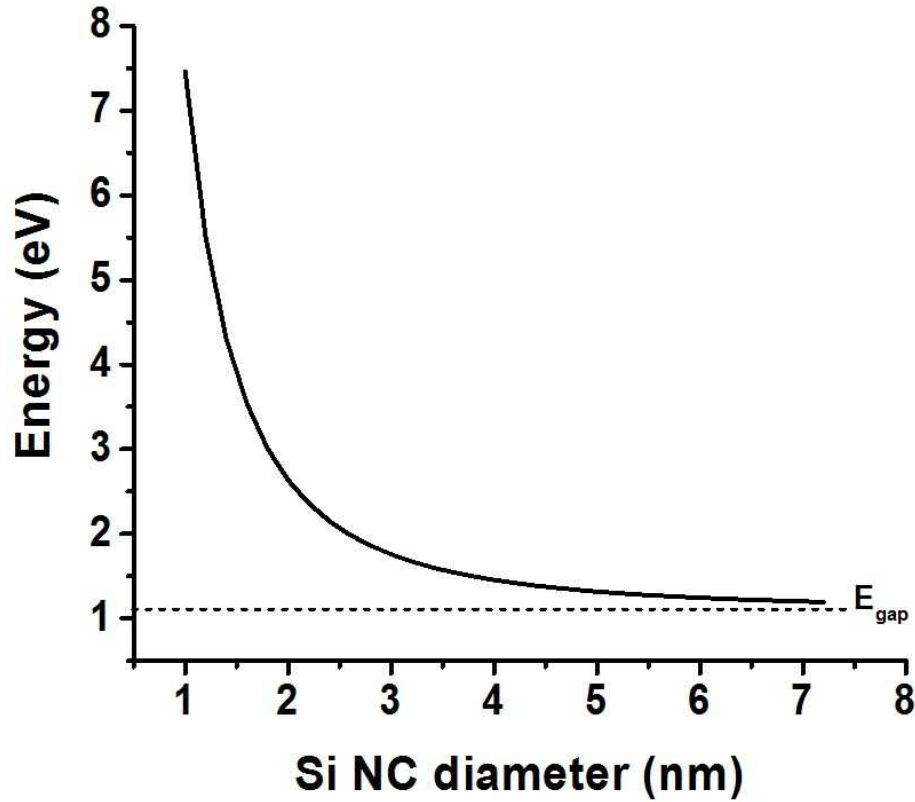


Figure 2.4: Variation of the energy gap obtained using EMA as a function of nanocrystal diameter

CHAPTER 3

Ultrafast photoluminescence spectroscopy

In this study, several ultrafast laser spectroscopy methods were employed to study the PL emission and carrier dynamics in colloidal functionalized silicon nanocrystals (Si NCs) and Si NC films with different volume filling fractions. Time-integrated photoluminescence (TIPL) and steady state photoluminescence (SSPL) spectroscopy were used to monitor the PL emission of the Si NCs while time-resolved PL (TRPL) was used to study the recombination lifetime of the excited carriers over sub-nanosecond to microsecond time scales. Optical pump-probe transient photoinduced absorption (TPA) spectroscopy of Si NC films was also conducted to probe the carrier dynamics at sub-picosecond time scales after photoexcitation.

3.1 Time-integrated PL and steady state PL spectroscopy

Figure 3.1 shows a schematic diagram and a picture of the experimental set-up in confocal geometry. The excitation source is either a 406 nm continuous wave diode laser (Toptica, iBeam-405-S) or a 400 nm second harmonic signal from a barium borate (BBO) crystal pumped by 800 nm pulses from a Ti:Sapphire laser (RegA900, 65 fs pulse width and 250 kHz repetition rate), for SSPL and TIPL, respectively. The excitation light was focused on the sample using a 20 \times , 200-mm focal length microscope objective (Mituyo, M Plan Apo). The TIPL and SSPL spectra were recorded using

a thermoelectric-cooled charge-coupled device (CCD) (Acton Pixis 400B, Princeton Instruments) coupled to a spectrometer (Acton SP2500, Princeton Instruments). The PL spectra were integrated for 120s and corrected to the spectral response of the system. A 435-nm long pass filter (Edmund optics) was placed at the entrance of the spectrometer to block the scattered light from the excitation pulses. The transmission of the long pass filter was 86% at 450 nm, followed by a sharp decrease in transmission at shorter wavelengths, as shown in Fig. 3.2. The filter cut-off region is shown as a blue shaded area in all the PL spectral plots.

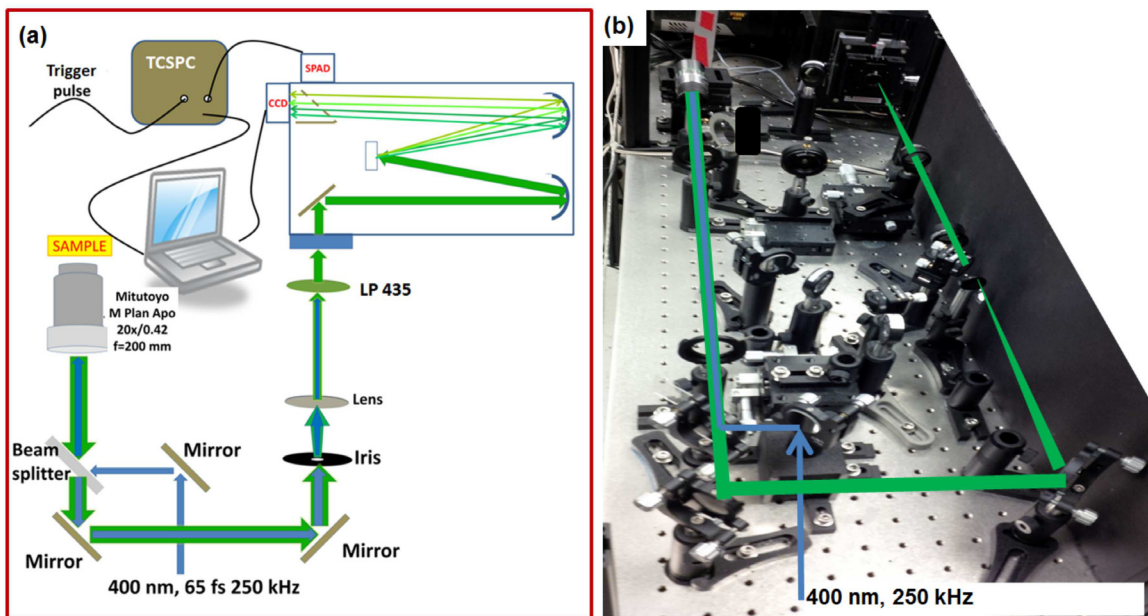


Figure 3.1: (a) Schematic diagram of the experimental set-up for SSPL, TIPL and nanosecond-TRPL. (b) Photo of the experimental set-up. The TIPL and SSPL were recorded using the CCD while the nanosecond-TRPL was recorded using a single photon avalanche photodiode (SPAD) and analyzed using time-correlated single photon counting (TCSPC).

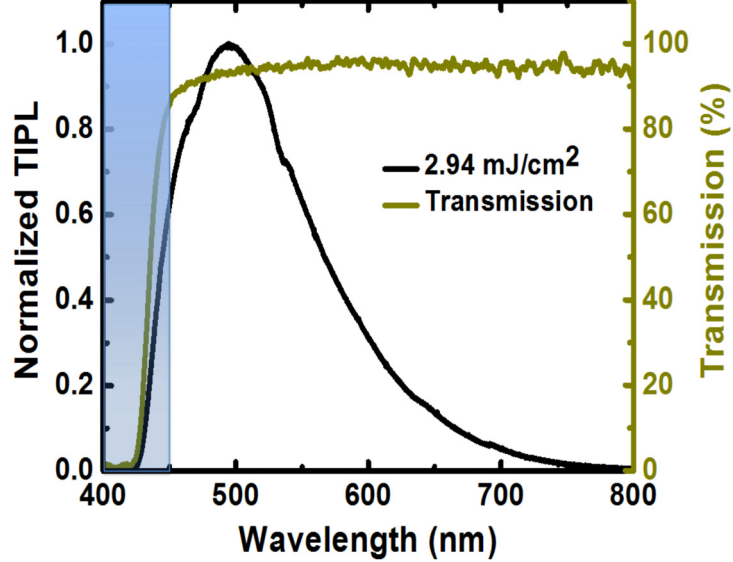


Figure 3.2: TIPL of 5.7-nm ammonia functionalized Si NCs by 400 nm pulses at excitation fluence of 2.94 mJ/cm^2 . The yellow line shows the transmission spectrum of the long pass filter showing 86% transmission at 450 nm and a sharp decrease in transmission below 450 nm. The blue shaded region is the filter cut-off region.

The wavelength calibration of the spectrograph was performed by using the room lights and centering the graph to the well-known 546.5 nm mercury spectral line using the spectrasense software. The spectral lines were collected using a CCD with spectral resolution of 0.09 nm for a grating with 1200 g/mm. A 300 g/mm grating was used in all the experiments because its blaze wavelength is 522 nm. The spectral response of the system was calibrated using a blackbody source of known temperature (LS-1 Tungsten Halogen Light source, 2800 K). Using Planck's law of blackbody radiation (Kutner 2003),

$$I(\nu, T) = \frac{2h\nu}{c^2} \frac{1}{e^{\frac{h\nu}{k_B T}} - 1} \quad (3.1)$$

(where I is the intensity as function of frequency and temperature, ν is the frequency, h is Planck's constant, c is the speed of light and T is the temperature in Kelvin), the theoretical spectra of the blackbody source was compared to the uncorrected spectra, and a calibration function was obtained and incorporated into the acquisition software. The entrance slit width was also calibrated to obtain

the best resolution. Figure 3.3 shows the spectral line from fluorescent room lights for different slit widths. The broad peak at 546.5 nm matches the mercury spectral line but the origin of the peak at 549 nm is unknown. A significant broadening in the spectra was observed for slit width of 400 μm to 1500 μm . The 100 and 50 μm slit widths gives the best spectral resolution of 0.8 ± 0.1 nm. In all calibration procedures, and PL and TRPL measurements, the entrance slit width was set to 200 μm to obtain a reasonable signal without losing the desired spectral resolution (1.0 ± 0.1 nm).

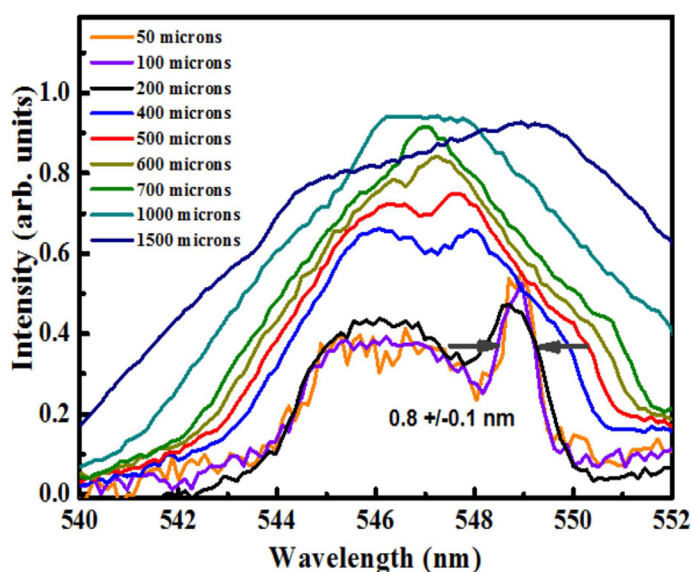


Figure 3.3: Spectral line of mercury at 546.5 nm from fluorescent lamp for different entrance slit widths. The best spectral resolution was observed at a slit width of 100 μm with a bandwidth of 0.8 ± 0.1 nm FWHM indicated by brown arrows.

3.2 Time-resolved Photoluminescence Spectroscopy

TRPL spectroscopy is used to monitor light emission from a sample as a function of time after excitation (Jung *et al.* 2002). Using this technique, it is possible to separate prompt fluorescence from delayed emission (Schols 2011). TRPL allows determination of the decay kinetics of light emitting materials by recording the emission intensity over a wide range of delay times after excitation.

For TRPL in general, carriers are excited with a pulsed or a modulated light source, and the emission is subsequently recorded while the excitation is off (Prasankumar *et al.* 2012). One thing to consider when doing TRPL measurements is the repetition rate of the pulsed or modulated light source. It is advantageous to use excitation sources with high repetition rates since it increases the count rates and allows better averaging which improves the signal-to-noise ratio at a given acquisition time. However, the time between each excitation pulse must be longer than the relaxation time of the excited carrier to the ground state. This condition ensures that re-excitation of the unrelaxed system is avoided. The TRPL signal is proportional to the radiative decay rate of the emitter when the response time of the system is shorter than the decay time. Hence, it is easier to measure the ultrafast PL dynamics of emitters with high radiative decay rate because more photons are emitted within a given time window.

More sophisticated techniques are necessary to perform TRPL measurements with better time resolution. As a general rule, time resolution comes at the expense of sensitivity. For high resolution and sensitivity, femtosecond laser pulses from mode-locked lasers are commonly employed. A short pulse excitation source is necessary because the overall time resolution is determined by the temporal response of the TRPL detection system as well as by the temporal width of the excitation pulse (Nejo 2003).

In this work, three TRPL set-ups were used to study the dynamics of the photoexcited carriers in Si NCs. A ns-TRPL set-up using time-correlated single photon counting (TCSPC) was used for the PL lifetime measurements in the sub-ns and ns time scales. Microsecond-lifetime components were measured using either a silicon photodiode coupled to a fast oscilloscope or a PMT detector with an acousto-optic modulator.

3.2.1 Time-correlated single photon counting

The TCSPC method employed in the ns-TRPL measurements consists of a detector, a discriminator, a logic gate and a counter, as illustrated in Fig. 3.4. The discriminator separates the single-photon pulses from the background noise. The discriminator output pulses are sent through a logic gate

and only pulses within the gate pulse are counted. The gate pulses are triggered externally by an electrical sync signal from the excitation pulse while the detector is a single photon avalanche photodiode (SPAD). To obtain the PL decay, the arrival times of individual photons over many excitation and PL cycles are recorded in a histogram. The arrival times are recorded with respect to the trigger (derived from the laser source) corresponding to times between the laser excitation and the corresponding photon arrival (start-stop-times) resolved down to a few tens of picoseconds. The resulting histogram of the number of photons detected within a certain arrival time window after excitation represents the PL decay.

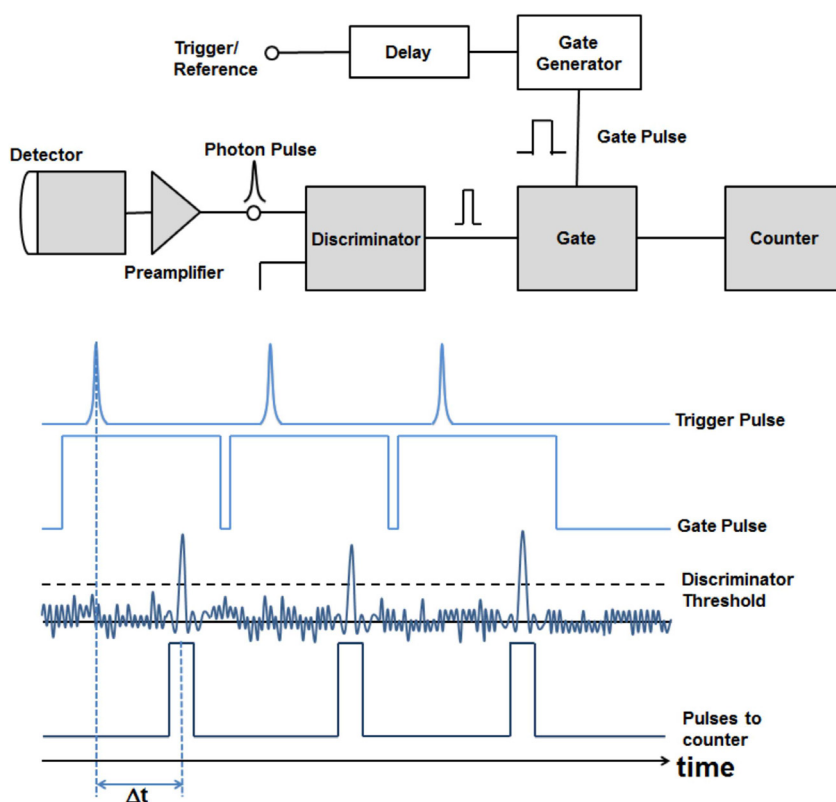


Figure 3.4: Schematic diagram of the TCSPC module for ns-TRPL measurements. Adapted with modification from Becker (2005).

During the TRPL measurements, it is necessary to maintain a low probability of registering more than one photon per cycle. This is done to guarantee that the histogram of photon arrivals represents the time decay one would have obtained from a single-shot time-resolved analog recording. In addition, since the dead times of detector and electronics occur for at least some tens of nanoseconds after a photon event, TCSPC systems are usually designed to register only one photon per excitation/emission cycle. If more than one photon event occurs in one excitation cycle, the system will only register the first photon but miss the following one or more. This would lead to an over-representation of early photons in the histogram, an effect called *pileup*. This leads to distortions of the PL decay, which typically results in the lifetime appearing shorter than the actual decay (PicoHarp 300, Manual).

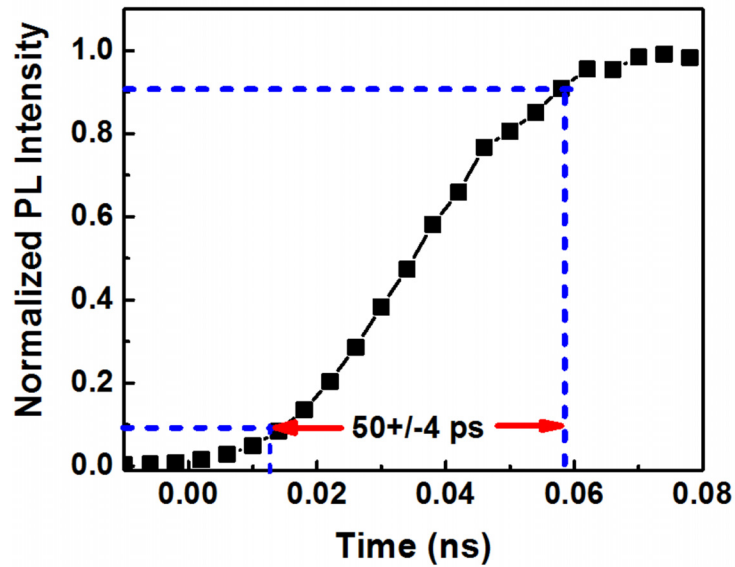


Figure 3.5: The rise time of PL measured with the TCSPC setup showing a time resolution of 50 ± 4 ps.

The PL lifetime decays of Si NCs in sub-ns time scales are measured using a TCSPC (PicoHarp 300) module coupled to a monochromator, as shown in Fig. 3.1. The photon detector is a SPAD (PDM Series by Micro Photon Devices) in which the maximum count rate is 50 MHz. The time resolution of the set-up is 50 ± 4 ps, obtained by measuring the rise time of the 400 nm scattered laser pulses (Fig. 3.5). This configuration can be used for spectrally-resolved PL lifetime measurements. Using the monochromator grating and a slit width of $200\ \mu\text{m}$, the PL lifetime of a particular emission wavelength with very narrow bandwidth, 1.0 ± 0.1 nm (determined by the monochromator's entrance and exit slit width) can easily be obtained. A screen shot of the acquisition program is shown in Fig. 3.6. The binning time or the step size can also be set from 4 ps to 32 ps. If the signal is weak, the acquisition time can be increased up to 1 hr. In addition, it is also possible to perform more detailed TRPL measurements wherein the PL intensity for each wavelength and time (time after photoexcitation) will be recorded. As a result, the temporal evolution of the PL spectral profile as well as the spectrally-resolved PL lifetime can be obtained simultaneously. A sample plot is shown in Fig. 3.7.

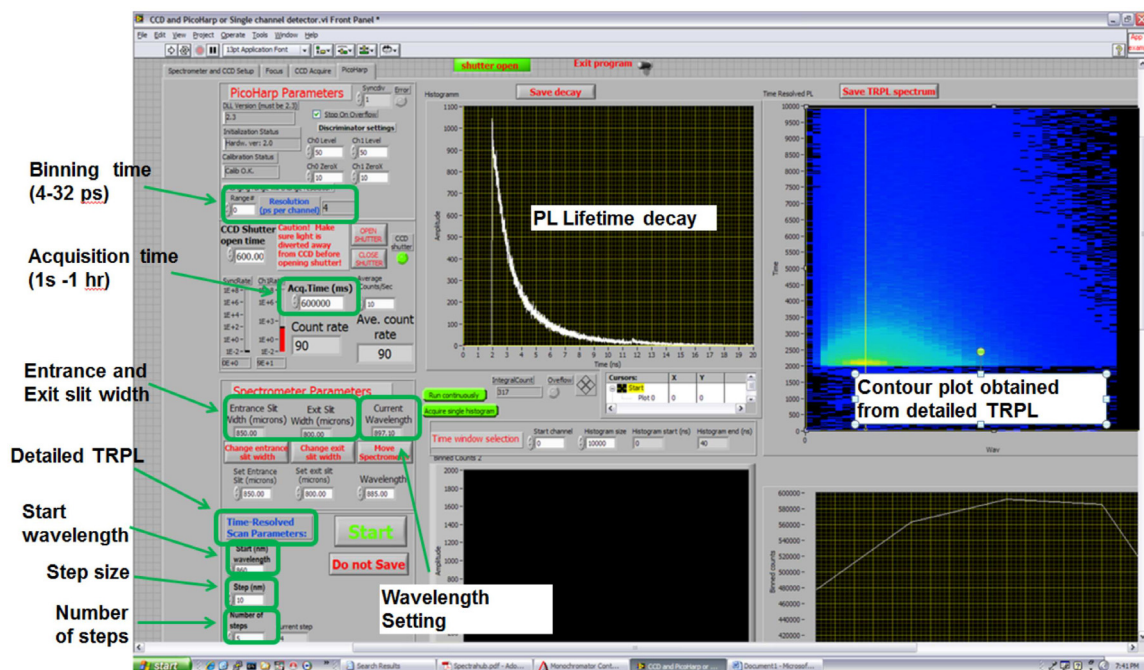


Figure 3.6: Acquisition program for the spectrally-resolved PL lifetime and detailed TRPL. The detailed TRPL records the PL lifetime per wavelength. A sample of the detailed TRPL signal is shown at the upper right window of the picture, a contour plot of the PL intensity as a function of wavelength and time after photoexcitation.

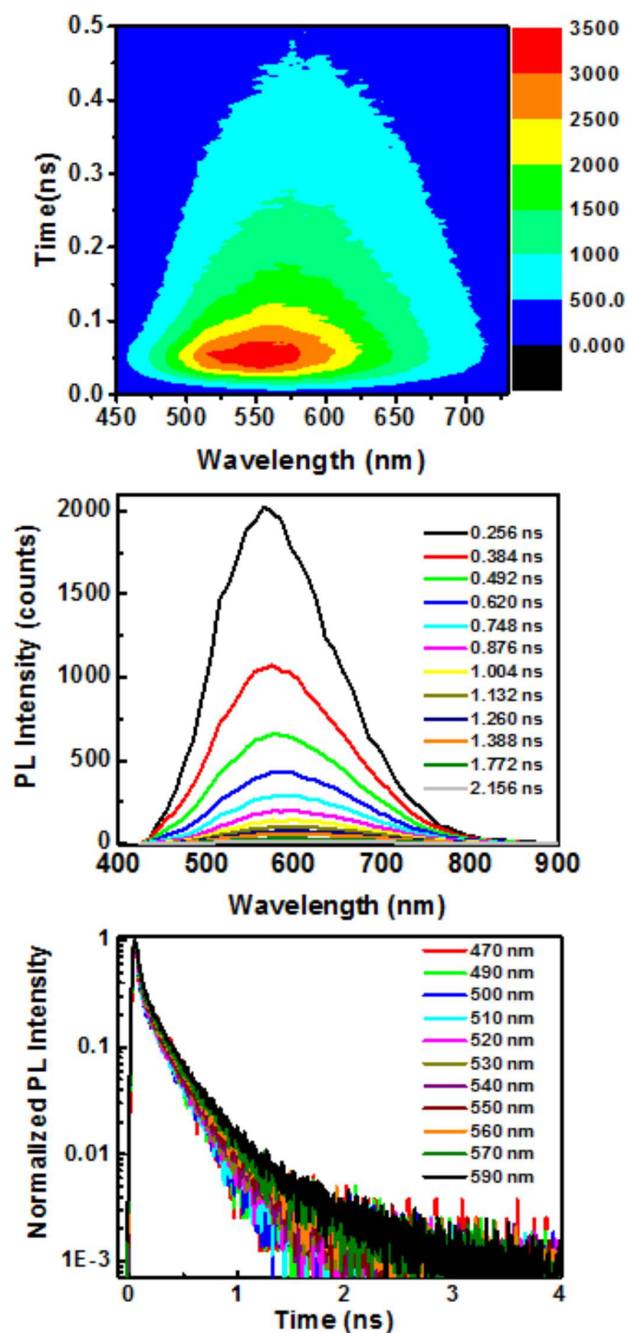


Figure 3.7: TRPL for acetal functionalized Si NCs. (a) PL intensity as a function of wavelength and time after photoexcitation. (b) Temporal evolution of the PL spectral profile. (c) Spectrally-resolved PL lifetime.

3.2.2 Microsecond-time-resolved photoluminescence spectroscopy

The microsecond-TRPL (referred to here as μ s-TRPL) lifetime of functionalized Si NCs was measured using a fast silicon photodiode (Thorlabs, PDA36A with rise time of 20.6 ns) coupled to a 300 MHz oscilloscope (Tektronix). The PL was excited by 400 nm, 50 fs excitation pulses from a frequency-doubled amplified Ti:Sapphire laser source (Coherent Legend Elite) operating at a repetition rate of 1 kHz. The excitation pulses were focused at the center of the sample using a lens with a focal length of 100 cm. A 435-nm longpass filter was used to block scattered 400 nm excitation light. Bandpass filters with 10 nm bandwidth were used to select emission wavelengths between 450 nm and 760 nm. The photodiode and the optical filters were placed on a path perpendicular to the excitation beam, as shown in Fig. 3.7. The photodiode gain setting was set to 30 and the PL lifetime was the average of 256 waveforms.

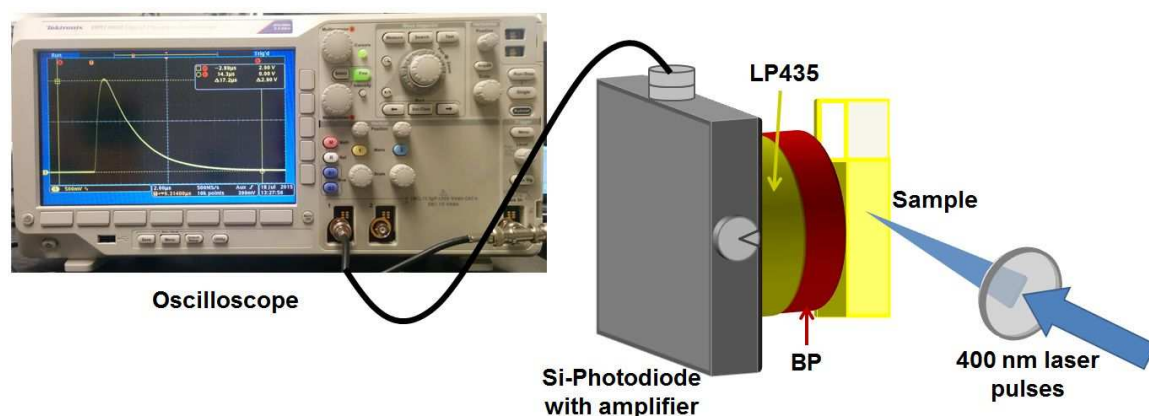


Figure 3.8: Schematic diagram of the experimental set-up for μ s-TRPL measurements.

A different μ s-TRPL set-up from Al Meldrum's lab at the Department of Physics, University of Alberta was used in the PL lifetime measurements of the Si NC films with different Si filling fractions. The PL was excited by a 445 nm diode laser coupled to an acousto-optic modulator set with a repetition rate of 200 Hz and pulse duration of 25.6 ns. The excitation pulses were

focused on the sample using a lens and the emitted PL was collected by a multimode fiber and sent to a single photon counting photomultiplier system with a multiscaler set to 200 ns time bins. The schematic diagram of the experimental set-up is shown in Fig. 3.9. For spectrally-resolved PL lifetime measurements, a bandpass filter with 10 nm bandwidth was used to select emission wavelengths between 700 nm and 900 nm. A 495-nm longpass filter was used to block scattered excitation light.

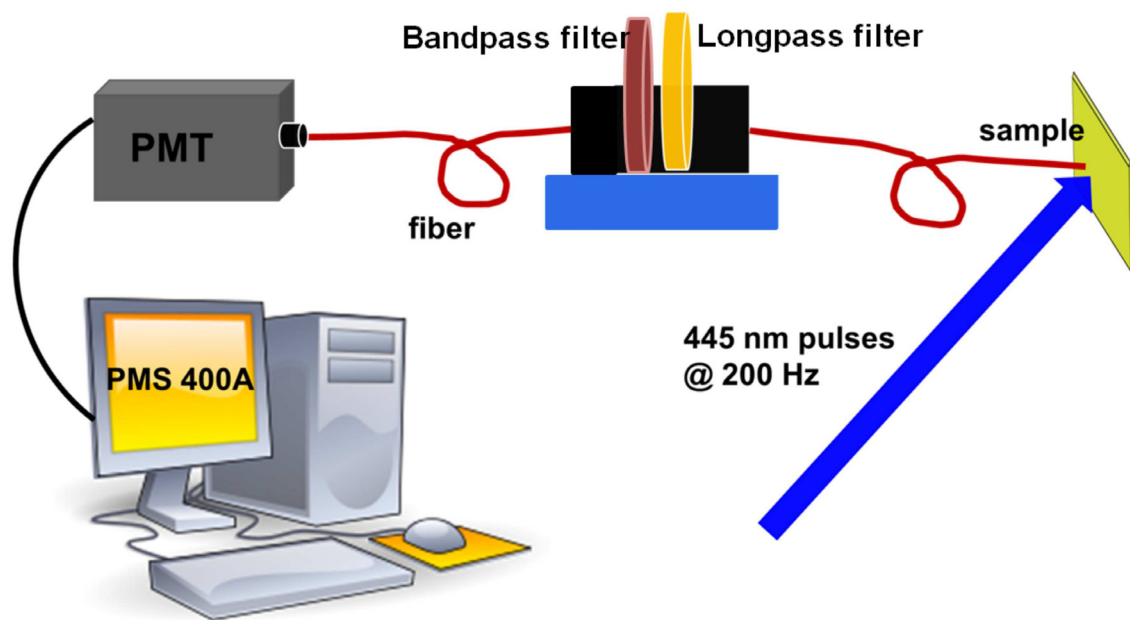


Figure 3.9: Alternate set-up for μs -PL lifetime measurements of Si NC films from Al Mel-drum's lab.

3.3 Optical pump-probe transient photoinduced absorption spectroscopy

Pump-probe spectroscopy is the most common ultrafast spectroscopy used to study the carrier dynamics in semiconductor materials, e.g. the recovery of a saturable absorber after its excitation (Fleischhaker *et al.* 2013), the speed of diffusion of photoexcited carriers (Titova *et al.* 2011), the melting of a sample after being hit by an intense pulse (Link *et al.*, 1999), and the trapping of photoexcited carriers at interface states (Cooke *et al.* 2006). Here, two-color pump-probe TPA spectroscopy was used to monitor the carrier dynamics in Si NC films with different filling fractions. A diagram of the experimental set-up is shown in Fig. 3.10. The output pulse from an amplified Ti:Sapphire laser which consists of a train of 65 fs pulses, each centered at 800 nm and delivered at a repetition rate of 250 kHz was split into high and low power beams. The high power beam was sent through a BBO crystal for generating 400 nm pulses that were focused on the sample for photoexciting charge carriers. Subsequently, the sample response was monitored using time-delayed 800 nm pulses. The 400 nm pump pulses were chopped by a mechanical chopper at 400 Hz. In addition, the 400 nm pump beam was incident on the sample at an angle of 28° with respect to the probe beam. By varying the delay time between the 400 nm pump and 800 nm probe pulses with an optical delay stage, the time evolution of pump-induced changes in the sample properties with sub-ps time resolution was monitored (Fig. 3.11).

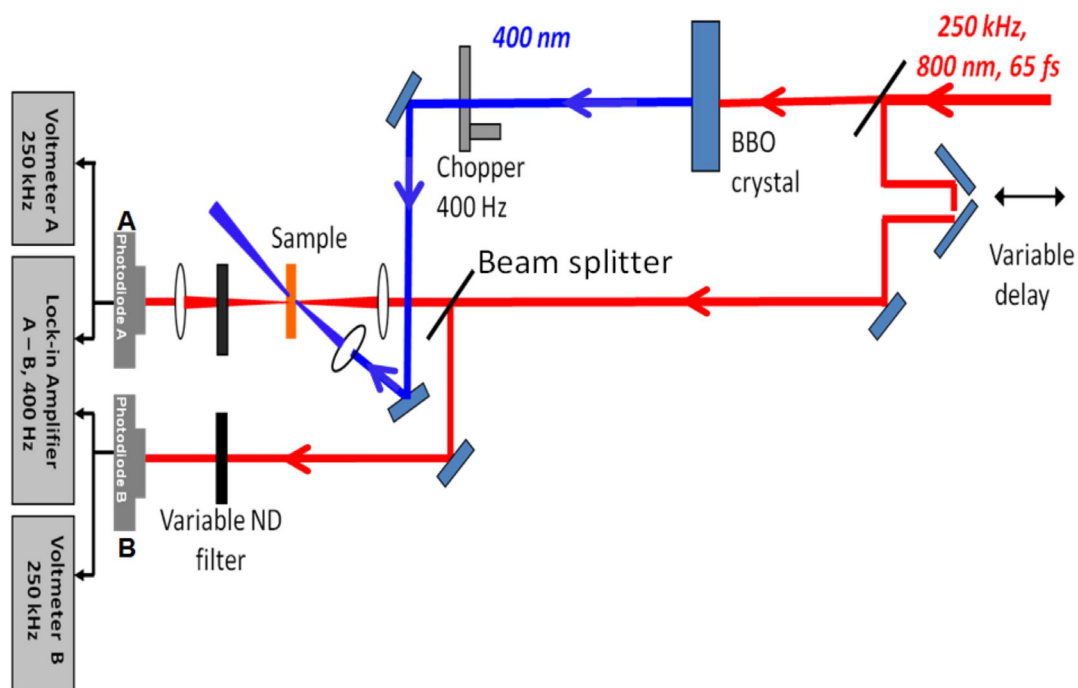


Figure 3.10: Schematic diagram of the pump-probe TPA set-up.

The 800-nm probe pulses were further split into two beams using a 55% transmission/ 45% reflection pellicle beam splitter. The 55% 800 nm pulse goes through the sample to photodiode A while the 45% 800 nm pulse goes directly to photodiode B, which serves as a reference for differential detection, as discussed later. The signals from photodiodes A and B were coupled to a lock-in amplifier referenced to the chopper to monitor the change in transmission of the 800 nm probe pulse induced by the 400 nm pump pulse. The output of the lock-in amplifier was sent to the computer for data acquisition and for control of the delay stage. The pump and probe pulse polarizations were set perpendicular to each other to minimize interference between them at the sample. In addition, the pump and probe powers were controlled using a variable neutral density filters.

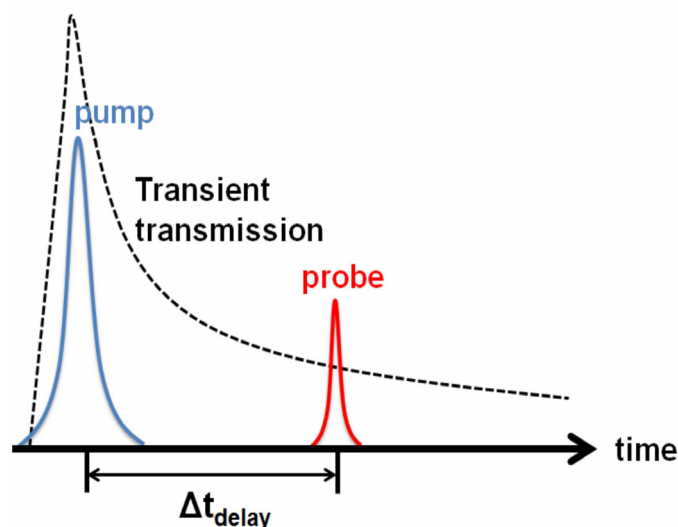


Figure 3.11: Time evolution of the transient absorption signal obtained using the pump-probe method.

In pump-probe experiments, it is a requirement to overlap the pump and probe beams spatially and temporally. The spatial overlap was achieved by focusing the pump beam to a spot larger ($\sim 1\text{mm}$) than that of the probe beam ($\sim 0.25\text{ mm}$). This ensures that the probe beam is covered completely by the pump beam and a uniform area in the sample was monitored. The spot size and position on the sample was monitored by a CCD camera to ensure that the probe beam spot is located within the pump beam spot.

To achieve temporal overlap, a Kerr gate detection was employed using a quartz glass slide as a Kerr medium. The glass slide was placed on the sample position and the delay stage was moved to change the probe beam arrival time. The reading on the lock-in amplifier was monitored as the delay stage moved until a maximum reading was achieved. The position of the delay stage that gives the maximum reading on the lock-in amplifier is the point where the pump and probe beams temporally overlapped. This position is known as t_0 .

The time resolution of the pump-probe set-up was determined using Kerr gate detection. The probe beam polarization was set at 45° with respect to the pump beam. A tetrahydrofuran (THF)

solution in a 2-mm path length vial was placed at the sample position and used as a Kerr medium. The TPA is shown in Fig. 3.12. The temporal resolution of the system is ~ 500 fs which is equal to the full width at half maximum of the TPA signal. The relatively large temporal resolution is due to non-collinear configuration of the set-up and the large spot size of both the pump and probe beams.

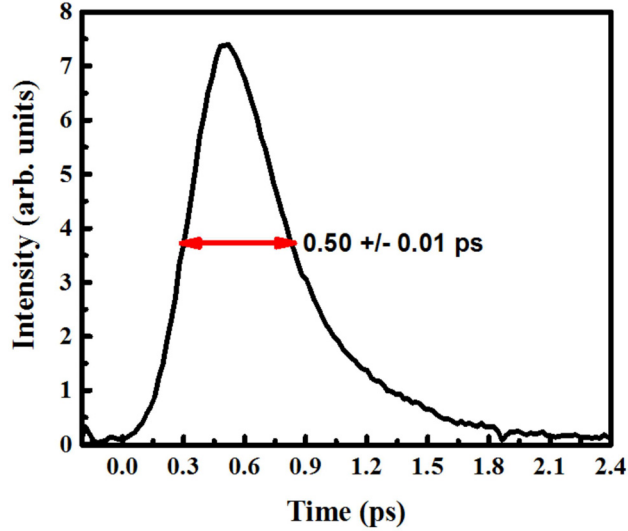


Figure 3.12: THF transmitted signal showing a 500 ± 10 fs full width of half maximum which corresponds to the time resolution of the system. The lock-in amplifier detection setting A-B was set to $20 \mu V$.

The differential signal $(A-B)/B$ is proportional to the differential transmittance $\Delta T/T_0$. However, the signal $(A-B)$ is detected at 400 Hz while the reference B is detected at 250 kHz, hence the signal $(A-B)/B$ does not reflect the absolute value for $\Delta T/T_0$. In addition, the $(A-B)/B$ signal is dependent on the lock-in amplifier's phase and cannot be used to distinguish between photoinduced enhanced transmission or enhanced absorption. To calibrate the signal, the ratio A/B which was measured using the AC voltmeters was used since both signals are detected at 250 kHz. As shown in Fig. 3.13(a), the A/B signal is less than 1 at T_0 which indicates pump induced enhancement in the absorption of the 800 nm probe beam. Comparing the differential signal $(A-B)/B$ with the calibrated signal $(\Delta T/T_0)$, the calibrated signal is significantly lower than the uncalibrated one (Fig. 3.13(b) and (c), respectively). All the TPA signals are averages of 3 scans.

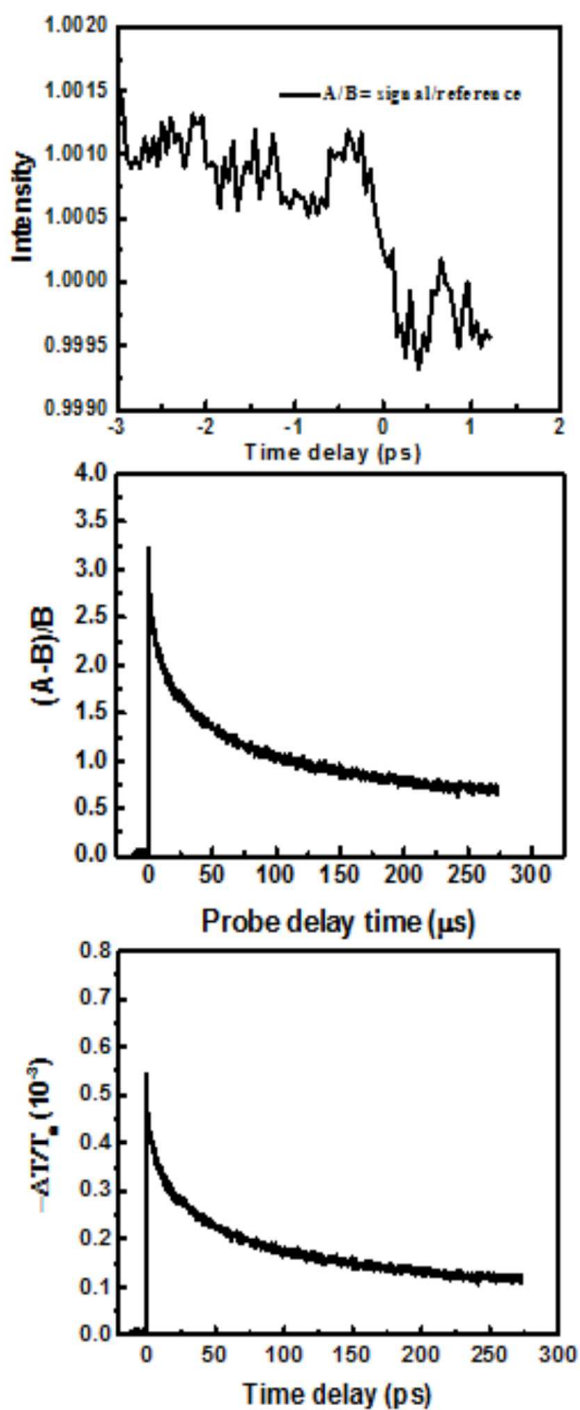


Figure 3.13: (a) Absolute data A/B . (b) The differential data $(A-B)/B$ as function of delay time. (c) The calibrated $-\Delta T/T_0$.

CHAPTER 4

The role of oxygen in the ultrafast photoluminescence from colloidal silicon nanocrystals¹

4.1 Introduction

Following the discovery of light-emitting porous silicon by Canham (1990), many materials based upon nanostructured silicon (e.g., silicon nanocrystals (Si NCs)) have been investigated as candidate active systems for optoelectronics devices, ultrafast data communication and data storage, as well as fluorescent labels and biological sensors (Barbagniovanni *et al.* 2014, Holman *et al.* 2010, Park *et al.* 2009, Alsharif *et al.* 2009, Liu *et al.* 2008, Erogbogbo *et al.* 2008, Pavesi *et al.* 2000). Despite these important practical advances, no clear consensus regarding the origin of optical emission from Si NCs exists (Kim *et al.* 2012, Zidek *et al.* 2011, de Boer *et al.* 2010, Sung *et al.* 2007, Garcia *et al.* 2003, Wolkin *et al.* 1999, Fan *et al.* 1998, Kovalev *et al.* 1994, Kanemitsu *et al.* 1994). Bulk Si does not show efficient luminescence because of its indirect bandgap (Alex *et al.* 1996).

¹Part of this Chapter has been published in Zhenyu Yang, Glenda B. De los Reyes, Lyubov V. Titova, Ilya Sychugov, Mita Dasog, Jan Linnros, Frank A. Hegmann, and Jonathan G. C. Veinot, ACS Photonics 2015, 2, 595-605.

However, efficient photoluminescence (PL) from nanostructured silicon has been widely observed and has been explained in the context of quantum confinement and/or defect and surface states (Hessel *et al.* 2011, Dohnalova *et al.* 2010, Dohnalova *et al.* 2010, Valenta *et al.* 2008, Valenta *et al.* 2008, Warner *et al.* 2005, Ledoux *et al.* 2002, English *et al.* 2002, Fauchet 1996, Littau *et al.* 1993, Voos *et al.* 1992).

As expected, PL resulting from the influence of quantum confinement in Si NC cores is size dependent and the emission maximum shifts to higher energy as the nanocrystal size decreases. In addition, the PL dynamics associated with Si NC core emission range throughout the nanosecond (ns) to microsecond (μ s) timescales. Long-lived PL in the μ s timescale observed in the yellow to infrared spectral region is often attributed to quasi-direct (Sychugov *et al.* 2011) and phonon-assisted radiative recombination in the core states of larger Si NCs (Mastronardi *et al.* 2011, Garcia *et al.* 2003). On the other hand, short-lived blue-green emission in the ns timescale is often attributed to quasi-direct recombination in smaller (diameter < 2 nm) Si NCs (Dohnalová *et al.* 2013, Valenta *et al.* 2008, Kanemitsu *et al.* 1994, Sankaran *et al.* 2005, Zhou *et al.* 2003, Wilcoxon *et al.* 1999).

Surface chemistry has also been implicated in the PL and emission dynamics of Si NCs (Dohnalová *et al.* 2014). Nanosecond PL in the blue-green and yellow-red spectral regions has been attributed to fast recombination of carriers in the interface states or defects introduced as a result of ligand passivation and/or oxidation (Kusova *et al.* 2010, Rosso-Vasic *et al.* 2009, Dohnalová *et al.* 2009, Pi *et al.* 2008, Gole *et al.* 1997, Augustine *et al.* 1995, Tsybeskov *et al.* 1994). For blue-emitting alkyl-functionalized Si NCs, charge transfer to the interface states has been suggested as one possible mechanism for nanosecond PL decay times (Dasog *et al.* 2014, Wolf *et al.* 2013, Dasog *et al.* 2013). For yellow/orange-emitting Si NCs, the origin of similarly short-lifetime PL and a concomitant blue-shifted PL maximum has been attributed to various silicon-oxygen species on the NC surfaces (Kim *et al.* 2012). Contrasting this, suggestions that surface oxidation leads to a decrease in Si NC size that induces a blue-shift of the PL emission maximum have appeared (Biteen *et al.* 2004). Complicating the community's understanding, other reports claim surface oxidation induces a red-shift of the PL maximum (Dohnalová *et al.* 2009, Wolkin *et al.* 1999). The authors explained this latter observation by invoking the presence of surface silanones (Si=O)

that purportedly introduce new electronic states that lead to “trapped-electron-to-band” recombination. While molecular analogues of the proposed silanone surface groups have been reported, they require substantial stabilization (Rodriguez *et al.* 2013, Muraoka, *et al.* 2011, Xiong *et al.* 2010, Xiong *et al.* 2009). In light of the extreme reactivity of the Si=O moiety and that the stabilization effects of the nanoscale silicon surface cannot be readily predicted, the presence of these species must be considered cautiously. Indeed, nanosecond PL lifetimes observed for alkyl-functionalized and hydride-terminated freestanding yellow/orange emitting Si NCs have been associated with significant surface oxidation (Kim *et al.* 2012, Augustine *et al.* 1995, Tsybeskov *et al.* 1994). These seemingly contradicting observations and proposals imply that an in-depth understanding of the influence of surface oxygen is still missing. Here, we investigate the origin of the blue-shift of the PL maximum and nanosecond PL lifetime observed for alkyl-functionalized Si NCs fabricated using two complementary hydrosilylation approaches (*i.e.*, thermal and photochemical initiation). Established differences associated with the efficacy of these closely related functionalization procedures allow for direct comparison of the impact of surface oxide on PL response.

4.2 Sample preparation and characterization

Well-defined Si NCs used in this study were prepared using a well-established procedure developed in the Veinot Laboratory of the Department of Chemistry, University of Alberta (Hessel *et al.* 2006). Briefly, commercial hydrogen silsesquioxane was thermally processed in a slightly reducing atmosphere (95% Ar / 5% H₂) at 1100 °C (for 3 nm Si NCs) and 1200 °C (for 5 nm Si NCs) to yield well-defined Si NCs embedded in a SiO₂-like matrix. Hydride-terminated Si NCs were freed from the oxide matrix *via* HF etching. Subsequent surface modification with dodecyl groups was achieved using thermal or photochemical hydrosilylation 1-dodecene. A deep orange solution was obtained after 3 hours from thermally-induced surface modification. In contrast, even after 15-hours of photochemical hydrosilylation, an orange/brown cloudy suspension was observed. This difference in appearance is reasonably attributed to the functionalization of the NC surfaces during thermal hydrosilylation that render them compatible with organic solvents and less efficient surface

passivation being achieved *via* the photochemically initiated reaction (*vide infra*). Figure 4.1 shows the transmission electron microscope (TEM) imaging and corresponding size distributions of the dodecyl-functionalized Si NCs. Thermally functionalized Si NCs have average diameters of $d = 3.1 \pm 0.4$ nm and 4.9 ± 0.6 nm slightly higher than photochemically functionalized Si NCs ($d = 3.0 \pm 0.4$ nm and 4.7 ± 0.6 nm). Statistically, the Si NCs modified using these two procedures possess nearly equivalent dimensions.

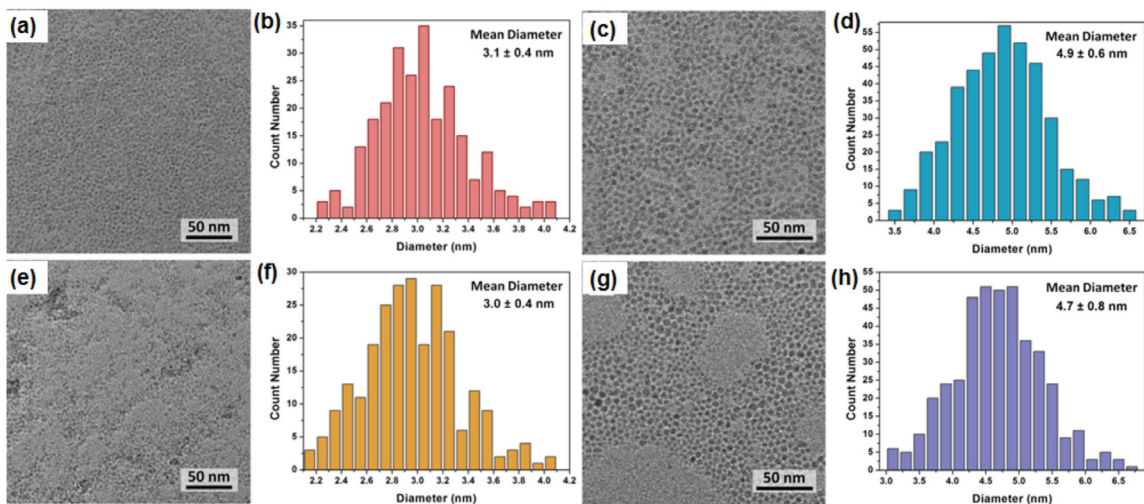


Figure 4.1: Brightfield TEM images and size distribution of ensembles dodecyl-passivated Si NCs functionalized via thermal (a-d) and photochemical (e-h) hydrosilylation approaches [Adapted from Yang, De los Reyes et al. 2015].

4.3 Experimental details

The TIPL and TRPL spectroscopy setups introduced in Chapter 3 were used for the spectroscopy measurements detailed in this chapter. The PL was excited by 400-nm pulses at excitation fluences of 1.62 mJ/cm^2 , 0.77 mJ/cm^2 , and 2.50 mJ/cm^2 for TIPL, sub-ns TRPL and μs -TRPL measurements, respectively. TIPL spectra were integrated for 120s and corrected to the spectral response of the

system. For sub-ns TRPL, the emission wavelength was chosen using the monochromator and each wavelength was integrated for 1 hr. In the case of μ s-TRPL, 10-nm band pass filters were used to select a particular emission wavelength and the PL lifetime is the average of 256 sampling rate. In all of the experiments, a 435-nm long pass filter was used to block the scattered excitation pulses.

4.4 Results and Discussion

Fourier transform infrared (FTIR) spectra of ~ 5 nm and ~ 3 nm Si NCs are shown in Fig. 4.2(a) and (b), respectively. Freshly etched hydride-terminated Si NCs (Fig. 4.2(a-i)) exhibit two distinct absorptions that are confidently attributed to Si-H_x stretching and scissoring (*i.e.*, 2000 cm^{-1} - 2100 cm^{-1} and 900 cm^{-1}). Following hydrosilylation with 1-dodecene, the Si-H_x features are replaced by intense vibrations at 2650 cm^{-1} - 2900 cm^{-1} and 1380 cm^{-1} - 1470 cm^{-1} indicative of C-H stretching and bending vibrations of dodecyl surface moieties. Consistent with other studies (Boukherroub *et al.* 2001, Sieval *et al.* 2001, Sieval *et al.* 2000), we note Si-O-Si stretching features at *ca.* 1100 cm^{-1} indicative of some surface oxidation. A straightforward comparison of the FTIR spectra suggests that the surfaces of photochemically-functionalized Si NCs consistently bear more Si-O species than their thermally-modified equivalents. All spectra (Fig.4.2(a) and (b)) confirm only Si, C, and O are present in the Si NC samples studied here.

X-ray photoelectron spectroscopy (XPS) is commonly used to gain insight into the nature (*i.e.*, speciation and quantity) of surface oxidation on alkyl-functionalized Si NCs (Yang *et al.* 2013, Hessel *et al.* 2011, Mastronardi *et al.* 2011, Hessel *et al.* 2008). The Si 2p spectral region of the high-resolution XP spectrum of the thermally and photochemically-modified 5 nm diameter particles are shown in Fig. 4.2(c) and (e), respectively. The emission feature at 99.3 eV arises from the Si(0) core of the Si NCs (Yang *et al.* 2013). The broad feature between *ca.* 100 eV and 104 eV is routinely fit to components at 100.3 eV (Si(I)), 101.4 eV (Si(II)), and 102.4 eV (Si(III)) arising from ligand functionalized surface and Si suboxides; an additional component at 103.4 eV (Si(IV)) is consistent with SiO₂ (Hessel *et al.* 2011, Nemanick, *et al.* 2006, Wallart *et al.* 2005, Bansal *et al.* 1996). Consistent with FTIR analyses (*vide supra*), spectral features attributable to surface oxides

appear for thermally and photochemically modified samples and the oxide features, in particular the significant Si(IV) emission, are more intense for photochemically functionalized samples. Of important note, the XPS spectrum of thermally modified 5 nm Si NCs is similar to that of its 3 nm counterpart (Fig. 4.2(d) and (f)), however the contribution of Si(IV) species is smaller in the former. In contrast, the photochemically modified 5 nm Si NCs showed the highest relative content of Si(IV) of all samples evaluated here.

Figures 4.3(a) and (b) show the time-integrated PL of surface-modified Si NCs ($d \sim 3$ nm and ~ 5 nm). The time-integrated PL maxima are summarized in Fig. 4.5. Regardless of the functionalization method employed, increasing the NC size from 3 nm to 5 nm induces a red-shift of the PL maximum (*i.e.*, 49 nm for thermal and 88 nm for 15 hr photochemical) suggestive of quantum confinement. All samples exhibit broad PL spectra with Gaussian-like profiles. The PL linewidths arising from thermally-modified Si NCs are broader than their photochemical counterparts. The origin of the observed broadening of Si NC PL is complex. While some broadening may arise from the distribution of particle sizes present in the sample (*i.e.*, as a result of quantum confinement), single dot spectroscopy studies of individual Si NCs also show broad emission spectra (Sychugov *et al.* 2014, Mason *et al.* 1998).

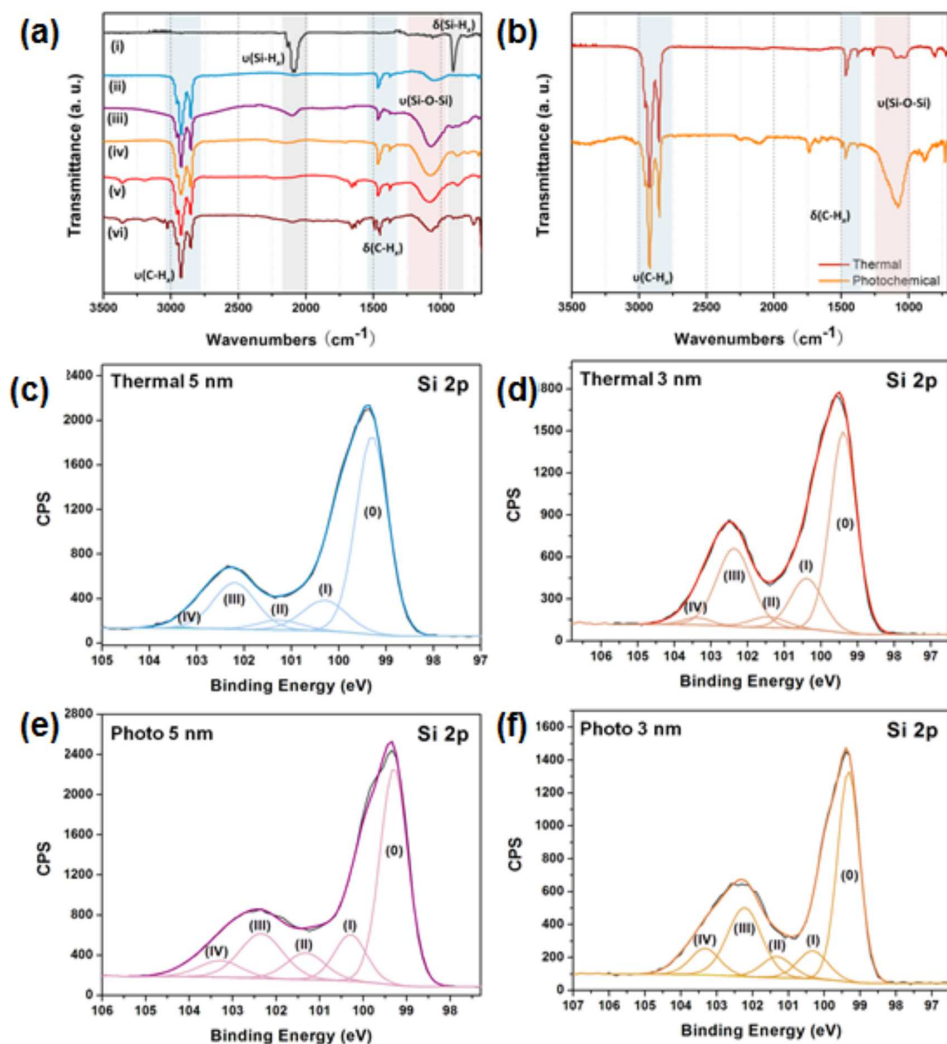


Figure 4.2: FTIR and XPS of dodecyl functionalized Si NCs. (a) FTIR of 5 nm hydride terminated (i), thermally-functionalized (ii), and photochemically-functionalized Si NCs (reaction time = 15 hrs (iii), 20 hrs (iv), 30 hrs (v), and 39 hrs (vi)). (b) FTIR of 3 nm dodecyl functionalized Si NCs. High-resolution XP spectra of the Si 2p spectral region for (c,d) thermally-functionalized and (e,f) photochemically-functionalized Si NCs (15 hrs reaction time). Fitting results are shown for the silicon spectrum with Si 2p_{3/2} signals. Si 2p_{1/2} components have been omitted for clarity [Adapted from Yang, De los Reyes et al. 2015].

A comparison of the optical response shows the PL maximum of photochemically-functionalized Si NCs (Fig. 4.3(b)) is blue-shifted from that of analogous thermally functionalized Si NCs (Fig. 4.3(a)). As noted above (Fig. 4.1), TEM analyses of the samples indicate there is no statistically relevant difference in their sizes. However, a qualitative inspection of the TEM size distributions suggests the PL may be influenced by a biasing of the particle size distribution that may result from the established size-dependent reactivity of photochemical hydrosilylation (Kelly *et al.* 2011). To explore this possibility, the Si NC diameter corresponding to the PL peak emission was calculated using the effective mass approximation (EMA) (Brus 1999, 1984, 1983):

$$E_{gap}^{opt} = E_{gap} + \frac{\hbar^2 \pi^2}{2R^2 \mu} - 1.786 \frac{e^2}{\epsilon_r R} \quad (4.1)$$

$$\mu = \frac{m_e^* m_h^*}{m_h^* + m_e^*} \quad (4.2)$$

where E_{gap} is the band gap of bulk silicon (1.12 eV), R is the nanocrystal radius, e is the electronic charge, ϵ_r is the relative permittivity (for silicon, $\epsilon_r = 11.68$), m_e^* and m_h^* are the effective masses of the electrons and holes ($0.19m_0$ and $0.286m_0$, respectively, where m_0 is the free electron rest mass) (Hessel *et al.*, 2011), and μ is the reduced mass. From Eq. (4.1), it is evident that a PL maximum of 815 nm (*i.e.*, PL observed here for $d \sim 5$ nm Si NCs modified using thermally-induced hydrosilylation) corresponds to a diameter of 4.1 nm; a PL maximum of 726 nm (*i.e.*, PL observed here for $d \sim 5$ nm Si NCs modified *via* a 15-hour photochemically-induced hydrosilylation) corresponds to a diameter of 3.3 nm. Based upon these calculated diameters and the presented TEM data, it is possible the PL from thermally-functionalized Si NCs has a strong contribution from a significant number ($\sim 24\%$) of particles with diameters ≤ 4.1 nm. However, fewer particles ($\sim 4.8\%$) with diameters ≤ 3.3 nm are present in photochemically-functionalized Si NCs. Hence, it is unlikely that the observed blue-shift of the time-integrated PL is due to excitation of these small particles alone. However, Biteen *et al.* (2004) reported that surface oxidation led to a decrease in NC size which resulted in an observed PL blue-shift. For the present study, even though the FTIR and XPS analyses show more surface oxide is present in photochemically-modified Si NCs, close examination of the TEM images shown in Fig. 4.1 affords no evidence of such a size reduction. In this context,

it is reasonable that any size reduction of the Si NC core arising from surface oxidation is negligible.

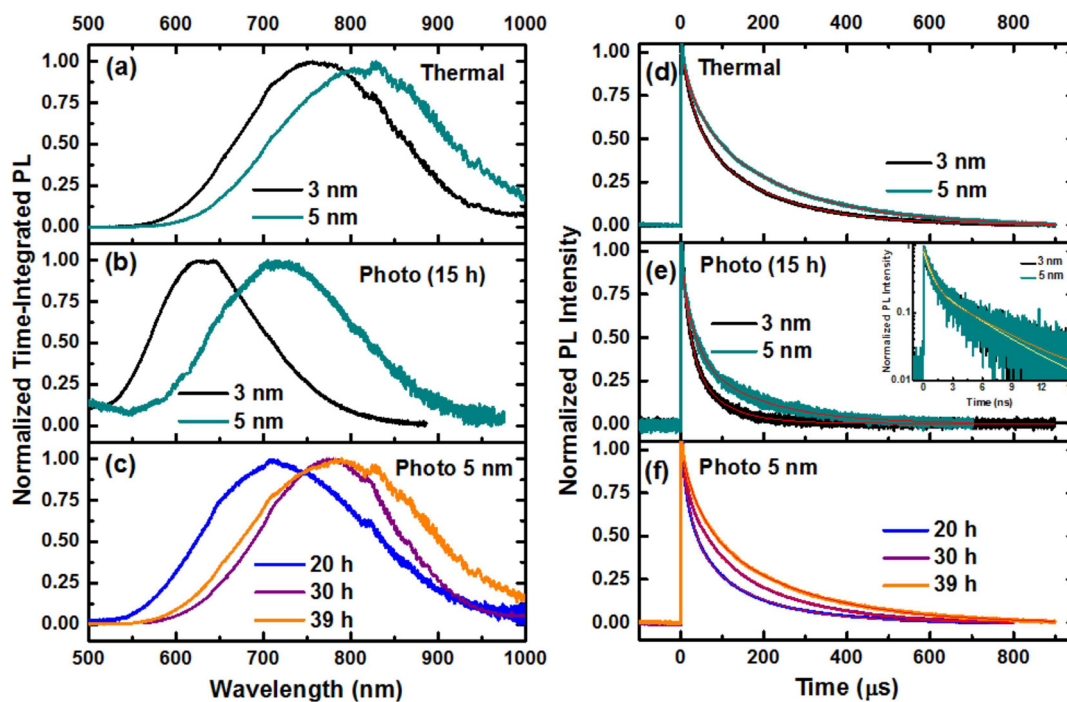


Figure 4.3: Time-integrated PL spectra of surface functionalized SiNCs prepared using (a) thermal and (b) photochemical hydrosilylation. (c) Reaction time dependence of PL arising from photochemically-modified SiNCs ($d = 5$ nm) upon excitation by $\lambda = 400$ nm laser pulses at 1.62 mJ/cm² fluence. Corresponding time-resolved PL decays are shown in panels (d), (e), and (f), respectively where the red lines stretched exponential fits to the data. The inset in panel (e) shows the nanosecond lifetime PL emission at 630 nm and 690 nm for 3 nm and 5 nm SiNCs, respectively. The orange and yellow lines are the biexponential fits to the 5 nm and 3 nm Si NCs, respectively.

Emission from oxidized porous silicon is normally comprised of two components, a slow yellow-orange-red band and a fast band in the blue-green region (Kontkiewicz *et al.* 1994, Anedda *et al.* 1993). It has been proposed that the slow band region originates from quantum core-state of Si NCs and has a characteristic decay of a few tens to a few hundreds of microseconds. The fast band emission has been attributed to oxygen-induced defects and decays in the nanosecond range (Kim *et*

al. 2012, de Boer *et al.* 2010, Pi *et al.* 2008). If the blue-shifted PL arising from photochemically-modified Si NCs arises from excitation of smaller nanocrystals and emission from defect sites, then both ns and μ s PL emission decay components are expected.

To test this hypothesis, the PL emission dynamics of all the samples presented here were explored (see Fig. 4.3(d) and (e), Fig. 4.4). The μ s-PL decays represent the overall time decay for the entire emission spectrum. The ns-component of the decay time was measured at particular emission wavelengths. The carrier recombination dynamics of the ns-PL component is bi-exponential according to:

$$y(t) = Ae^{[-(t/\tau_1)]} + Be^{[-(t/\tau_2)]} + C \quad (4.3)$$

where τ_1 and τ_2 are the decay times and C is a constant offset much smaller than A and B. The μ s-PL component exhibits a stretched exponential decay:

$$y(t) = Ae^{-(t/\tau)^\beta} + y_0 \quad (4.4)$$

where τ is the decay time, β is the dispersion factor which can take values between 0 and 1, and y_0 is a constant offset. Aside from stretched exponential, single and bi-exponential fits were also tested, but the stretched exponential gave the best fit. The carrier recombination lifetime values are summarized in Fig. 4.5.

The photoexcited state lifetime of $d \sim 3$ nm Si NCs modified using thermally-induced hydrosilylation is $\tau = 78.6 \pm 0.1 \mu$ s; this is similar to previously reported values for Si NCs and is attributed to recombination within the Si(0) core (Hao *et al.* 2009, Garcia *et al.* 2003, Littau *et al.* 1993). For the same size of photochemically-modified Si NCs, the μ s-component was notably faster ($\tau = 22.0 \pm 0.3 \mu$ s) and exhibited a ns-component with $\tau_1 = 0.64 \pm .01$ ns and $\tau_2 = 4.40 \pm .05$ ns at 630 nm (Fig. 4.3(e) inset). Unlike the μ s-PL component, the ns PL exhibits a double exponential decay as clearly shown in the semi-log plot in the inset of Fig. 4.3(e). It is important to note that no ns-lifetime component is observed for thermally-functionalized Si NCs (Fig. 4.4(b)). For a given hydrosilylation method, the measured PL dynamics for 5 nm diameter Si NCs is similar to that observed for analogous 3 nm diameter Si NCs. The μ s-component for the $d \sim 5$ nm thermally-modified

Si NCs showed a decay time of $\tau = 130.5 \pm 0.1 \mu\text{s}$; nanosecond and microsecond lifetimes coexist for 5 nm diameter Si NCs that were photochemically functionalized (Fig. 4.3 and 4.5). The μs -PL decay times for the 5-nm diameter Si NCs are longer than those for the 3 nm diameter Si NCs, consistent with previous studies (Dohnalová *et al.* 2014, Garcia *et al.* 2003).

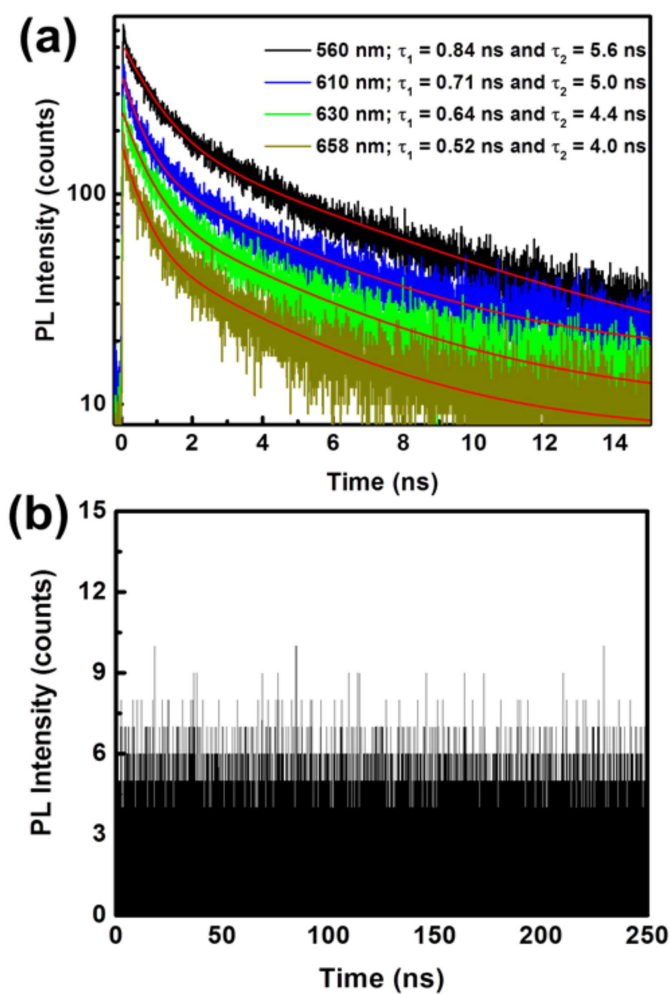


Figure 4.4: Time-resolved PL measured at the indicated wavelengths for 3 nm Si NCs functionalized via (a) photochemical and (b) thermal hydrosilylation. The red curve in (a) is the bi-exponential fit to the experimental data. The PL lifetime for thermal functionalized Si NCs was measured at 715 nm. The standard error for the fitted lifetimes is $\leq 1.5\%$.

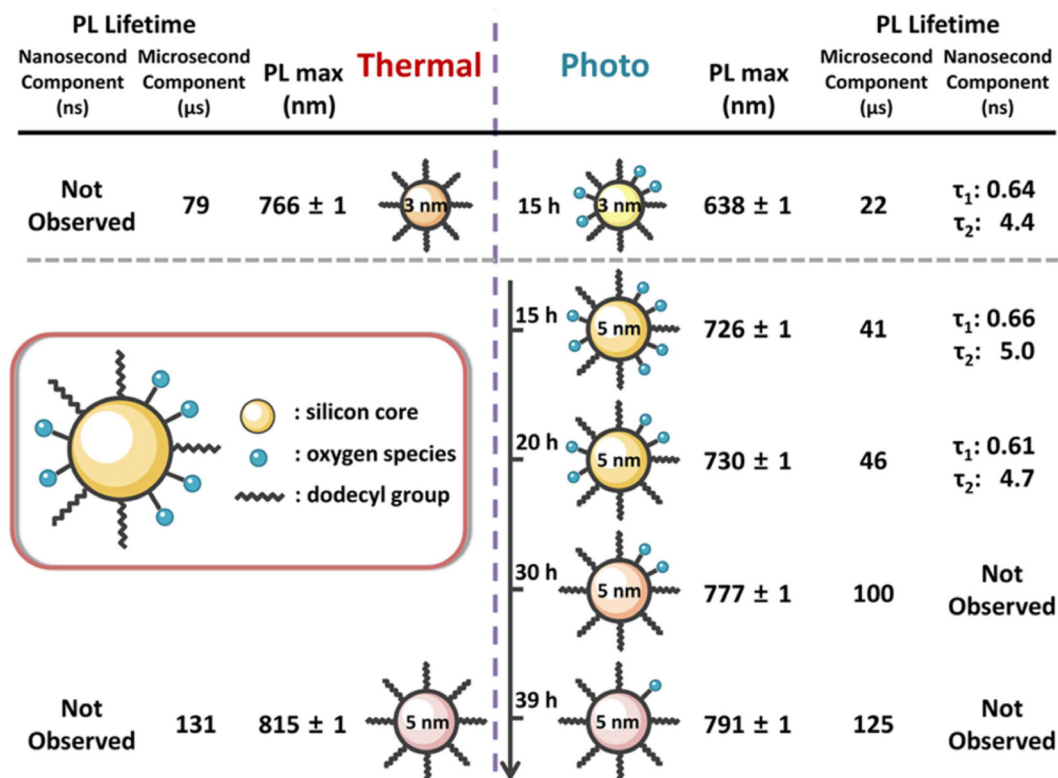


Figure 4.5: Summary of time-integrated PL maxima and time-resolved PL lifetimes for surface functionalized Si NCs. The standard error for the μ s-PL lifetime component is $\leq 1\mu$ s while that of the ns-PL lifetime is $\leq 1.5\%$.

Multi-exponential decay behavior in the nanosecond and microsecond ranges have also been reported for colloidal Si NCs dispersed in chloroform (He *et al.* 2008) and hexane (Sykora *et al.* 2008), as well as Si NCs embedded in an SiO₂ matrix (de Boer *et al.* 2010). Unlike the ns-decays commonly reported for blue/blue-green-emitting Si NCs, the ns-PL components observed for photochemically-modified Si NCs occur at wavelengths commonly associated with “slow band” emission (yellow-red) (see Fig. 4.4(a) and 4.8(c)). Kim *et al.* (2012) observed similar ns-PL decay times from freshly-etched freestanding Si NCs with an emission maximum at 657 nm. They proposed that the blue-shift of the PL maximum and reduction in carrier recombination lifetime from 49.9 μ s to ~ 3 ns after removing the SiO₂ matrix was associated with oxide and interface defects arising from surface oxidation. In

our case, surface oxides are present in thermally and photochemically functionalized Si NCs (*vide supra*). However, XPS and FTIR data indicate that the photochemically-modified Si NCs have substantially more silicon oxide and that the speciation of oxides differs significantly for the two surface functionalization methods (*vide supra*). We propose that the blue-shift of the PL maximum as well as the existence of ns-lifetime components for photochemically-modified Si NCs is related to differences (*i.e.*, quantity and speciation) in the surface oxidation. Although the PL emission shifts to lower energy when the size is increased, the general trend of the PL lifetime decay of these 5 nm samples is similar to that of the 3 nm samples for a given hydrosilylation method. The stark similarities (*i.e.*, quantity and speciation) of the oxide species determined by FTIR and XPS, as well as the PL dynamics, strongly suggest the origin of the ns lifetime is the same for the 3 nm and 5 nm Si NCs prepared using 15 hr photochemical hydrosilylation. In addition, the decay time of the μ s-PL component from the 15 hr photochemically-modified Si NCs is significantly less than that observed for their thermally-modified counterparts. This observation suggests the μ s-PL component observed from photochemically-functionalized Si NCs is dominated by emission from smaller NCs within the distribution (*vide infra*). All these results support the initial hypothesis that the observed PL blue-shift in photochemically-modified Si NCs can be attributed to the emission from smaller NCs in addition to emission from oxygen-induced defects.

Consistent with reports related to different hydrosilylation reactions on silicon surfaces (Kelly *et al.* 2011, Cicero *et al.* 2000), we contend that the limited reaction time (*i.e.*, 15 hrs) used for photochemical hydrosilylation led to incomplete surface functionalization. Surface oxidation may also occur during purification. Furthermore, it is reasonable that prolonging the photochemical modification procedure would provide a more complete passivation of the Si NC surfaces and allow for indirect tailoring of the amount of surface oxidation resulting from the workup procedures (Sun *et al.* 2005, Cicero *et al.* 2000, Effenberger *et al.* 1998). To investigate this possibility, a series of time-dependent photochemical hydrosilylation experiments were performed. Herein, $d \sim 5$ nm Si NCs were chosen as the model because their comparatively slow photochemical hydrosilylation provides a larger range of surface passivation. FTIR spectra of Si NCs show a less intense Si-O-Si stretching absorption at longer reaction time (Fig. 4.2(a)) while Si (IV) contribution in the Si 2p region of the

XPS spectra decreased after prolonged photochemical hydrosilylation, consistent with less surface oxidation and supporting our hypothesis (Fig 4.6). To provide a semi-quantitative measure of the degree of Si NC surface oxidation as a function of photochemical hydrosilylation reaction time, we estimated the relative oxidation purely based on the Si (IV) contribution in the Si 2p region of the XPS spectra. This was achieved by normalizing the area under Si (IV) component to total area of the entire Si 2p emission. We intentionally neglected sub-oxide contributions because their exact chemical identity was not straightforward to elucidate. As shown in Fig. 4.7, the XPS-derived relative oxidation decreases with prolonged reaction time. It is reasonable that this trend results from a more complete surface passivation/functionalization with longer reaction times. Concurrently, the intensities of signals arising from silicon sub-oxides (*i.e.*, Si(I), Si(II), and Si(III)) increase slightly (Fig. 4.6) consistent with the proposal that more hydride terminated Si surface sites have been modified by alkyl ligands.

Figure 4.3(c) shows the time-integrated PL spectra of photochemically-modified Si NCs after functionalization for the indicated reaction times; the evolution of the PL emission maximum is summarized in Fig. 4.5. The PL arising from the 20-hour sample is centered at *ca.* 730 nm. Extending the reaction time to 30 hours induced an obvious red-shift to *ca.* 777 nm. The magnitude of the red-shift continues to increase with increased reaction time and after 39 hours, the PL maximum of Si NCs centers at *ca.* 791 nm - close to the 815 nm PL peak obtained for Si NCs prepared using thermal hydrosilylation. These results support the proposal that longer photochemical reaction times lead to more complete surface functionalization.

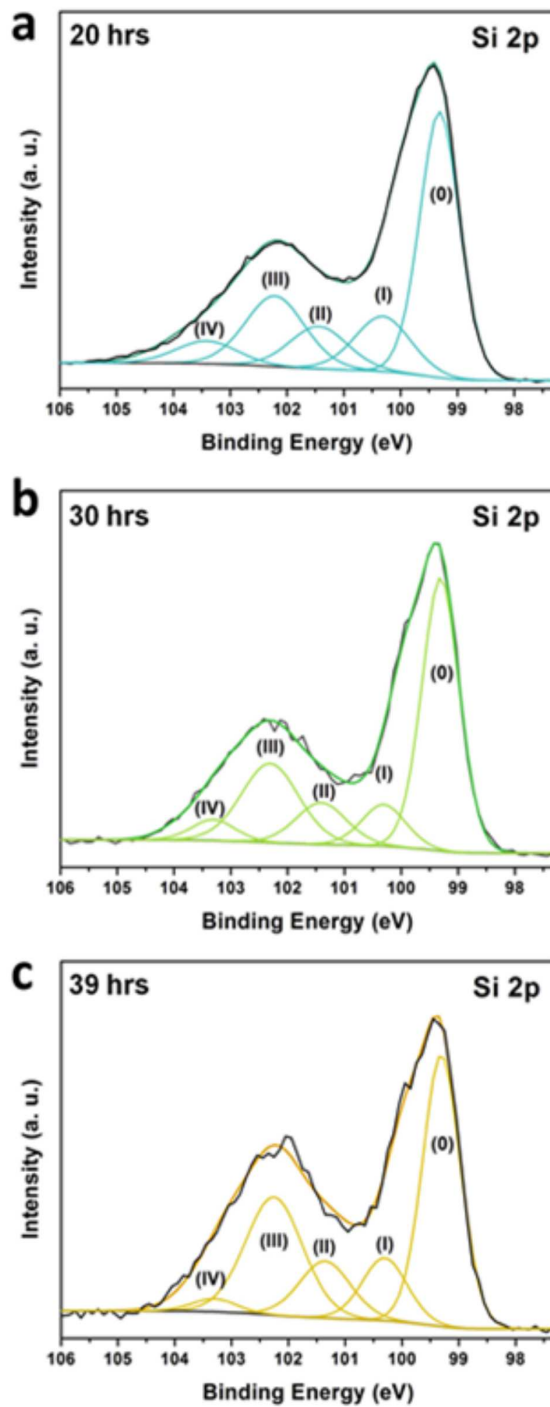


Figure 4.6: High-resolution XPS spectra of the silicon region for purified functionalized 5 nm SiNCs after (a) 20, (b) 30, and (c) 39 hour photochemical hydrosilylation. Si 2p_{1/2} signals have been omitted for clarity [Adapted from Yang, De los Reyes et al. 2015].

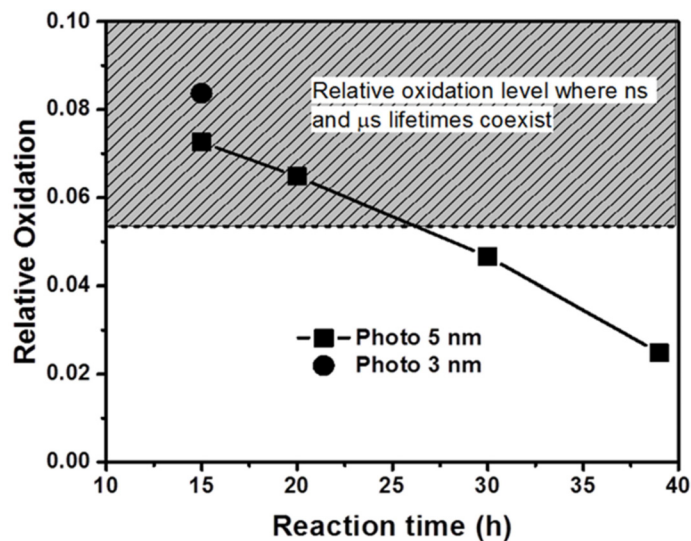


Figure 4.7: XPS-derived relative oxidation of photochemically functionalized SiNCs as a function of reaction.

To explore the impact of surface oxidation on the PL emission dynamics of the present surface functionalized Si NCs, the time-integrated PL maximum and microsecond decay component were plotted as a function of XPS-derived relative oxidation. Figures 4.8(a) and (b) show that as the relative oxidation increases, the time-integrated PL maximum shifts to higher energy while the decay time of the μs -PL component decreases. Again, we assert that this shift of the PL maximum to higher energy does not arise from an oxygen-induced reduction in NC size (*vide supra*). A reasonable explanation for this behavior is an increase in the number of luminescent defect centers associated with increased surface oxidation. Based upon literature accounts, carrier trapping at defect sites occurs very rapidly and can dominate, if not totally quench, core-state related emission (Klimov *et al.* 1998, Sailor *et al.* 1997, Fisher *et al.* 1994, Lauerhaas *et al.* 1992). Oxygen-induced-defect quenching of the PL is more likely observed in larger NCs within an ensemble since they are functionalized more slowly and therefore have more surface oxides than smaller NCs (Kelly *et al.* 2011). As a result, the PL from the larger Si NCs is quenched more than that from smaller NCs, contributing to the observed PL blue-shift, consistent with computational studies (Lockwood *et al.* 2009, Belyakov

et al. 2008). This explains the decrease in the decay time of the μs -PL component with increased relative oxidation. The absolute quantum yield (AQY) measurements of the 3 nm Si NCs show that photochemically functionalized Si NCs exhibit a comparatively higher AQY ($66 \pm 8 \%$) than its thermal counterpart (AQY = $41 \pm 3\%$). This result suggests that oxygen moieties at the NC surface create radiative centers since higher AQY is observed for the more oxidized NCs. From this we conclude that the measured ns decay is a radiative process that originates from oxygen-induced defects. It is important to note that while both thermal and photochemical hydrosilylation resulted in partial surface oxidation, the ns component was only detected at comparatively high surface oxidation levels. It is possible that the PL of thermally functionalized Si NCs has a ns component as well, but because the surface oxidation is present in much lower quantities, the ns signal is below the detection limit of our system. Based upon AQY and PL dynamics measurements, it is likely that the observed blue-shift of PL maximum arises from a combination of emission from smaller NCs and from oxygen-induced surface defect sites.

The shaded area in Fig. 4.8(a) corresponds to the relative oxidation region where both ns- and μs -PL components were observed. It is evident that regardless of NC size, an increase in surface oxidation leads to a blue-shift of PL maximum accompanied by a short-lived ns-PL component. This result is consistent with the assumption that the ns-PL component is associated with the increase of defect sites as the relative surface oxidation increases. Contrary to other reports (Dohnalová *et al.* 2013, Wolkin *et al.* 1999), we conclude from the present data (*i.e.*, Fig. 4.4(a) and 4.8(c)) that oxygen-defect-related PL may occur at energies higher than the core-states.

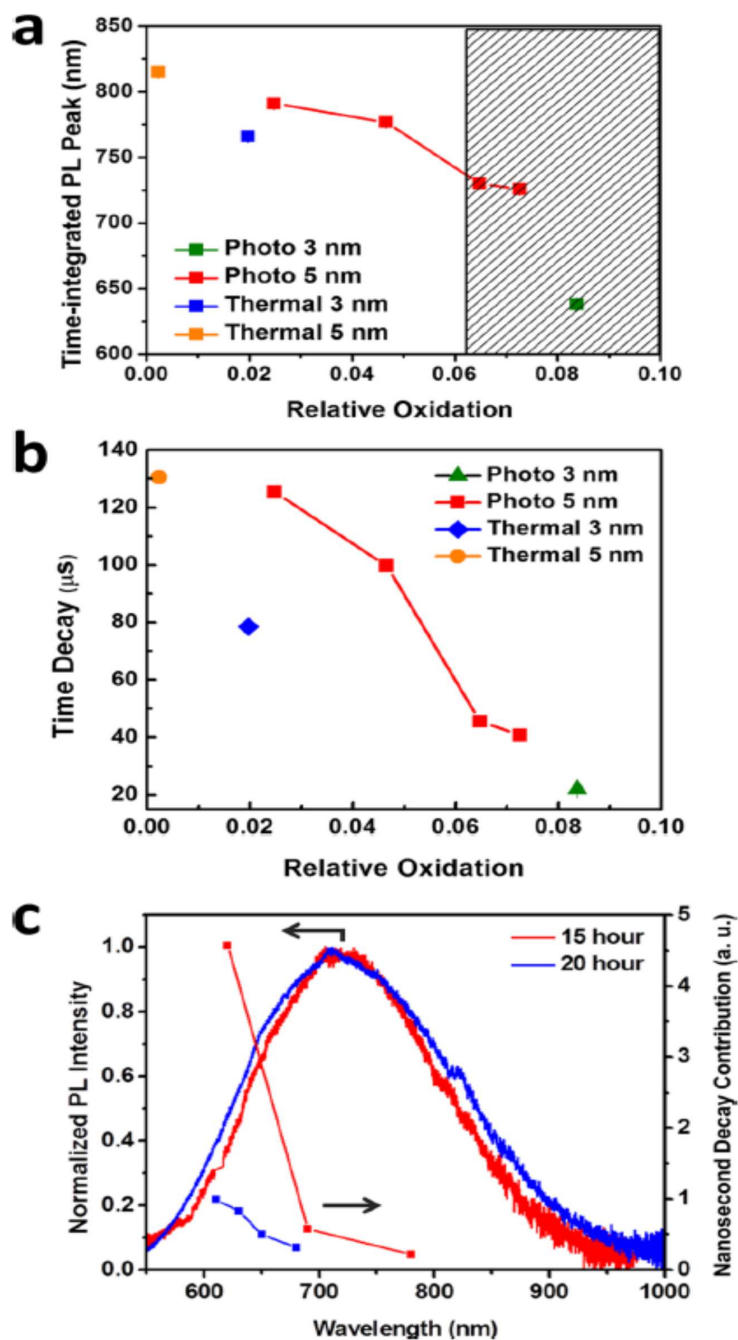


Figure 4.8: (a) Maxima of time-integrated PL spectra and (b) microsecond PL lifetime components for Si NCs prepared using thermal and photochemical hydrosilylation as a function of XPS-derived relative surface oxidation. The shaded area in (a) corresponds to the relative oxidation region in which nanosecond and microsecond PL lifetimes coexist. (c) Time-integrated PL spectra for 5 nm photochemically-functionalized Si NCs with reaction times of 15 and 20 hours. The corresponding magnitude of the spectrally-resolved nanosecond PL decay contribution is also shown.

Figure 4.8(c) shows the relative amplitude of the ns-PL component of the 15-hour and 20-hour photochemically-functionalized Si NCs. The observed increase in the amplitude of the ns-PL component at higher energies affirms the hypothesis that carrier radiative recombination at oxygen-induced defects contributes to the PL blue-shift. A similar result was observed for 3-nm photochemically-functionalized Si NCs. Based upon our hypothesis, if the PL blue-shift is minimized/eliminated by ensuring complete surface passivation, the defect-related ns-PL component should be suppressed and ultimately disappear if prolonged photochemical reaction is employed. Indeed, this is the case for the present reaction time-dependent experiments, as shown in Fig. 4.5. All samples exhibit μ s-PL components while ns-PL components were only detected for samples obtained from shorter photochemical reaction times (*i.e.*, 15 and 20 hours, shown in Fig. 4.5). In addition, the 39-hour photochemically-functionalized Si NCs exhibit PL emission dynamics very similar to that of the thermally-functionalized Si NCs.

4.5 Conclusion

The interconnection between Si NC size-independent PL blue-shift, nanosecond excited-state lifetime and XPS-derived relative oxidation has been examined and confirmed through systematic investigations of dodecyl-functionalized Si NCs. Differences in the effectiveness of thermal and photochemical hydrosilylation methods to passivate Si NC surfaces provide an opportunity to control the degree of surface modification on alkyl-terminated Si NCs and by extension, surface oxidation. PL emission maxima arising from Si NCs functionalized using 15-hr photochemical hydrosilylation (both 3 nm and 5 nm) are significantly blue-shifted compared to their thermal counterparts. The difference in emission energies cannot be solely attributed to quantum confinement effects because the difference in average diameters and size distributions is small, if not negligible. A microsecond PL lifetime component was observed for all samples, regardless of functionalization methodology, and has been attributed to Si NC core state recombination. Size-independent nanosecond lifetime components (< 7 ns) were only observed for samples prepared using the photochemical approach that exhibit substantial relative surface oxidation. Time-dependent experiments indicate that the observed blue-

shift of PL maxima and nanosecond lifetime in photochemically-modified Si NCs are related to the degree of surface oxidation resulting from incomplete functionalization of the Si NC surface.

CHAPTER 5

Effect of surface passivation on the emission dynamics of colloidal silicon nanocrystals¹

5.1 Introduction

Since the discovery of light-emitting porous silicon by Canham (1990), different silicon nanostructures, such as organically passivated silicon nanocrystals (Si NCs) (Yang, De los Reyes *et al.* 2015, Dasog, De los Reyes *et al.* 2014, Beard *et al.* 2007), Si NCs embedded in an SiO₂ matrix (Titova *et al.* 2011, Zhang *et al.* 1995), Si/SiO₂ core-shell structure (Vinciguerra *et al.* 2000), have been investigated as potential materials for optoelectronic and biological applications. However, nanostructured Si is generally viewed as a poor light emitter compared to direct bandgap materials (Harris *et al.* 2012, Mi *et al.* 2009, Ashmore *et al.* 2002, Mashford *et al.* 2013, Dabbousi *et al.* 1997, Alivasatos 1996). A vast majority of efforts in improving light emission in nanostructured Si has been focused on the influences of quantum confinement (QC) via particle size reduction (Kim *et al.* 2004, Zacharias *et al.* 2002, Holmes *et al.* 2001, Vinciguerra *et al.* 2000, Wilcoxon and Samara 1999). By utilizing the QC effect, PL emission from Si NCs has been tuned from the infrared to the visible (Dohnalová *et al.* 2013, Hessel *et al.* 2011, Creazzo *et al.* 2010, Kang *et al.* 2009, English *et al.* 2002,

¹Part of this Chapter has been published in Mita Dasog, Glenda B. De los Reyes, Lyubov V. Titova, Frank A. Hegmann, Jonathan G.C. Veinot, ACS Nano 2014, 8(9), 9636-9648.

Ledoux *et al.* 2000). However, a dramatic decrease in QY is observed as the size of the NC is reduced to less than 2 nm (Miller *et al.* 2012, Mastronardi *et al.* 2011, Garcia *et al.* 2003). This reduction in QY for smaller nanocrystals is attributed to significant increase in nonradiative recombination pathways related to surface and other traps that dominate the radiative recombination process.

Doping of Si NCs with shallow impurities has also been explored as a potential route to enhance the PL properties. Si NCs have been doped or co-doped with phosphorus, boron, and nitrogen atoms (Ma *et al.* 2012, Pi *et al.* 2012, Pi *et al.* 2011, Sato *et al.* 2009, Hao *et al.* 2008, Fuji *et al.* 2002, Mimura *et al.* 2000). Initial results indicated improvement in PL properties of phosphorus- and boron-doped Si NCs, but it quickly became evident that the enhancement was sensitive to dopant concentrations, fabrication methods, and location of the dopant atoms. These factors cannot easily be controlled, hence doping is not a straightforward method to tailor the optical properties of Si NCs. Recently, Nie *et al.* (2014) showed that surface engineering can offer a means of creating brighter carbon dots with tunable PL and shorter lifetimes. A tunable emission was obtained using surface functional groups that introduced new energy level for electron transitions which resulted in continuously adjustable full color emission. While such reports of enhancement have appeared, limited studies were performed to improve and tune the PL emission from Si NCs using surface groups.

In this study, the effect of surface passivation on the emission dynamics of colloidal Si NCs is reported. By changing the surface passivation but keeping the nanocrystal size the same, we observed that the time-integrated PL (TIPL) can be tuned across the visible spectrum. Time-resolved PL (TRPL) measurements revealed that photoexcited carriers exhibit fast recombination in the ns time scale characteristic of surface-related emission.

5.2 Sample Preparation

The syntheses of the functionalized Si NCs used in this study have been described in detail elsewhere (Dasog *et al.* 2014, Dasog *et al.* 2013, Hessel *et al.* 2006). Briefly, commercial hydrogen silsesquioxane was thermally processed in a slightly reducing atmosphere (95% Ar / 5% H₂) at 1100 °C to

yield well-defined Si NCs embedded in a SiO₂-like matrix. Hydride terminated Si NCs were routinely obtained following the removal of the oxide matrix upon treatment with an alcoholic HF acid solution. The surface of the Si NCs was passivated using dodecyl, trioctylphosphine oxide (TOPO), acetal and dodecylamine. Dodecyl functionalization of Si NCs was conducted in inert atmosphere and in air to determine the effect of oxygen in the PL properties. The samples were dissolved in toluene and placed in a cuvette for TIPL and TRPL measurements.

5.3 Experimental details

The TIPL and TRPL spectroscopy set-ups introduced in Chapter 3 were used for the measurements described in this chapter. The PL was excited by 400-nm pulses at excitation fluences ranging from 0.56 mJ/cm² to 2.3 mJ/cm². The TIPL spectra were integrated for 120 s and corrected to the spectral response of the system. For sub-ns TRPL, the emission wavelength was chosen using the monochromator and each wavelength was integrated for 1 hr. In the case of μ s-TRPL, 10-nm band pass filters were used to select a particular emission wavelength and the PL lifetime was extracted from the average of 256 PL decay waveforms. A 435-nm long pass filter was used in the TIPL and PL lifetime measurements to block the scattered 400 nm excitation pulses. The filter's transmission cut-off region is represented by a blue shaded area in the PL spectral plots.

5.4 Results and discussion

5.4.1 Dodecylamine functionalized silicon nanocrystals

Figure 5.1(a) shows the scheme for dodecylamine functionalized Si NCs which exhibits blue emission that is visible to the eye (Fig. 5.1(b)). A high resolution XPS spectrum of the Si 2p region shows two distinctive peaks corresponding to Si(0) core atoms with a peak at 98.8 eV and surface Si atoms attached to either N or O with a peak at 102 eV (Fig. 5.1(c)). The N 1s region can be fitted to two peaks (Fig. 5.1(d)). The peak at 397.8 eV is characteristic of bridging nitrogen atoms (Si-N-Si). The

species responsible for the emission at 399.5 eV remains unclear, however, it is tentatively assigned to silicon oxynitride species (Dasog *et al.* 2013). The Fourier transform infrared (FTIR) spectra of neat dodecylamine and dodecylamine modified Si-NCs are shown in Fig. 5.1(e). Characteristic N-H stretches *ca.* 3300 - 3100 cm^{-1} and 1600 cm^{-1} are observed in neat dodecylamine (Fig. 5.1(e-i)) but are absent from the dodecylamine functionalized Si-NC spectrum (Fig. 5.1(e-ii)) consistent with an amine group reacting with the silicon surface. Absorption peaks attributable to C-H stretches from the alkyl chain are observed at *ca.* 2900 cm^{-1} and 1470 cm^{-1} in neat dodecylamine and functionalized Si-NCs. Partial oxidation of Si-NCs is evidenced by Si-O-Si stretch features *ca.* 1120 cm^{-1} . Transmission electron microscopy (TEM) analysis of 200 particles indicates that the NCs have an average diameter of 3.8 ± 0.7 nm (Fig. 5.1(f)).

Figure 5.2(a) shows the TIPL of 3.8 nm dodecylamine functionalized Si NCs with a PL maximum at ~ 475 nm. The asymmetry in the PL spectral profile is due to higher energy components of the PL being truncated by the transmission of the optical filter. The measured PL is significantly blue-shifted compared to the quantum confinement (QC) prediction (Fig. 2.4) for the same NC size (Dohnalová *et al.* 2013, Rodriguez-Nunez *et al.* 2012, Wolkin *et al.* 1999). TRPL in the ns range revealed that the PL lifetime exhibits a bi-exponential decay,

$$I(t) = A_1 e^{[-(t/\tau_1)]} + A_2 e^{[-(t/\tau_2)]} + C \quad (5.1)$$

where τ_1 and τ_2 are the decay times and C is a constant offset much smaller than A_1 and A_2 . At 470 nm emission wavelength, the measured PL lifetimes are $\tau_1 = 1.45 \pm 0.01$ ns and $\tau_2 = 6.08 \pm 0.02$ ns. However, no microsecond PL decay was observed for the entire emission range, inconsistent with bandgap transitions within the Si core reported elsewhere (Mastronardi *et al.* 2012, Garcia *et al.* 2003). Based on the TIPL and the absence of a microsecond PL component, quantum confined emission from the silicon core can be ruled out as the origin of the ns-blue PL. It is more likely that the observed blue emission is related to carrier trapping/charge transfer to silicon oxynitride species at the surface of the NC. Similar observations have been reported for silicon oxynitride films (Huang *et al.* 2014, Augustine *et al.* 1995).

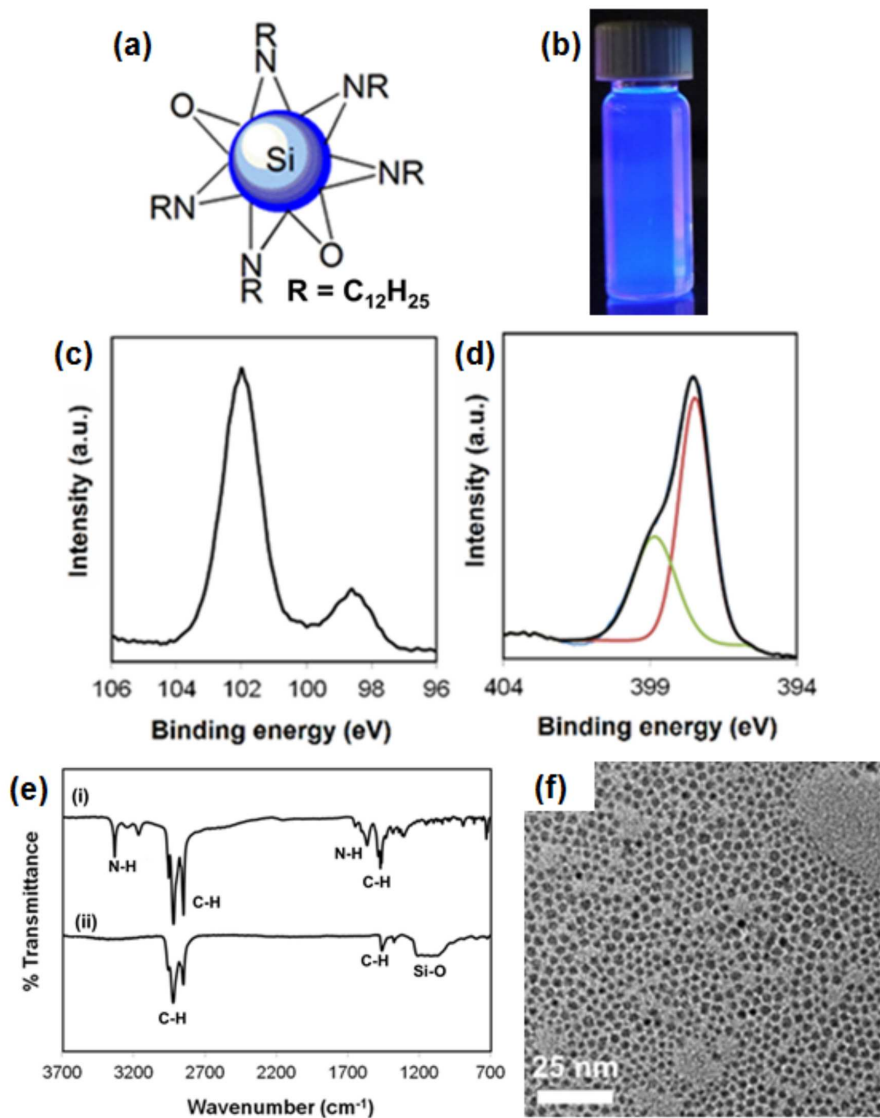


Figure 5.1: Characterization details of dodecylamine functionalized Si NCs. (a) Schematic representation of the functionalized Si NCs and (b) visible PL upon excitation by 365 nm from a UV lamp. XPS spectrum of (c) the Si 2p region and (d) the N 1s region. The black line in (d) is a fit to the experimental data. (e) FTIR spectra of (i) neat dodecylamine and (ii) dodecylamine functionalized Si NCs, and (f) bright field TEM image [Adapted from Dasog, De los Reyes et al. 2014].

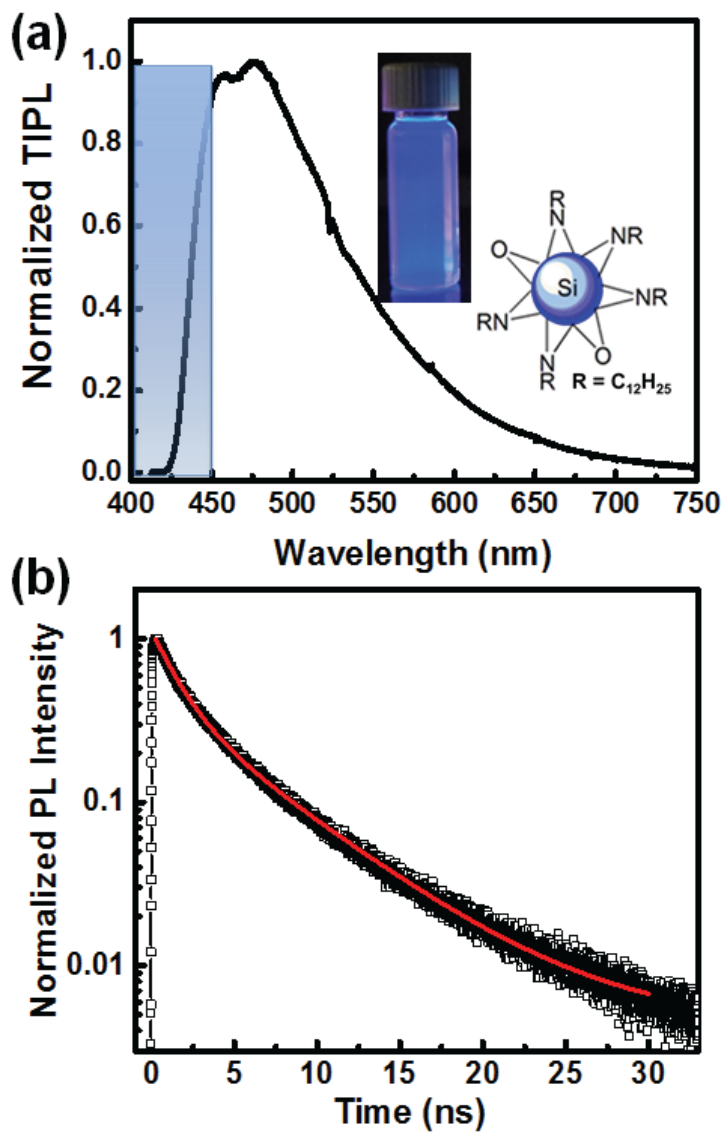


Figure 5.2: (a) Time-integrated PL spectra of dodecylamine functionalized SiNCs excited by 400 nm laser pulses at 1.41 mJ/cm² fluence. (b) TRPL decay measured at 470 nm. The red line in (b) is a bi-exponential fit to the data.

5.4.2 Acetal functionalized silicon nanocrystals

The acetal functionalized Si NCs (Fig. 5.3(a)) exhibits blue-green emission when excited by 400 nm laser pulses, as shown in Fig. 5.3(b). The FTIR spectrum of the freshly prepared hydride-terminated Si NCs reveal Si-H stretches *ca.* 2100 cm^{-1} and 920 cm^{-1} while the FTIR spectrum of acetal functionalized Si NCs exhibits features attributable to C-H stretch *ca.* 2920 cm^{-1} and C-O, Si-O-C, Si-O-Si stretches between 1300 cm^{-1} - 1080 cm^{-1} appear (Fig. 5.3(c)). The acetal functionalized Si-NCs have an average diameter of $3.4 \pm 0.5\text{ nm}$ as determined from TEM analysis (Fig. 5.3(d)).

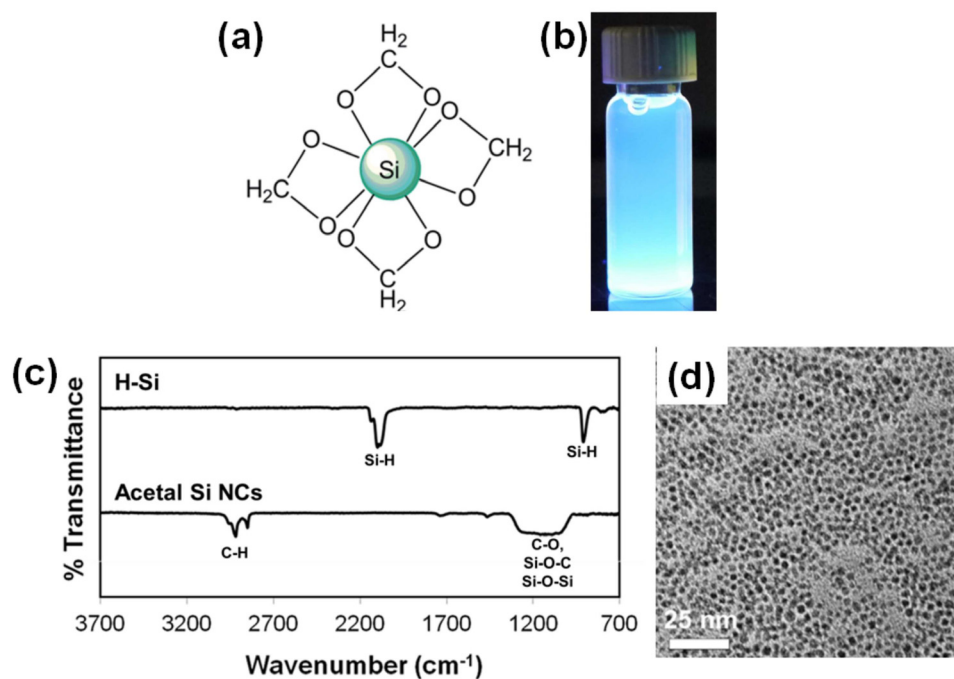


Figure 5.3: Characterization details of acetal functionalized Si NCs. (a) Scheme for the functionalized Si NCs, (b) visible PL upon excitation by a 365 nm UV lamp, (c) FTIR of hydride terminated Si NCs and acetal functionalized Si NCs, and (d) bright field TEM image [Adapted from Dasog, De los Reyes et al. 2014].

Figure 5.4 shows the TIPL spectrum of acetal functionalized Si NCs with peak emission at ~ 490 nm. Analogous to dodecylamine functionalized Si NCs' behavior, the observed PL is blue-shifted with respect to the QC prediction and microsecond PL was not observed for the entire emission wavelength. Hence, it is unlikely that the observed PL is due to QC.

To probe the nature of the emitting state in this functionalized Si NCs, detailed sub-ns TRPL measurements were conducted. Using this method, the temporal evolution of the spectral profile can be monitored. In doing so, it is possible to determine the different emitting states since they will exhibit different spectral profiles and lifetimes (Sykora *et al.* 2008). Figure 5.5(a) shows the contour plot of the PL intensity as a function of wavelength and time after photoexcitation. From the PL intensity plot, the temporal evolution of the PL spectra was extracted and shown in Fig. 5.5(b). The PL peak shifts from ~ 490 nm to ~ 516 nm at 9.968 ns after photoexcitation, no further shift is observed after this time. While the PL peak position is shifting towards lower energy, it does not indicate that the shift is due to different distinct emissive states (*e.g.*, core states and surface states) in which an isostilbic point exists as observed by Sykora *et al.* (2008). Figure 5.5(c) shows the spectrally-resolved PL dynamics which exhibit bi-exponential decay according to Eq. 5.1. At the peak emission wavelength of 490 nm, the measured PL lifetime is $\tau_1 = 1.29 \pm 0.01$ and $\tau_2 = 4.78 \pm 0.04$ ns. The PL lifetime as a function of emission wavelength is summarized in Fig. 5.5(d). As seen from the plot, the photoexcited state lifetime increases with emission wavelength, and all decay times are less than 6 ns. Similar luminescence has been observed in carboxylic acid functionalized Si surfaces (Manhat *et al.* 2011, Green *et al.* 1997) and oxidized silicon carbide (SiC) NCs (Li *et al.* 2011, Fan *et al.* 2008). Based upon literature reports, the blue-green PL is tentatively attributed to silicon carboxy sites and the shift in the PL peak position is possibly due to different interband transitions within the surface functional group.

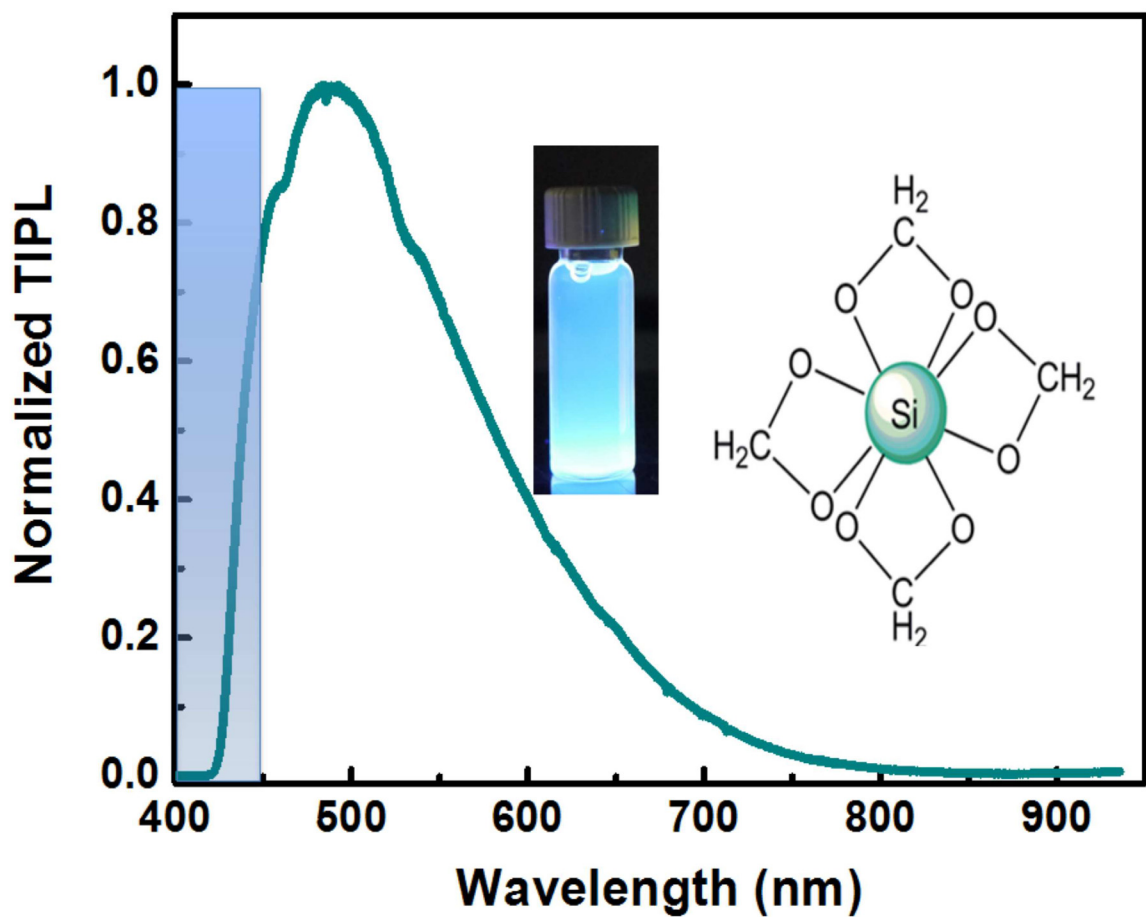


Figure 5.4: TIPL spectrum of acetal functionalized Si NCs excited by 400 nm laser pulses at an excitation fluence of 1.98 mJ/cm^2 . Insets are the proposed scheme and the visible PL upon excitation by 365 nm UV lamp.

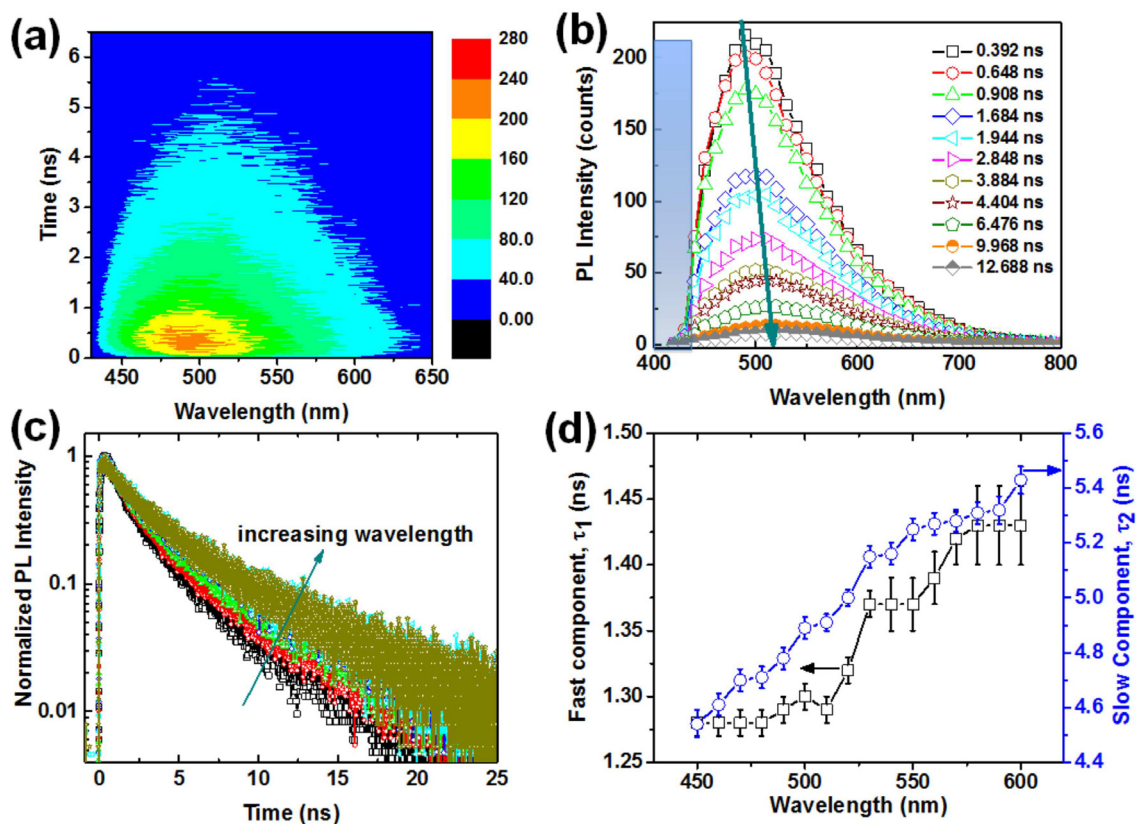


Figure 5.5: Detailed sub-ns TRPL of acetal functionalized Si NCs. (a) PL intensity as a function of wavelength and time after photoexcitation. (b) Temporal evolution of the PL spectral profile and (c) spectrally-resolved PL lifetime extracted from (a). (d) PL lifetimes obtained from the bi-exponential fit of the spectrally-resolved PL decays. The PL was excited by 400-nm pulses at an excitation fluence of 0.56 mJ/cm^2 .

5.4.3 TOPO functionalized Si NCs

The schemes for TOPO functionalized Si NCs are shown in Fig. 5.6(a) and (c) for 8 hours and 4 weeks reaction time, respectively. TOPO functionalized Si NCs that undergo an 8 hours reaction

time emit yellow light while the TOPO functionalized Si NCs with 4 weeks reaction time show strong purple emission when illuminated by 365 nm light from an UV lamp (Figs. 5.6(b) and (d), respectively). Figure 5.6(e) shows the FTIR spectra of neat TOPO and TOPO functionalized Si NCs. In both spectra, the P=O stretch *ca.* 1120 cm^{-1} and C-H stretches *ca.* 2870 cm^{-1} , 1470 cm^{-1} , and 1370 cm^{-1} are observed. A weak Si-O stretch is observed in TOPO functionalized Si NC at 1080 to 1040 cm^{-1} , consistent with the presence of an oxide. Unfortunately, following the reaction with TOPO, it is not possible to conclusively identify the exact character of the oxidized Si-NC surface. Based upon FTIR data, it is reasonable that it consists of bridging Si-O-Si moieties, as shown in Fig. 5.6(e-ii).

Bright field TEM imaging shows Si NCs with an average diameter of 3.2 ± 0.5 nm, however the quality of the image is poor due to the presence of a large excess of organic ligand (Fig. 5.6(f)). Attempts to remove the excess TOPO via selective precipitation and low temperature crystallization resulted in agglomeration/precipitation of the Si NCs (Veinot's lab at Department of Chemistry, University of Alberta).

It has been observed that oxidation of TOPO functionalized Si NCs continues and proceeds slowly over a year. Initially, a moderate blue shift of the PL maximum is observed, followed by a complete quenching of the PL. To investigate the role of TOPO in the PL properties of functionalized Si NCs, the synthesis was repeated using a larger amount of TOPO and the reaction time was extended to 4 weeks. From the initial yellow emission, the TOPO functionalized Si NCs with 4 weeks reaction time exhibit purple emission under 365 nm excitation, as shown in Fig. 5.6(d). In addition, XPS analysis of the TOPO functionalized Si NCs with 4 weeks reaction time, shown in Fig. 5.7(a), reveals a strong Si-O emission peak at 100.6 eV and 102.1 eV attributed to Si suboxides and a peak at 103.4 eV attributed to SiO_2 . Surprisingly, a silicon core signal at 99.3 eV (Yang, De los Reyes *et al.* 2015, Dasog *et al.* 2013) was not detected. This result was further confirmed by XRD analysis of the sample shown in Fig. 5.7(b). The only 2θ peak is at 22.80° , which is attributed to amorphous silica (Vicente *et al.* 2009). Based on these results, we hypothesize that the original Si core becomes silicon oxide, SiO_x . The proposed scheme is shown in Fig. 5.6(c).

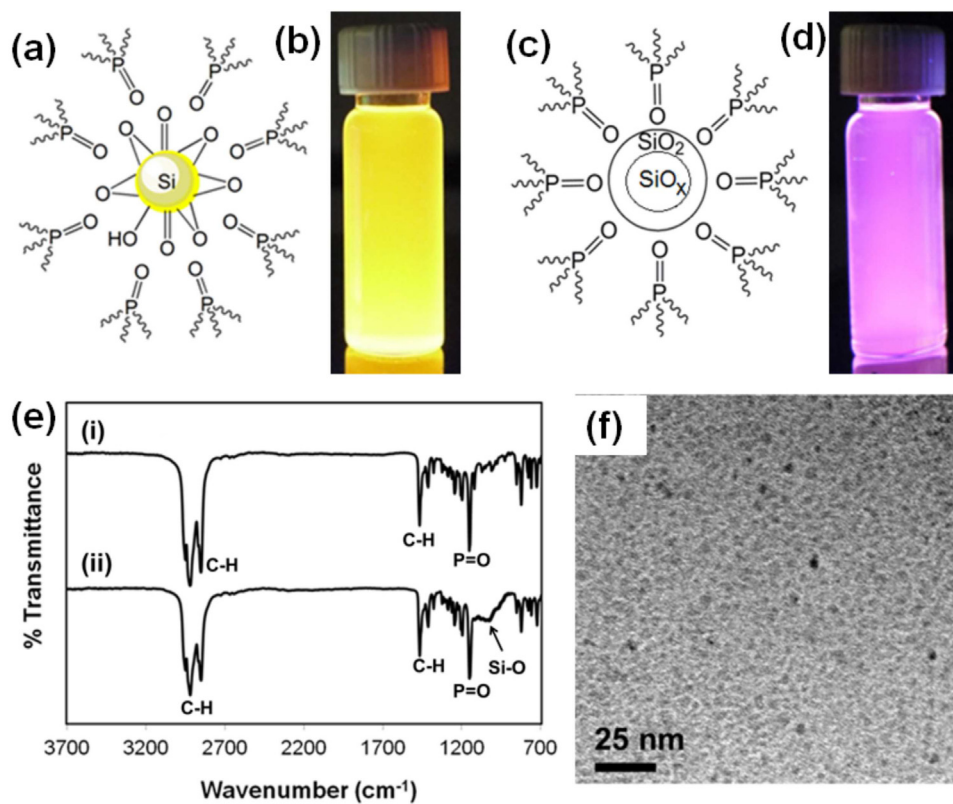


Figure 5.6: Characterization details of TOPO functionalized Si NCs. Scheme for TOPO Si NCs functionalized for (a) 8 hours and (c) 4 weeks, while (b,d) are the corresponding visible PL upon excitation by 365 nm UV lamp. (e) FTIR of (i) neat TOPO and (ii) TOPO Si NCs functionalized for 8 hours and (f) is the corresponding bright field TEM image (Veinot Lab).

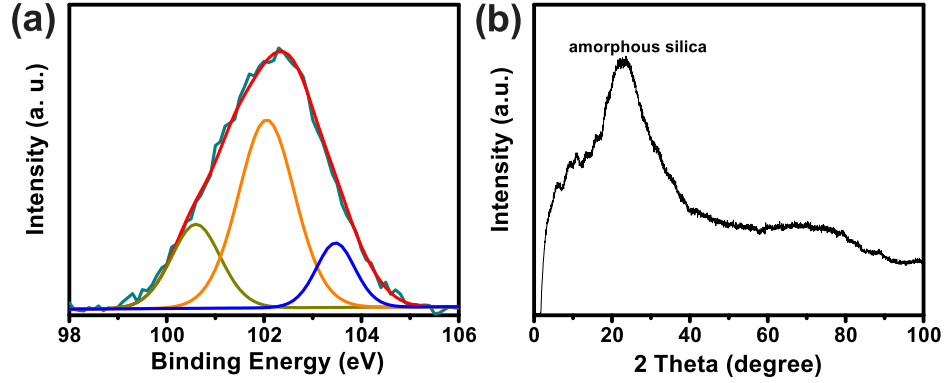


Figure 5.7: (a) XPS spectrum of the Si 2p region and (b) XRD analysis of the 4 weeks TOPO functionalized Si NCs (Veinot group).

The TIPL spectra of the TOPO functionalized Si NCs are shown in Fig. 5.8. The 8-hour TOPO functionalized Si NCs exhibit a PL peak emission at ~ 593 nm while the 4-week TOPO functionalized Si NCs exhibit two distinct emission peaks at ~ 450 nm and ~ 650 nm. The exact location of the 450-nm peak is uncertain due to the filter transmission cutoff which exhibits $\sim 86\%$ transmission at 450 nm followed by a sharp decrease in transmission at shorter wavelengths. The existence of the two PL peak in the blue and red spectral regions explains the observed purple PL.

TRPL measurements of the TOPO functionalized Si NCs were performed over μs and sub-ns time scales to differentiate core emission from surface/interface-related emission, as shown in Fig. 5.9. Both μs and ns PL lifetimes are observed for TOPO Si NCs functionalized for 8 hours (Fig. 5.9(a)). However, only ns lifetimes are measured for the 4-week TOPO functionalized Si NCs, as shown in Fig. 5.9(b). The μs -component of the PL lifetime of the 8-hour TOPO functionalized Si NCs exhibits a stretched exponential decay,

$$y = A * \exp\left[-\left(\frac{t}{\tau}\right)^\beta\right] + C \quad (5.2)$$

where τ is the decay time, β is the dispersion factor which can take values between 0 and 1, and

C is a constant offset much smaller than A. On the other hand, the sub-ns TRPL exhibits a bi-exponential decay according to Eq. (5.1). The ns-PL lifetime components of the 8-hour TOPO functionalized Si NCs are $\tau_1 = 0.68 \pm 0.04$ ns and $\tau_2 = 5.20 \pm 0.20$ ns measured at 590 nm while the μ s-PL decay component is 19.6 ± 0.2 μ s with $\beta = 0.5$ measured at 690 nm. The ns-PL decays of the 4-week TOPO functionalized Si NCs ($\tau_1 = 1.48 \pm 0.01$ ns and $\tau_2 = 5.87 \pm 0.10$ ns for 445 nm emission and $\tau_1 = 1.22 \pm 0.01$ ns and $\tau_2 = 5.02 \pm 0.10$ ns for 640 nm emission) are comparable to that of the 8-hour TOPO functionalized Si NCs. The PL decay measured at 445 nm emission wavelength is slightly higher than that for 640 nm emission which indicates that the blue-component of the PL in the 4-week TOPO functionalized Si NCs is due to a different emissive state. Hence, based on TIPL, XRD, XPS and TRPL results, we tentatively propose a $\text{SiO}_x/\text{SiO}_2$ structure surrounded by TOPO for the 4-week functionalized Si NCs (Fig. 5.6(c)). The blue component of the PL is tentatively assigned to the silicon oxide core, SiO_x , consistent with literature reports (Qiu *et al.* 2005, Peng *et al.* 2002, Qin *et al.* 1997). The ns-PL lifetime measured at the yellow-red emission wavelengths is similar to the recently reported ns-PL lifetime in oxidized dodecyl functionalized Si NCs prepared using photochemical hydrosilylation (Yang, De los Reyes *et al.* 2015) and was attributed to oxygen-induced defects at the surface of the nanocrystals.

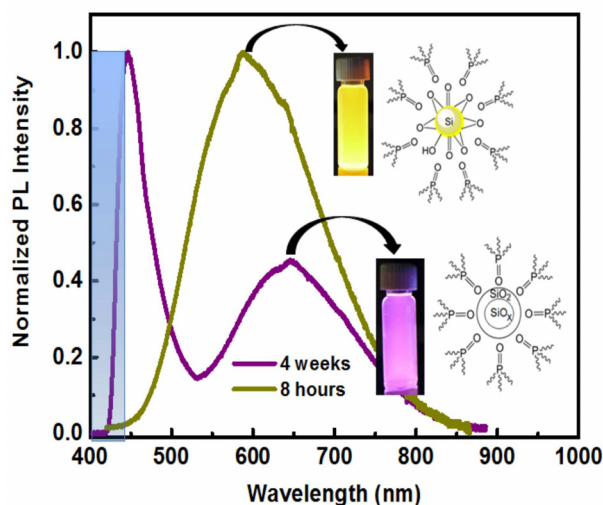


Figure 5.8: TIPL of 8 hours (yellow line) and 4 weeks (purple line) TOPO functionalized Si NCs. The PL was excited by 400-nm pulses at an excitation fluence of 2.3 mJ/cm^2 .

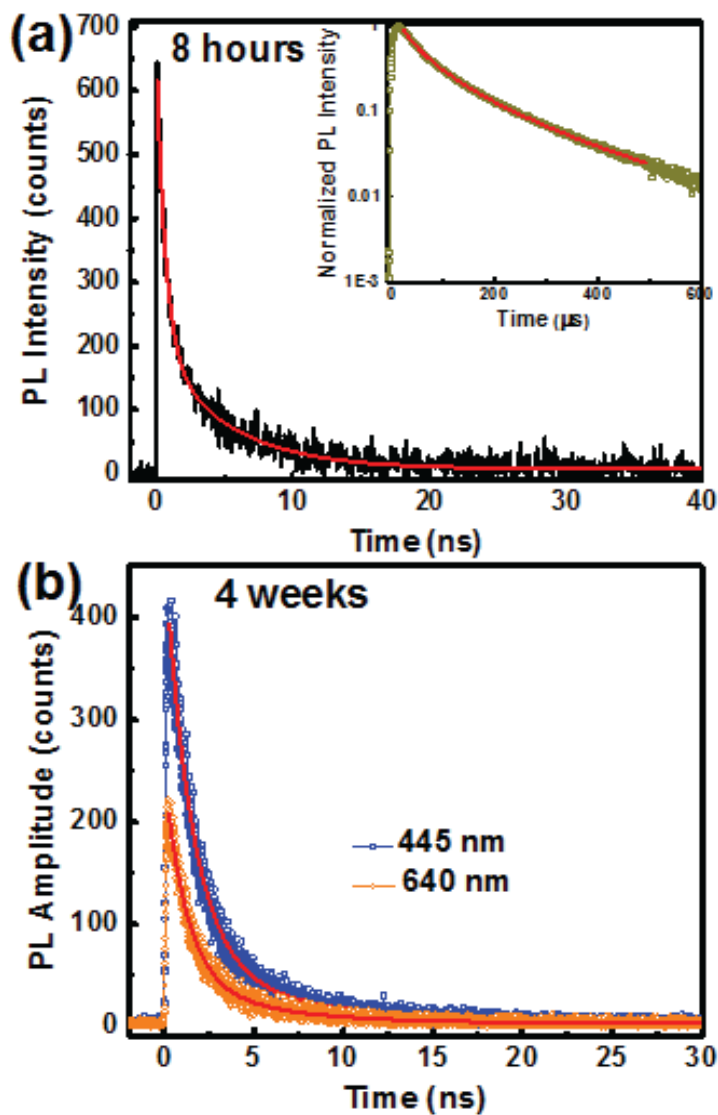


Figure 5.9: TRPL dynamics of TOPO functionalized Si NCs with (a) 8 hours and (b) 4 weeks reaction time. The inset in panel (a) is the μ s-component of the PL lifetime of the 8-hour TOPO functionalized Si NCs measured at an emission wavelength of 600 nm. The PL lifetimes in the sub-ns time scale were measured at 590 nm for the 8-hour TOPO functionalized Si NCs and at 445 and 640 nm for the 4-week TOPO functionalized Si NCs. The red lines are bi-exponential and stretched exponential fits to the ns and μ s lifetime components, respectively.

5.4.4 Dodecyl functionalized Si NCs

The thermal hydrosilylation process of dodecyl functionalized Si NCs is done in inert atmosphere and ambient air environments. The schemes for the dodecyl functionalized Si NCs are shown in Fig. 5.10(a) and (c) for inert atmosphere and air environments, respectively. Upon illumination by a 365 nm UV lamp, the dodecyl functionalized Si NCs prepared under an inert atmosphere exhibit red PL (Fig. 5.10(b)) while the dodecyl Si NCs prepared in oxygen environment show an orange PL (Fig. 5.10(d)). A representative FTIR spectrum (Fig. 5.10(e)) of dodecyl Si NCs prepared in an inert atmosphere shows characteristic C-H and C-C stretching features at *ca.* 2900 cm^{-1} and 1450 cm^{-1} , respectively. There is no evidence of Si-H (*ca.* 2100 cm^{-1}), C=C (*ca.* 1600 cm^{-1}) or Si-O (*ca.* 1100 cm^{-1}) at the sensitivity of FTIR, analysis consistent with effective functionalization and negligible oxidation. In the case of dodecyl Si NCs prepared in air, the FTIR spectrum shows an additional feature at *ca.* 1100 cm^{-1} attributed to a Si-O stretch (Fig. 5.10(f)), indicative of partial surface oxidation. The dodecyl functionalized Si NCs prepared in air will be referred to here as oxidized dodecyl Si NCs and those prepared in the inert atmosphere will be called oxygen-free dodecyl Si NCs. Figs. 5.10(g) and (h) show the typical bright field TEM image of oxygen-free dodecyl Si-NCs and oxidized dodecyl Si NCs, respectively. The average NC diameter of oxygen-free dodecyl Si NCs is 3.5 ± 0.6 nm and 3.6 ± 0.7 nm for partially oxidized dodecyl Si NCs.

Oxygen-free dodecyl Si NCs show characteristic red PL centered at ~ 735 nm, as shown in Fig. 5.11(a). The TIPL spectrum obtained from a toluene solution of oxidized dodecyl Si NCs shows a maximum emission at ~ 630 nm, significantly blue-shifted compared to that of oxygen-free dodecyl Si NCs. Since the average diameter of the oxidized dodecyl Si NCs is statistically equivalent to that of the oxygen-free dodecyl Si NCs, a difference in the PL peak emission is unexpected. The PL emission of the oxygen-free dodecyl Si NCs agrees well with QC emission from the same size Si NCs (Dohnalová *et al.* 2013, Rodriguez-Nunez *et al.* 2012, Wolkin *et al.* 1999).

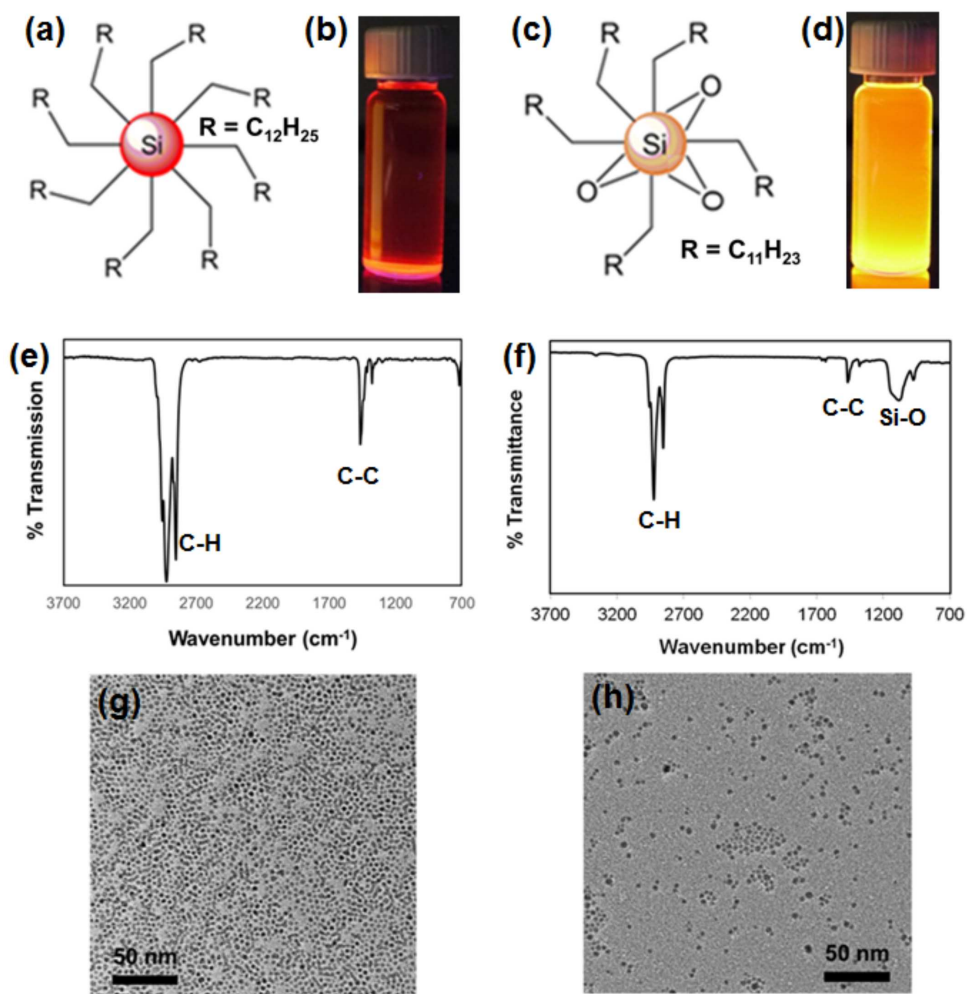


Figure 5.10: Characterization details of dodecyl functionalized Si NCs. Scheme for Si NCs functionalized in (a) air and in (c) inert atmosphere while (b, d) are the corresponding visible PL upon excitation by 365 nm UV lamp. FTIR and bright field TEM image of dodecyl Si NCs functionalized in inert atmosphere (e and g, respectively) and dodecyl Si NCs functionalized in air (f and h, respectively).

Figures 5.11(b) and (c) show the TRPL of oxygen-free and oxidized dodecyl Si NCs, respectively. The PL decay of oxygen-free dodecyl Si NCs exhibit stretched exponential behavior according to Eq. (5.2) with a lifetime of $87 \pm 1 \mu\text{s}$ and $\beta = 0.71$, and no ns-PL lifetime component was observed. On the contrary, the oxidized dodecyl Si NCs did not exhibit any μs lifetime. In fact, a faster radiative recombination process of the photoexcited carriers in the ns time scale is observed. The PL lifetime follows a bi-exponential behavior where $\tau_1 = 0.41 \pm 0.01 \text{ ns}$ and $\tau_2 = 2.91 \pm 0.04 \text{ ns}$ (Fig. 5.11(c)). The origin of this emission is difficult to conclusively identify. However, in light of the excited-state lifetime and the presence of Si-O stretch in the FTIR spectra, it likely results from an unidentified oxygen-related interface state. This result is analogous to that of TOPO functionalized Si NCs and photochemically hydrosilylated dodecyl Si NCs (Yang, De los Reyes *et al.* 2015). Yang *et al.* (2015) recently showed that at significant levels of surface oxidation, dodecyl functionalized Si NCs exhibit ns-PL lifetime component accompanied by a PL blue-shift. The absence of a μs -PL lifetime in the oxidized dodecyl Si NCs is probably due to complete PL quenching of the Si core emission by the oxygen-related interface state.

We also explore the effect of the solvent polarity on the PL emission of the functionalized Si NCs (solvatochromic studies). The PL peak emission of the functionalized Si NCs was monitored as the solvent polarity was changed. We observed that only dodecylamine and acetal functionalized Si NCs exhibit solvent polarity-dependent PL peak emission, as shown in Fig. 5.12. Both samples exhibit a PL redshift as the polarity index of the solvent increases. This result is consistent with the formation of CT states associated with the surface functional group (Deibel *et al.* 2010).

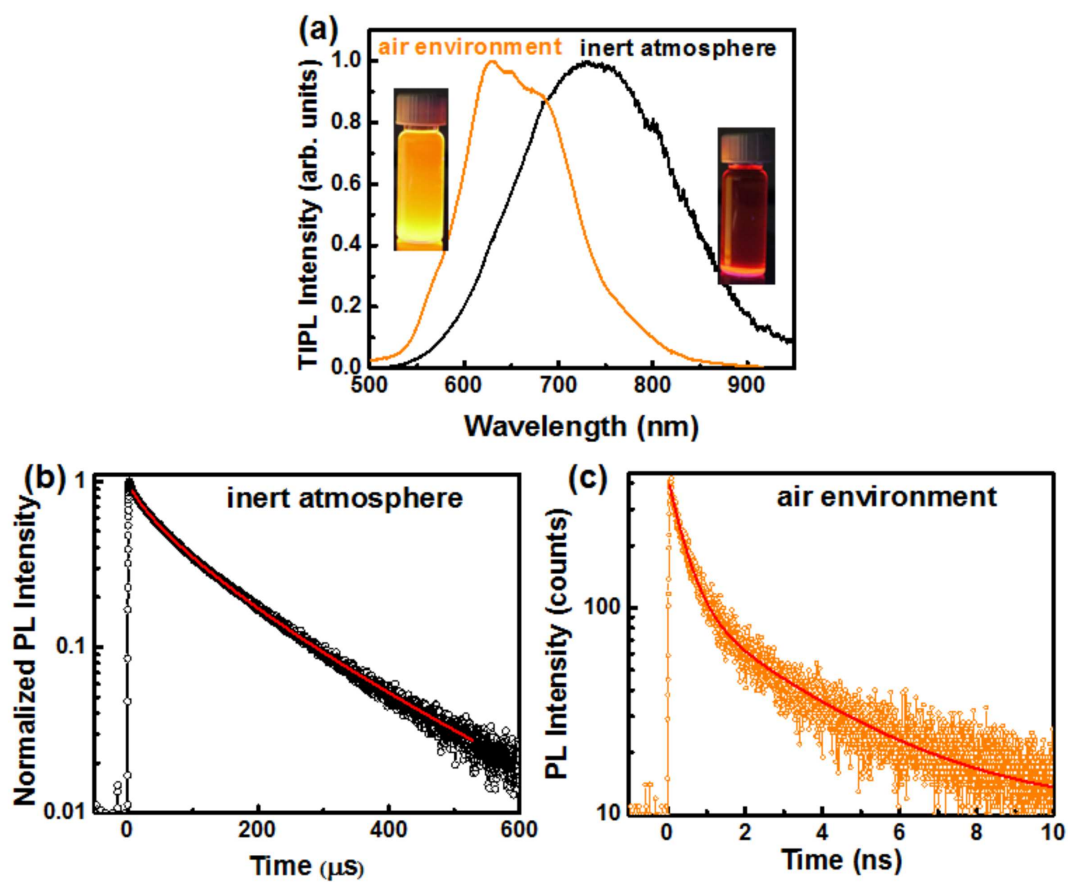


Figure 5.11: (a) TIPL of dodecyl Si NCs functionalized in air (orange line) and in inert atmosphere (black line). μ s- and ns-TRPL of dodecyl Si NCs functionalized in (b) inert atmosphere and (c) air measured at 680 and 650 nm, respectively. The red lines are the stretched exponential and bi-exponential fit to the μ s and ns lifetime, respectively.

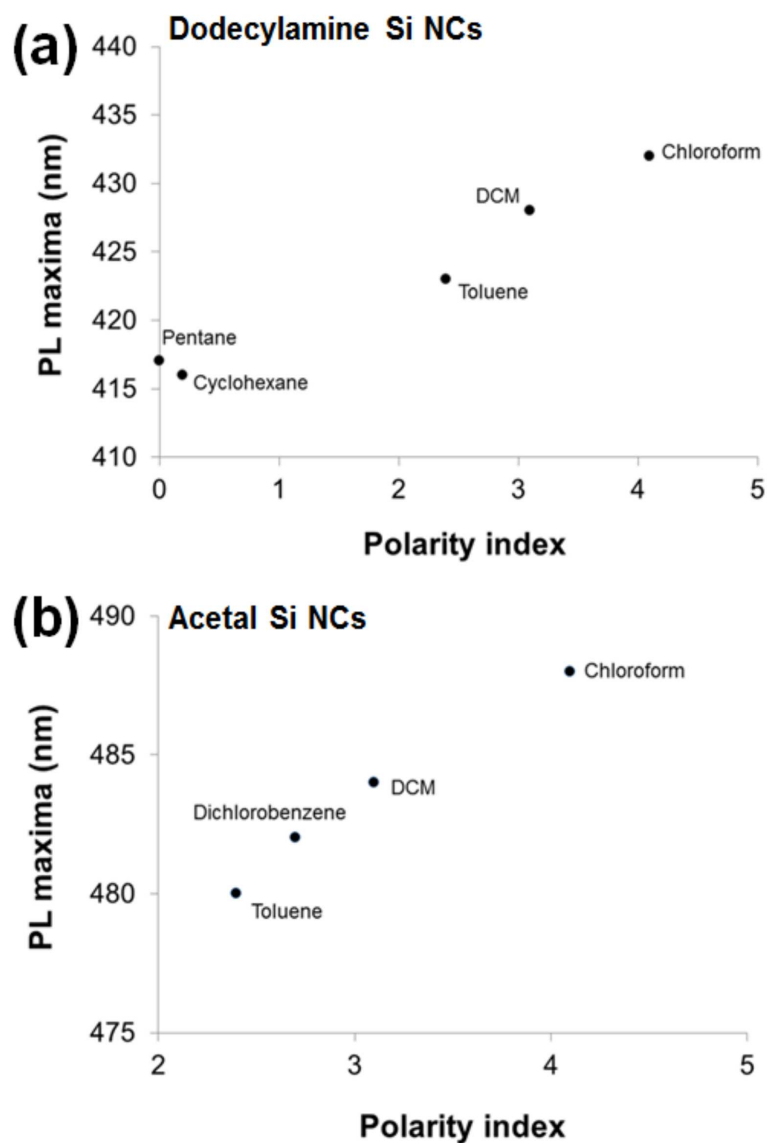


Figure 5.12: Solvatochromic studies of (a) dodecylamine and (b) acetal functionalized Si NCs. The position of the PL maximum was monitored as the solvent polarity index was changed. The Si NC concentration was 0.4 mg/mL and the excitation wavelength was 350 nm.

All of the Si NCs prepared for this study have an average particle diameter between 3 nm - 4 nm, as shown in Table 5.1. The widely used effective mass approximation (EMA) (see Eq. 2.26 and Fig. 2.4) predicts particles in this size range should emit in the spectral region between 690 nm and 810 nm if the emission arises from a bandgap transition (Moskalenco *et al.* 2007, Kupchak *et al.* 2006). This EMA prediction is in good agreement with a recent scanning tunneling spectroscopy (STS) investigation of individual Si NCs (Wolf *et al.* 2013). Furthermore, the bandgap transition in this size range of Si NCs normally exhibits PL lifetimes of 60 μ s to 100 μ s (Garcia *et al.* 2003, Delerue *et al.* 1993). Clearly this is not the case for most of the functionalized Si NCs studied here, as shown in Table 5.1. Only dodecyl Si NCs functionalized under inert conditions show the EMA predicted PL properties. Si NCs that possess oxide-based defect states (*i.e.*, TOPO Si NCs functionalized for 4 weeks and oxidized dodecyl Si NCs) show ns-PL lifetime components with the PL maximum blue-shifted compared to EMA predictions. Similar PL blue-shifts have been reported by Lockwood *et al.* (2011) when Si-H bonds in hydride terminated Si NCs are broken by UV irradiation and replaced by Si-O bonds. The ns-PL emission from these samples likely originates from the oxygen-induced defect states.

Alternatively, Si NCs functionalized with dodecylamine and acetal groups exhibit significant blue-shifts with ns excited state lifetimes. In addition, the PL peak emission in these functionalized Si NCs is dependent on the polarity of the solvent. Charge transfer state emission has been reported in xanthene dye-sensitized TiO₂ (Ramakrishna *et al.*, 2001), organic molecules (Seo *et al.*, 2004, Laguitton-Paquier *et al.*, 1996), and polythiopenene:fullerene derivative blends (Arndt *et al.*, 2015). The CT state emission dynamics in these materials are in the ps to ns time scales. Based upon these literature accounts, the ns-blue-green PL observed in dodecylamine and acetal functionalized Si NCs is tentatively assigned to CT state associated with the functional group. Emission from CT states in functionalized Si NCs is discussed further in Chapter 6.

Table 5.1: Summary of the NC diameters, TIPL maxima and TRPL lifetimes of the surface functionalized Si NCs.

Functionalized Si NCs	NC diameter	PL Maximum	PL Lifetime	
			ns-component	μ s-component
Dodecylamine Si NCs 	3.8 ± 0.7 nm	~475 nm	$\tau_1 = 1.45 \pm 0.01$ ns $\tau_2 = 6.08 \pm 0.02$ ns	NA
Acetal Si NCs 	3.4 ± 0.5 nm	~490 nm	$\tau_1 = 1.29 \pm 0.01$ ns $\tau_2 = 4.78 \pm 0.04$ ns	NA
TOPO Si NCs (8 hours) 	3.2 ± 0.5 nm	~593 nm	$\tau_1 = 0.68 \pm 0.04$ ns $\tau_2 = 5.20 \pm 0.20$ ns	20 ± 1 μ s
TOPO Si NCs (4 weeks) 	No Si core detected	~450 nm	$\tau_1 = 1.48 \pm 0.01$ ns $\tau_2 = 5.87 \pm 0.10$ ns	NA
		~650 nm	$\tau_1 = 1.22 \pm 0.01$ ns $\tau_2 = 5.02 \pm 0.10$ ns	
Dodecyl Si NCs (air environment) 	3.6 ± 0.7 nm	~ 630 nm	$\tau_1 = 0.41 \pm 0.01$ ns $\tau_2 = 2.91 \pm 0.04$ ns	NA
Dodecyl Si NCs (inert atmosphere) 	3.5 ± 0.6 nm	~735 nm	NA	87 ± 1 μ s

5.5 Conclusions

In conclusion, the PL peak emission from Si NCs can be tuned across the visible spectrum via surface engineering without changing the NC size. The observed PL emission from these functionalized Si NCs originates from three different emissive states. Quantum confined core state emission with μs PL lifetime is observed in dodecyl functionalized Si NCs prepared in inert atmosphere. Oxide-based defect state emission is observed in TOPO Si NCs and dodecyl Si NCs prepared in an air environment. The PL from this oxide-based defect state is blue-shifted compared to the QC prediction and the PL lifetime is in ns time scale. Lastly, CT state emission characterized by ns excited-state lifetime is tentatively assigned to PL emission observed in dodecylamine and acetal functionalized Si NCs. While the specific nature of these emissive sites remains unknown, this study highlights the importance of surface states and the crucial role they play in the optical properties of Si-NCs.

CHAPTER 6

Charge transfer state emission dynamics in functionalized silicon nanocrystals¹

6.1 Introduction

Nanostructured silicon (Si) has received significant attention owing to its strong tunable visible photoluminescence (PL) that has potential applications in optical devices such as light emitting diodes, (Cheng *et al.* 2010, Hirschman *et al.* 1996) and silicon-based full color displays, (Maier-Flaig *et al.* 2013) as well as biological tags, (Erogbogbo, *et al.* 2008) among others. PL from silicon nanocrystals (Si NCs) can be tuned from infrared to visible either by making NCs smaller than exciton Bohr radius (~ 4.5 nm) (Barbagiovanni *et al.* 2014, Pradhan, *et al.* 2008, Kanemitsu *et al.* 2002, Ledoux *et al.* 2002) or by changing the surface passivation using organic compounds (Dasog *et al.* 2014, Dohnalová *et al.* 2014). While it is possible to achieve blue emission from quantum confinement (QC) effects in Si NCs with diameters less than 2 nm, such small nanocrystals typically exhibit a significant reduction in the PL quantum yield (QY) due to higher nonradiative recombination rates (Dohnalová *et al.* 2014, Mastronardi *et al.* 2011, Goller *et al.* 2010). In the case

¹A version of this chapter has been submitted in Glenda B. De los Reyes, Mita Dasog, MengXing Na, Lyubov V. Titova, Jonathan G. C. Veinot, and Frank A. Hegmann, “Charge transfer state emission dynamics of blue-emitting functionalized silicon nanocrystals”, Physical Chemistry Chemical Physics Manuscript ID CP-ART-08-2015-004819.

of organic capped Si NCs, emission depends mostly on surface passivation (Dohnalová *et al.* 2014, Dasog *et al.* 2014). Compared to hydrogen-terminated Si NCs which exhibit QC emission, organic capped Si NCs show higher QY, better control of surface oxidation, more stable optical properties, and faster recombination rates (on the order of 10^7 s^{-1}), which makes this material well suited for optoelectronic applications (Dohnalová *et al.* 2014, English *et al.* 2002).

Of the visible-range PL from Si NCs, blue emission is considered the most intriguing because of the relatively small indirect bandgap of bulk Si (1.1 eV) and the wide variety of potential emission mechanisms that have been proposed. Besides QC in Si NCs with diameters $d < 2 \text{ nm}$ (Valenta *et al.* 2008, Sankaran *et al.* 2005), blue emission has also been discussed in terms of surface oxygen-related defects (Lioudakis *et al.* 2007), amorphous surface layers (Hannah *et al.* 2014), and near-interface traps (Yang *et al.* 2011). Recently, blue emission from CT states in Si NCs has been suggested by Dasog *et al.* (2014, 2013) based on solvatochromic studies that showed a dependence of the PL peak emission on the polarity of the solvent. To date, a detailed study of the PL dynamics of these materials, which provides insights into the specific nature of the blue emission process, has not yet been performed.

Here, we used time-resolved photoluminescence (TRPL) to probe the emission dynamics in blue-emitting functionalized Si NCs with different NC sizes and surface passivation prepared by reacting dodecylamine with chloride-terminated Si NCs and ammonium bromide with hydride-terminated Si NCs. We show that the blue emission originates from a CT state at the Si/SiO_xN_y interface. Understanding the dynamics of the CT emission process will have an impact on potential applications of such blue-emitting Si NCs in optoelectronics. In particular, since CT is an intermediate step for charge separation, it is important to understand CT dynamics for designing efficient Si NC-based solar cells.

6.2 Sample Preparation and Characterization

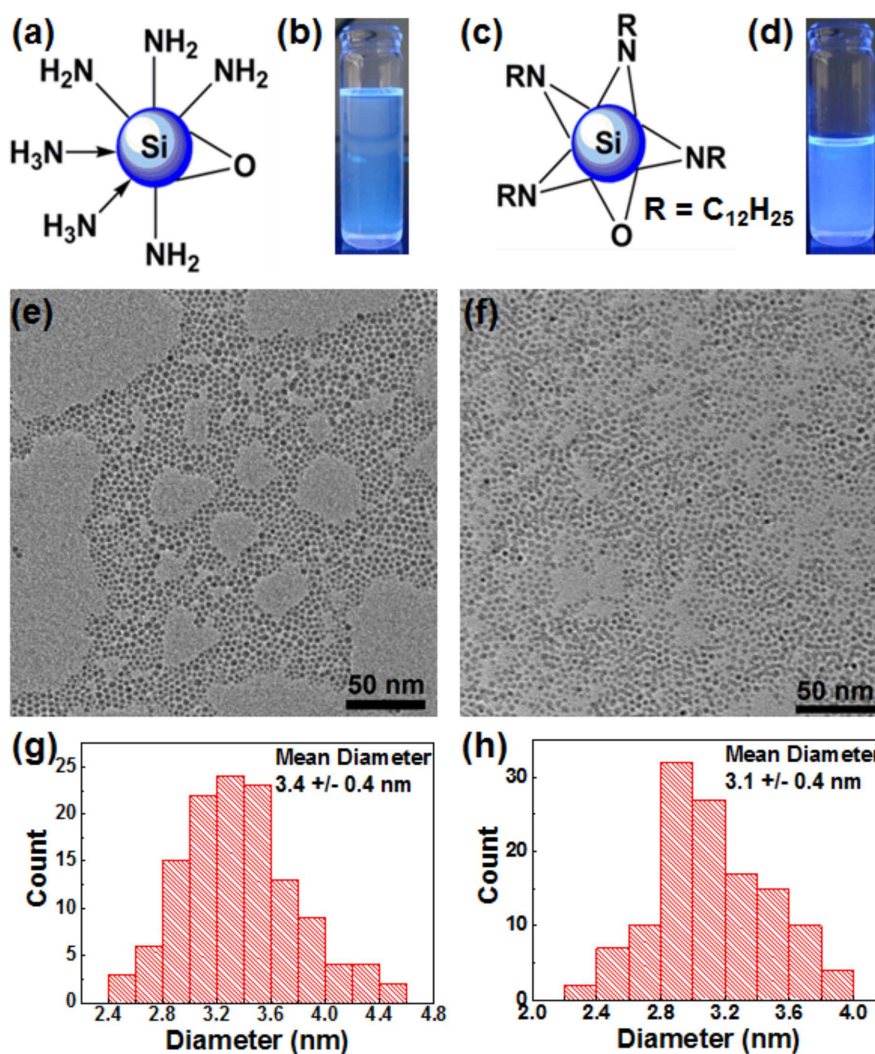


Figure 6.1: Schemes for (a) ammonia and (c) dodecylamine functionalized Si NCs. Visible PL of (b) ammonia and (d) dodecylamine functionalized Si NCs excited by 365 nm UV lamp. TEM images of ~ 3 nm (e) ammonia and (f) dodecylamine functionalized Si NCs. Histograms of the NC size distribution showing an average diameter of (g) 3.4 ± 0.4 nm for ammonia functionalized Si NCs and (h) 3.1 ± 0.4 nm for dodecylamine functionalized Si NCs.

The details of the syntheses of the colloidal Si NCs used in this study can be found elsewhere (Dasog *et al.* 2014, Dasog *et al.* 2013, Dasog *et al.* 2012). Briefly, commercial hydrogen silsesquioxane was thermally processed in a slightly reducing atmosphere (95% Ar / 5% H₂) at 1100 °C (for ~3 nm Si NCs) and 1200 °C (for ~6 nm Si NCs) to yield well-defined Si NCs embedded in a SiO₂-like matrix. Hydride-terminated Si NCs were obtained from the oxide matrix *via* HF etching. The Si NCs were functionalized using dodecylamine and ammonium bromide to obtain nitrogen-bonded colloidal Si NCs. The schemes for ammonia and dodecylamine functionalized Si NCs are shown in Fig. 6.1(a) and (c), respectively. Both samples exhibit visible blue PL when excited by 365 nm UV lamp, as shown in Fig. 6.1(b) and (d). Selected-area electron diffraction (Fig. 6.2) shows high crystallinity for the ammonia and dodecylamine functionalized Si NCs. Typical TEM images of the functionalized Si NCs are shown in Fig. 6.1(e), 6.1(f), 6.3(a), and 6.3(c). Two different sizes of dodecylamine and ammonia functionalized Si NCs were prepared to determine the effect of NC size on the PL emission dynamics for this particular set of functionalized Si NCs. Analysis of TEM micrographs shows that ammonia functionalized Si NCs have average diameters of 3.4 ± 0.4 nm and 5.7 ± 0.6 nm (Fig. 6.1(g) and 6.3(b)) while dodecylamine functionalized Si NCs have average diameters of 3.1 ± 0.4 nm and 5.8 ± 0.7 nm average diameters (Fig. 6.1(h) and 6.3(d)).

Surface passivation was verified using fourier transform infrared (FTIR) and Raman spectroscopies, as shown in Fig. 6.4. FTIR measurements revealed that the functionalized Si NCs exhibit partial surface oxidation, as evidenced by a Si-O-Si stretching mode *ca.* 1120 cm⁻¹. Figure 6.4(a) shows that both neat ammonium bromide and ammonia functionalized Si NCs show strong N-H absorptions at 3000 cm⁻¹ - 3100 cm⁻¹, consistent with ammonia passivation of the Si surface. On the other hand, Fig. 6.4(b) shows a characteristic N-H stretch at *ca.* 3300 cm⁻¹ in neat dodecylamine, which is absent from the Si NC spectrum, consistent with an amine group attaching to the Si surface. Features attributable to C-H stretches of the alkyl chain are observed at *ca.* 2900 cm⁻¹ and 1470 cm⁻¹ in neat dodecylamine and functionalized Si NCs. Si-N vibrational modes at *ca.* 840 cm⁻¹ for both ammonia functionalized Si NCs and dodecylamine functionalized Si NCs were observed in Raman spectra (Fig. 6.4(c) and (d)) further confirming the nitrogen bonding to the Si surface. Si-Si vibrational modes were also observed at *ca.* 520 cm⁻¹.

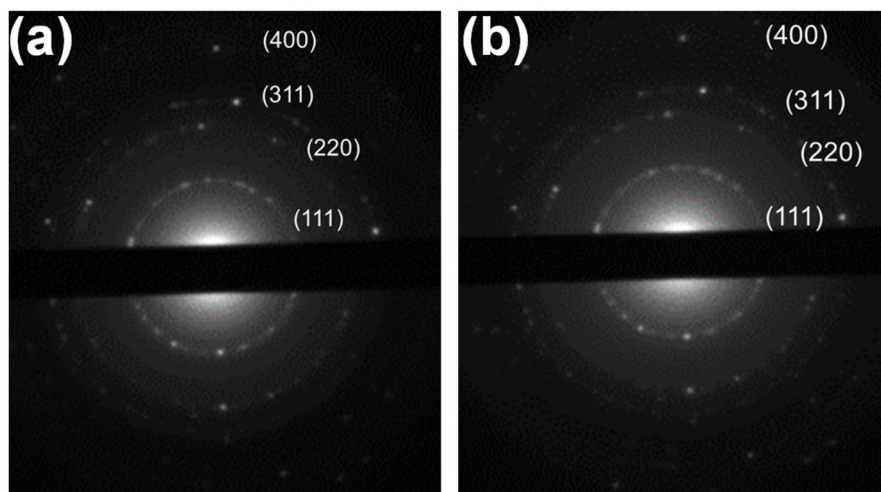


Figure 6.2: Electron diffraction pattern of (a) ammonia and (b) dodecylamine Si NCs.

6.3 Experimental details

The time-integrated PL (TIPL) and TRPL spectroscopy setup introduced in Chapter 2 were used for the spectroscopy measurements in this chapter. Briefly, TRPL spectroscopy measurements on sub-ns and μs time scales were carried out at room temperature on functionalized Si NCs dissolved in toluene. Si NC solutions were placed in 10-mm quartz cuvettes for PL measurements. For nanosecond-TRPL (referred to here as ns-TRPL) measurements, samples were excited using 400 nm pulses at an average excitation fluences ranging from 0.2 to 2.9 mJ/cm^2 . The TIPL spectra were detected by a thermoelectrically-cooled CCD coupled to a monochromator. For comparison, steady-state PL (SSPL) measurements were also carried out using a continuous-wave 406 nm laser diode with average excitation power of 4.8 mW. All of the PL spectra were corrected to the spectral response of the system.

Microsecond-TRPL (referred to here as μs -TRPL) was performed using 400 nm, 50 fs excitation pulses from a frequency-doubled amplified Ti:sapphire laser source (Coherent Legend Elite)

operating at a repetition rate of 1 kHz. The average excitation power was 4.5 mW focused to a spot size of $500 \mu\text{m}$, resulting in a fluence of $2.29 \text{ mJ}/\text{cm}^2$. Bandpass filters with 10 nm bandwidth were used to select emission wavelengths between 450 nm and 760 nm. A 435-nm longpass filter was used in all the PL measurements to block scattered excitation light. The transmission of the longpass filter was 86% at 450 nm, followed by a sharp decrease in transmission at shorter wavelengths, as shown in Fig. 6.5. The filter cut-off region is shown as a blue shaded area in all the PL spectral plots.

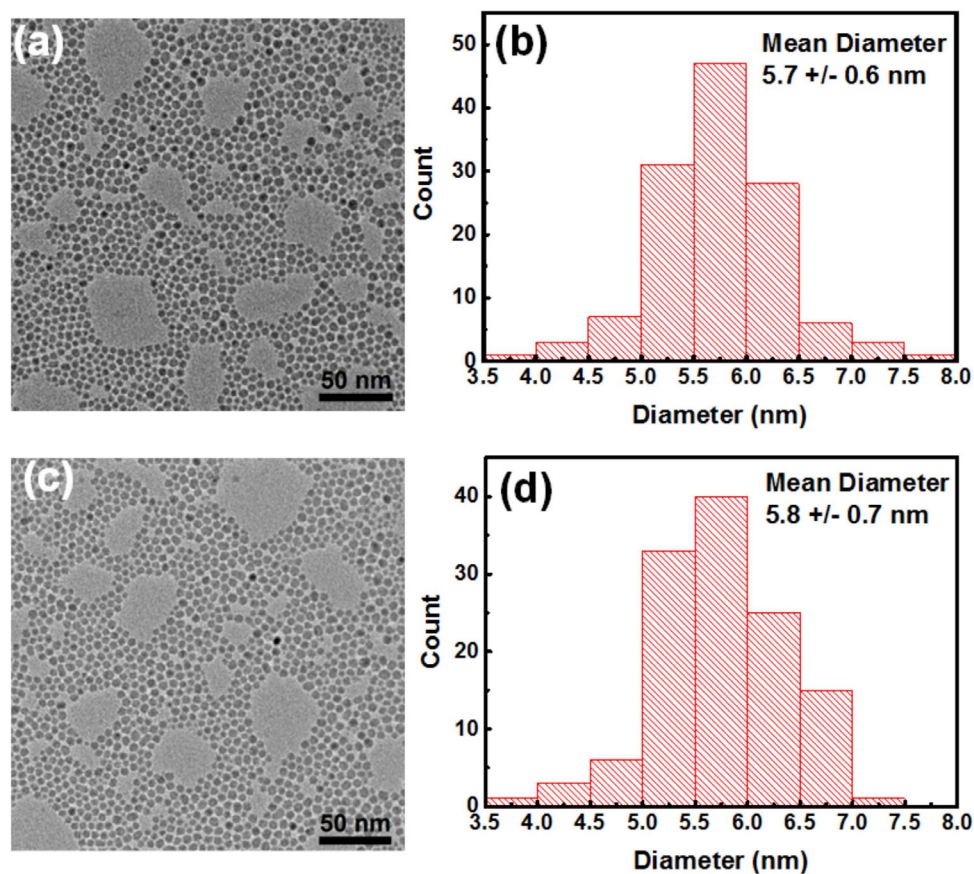


Figure 6.3: TEM images of $\sim 6 \text{ nm}$ (a) ammonia and (b) dodecylamine functionalized Si NCs while (c) and (d) are their corresponding size distributions, respectively.

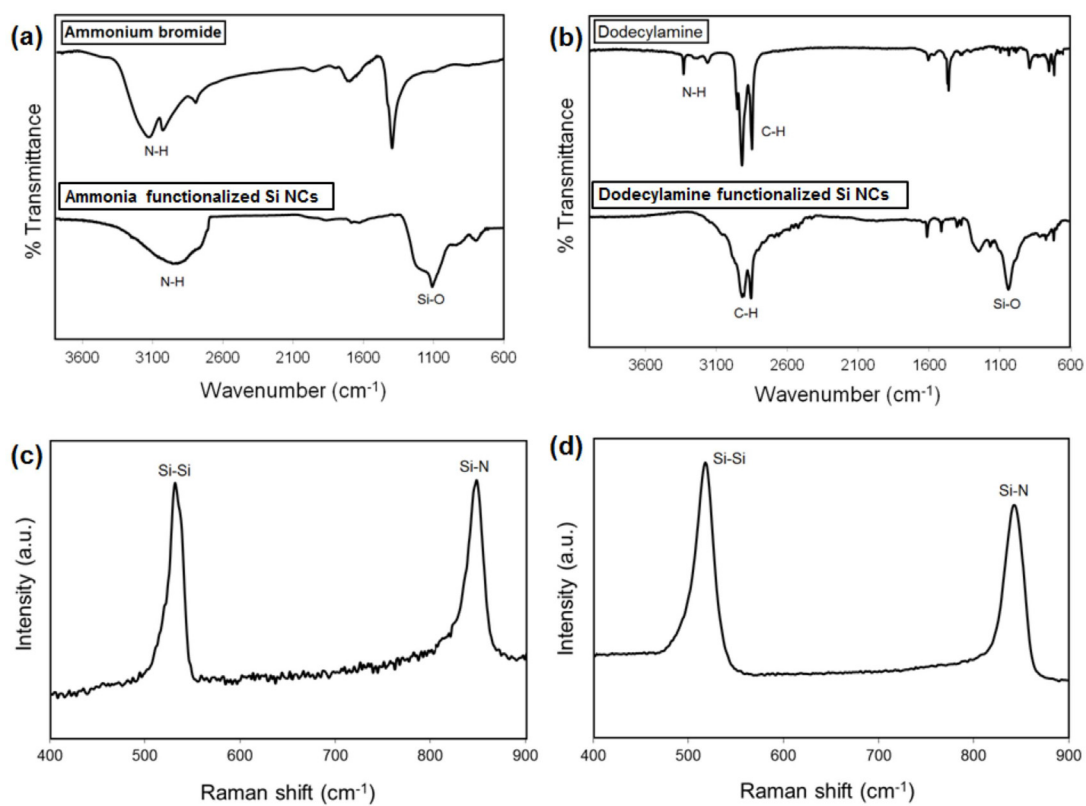


Figure 6.4: FTIR spectra of (a) ammonium bromide and ammonia functionalized Si NCs and (b) dodecylamine ligand and dodecylamine functionalized Si NCs. (c,d) are the corresponding Raman spectra of functionalized Si NCs.

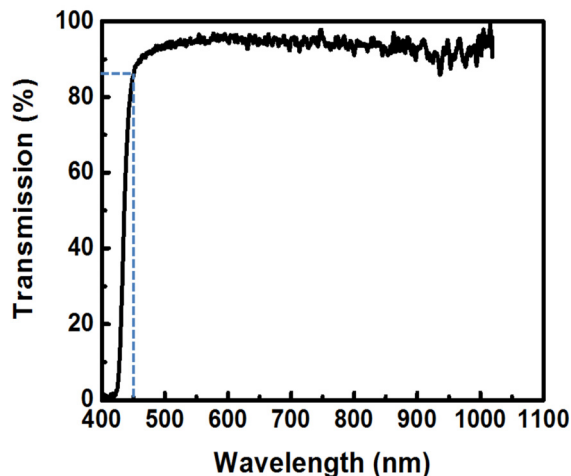


Figure 6.5: Transmission spectrum of the long pass filter showing 86% transmission at 450 nm (blue broken line) and a sharp decrease below 450 nm.

6.4 Results and discussion

Figures 6.6(a) and (b) show the TIPL of the ammonia and dodecylamine functionalized Si NCs, respectively. The high-energy shoulder of the PL is truncated by the transmittance of the optical filter (Fig. 6.5). All samples exhibit a strong blue emission that is visible to the eye. Interestingly, the TIPL spectra show size-independent PL spectral profiles, with peak emission at ~ 493 nm for ammonia functionalized Si NCs and at ~ 479 nm for dodecylamine functionalized Si NCs. Size-independent PL emission is incompatible with quantum confined core state emission (Belyakov *et al.* 2008, Ledoux *et al.* 2002, Delerue *et al.* 1993). In addition, all the measured PL are significantly blue shifted with respect to the Si core bandgap transition reported elsewhere for Si NCs with similar diameters (*i.e.*, QC emission at ~ 700 nm for 3.1 nm and ~ 795 nm for 5.8 nm Si NCs) (Wolf *et al.* 2013, Sa'ar *et al.* 2005). It is important to emphasize that there was no observed photoluminescence from the isolated dodecylamine and ammonia ligands when excited by 400 nm pulses. Hence, it is unlikely that the observed size-independent blue PL in these functionalized Si NCs arises as a result of core state recombination.

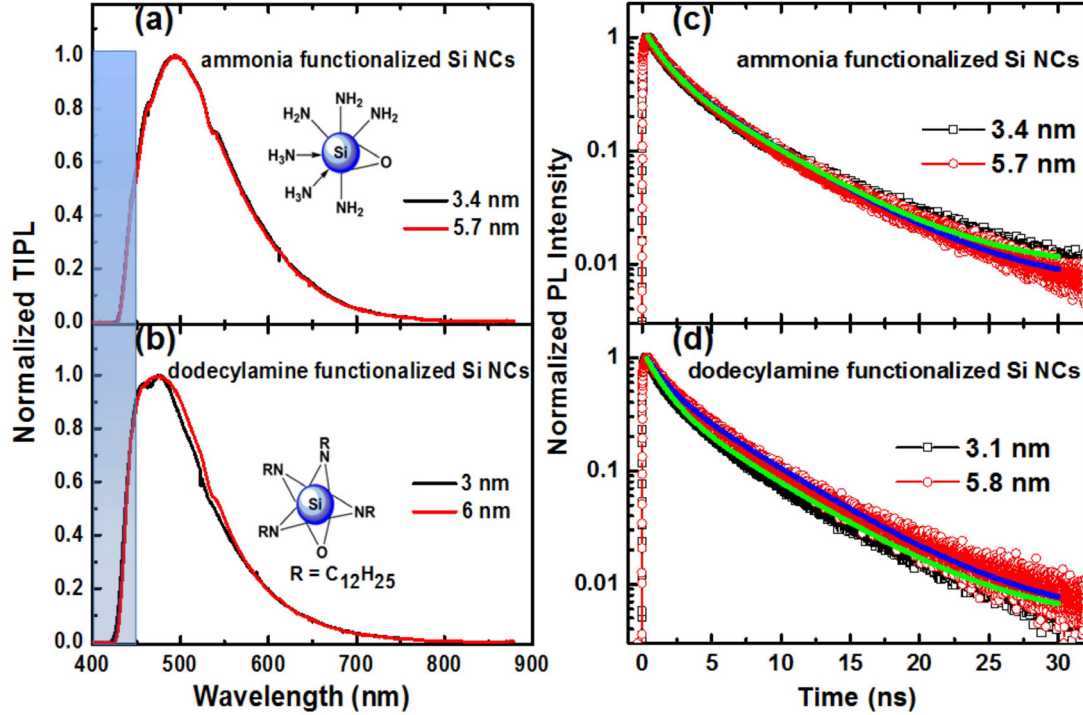


Figure 6.6: TIPL of ~ 3 nm (black) and ~ 6 nm (red) (a) ammonia and (b) dodecylamine functionalized Si NCs excited by 400-nm pulses at an excitation fluence of 0.42 mJ/cm^2 . The shaded area represents the cut-off region of the long pass filter. The corresponding ns-TRPL decays at 470 nm are shown in (c) and (d), respectively. The green and blue lines are the bi-exponential fits to the ~ 3 nm and ~ 6 nm Si NCs, respectively. Fit parameters are given in the text and Table 6.1.

Figures 6.6(c) and (d) show the ns-TRPL emission dynamics for ~ 3 nm and ~ 6 nm ammonia and dodecylamine functionalized Si NCs, respectively, measured at 470 nm. The PL lifetime exhibits a bi-exponential decay,

$$I(t) = A_1 e^{[-(t/\tau_1)]} + A_2 e^{[-(t/\tau_2)]} + C \quad (6.1)$$

where τ_1 and τ_2 are the decay times and C is a constant offset much smaller than A_1 and A_2 . As can be seen from the plots, the PL dynamics of both functionalized Si NCs at an emission wavelength of 470 nm are independent of nanocrystal size. As summarized in Table 6.1, ammonia functionalized

Si NCs have lifetimes of $\tau_1 = 1.81 \pm .004$ ns and $\tau_2 = 6.12 \pm .001$ ns for $d = 3.4$ nm and $\tau_1 = 1.81 \pm .001$ ns and $\tau_2 = 6.10 \pm .006$ ns for $d = 5.7$ nm. Dodecylamine functionalized Si NCs exhibit slightly shorter PL lifetimes of $\tau_1 = 1.46 \pm .01$ ns and $\tau_2 = 5.76 \pm .01$ ns for $d = 3.1$ nm and $\tau_1 = 1.64 \pm .01$ ns and $\tau_2 = 5.86 \pm .02$ ns for $d = 5.8$ nm. We also explored the dependence of the PL lifetimes on emission wavelength (Table 6.1 and Figure 6.7). All the samples exhibit very fast PL lifetimes shorter than 7 ns. In addition, the PL lifetimes of all the samples do not vary significantly with emission wavelength (the difference is $\leq 11\%$ between 470 nm to 620 nm, as seen in Table 6.1). Bi-exponential PL decays are typically observed as a result of energy transfer either from core/band edge states to surface states or from smaller to larger NCs (Ajayi *et al.* 2014, Foreman *et al.* 2006, Kagan *et al.* 1996). However, the PL red-shift upon energy transfer predicted by these mechanisms is not observed here. μ s-TRPL measurements performed from 450 to 760 nm did not exhibit any long-lived PL lifetime, as shown in Fig.6.8, in stark contrast with QC emission of NCs of similar size (3-6nm) that is known to exhibit a μ s-PL decay in the range of 20 - 130 μ s (Yang *et al.* 2015, Mastronardi *et al.* 2011, Kim *et al.* 2004).

Table 6.1: Summary of the fit parameters according to Eq. 6.1 for spectrally-resolved PL dynamics of the functionalized Si NCs. The error in the lifetimes τ_1 and τ_2 is ≤ 0.02 ns. The error in the amplitude coefficients A_1 and A_2 is < 0.005 . The value of the constant offset, C (not listed here), ranges from 0.001 - 0.006.

Wavelength (nm)	Ammonia functionalized Si NCs								Dodecylamine functionalized Si NCs							
	3.4 nm				5.7 nm				3.1 nm				5.8 nm			
	τ_1 (ns)	A_1	τ_2 (ns)	A_2	τ_1 (ns)	A_1	τ_2 (ns)	A_2	τ_1 (ns)	A_1	τ_2 (ns)	A_2	τ_1 (ns)	A_1	τ_2 (ns)	A_2
470	1.81	0.61	6.12	0.39	1.81	0.59	6.10	0.41	1.46	0.63	5.76	0.39	1.64	0.51	5.86	0.49
505	1.78	0.58	6.15	0.42	1.81	0.51	6.16	0.49	1.45	0.61	5.93	0.36	1.61	0.51	5.95	0.49
555	1.65	0.56	6.16	0.44	1.77	0.45	6.30	0.55	1.35	0.60	5.89	0.40	1.66	0.46	6.07	0.54
620	1.60	0.60	6.20	0.40	1.80	0.54	6.15	0.46	1.34	0.67	5.80	0.33	1.51	0.57	5.88	0.43

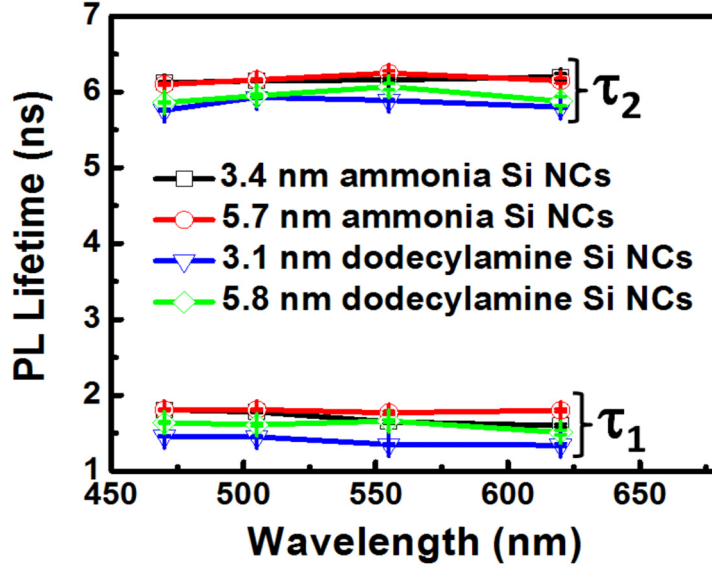


Figure 6.7: Spectrally-resolved ns-PL dynamics of functionalized Si NCs.

We estimate the radiative recombination lifetime, τ_R using the relative PL quantum yield, QY, and the weighted average lifetime, $\langle \tau \rangle$, given by (English *et al.* 2002):

$$QY = \frac{\langle \tau \rangle}{\tau_R} \quad (6.2)$$

$$\langle \tau \rangle = \sum_{i=1}^n \frac{A_i \tau_i^2}{A_i \tau_i} \quad (6.3)$$

The radiative recombination rate is then given by $k_R = 1/\tau_R$. The relative PL quantum yield, QY, for dodecylamine and ammonia functionalized Si NCs have recently been reported by Dasog *et al.* (2014, 2013). Ammonia functionalized Si NCs have a QY of 22%, while dodecylamine functionalized Si NCs exhibit a QY of 32%. Using the PL lifetimes at the peak emission wavelengths, radiative recombination rates of $k_R = 0.45 \times 10^8 \text{ s}^{-1}$ and $0.72 \times 10^8 \text{ s}^{-1}$ are obtained for ammonia and dodecylamine functionalized Si NCs, respectively. These fast radiative recombination rates suggest dipole-allowed transitions, such as observed in CdSe NCs (de Mello Donega *et al.* 2003).

This result further confirms that the observed radiative process is unlikely to be due to emission from the Si core, since radiative recombination rates from QC states in similar size Si NCs is expected to be in the range of 10^3 s^{-1} to 10^5 s^{-1} (Dohnalová *et al.* 2014). The nonradiative decay rate k_{NR} can be computed using $QY = k_R/(k_R + k_{NR})$. The non-radiative processes for both functionalized Si NCs are slightly faster ($k_{NR} = 1.50 \times 10^8 \text{ s}^{-1}$ for dodecylamine and $k_{NR} = 1.59 \times 10^8 \text{ s}^{-1}$ for ammonia) than the radiative process. These efficient recombination processes lead to the observed ns-PL decay.

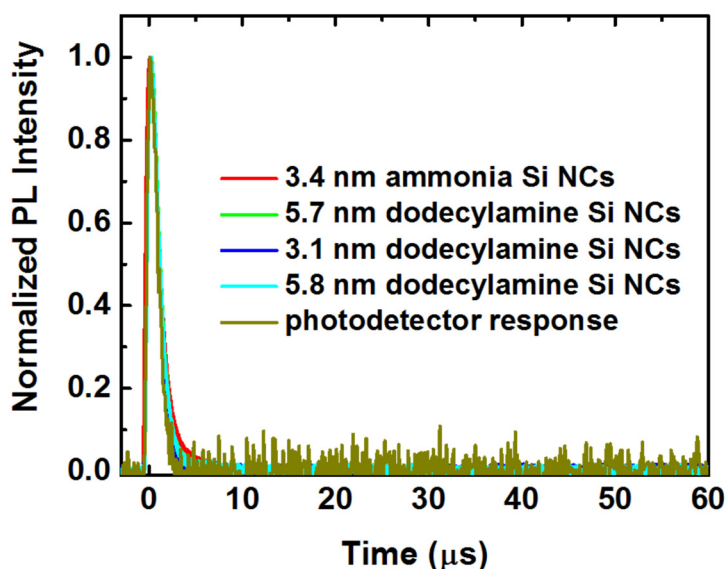


Figure 6.8: Microsecond-TRPL measurements of the functionalized Si NCs at 560 nm using a fast Si photodetector. The photodetector response was measured using scattered light from the 400 nm excitation pulse.

An extensive ns-TRPL study was conducted to further probe the nature of the blue-emitting state in this set of functionalized Si NCs (Fig. 6.9). By monitoring the temporal evolution of the PL spectral profile, it is possible to determine the light-emitting states responsible for the observed PL since they will exhibit unique PL spectral profiles and lifetimes (Sykora *et al.* 2008). Figures 6.9(a) and (b) show the ns-TRPL intensity for the ~ 3 nm ammonia and dodecylamine functionalized Si

NCs, respectively, as a function of emission wavelength and time after photoexcitation. From these plots, the temporal evolution of the PL after photoexcitation was extracted, as presented in Figures 6.9(c) and (d). Interestingly, the spectral profile of both functionalized Si NCs does not change with time while the peak position is consistent with the TIPL results (Fig. 6.6(a) and (b)). Notably, excellent agreement between the normalized temporally-resolved PL and the SSPL (Fig. 6.9(e) and (f)) is observed. A PL peak that is independent of time is consistent with the absence of a μs -PL component in these Si NCs. Furthermore, the time-independent spectral profile also implies that a single emitting state is responsible for the observed ns-PL.

Based on the results of the TIPL (Fig. 6.6) and TRPL (Fig. 6.9) measurements, we conclude that the observed ns-blue PL is not from intrinsic core emission. We can also rule out no-phonon hot carrier recombination described by de Boer *et al.* (2010) since the observed PL does not exhibit a PL red-shift when the size of the NCs is decreased, as shown in Fig. 6.6. It has been shown that Auger recombination could result in a PL blue-shift where carriers are promoted to higher energy levels (Diamare *et al.* 2013). Although the time resolution (50 ± 4 ps) of our setup prevents us from observing Auger recombination, which normally occurs on time scales <100 ps, (Sevik *et al.* 2008) excitation-fluence-dependent PL emission and PL dynamics measurements can elucidate whether non-radiative Auger processes give rise to the observed fast blue PL. Fig. 6.10(a) and (b) show the excitation-fluence-dependent TIPL and ns-TRPL dynamics, respectively of the ~ 6 nm ammonia functionalized Si NCs. The TIPL of ammonia-functionalized Si NCs increases linearly with excitation pump fluence, inconsistent with Auger processes. The spectrally-resolved PL lifetimes are also independent of excitation fluence ($\leq 1\%$ variation over the fluence range used here), as shown in the inset of Figure 6.10(b). In addition, the absence of a PL red-shift (Fig. 6.9(c) and 6.9(d)) at early times after photoexcitation rules out multiple carrier generation that could result in Auger recombination processes (Schaller *et al.* 2006). Recently, Hannah *et al.* suggested that fast PL from Si NCs in the 400 nm - 600 nm emission bands is due to a surface layer of amorphous Si (Hannah *et al.* 2014). This is unlikely the case for our samples as we do not observe any amorphous Si-Si peak at ~ 480 cm^{-1} in our Raman spectra (Wu *et al.* 1996), as seen in Fig. 6.4(c) and (d).

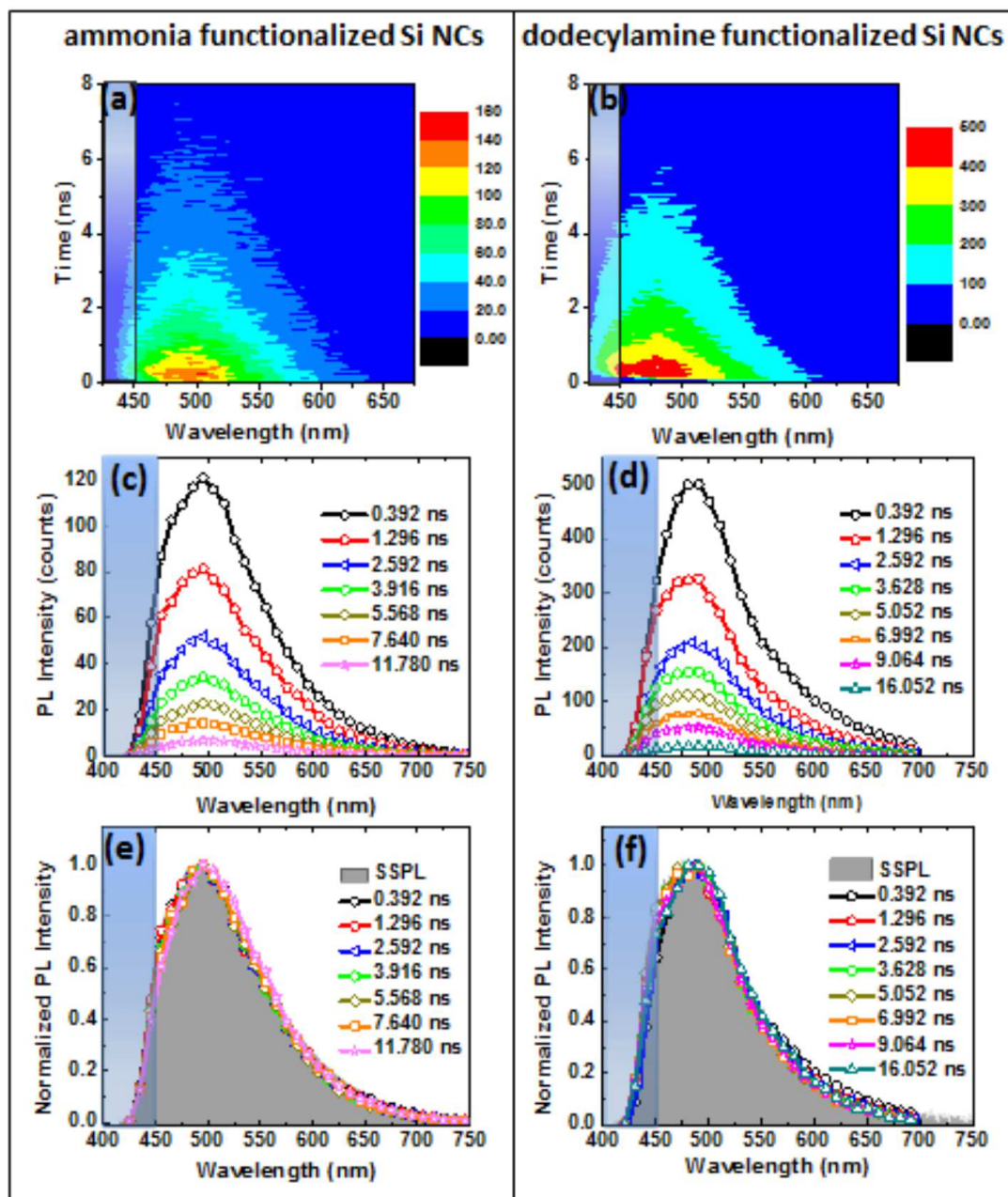


Figure 6.9: TRPL intensity as a function of wavelength and time for ~ 3 nm (a) ammonia and (b) dodecylamine functionalized Si NCs. The color scale represents photon counts. (c) and (d) are the corresponding temporally-resolved PL spectra at specific times after excitation and averaged within a time window of 0.4 ns. Comparison of the SSPL (grey shaded area) and the normalized PL of (e) ammonia and (f) dodecylamine functionalized Si NCs. The blue-shaded area represents the cut-off region of the long pass filter. PL was excited by 400-nm pulses at an excitation fluences of 0.48 mJ/cm² and 0.55 mJ/cm² for ammonia and dodecylamine functionalized Si NCs, respectively.

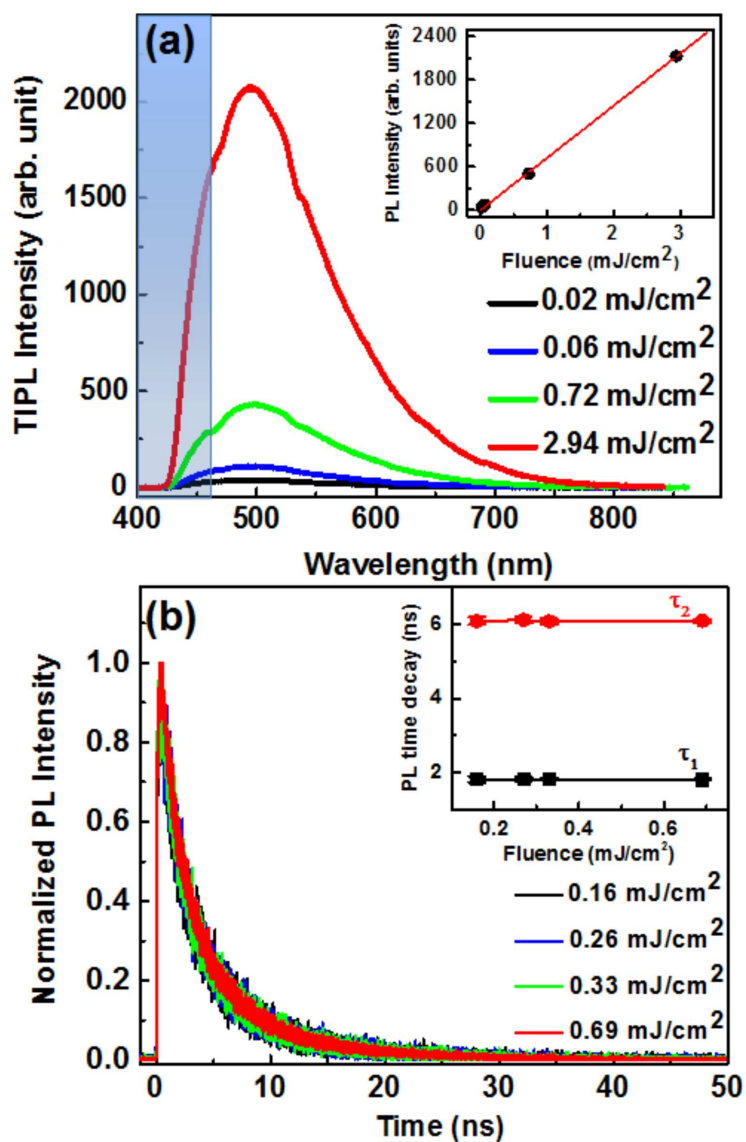


Figure 6.10: Fluence-dependence of (a) TIPL and (b) ns-TRPL dynamics at 493 nm for ~ 6 -nm ammonia functionalized Si NCs. Insets show the fluence-dependence of the (a) PL intensity and (b) PL lifetimes, respectively. The blue-shaded area represents the cut-off region of the long pass filter.

Our results suggest that the observed ns-blue emission is due to radiative recombination at interface-related states by ultrafast carrier trapping or charge transfer (CT) (English *et al.* 2002, Tsybeskov *et al.* 1994). The complete quenching of the Si core emission indicates that carrier trapping/CT depopulates the Si core at a rate much faster than intraband thermalization. Trojanek *et al.* (2006) showed that the carrier trapping/CT process occurs in ~ 400 fs, approximately two orders of magnitude faster than the intraband relaxation time ($\sim 1-10$ ps) in quantum confined materials. Hence, we propose that the observed ns-blue PL is related to surface passivation. The FTIR and Raman spectra in Figure 6.4 show that both Si-O and Si-N surface bonds are present. However, the fast blue emission cannot be attributed to either one of these bonds. Dohnalová *et al.* (2013) and Wolkin *et al.* (1999) show that when the surface of Si NCs is terminated by oxygen, a PL red-shift is observed followed by an increase in the PL lifetime from ns to μ s time scales. Also, computational studies reveal that the same PL redshift was observed when oxygen-free Si NC surfaces were passivated by nitrogen (Pi *et al.* 2011). On the other hand, Fuzell *et al.* (2013) suggested that blue emission from nitrogen-bonded Si NCs is due to CT to low lying nitrogen traps while oxygen impurities generate deeper traps. Here, however, we associate the fast blue PL emission to silicon oxynitride (SiO_xN_y) species at the surface of the nanocrystals, as confirmed by XPS (Dasog *et al.* 2014, Dasog *et al.* 2013). Wang *et al.* (2014) proposed that both organic ligands and surface oxidation are necessary to form a novel surface state that is responsible for the ultrabright PL and that the structure of the ligand is crucial in determining whether such a state can dominate the entire process. However, it is unlikely that the emission is due to direct excitation of the SiO_xN_y surface group since its bandgap is between 4.5 - 8.0 eV (Gritsenko 1998) while the excitation energy used here is only 3.1 eV. Furthermore, absorption measurements shown in Fig. 6.11 exhibit size-dependent absorption edges commonly observed for nanostructured Si (Garcia *et al.* 2003).

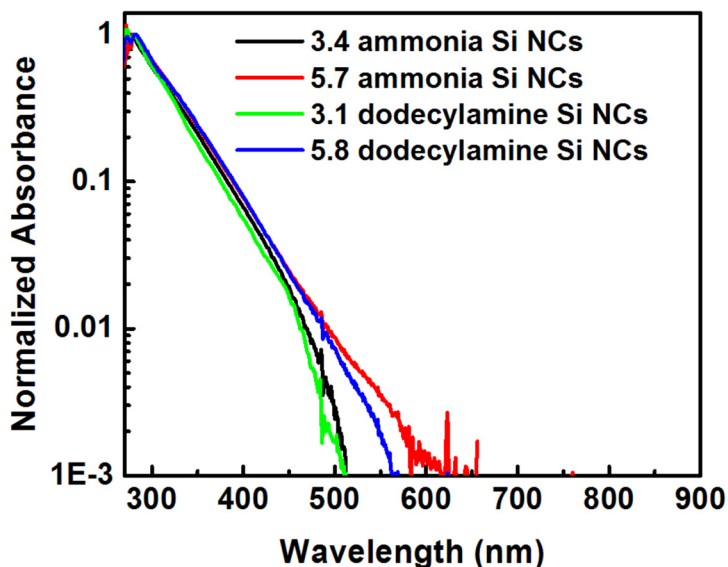


Figure 6.11: Normalized absorbance of different sizes of functionalized Si NCs.

The CT state, which occurs at the Si/SiO_xN_y interface, is therefore responsible for the observed ns-blue PL as illustrated in Fig. 6.12. The Si NC, with a bandgap of E_{gap}^{QC} (>1.1 eV bandgap of bulk silicon), is excited by 400 nm (3.1 eV) light creating an electron-hole pair. The photoexcited electron rapidly transfers to the SiO_xN_y forming the CT state located at the interface. The CT thermalization process occurs at a much faster rate than the thermalization process within the bands of the Si core resulting in quenching of the QC core emission that typically emits red PL with a lifetime in the μ s time scale, as shown by the red solid downward vertical arrow in Fig. 6.12. After a fast thermalization within the CT state, the bound electron-hole pair recombines emitting ns-blue PL. Deibel *et al.* (2010) pointed out that when sufficient wavefunction overlap of the electron and hole forming the CT state occurs, significant luminescence can be achieved. In addition, Dasog *et al.* (2014, 2013) recently showed that these functionalized Si NCs exhibit solvent-polarity dependent (solvatochromic) PL, consistent with a CT state at the interface. The difference in PL spectra and lifetimes of ammonia and dodecylamine functionalized Si NCs can be attributed to the difference in structure of the SiO_xN_y species, which affects the CT state. Indeed, Augustine *et al.* (1995) used

various amorphous silicon oxynitride ($a\text{-SiO}_x\text{N}_y\text{:H}$) thin films prepared by PECVD to demonstrate tunable visible PL emission with a characteristic decay of <10 ns. Moreover, similar to the PL emission dynamics observed here, CT state PL lifetimes observed in polymer-fullerene systems exhibit bi-exponential decay (Veldman *et al.* 2008, Loi *et al.* 2007).

The CT state emission from our functionalized Si NCs exhibits complete blue PL with no other components attributable to core emission, and is therefore a more efficient blue emitter compared to oxygen-related defects and amorphous surface layers where the blue emission is just a small part of the total PL (Hannah *et al.* 2014, Lioudakis *et al.* 2007). Compared to QC blue emission from Si cores, CT state emission is likely to exhibit higher PL QY and faster radiative recombination since it has been shown that a significant decrease in QY is observed when the Si NCs diameters are less than 2nm (Mastronardi *et al.* 2011). Mastronardi *et al.* (2011) observed that as the NC size decreases, the non-radiative recombination rate dominates the radiative rate which results in a decrease in the absolute QY. Hence, blue emission from CT states is a promising candidate for applications in Si-based LEDs, as luminescent tags in imaging, and in other applications where efficient emission in the blue region of spectrum is required. Understanding the CT state emission dynamics is also important for Si NC-based photovoltaics, where CT states are the intermediate process necessary for charge dissociation that can result in the generation of photocurrent (Loi *et al.* 2007). Since CT recombination is considered an energy loss, preventing it to happen by ensuring charge separation occurs before recombination happens will result in better performance of photovoltaics and solar cells. The key to achieving this is knowing the characteristic time of the charge transfer state emission. Hence, we hope that the result of this study will encourage further studies of this process that will likely help in designing efficient Si NC-based photovoltaic and solar cells.

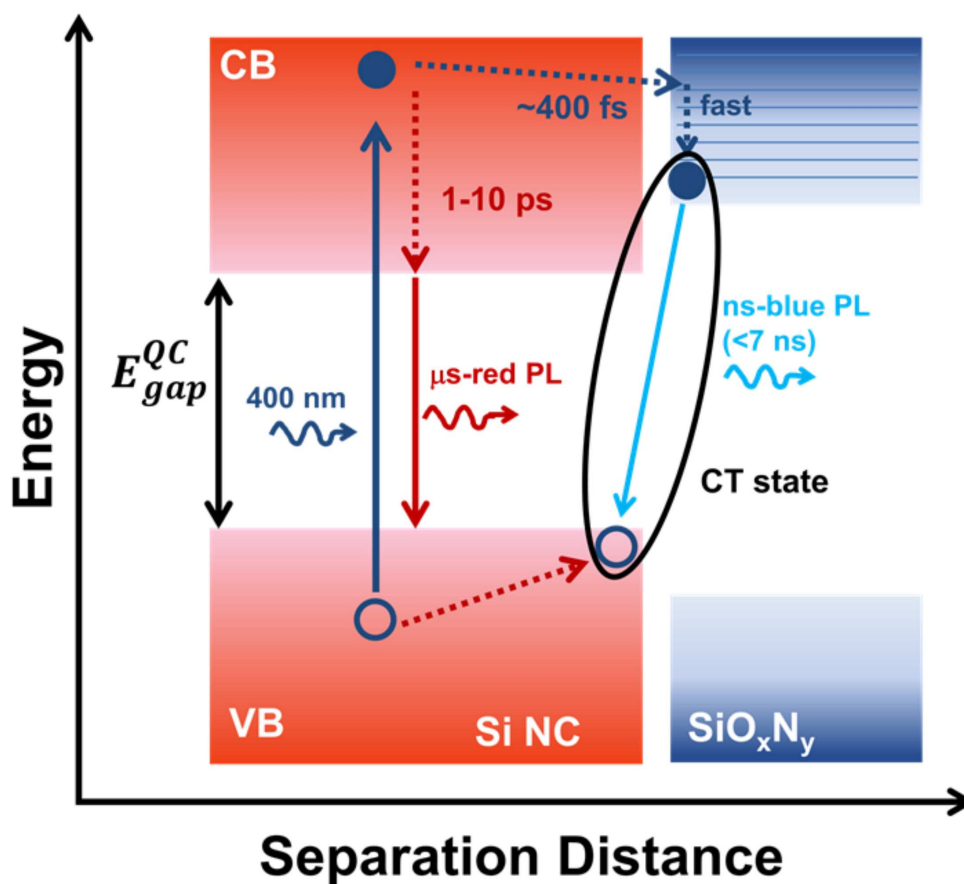


Figure 6.12: Energy diagram for the CT state emission dynamics. Electrons are first photoexcited within the Si NC core and then rapidly transfer to the SiO_xN_y, creating a CT state at the interface. The CT process quenches the emission from the Si core, which is normally expected to emit red PL over μs time scales, as shown by the solid red downward arrow. Radiative recombination of the electron and hole in the CT state results in blue PL over ns time scales, as indicated by a solid blue downward arrow. (CB = conduction band; VB = valence band). The electron transfer (dashed blue arrow) and thermalization times (dashed red downward arrow) are adopted from Trojanek et al. (2006).

6.5 Conclusion

In summary, the PL dynamics of blue-emitting ammonia and dodecylamine functionalized Si NCs with average diameters of ~ 3 and ~ 6 nm was investigated. The NC-size-independent blue emission is attributed to CT states at the Si/SiO_xN_y interface with a radiative recombination rate of $\sim 5 \times 10^7$ s⁻¹. In addition, the CT state emission spectral profile is independent of the time after excitation. The size-independent PL and the absence of μ s-PL from all of our samples suggest a very efficient electron transfer from the Si NC core excited states to the CT state. Understanding the CT state emission dynamics in blue-emitting Si-NCs will impact their application in optoelectronic devices.

CHAPTER 7

Carrier dynamics of photoexcited Si nanocrystal films with different Si filling fractions

7.1 Introduction

In recent years, silicon nanocrystal (Si NC) composite films have been investigated as promising candidates for Si-based photonic devices that are used to amplify (Dal Negro *et al.* 2003, Luterova *et al.* 2002, Khriactchev *et al.* 2001, Pavesi *et al.* 2000), guide (Lipson 2005, Schonbrun *et al.* 2005), and generate light (Irrera *et al.* 2002, Iacona *et al.* 2002, Photopoulos *et al.* 2000, Fujita *et al.* 1999, Rebohle *et al.* 1997, Qin *et al.* 1995). Si NC-based photonics devices have several important advantages over commonly used materials, such as organic semiconductors and II-VI and II-VI NC systems (*e.g.*, CdSe, CdTe) which include compatibility with microelectronic fabrication technology, abundance of Si source material, low cost fabrication (Jurbergs *et al.* 2006), and non-toxicity (Shiohara *et al.* 2009). Although different forms of Si NCs have been developed, such as nanostructured porous silicon (Boukherroub *et al.* 2001, Sham *et al.* 1993), passivated by organic ligands (Kusova *et al.* 2010), or embedded in different insulating matrices (Tewary *et al.* 2006), Si NCs embedded in amorphous SiO₂ matrix have gained considerable interest due to their photoluminescence (PL) stability with time for light emission applications and nanoelectronics applications (Meldrum *et al.* 2004, Heitmann *et al.* 2005). It has been shown that in this material system, surface-related states

play an important role in various relaxation mechanisms over a broad range of photon excitation energy (Othonos *et al.* 2008). In addition, the ultrafast non-linear optical gating/up-conversion method (Zidek *et al.* 2010) and transient photoinduced absorption (TPA) (Othonos *et al.* 2008) measurements reveal a fast sub-ps relaxation of the photoexcited carriers from the initial excited states within the NC core to the surface-related states. While a clear consensus about the rate of carrier trapping by the surface-related traps has been achieved, the interpretation of the microsecond lifetime normally obtained using microsecond- time-resolved photoluminescence (μ s-TRPL) spectroscopy is still under debate. Dovrat *et al.* (2004) and Wen *et al.* (2007) attributed the μ s-PL lifetime to radiative recombination within the Si core states based on temperature-dependent TRPL measurements whereas Trojanek *et al.* (2006) and Sykora *et al.* (2008) assigned it to recombination of carriers trapped on the surface/interface states. It is clear from these studies that a complete overall picture of the relaxation and recombination processes in this material system has not yet been established. Hence, a need to study the carrier dynamics in Si NC films over sub-ps, sub-ns, and μ s time scales is necessary to obtain a complete overall picture of the dynamics of photoexcited carriers and light emission in this material system.

Here, we have applied two complimentary optical techniques to study ultrafast processes in photoexcited Si NC films with varying Si volume filling fractions and NC sizes. TPA with sub-ps time resolution was used to probe the photoexcitation dynamics of the NCs and TRPL measurements in sub-ns and microsecond time scales were used to study radiative carrier recombination processes. Fluence-dependent time-integrated PL (TIPL) and TRPL measurements were also conducted to elucidate the role of state filling in the emission properties of Si NCs embedded in an amorphous SiO₂ matrix.

7.2 Sample Preparation

Si NC films were formed (Al Meldrum's laboratory in the Department of Physics at the University of Alberta) by annealing non-stoichiometric SiO_x ($x = 0.6$ to 1.4) films deposited on a fused quartz substrate in a 5% H₂ and 95% N₂ environment at 1.2 atm and a temperature of 1100 °C. Thermal

annealing at temperatures greater than 900 °C resulted in phase separation and the formation of crystalline Si NCs embedded in SiO₂. Silicon films with $x = 1.0, 1.2$ and 1.4 were 1.0- μm thick while films with $x = 0.8, \text{ and } 0.6$ were 200-nm thick. Assuming complete phase separation of Si and SiO₂, the resulting silicon volume filling fractions, ρ_{Si} are: 16% ($x = 1.4$), 23% ($x = 1.2$), 31% ($x = 1.0$), 40% ($x = 0.8$), and 51% ($x = 0.6$). As has been previously reported, annealing at greater than 900 °C leads to the formation of isolated silicon nanocrystals with average nanocrystal diameters of 6.2 ± 1.1 nm for $x = 1.0$ and 11.7 ± 7 nm for $x = 0.6$ (Meldrum *et al.* 2006). Based upon this result, it is reasonable to assume that as the ρ_{Si} decreases (x increases) the size of the Si NC also decreases. Electron energy-loss spectroscopy (EELS) on the SiO_{1.0} and SiO_{0.6} films has shown that a small fraction of unsegregated SiO still remains even after annealing at 1100 °C (Wang *et al.* 2007).

7.3 Experimental details

Two complimentary optical techniques were used to study ultrafast processes in photoexcited Si NC films with varying Si volume filling fractions and the NCs' size. Time-resolved photoluminescence (TRPL) measurements were used to study the carrier recombination processes and differentiate core state emission from those that originate from interface or surface-related traps. On the other hand, TPA was used to monitor the carrier dynamics after photoexcitation with sub-ps time resolution. Time-integrated PL (TIPL) and steady-state PL (SSPL) spectroscopy were also conducted to determine the effect of the Si volume filling fraction on the optical emission properties of the Si NC films.

The time-resolved spectroscopy (sub-ns and μs time scales) and the optical pump-probe transient absorption set-ups introduced in Chapter 3 were used in this study. Briefly, TIPL and ns-TRPL used 400 nm excitation pulses (pulse width of 65 fs and a repetition rate of 250 kHz) while the SSPL was excited by a continuous 406 nm diode laser. The TIPL and SSPL were collected by a CCD coupled to a monochromator and integrated for 120s. For sub-ns TRPL, the PL dynamics were analyzed using time-correlated single photon counting (TCSPC). A spectrally-resolved PL lifetime was obtained by choosing a particular emission wavelength using the monochromator and each wavelength

was integrated for 1 hr. A 435-nm longpass filter was used to block scattered 400 nm excitation light.

For μs -TRPL, the PL was excited by a 445 nm diode laser coupled to an acousto-optic modulator set with a repetition rate of 200 Hz and pulse duration of 25.6 ns (Meldrum Lab). The resulting PL dynamics were measured with a single photon counting photomultiplier system with a multiscaler set to 200 ns time bins. For spectrally-resolved PL lifetimes measurements, a bandpass filter with 10 nm bandwidth was used to select emission wavelengths between 700 nm and 900 nm. A 495-nm longpass filter was used to block scattered excitation light.

The TPA measurements were conducted using the optical pump-probe technique described in Chapter 3. The sample was excited by 400 nm pump pulses to generate charge carriers. Subsequently, the sample response was monitored using time-delayed 800 nm pulses. By varying the delay time between the 400 nm pump and 800 nm probe pulses with an optical delay stage, it is possible to study the time evolution of pump-induced changes in the sample properties with sub-ps time resolution. All measurements were performed at room temperature.

7.4 Results and Discussion

The SSPL spectra of the Si NC films are shown in Fig. 7.1(a). As can be seen from the plot, the measured PL is strongly dependent on the Si content. A strong PL emission is observed for the film with the lowest Si content, $x = 1.4$ ($\rho_{Si} = 16\%$), and subsequently decreases with increasing Si content. Eventually, the PL is completely quenched at silicon filling fractions of $\rho_{Si} \geq 40\%$ ($x \leq 0.8$). Titova *et al.* (2011, 2012) recently reported that a percolation threshold at $\rho_{Si} = 38\%$ is observed in these Si NCs films. The observed PL quenching coincides with the onset of long-range percolative transport. It is possible then that the delocalization of the photoexcited carriers in the interconnected NC networks above percolation threshold suppresses the photoluminescence. Conversely, the PL is enhanced below the percolation threshold due to strong localization of the carriers (electrons and holes) within the NCs. Similar observations regarding the incompatibility of

long-range carrier transport and optical emission in Si NC films have been made earlier based on steady-state photoconductivity measurements (Balberg *et al.* 2007).

Aside from a decrease in PL intensity, a PL redshift is also observed as the Si filling fraction increases. It is important to emphasize that a higher Si filling fraction means a larger NC size. Hence, the observed PL redshift is consistent with quantum confinement (QC). On the other hand, the TIPL for $x = 1.4$ ($\rho_{Si} = 16\%$) excited by 400 nm pulses is blue-shifted compared to the SSPL as shown in Fig. 7.1(b). In addition, the TIPL shifts to higher energy (shorter wavelength) as the fluence increases. It is also observed that at higher fluence, a second peak at ~ 834 nm evolves. A saturation in the PL blue-shift as well as an increase in the intensity of the second peak (~ 834 nm) is observed at a fluence of 1.4 mJ/cm^2 . The observed PL blue-shift at higher fluence is indicative of state filling/absorption bleaching of the initial excited state due to excitation of multiple carriers within the NC. The Pauli exclusion prohibits excited carriers from occupying the same excited state. When multiple carriers are excited, several scenarios can happen. Carriers can transfer to neighboring trap states, recombine thru the Auger process or relocate to unexcited nanocrystals. Electron transfer to unexcited nanocrystal is highly unlikely since THz conductivity measurements revealed that for $\rho_{Si} < 38\%$, the carriers are highly localized within the NC (Titova *et al.* 2011). Nonradiative Auger recombination is typically observed when two or more electrons are excited within the NC. It results in the promotion of one of the electrons to a higher energy state, which at most is twice that of the excitation energy. Consequently, a PL blue shift and PL up-conversion (emission energy is higher than the excitation energy) will be observed, as previously shown in the transient PL and absorption measurements in Si/SiO₂ NCs prepared via ion implantation (Trojanek *et al.* 2005). If Auger recombination is involved, the electron that gains energy will be promoted to higher excited states of up to 6.2 eV (twice the excitation energy 3.1 eV), much higher than the direct bandgap of Si (3.4 eV). In this case, a PL up-conversion will occur, but it might be beyond the detection limit of our system (CCD detection limit is 400 nm). On the other hand, if up-conversion exists, a tail of the emission should at least be observed between 435 nm to 650 nm, however it was not observed. Carrier trapping followed by radiative recombination at the nearby traps or surface-related defects with energy levels higher than the Si core states seems to be the plausible explanation

for the observed PL blue-shift. Compared to Auger processes which typically occur between 10 ps - 100 ps (Trinh *et al.* 2012, Sevik *et al.* 2008) and core state thermalization (typically occurs between 1-10 ps) (Diamare *et al.* 2013), carrier trapping occurs at much faster rate which is less than 1 ps (Zidek *et al.* 2010, Othonos *et al.* 2008). In addition, a PL blue shift due to emission from surface related defects has been recently shown in oxidized Si NCs and amorphous Si films (Yang, De los Reyes *et al.* 2015, Huang *et al.* 2006), as discussed in Chapter 4.

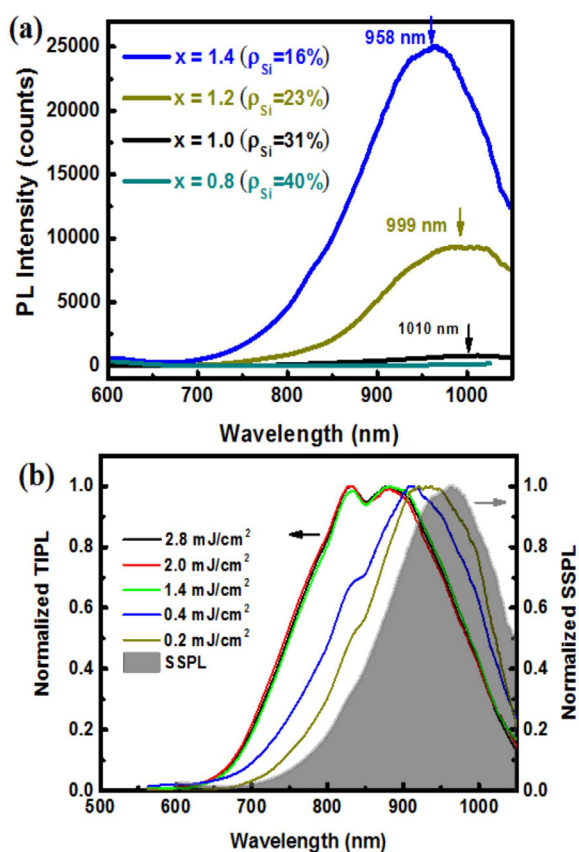


Figure 7.1: (a) SSPL of the Si NC films with different filling fraction excited by 405 nm cw laser at 5 mW. The arrows indicate the peaks of the PL spectra. (b) Comparison of the normalized SSPL and TIPL at different fluences for $x = 1.4$ ($\rho_{Si} = 16\%$).

Figure 7.2(a) shows typical μs -PL from the Si NC films. The PL decay represents the total PL lifetime for each value of ρ_{Si} (or x) and follows a non-exponential behavior that is accurately described by a stretched exponential (Eq. 3.3). A stretched exponential decay function is frequently used to describe dispersive processes in disordered systems with a distribution of relaxation times (Meldrum *et al.* 2004, Linnross *et al.* 1997, Redfield *et al.* 1996, Kakalios *et al.* 1987). As can be seen from the plot, both the PL lifetime and the dispersion factor β vary inversely with ρ_{Si} (or the size of the NC). The PL lifetimes are $\tau = 249 \pm 1 \mu\text{s}$ for $\rho_{\text{Si}} = 16\%$, $\tau = 205 \pm 1 \mu\text{s}$ for $\rho_{\text{Si}} = 23\%$, and $\tau = 143 \pm 1 \mu\text{s}$ for $\rho_{\text{Si}} = 31\%$. This observation is inconsistent with QC, where smaller NCs are expected to have shorter lifetime (a NC with $\rho_{\text{Si}} = 16\%$ is smaller than a NC with $\rho_{\text{Si}} = 31\%$), but strongly highlights the effect of the environment on the PL emission dynamics of the Si NCs in the SiO_2 matrix. Photoexcited carriers in films with higher ρ_{Si} are more affected by the NC's environment such as inter-crystallite boundaries, defects and surface recombination centers that could promote non-radiative relaxation channels (Dovrat *et al.* 2004). Hence, it is more likely that the observed decrease in PL lifetime with increasing ρ_{Si} is due to a subsequent increase in the non-radiative relaxation pathways in larger NCs, consistent with previous studies (Korinek *et al.* 2014, Hiller *et al.* 2010, Kim *et al.* 2007). This analysis is also consistent with the observed decrease in β as the size of the NC increases. It is possible that the excited carriers in the larger NC (higher ρ_{Si}) diffused more to nearby defects or inter-crystallite boundaries. The presence of large NC size distribution in $\rho_{\text{Si}} = 31\%$ can be another source of the significant decrease in β .

Spectrally-resolved μs -PL were also measured as shown in Fig. 7.2(b). It can be observed in the plot that both the PL lifetime and β increase with the emission wavelength. The increasing PL lifetime with emission wavelength is consistent with the assumption that the photon energy (emission wavelength) probes Si NCs of different sizes, since our samples exhibit large size distribution. Based on QC, larger NCs are expected to emit PL at longer wavelengths (smaller energy) (Barbagiovanni *et al.* 2014), and hence would exhibit longer PL lifetime consistent with previous results (Korinek *et al.* 2014, Timmerman *et al.* 2012, Trojanek *et al.* 2005, Linnros *et al.* 1997). The exact nature of the dependence of β on the emission wavelength is not yet clear. However, it is possible that the variation in β is indicative of the dependence of non-radiative defect concentration on NC size,

consistent with literature reports (Hiller *et al.* 2010, Goller *et al.* 2010). Hiller *et al.* (2010) observed that non-radiative defect concentration increases as the NC size decreases. They attribute it to larger number of surface atoms in smaller NC.

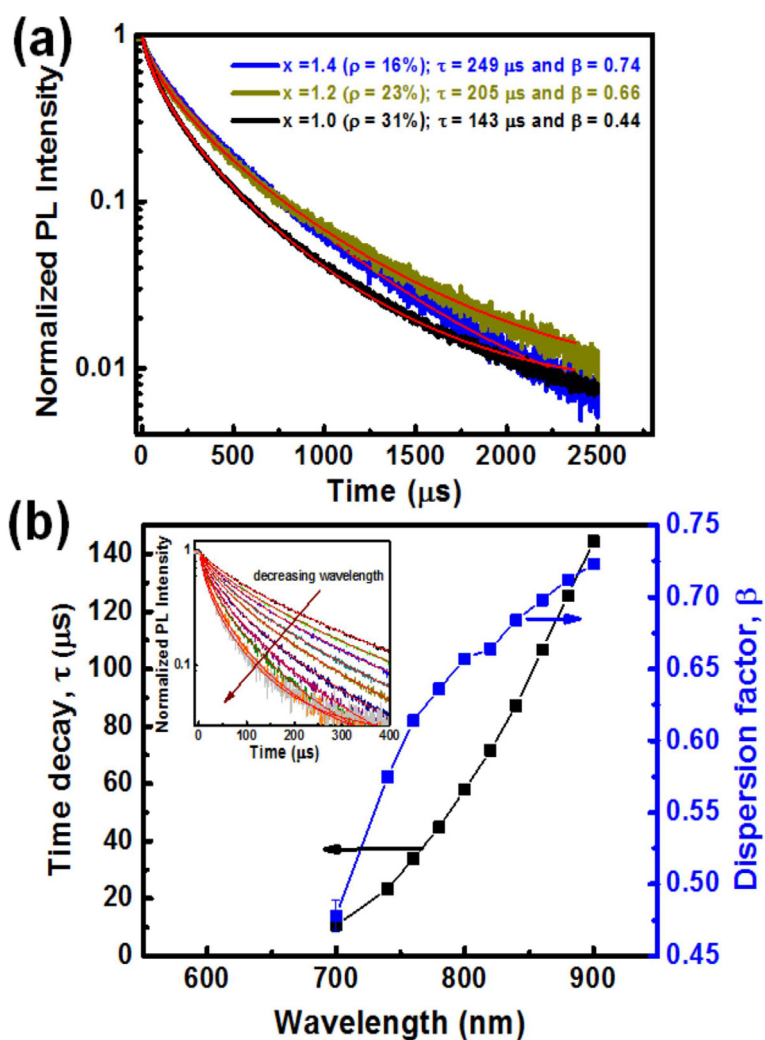


Figure 7.2: (a) Microsecond PL decay lifetimes for different silicon volume filling fractions that follows stretched exponential behavior. The standard error is $1 \mu\text{s}$ for τ and 0.001 for β . The red curve is the fit to the data. (b) Spectrally-resolved PL lifetime and dispersion factor β as a function of emission wavelength for $x = 1.4$ ($\beta = 16\%$). Inset: PL decay curves at different emission wavelengths.

Time-resolved measurements in the sub-ns time scale using TCSPC method were also performed, as shown in Fig. 7.3. It is evident from the plots that regardless of the silicon volume filling fraction, a ns-PL lifetime component is observed. Due to the poor quality of the signal (even after 1 hour acquisition time) the exact PL lifetime is difficult to determine, but it is clear from all the plots that the lifetime is less than 1 ns. Also, as seen in Fig. 7.3(a), the initial component of the lifetime is very fast (at emission wavelengths of 720 nm and 800 nm) and below the 50 ps time resolution of the set-up. In addition, the PL lifetime intensity varies inversely with the emission wavelength and a dramatic drop in intensity (comparable to the system noise level) at higher emission wavelength is observed (900 nm for $x = 1.4$ and 1.2 , and at 830 nm for $x = 1.0$). Comparing the behavior of the intensity of the μ s- and ns-PL lifetime components (Fig. 7.4), an opposite trend is observed. The μ s-PL lifetime intensity increases with emission wavelength while the ns-PL lifetime intensity increases with decreasing wavelength. It will be recalled in Fig. 7.1(b) that the TIPL is blue shifted compared to the SSPL and at higher excitation fluence a second peak at lower wavelength appears. Based on these results, it is clear that the observed ns-PL lifetime is related to the PL blue-shift and as initially proposed, is possibly due to recombination of carriers at the surface-related defects.

The effect of excitation fluence on the carrier dynamics is also explored here. As shown in Fig. 7.5(a), the ns-PL lifetime intensity increases linearly with excitation fluence. This result confirms that the PL blue-shift observed at higher fluence (Fig. 7.1 (b)) is not due to Auger processes. On the other hand, the μ s-PL lifetime component decreases as the power increases, a similar trend is observed for β . It is important to emphasize that during the lifetime measurements, the sample was not moved to ensure that the same NC region is being excited. A decrease in the μ s-PL lifetime component reveals that at higher fluence, occupation of the excited states results in bleaching of the absorption (state filling). As a result, the excited carriers can either recombine non-radiatively through Auger processes or transfer to nearby defects or surface-related traps. The non-radiative Auger process has already been ruled out; hence, charge transfer to nearby defects is most likely the reason for the observed decrease in the μ s-PL lifetime component. This hypothesis is supported by the observed decrease in β , which implies a higher diffusion of carriers to nearby traps as excitation fluence increases. These results are consistent with the increasing ns-PL lifetime

intensity (Fig. 7.5(a)) and strongly support the initial hypothesis that the PL blue shift observed at higher excitation fluence (Fig. 7.1(b)) is due to carrier trapping accompanied by recombination of the trapped carriers. Similar analysis has been previously reported for annealed silicon-rich silicon oxide that exhibit higher PL quantum yield for decreasing Si volume filling fraction (Khriachtchev *et al.* 2009). The increase in PL quantum yield was attributed to carrier migration to surface-related states followed by recombination at their localized emitting centers.

To gain a better understanding of the carrier dynamics at early times after photoexcitation, TPA measurements using optical pump-probe techniques were conducted. The resulting negative differential transmission curves are shown in Fig. 7.6. A positive transient absorption signal is initially observed in all samples indicative of excited state absorption. The transient absorption signal of all the samples exhibits rapid initial rise but did not recover for samples with ρ_{Si} of 16% to 31%, indicative of a long lifetime component, probably in the μs range, that is beyond the range of the set-up. On the other hand, after a time delay of 50 ps, a negative transient absorption signal is observed in samples with ρ_{Si} of 40% and 51%. This increase in transmission is unlikely a result of stimulated emission since these samples do not exhibit PL. It is possible that the increase in transmission is possibly a result of heating in these thinner films (thickness is 200 nm) which leads to a significant increase in lattice temperature. A similar observation is reported in polycrystalline Si films with different thicknesses (Al Harthy 2008). Si NC films with ρ_{Si} of 16% to 31% exhibit a very fast sub-ps initial decay, as shown in Fig. 7.6(b). Othonos *et al.* (2008) also observed similar behavior from transient absorption measurements of oxidized Si NCs which is attributed to carrier transfer from the nanocrystal to surrounding surface-related states. This result is consistent with the initial hypothesis that the origin of the PL blue shift at higher excitation fluence is due to carrier trapping followed by radiative recombination of the trapped carriers. Closer examination of the rise in TPA signal reveals a delay of ~ 0.62 ps in reaching the maximum PA for Si films with ρ_{Si} of 40% and 51% which suggests that the PA did not occur at the initial excited state location. As previously reported, these Si NC films exhibit long-range conduction at the initial 10 ps after photoexcitation (Titova *et al.* 2011) which indicates rapid transport of carriers to nearby nanocrystals after photoexcitation. This observation is consistent with the proposal that the excited

state absorption occurs at a different excited state location. The decay curves at a later times (after the initial fast decay in $\rho_{Si} = 16\%$ to 31% and a delay of 0.62 ps for $\rho_{Si} = 40\%$ and 51%) follow a stretched exponential behavior described in Eq. 3.3. In addition, as shown in Fig. 7.6(a), the carrier relaxation time is dependent on the Si volume filling fraction. While all samples exhibit decay times less than 100 ps, the behavior of the decay time and β do not follow a trend. The β values observed from TPA measurements are much lower than that from μ s-TRPL measurements. Notably, the PA lifetime decay for $\rho_{Si} = 16\%$ is comparable to that obtained from the ns-TRPL PL lifetime.

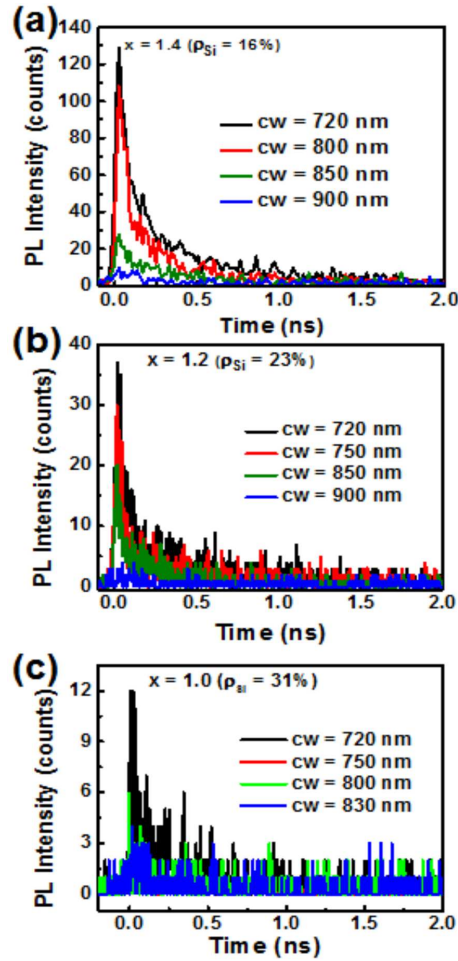


Figure 7.3: ns-TRPL of Si NC films with different silicon filling fractions: (a) 16%, (b) 23%, and (c) 31%. The PL was excited by 400 nm laser pulses at an excitation fluence of 0.25 mJ/cm² [cw=center of the emission wavelength].

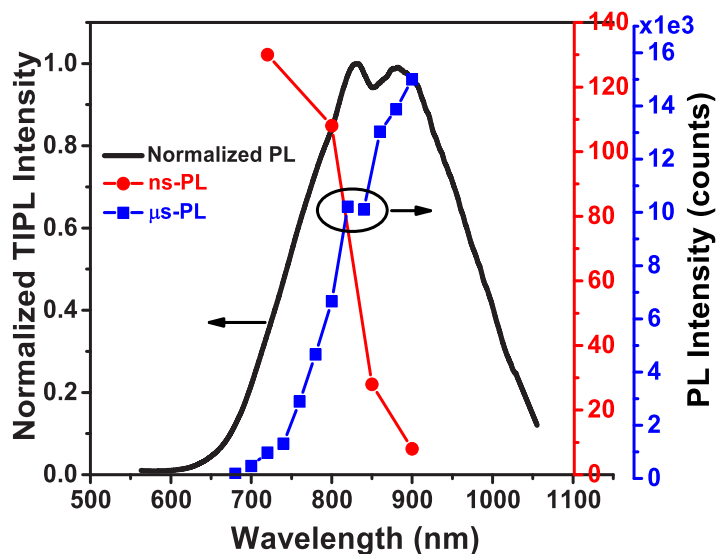


Figure 7.4: TIPL spectra of Si NC films with $\rho_{Si} = 16\%$ ($x = 1.4$) excited by 400 nm laser pulses at an excitation fluence of 2.0 mJ/cm^2 . The ns- and μ s-PL lifetime intensities are also shown.

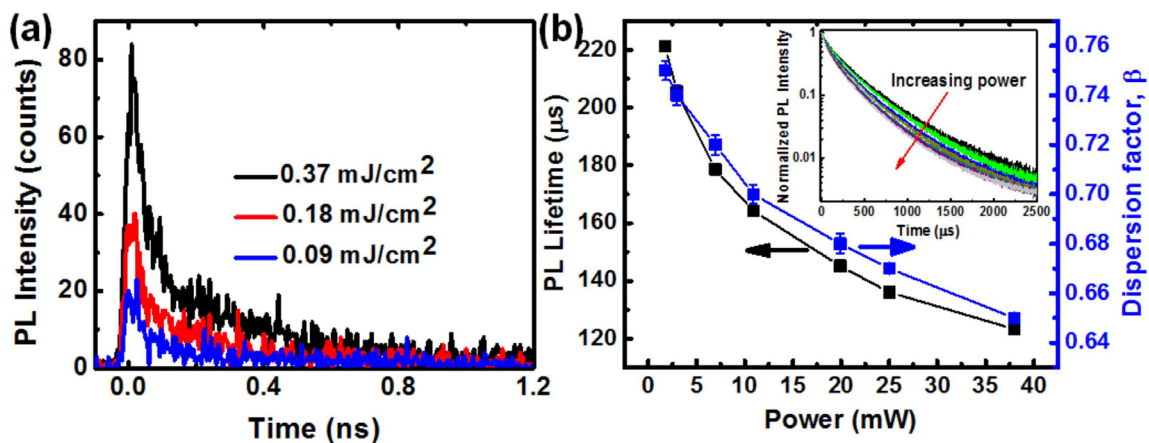


Figure 7.5: Fluence dependent TRPL of Si NC film with $\rho_{Si} = 16\%$ ($x = 1.4$) in (a) sub-ns and (b) μ s-time scales. The ns-TRPL is measured at emission wavelength of 750 nm while the μ s-TRPL is the total PL lifetime. Also shown is the dispersion factor β as a function of pump power. Inset is the semi-log plot of the μ s-PL lifetime as a function of excitation power.

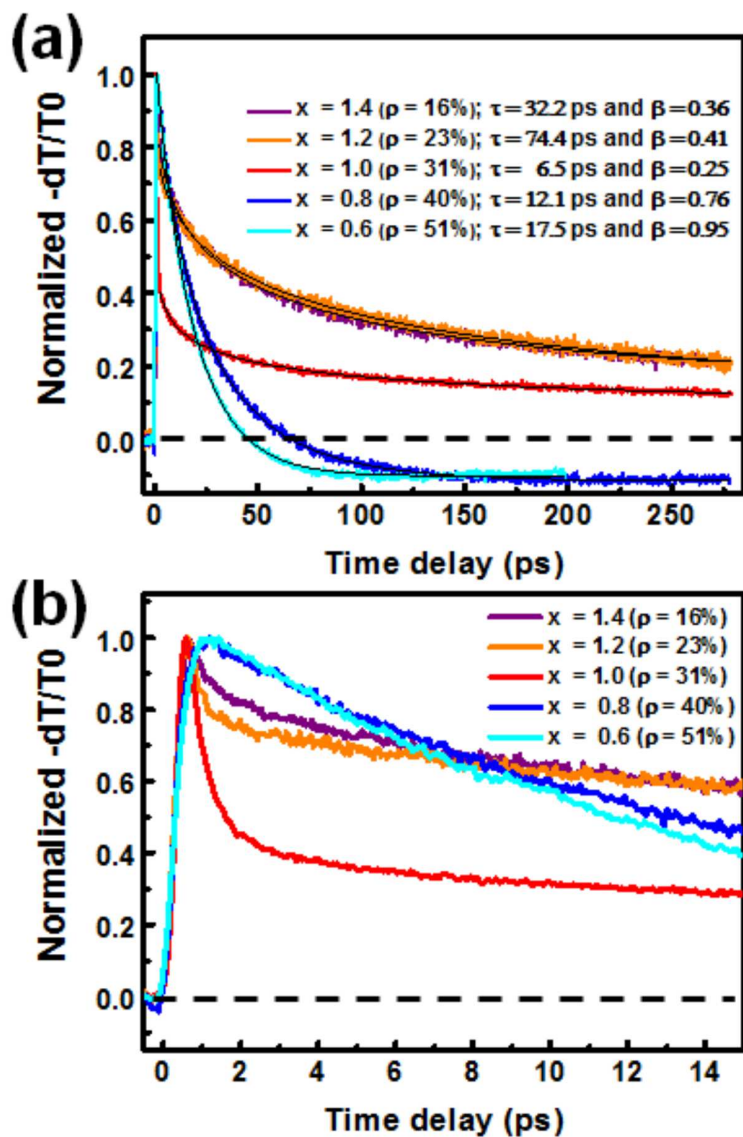


Figure 7.6: Effect of Si volume filling fraction on the transient PA decay as probed by 800 nm pulses. (b) Zoom-in of the initial 15 ps of the decay. Excitation fluence is $9.2 \mu\text{J}/\text{cm}^2$ and the probe fluence is $6.7 \mu\text{J}/\text{cm}^2$. The error in τ is ≤ 0.8 ps while error in β is ≤ 0.004 .

7.5 Conclusion

In summary, the optical properties of Si NC films with different filling fraction, ρ_{Si} , are explored. Strong PL emission in the infrared spectral region is observed for films that have ρ_{Si} below the percolation threshold of 38%. SSPL shows that the PL peak emission blue shifts as ρ_{Si} decreases, attributed to QC. The fluence-dependent TIPL and TRPL measurements reveal a state filling effect at higher excitation fluence which results to a PL blue-shift. Detailed studies of the carrier dynamics reveal the coexistence of microsecond, sub-100 ps and sub-ps lifetime decays. The sub-ps decay observed in the transient PA measurements is attributed to carrier trapping at the nearby traps or surface-related states. The sub-100 ps component observed in ns-TRPL and transient PA measurements is assigned to recombination of the trapped carriers while the microsecond lifetime component is attributed to recombination in the quantum confined core states.

CHAPTER 8

Ultrafast near-field scanning optical microscopy

8.1 Introduction

The growing field of nanotechnology requires special tools capable of probing ultrafast surface dynamics on atomic scales in order to reveal the fundamental relationships between material structures and its properties. Time-resolved laser spectroscopy is the only technique capable of directly studying the material dynamics on sub-picosecond or femtosecond time scales (Yarotski *et al.* 2000). However the spatial resolution of this method alone is limited by diffraction to several hundreds of nanometers. On the other hand, near field scanning optical microscopy (NSOM) gives a resolution that is better than the resolution of a conventional and confocal microscopy that is dependent on the excitation wavelength ($\lambda/2$). The resolution of the NSOM is dependent on the size of the aperture in the probe tip which scans the surface of the sample at a distance much smaller than the diameter of the aperture (Synge 1982). Recent developments in near field microscopy show that a resolution of up to ~ 10 nm is possible by decreasing the aperture size to 15 nm - 20 nm (Kaupp *et al.* 1997). Thus the obvious step in pursuing the ultimate probe mentioned above is to combine the advantages of both NSOM and ultrafast laser spectroscopy into a single instrument that should be free of limitations posed by each separate method and that should provide simultaneous picosecond/femtosecond temporal resolution and nanometer spatial resolution.

The probes that have proposed and applied in NSOM come in three varieties: (1) those that use apertures (Hecht *et al.* 2000, Betzig *et al.* 1991, Binnig *et al.* 1986), those involving near-field scattering mechanisms (Eisele, Cocker *et al.* 2014, Hartschuc 2008, Danckwerts *et al.* 2007, Zayats *et al.* 2004, Bouhelier *et al.* 2003, Hamman *et al.* 2000), and those dependent on luminescence effects (Raymond *et al.* 2011, Lewis *et al.* 1998). Most commonly used NSOM tips are metal coated, pulled single mode optical fibers which were introduced by Betzig *et al.* (1991). These NSOM tips coupled with ultrafast laser pulses have been widely used in spectroscopy. The most commonly observed implementation of ultrafast NSOM is in photoluminescence (PL) microscopy. NSOM PL has been demonstrated to be useful for studies involving organic, biological (Raymond 2011, Szymanski *et al.* 2005, Lewis *et al.* 1998), and semiconductor nanostructures (Leong *et al.* 1996, Gregor *et al.* 1995, Grober *et al.* 1994). Recently, NSOM PL has also been used for direct photocurrent mapping of organic solar cells (McNeill *et al.* 2004).

Aside from NSOM PL microscopy, NSOM coupled with ultrafast laser pulses has also been demonstrated to be an efficient tool in probing the relaxation and photoexcitation dynamics of excited carriers using NSOM time-resolved PL and pump-probe measurements, respectively. NSOM time-resolved PL has been utilized to study the spatiotemporal dependence of excitonic spin behavior in patterned magnetic heterostructures (Levy *et al.* 1996) and to investigate the recombination of excess carriers in oxidized silicon (Rosa *et al.* 1997). On the other hand, ultrafast NSOM pump-probe measurements were used to probe the carrier transport in quantum wires (Guenther *et al.* 1999) and quantum wells (Nechay *et al.* 1999). In addition, Vertikov *et al.* (1996) studied heat propagation in patterned gold nanostructures by monitoring the reflectivity changes.

As discussed above, ultrafast NSOM-fiber spectroscopy has proven to be useful in exploring the ultrafast dynamics of nanostructures (Betzig *et al.* 1993, Nechay *et al.* 1999). However, the time resolution of this system is reduced due to nonlinear effects in the fiber while the spectrum of the measured output pulse is sometimes distorted by stimulated Raman scattering. To avoid these limitations, we attempted constructing an ultrafast NSOM pump-probe transient absorption set-up by coupling both the ultrafast pump and probe pulses using single mode fibers to a commercially available NSOM system.

8.2 Ultrafast near-field scanning optical microscopy

8.2.1 Near-field scanning optical microscope

High spatial resolution in on the nanometer scale is not possible to attain in a conventional microscope because its resolution is diffraction limited (Betzig *et al.* 1991). According to the Rayleigh criterion (Spencer 1982), the highest resolution achievable in any conventional microscope is

$$d = \frac{0.61\lambda}{NA} \quad (8.1)$$

where λ is the wavelength of light in vacuum and NA is the numerical aperture of the objective. The highest NA for an objective is 0.95 for air and 1.4 for oil immersion objective (Dokland *et al.* 2006). This implies that the highest resolution possible for visible illumination of a microscope is $\sim \lambda/2$, *i.e.* a green 532 nm excitation light will result in 266 nm spatial resolution.

In 1928, Synge (1928) suggested that by scanning a tiny aperture in close proximity across the sample, the diffraction limit can be avoided. This is possible since at a sample-aperture distance much shorter than the wavelength of the excitation light, the evanescent or “near field” components of the scattered light would interact with the sample, rather than the propagating or “far field” components. By collecting the light emitted by or transmitted through the sample, an image can thus be built up that is free from the limits imposed by diffraction of the far field components (Prasankumar *et al.* 2012). In this case, the resolution is only limited by the diameter of the aperture and no longer by the wavelength. This idea is illustrated in the Fig. 8.1 below and is the principle behind the modern NSOM instrument.

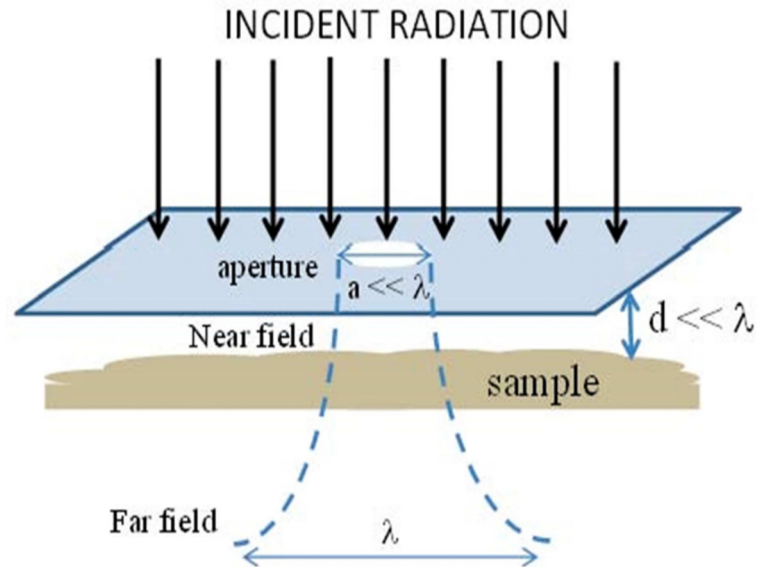


Figure 8.1: Schematic diagram of the high spatial resolution scanning that overcomes the diffraction limit. [Adapted from Synge 1928]

The NSOM instrument that was used in this study is a commercially available scanning probe microscope from WiTec (Alpha300S) which consists of a standard $20\times$ objective and an inertial drive assembly which magnetically holds the cantilever arm and the cantilever itself. The objective is used to focus the excitation beam as well as beam deflection laser onto the cantilever, as illustrated in Fig. 8.2. The scanning probe is a microstructured cantilever sensor consisting of a silicon cantilever with a hollow SiO_2 tip. The cantilever dimensions are $150\ \mu\text{m}$ in width, $700\ \mu\text{m}$ in length, and $5\ \mu\text{m}$ in thickness. The pyramid tip typically has a base of $20\ \mu\text{m}$ and a height of $10\ \mu\text{m}$. The hollow aperture is surrounded by a $100\ \text{nm}$ - $150\ \text{nm}$ thick layer of aluminum providing mechanical contact. Typical aperture sizes are $50\ \text{nm}$ and $100\ \text{nm}$. An SEM image of the microstructured cantilever sensor is shown in Fig. 8.3.

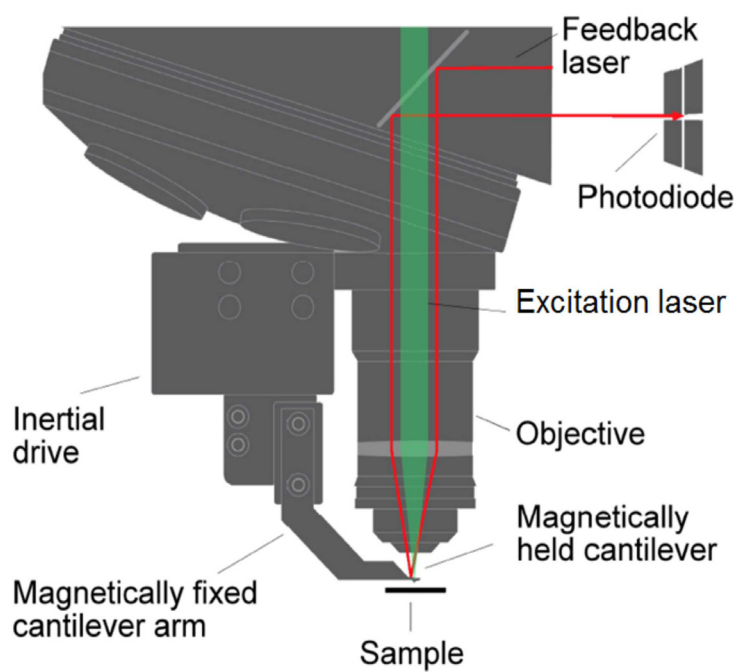


Figure 8.2: Schematic diagram of the NSOM instrument (Witec Manual 2012). The feedback laser (red line) is used to control the distance between tip and the sample.

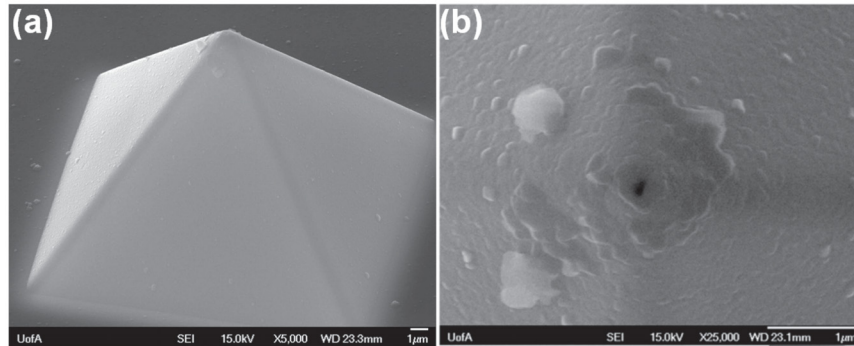


Figure 8.3: SEM images of the cantilever tip showing (a) the pyramid tip and (b) the zoom in of the pyramid tip showing an aperture with diameter of 100 nm.

The spatial resolution of the ultrafast NSOM was determined using an Al hexagonal pattern (Kentax, Munster, Germany) deposited on a glass slide. A 532 nm diode laser was coupled to the 100-nm NSOM probe using a 20 \times objective. The transmitted light is collected by a 60 \times objective in the far field and sent to the NSOM avalanche photodiode (APD). The transmitted image was processed using WiTec Project 6.0 software (Fig. 8.4(a)). A spatial resolution of \sim 105 nm was obtained by getting the full-width at half-maximum (FWHM) of the variation in the count rate along the line drawn in the NSOM image (Fig. 8.4(b)).

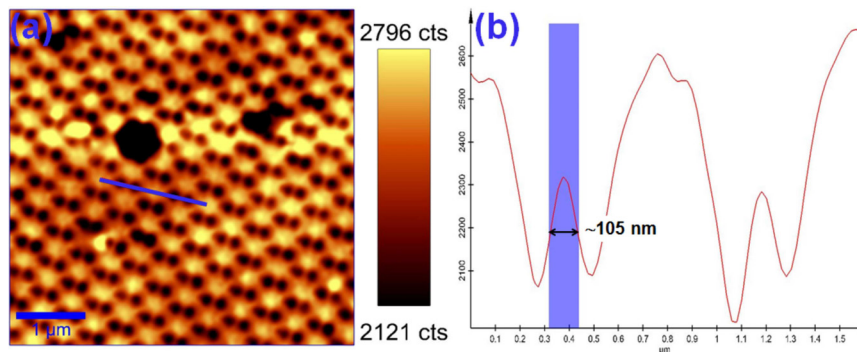


Figure 8.4: (a) NSOM transmission image of Al projection pattern and (b) corresponding variation of the count rate along the blue line of the near field transmitted image.

8.2.2 Coupling the ultrafast laser to the NSOM instrument

The 800 nm laser pulses from a Ti:Sapphire laser with transform-limited pulse width of 65 fs and repetition rate of 250 kHz was coupled to the NSOM system using a 23-cm long single mode fiber (OZ Optics), as shown in Fig. 8.5. The core diameter of the fiber was made small ($5\ \mu\text{m}$) to ensure single mode propagation of the 800 nm pulses. To compensate for the positive dispersion induced by the fiber, the femtosecond laser pulses were negatively pre-chirped to 1 ps resulting in an output pulse width of 200 fs. The polarization and input power to the fiber was controlled by the combination of polarizer and half wave plate. A fiber coupler with XYZ adjustment screws mounted on a 3D stage was used to optimize the coupling efficiency of the fiber. The optimum power throughput of the fiber is 45% and the power throughput of the NSOM system without the cantilever is $\sim 34\%$ for wavelengths from 500 nm to 800 nm. The ultrafast NSOM system is coupled to the spectrometer using a multimode fiber. The spectrometer is equipped with an ultrasensitive CCD and single photon avalanche photodiode that are used for time-integrated and time-resolved PL measurements (TIPL and TRPL), respectively. The TRPL decay was analyzed using a time-correlated single photon counting (TCSPC). The schematic diagram of the set-up is shown in Fig. 8.6.

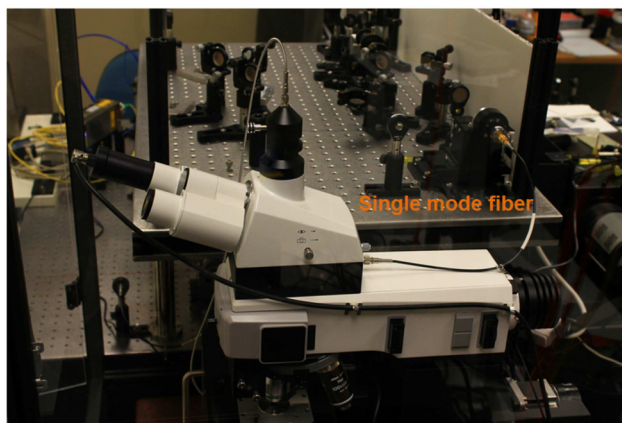


Figure 8.5: The experimental set-up showing the single mode fiber coupled to the NSOM system.

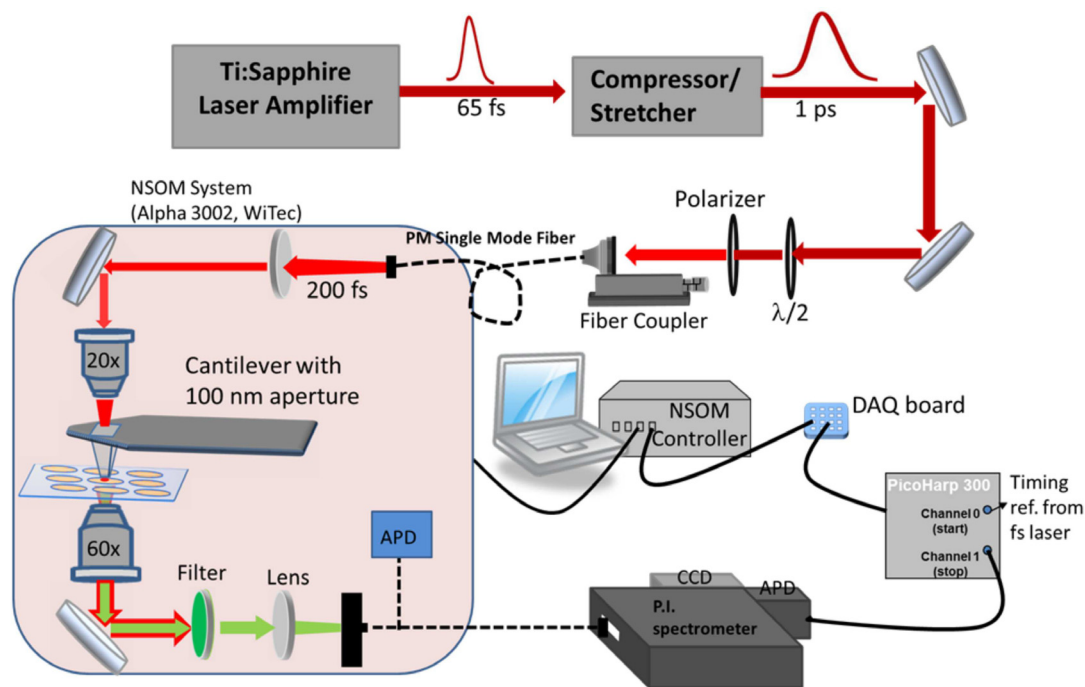


Figure 8.6: Schematic diagram of the experimental set-up. The 800 nm laser pulses were free-space coupled to the single mode fiber. The fiber's output pulses exhibiting a 200 fs pulse width was coupled to the NSOM system. A 20 \times objective was then used to focus the excitation pulses to the hollow cantilever probe. The transmitted signal was collected by 60 \times objective and sent to an APD for NSOM the transmitted image or to the spectrometer for the TIPL and TRPL measurements. A combination of polarizer and half wave-plate was used to control the power input to the fiber as well as the polarization of the input laser pulses to obtain maximum throughput.

The ultrafast NSOM capabilities were tested by exciting the PL from a cluster of CdSe/ZnS core-shell nanocrystals drop coated on fused silica glass. First, the topography of the sample (Fig. 8.7(a)) was obtained simultaneously with transmitted NSOM image collected by the NSOM APD. To get the PL spectra for a particular cluster, the NSOM tip was held stationary on top of one of the clusters (marked by a black circle in the topography) and the fiber connection was transferred from NSOM APD to the spectrometer (Fig. 8.7(c)). A bandpass filter of 335 nm - 650 nm was used to block the excitation pulses and allow only the transmission of the induced PL. By sending the

transmitted signal to the CCD, the TIPL spectrum centered at 576 nm is obtained. After getting the PL spectrum, the carrier lifetime was measured using the TCSPC system. As shown in the inset of Fig. 8.7(d), the PL lifetime exhibits an initial fast rise of 54 ± 1 ps which corresponds to the time resolution of the ultrafast NSOM PL system. The TRPL measured at 570 nm exhibits a single exponential decay with a lifetime of 7.53 ± 0.3 ns, consistent with literature reports (Hao *et al.* 2013, Nguyen 2010).

To determine if the ultrafast NSOM set-up is capable of producing a temporally-resolved PL image, the output of the TCSPC was coupled to the auxiliary channel of the NSOM controller to record the induced PL in CdSe/ZnS clusters. The time decay signal was binned such that only the first 5.5 ns part of the decay time is sent to the NSOM auxiliary channel that will be converted into image. The integration time of the TCSPC was set to 1s while the acquisition time in the NSOM scan was set to 1.2 s per pixel (scan size is 256×256). A longer acquisition time was set in the NSOM scan to accommodate any possible time lapse between the motion of the tip and the signal from the TCSPC. Finally, the ultrafast NSOM time-resolved PL image and topography were obtained simultaneously by scanning the surface of the sample. The results are summarized in Fig. 8.7. The bright areas in the topography (Fig. 8.7(a)) correspond to the CdSe/ZnS clusters while that in the temporally-resolved PL image (Fig. 8.7(b)) correspond to higher PL counts. As shown in Fig. 8.7(a) and (b), the temporally-resolved PL image is very similar to the obtained topography which indicates that the measured PL intensity originates from CdSe/ZnS nanocrystal clusters. This result demonstrates that the set-up can be utilized for ultrafast NSOM temporally-resolved PL microscopy.

While this result is encouraging, it was also observed that the cantilever probe was damaged by the excitation pulses. The cantilever aperture increased significantly after the scan which implies that the spatial resolution of the system is significantly reduced. Reducing the excitation power to 0.1 mW (fiber output power which corresponds to $35 \mu\text{W}$ power, incident on the cantilever probe) did not solve the problem, as shown in Fig. 8.8. This observation would pose limitations in the capability of the ultrafast NSOM system. Avoiding tip damage would mean that the excitation pulses should be made much smaller than $35 \mu\text{W}$ which would limit the use of the system to samples that have significantly higher PL quantum yield.

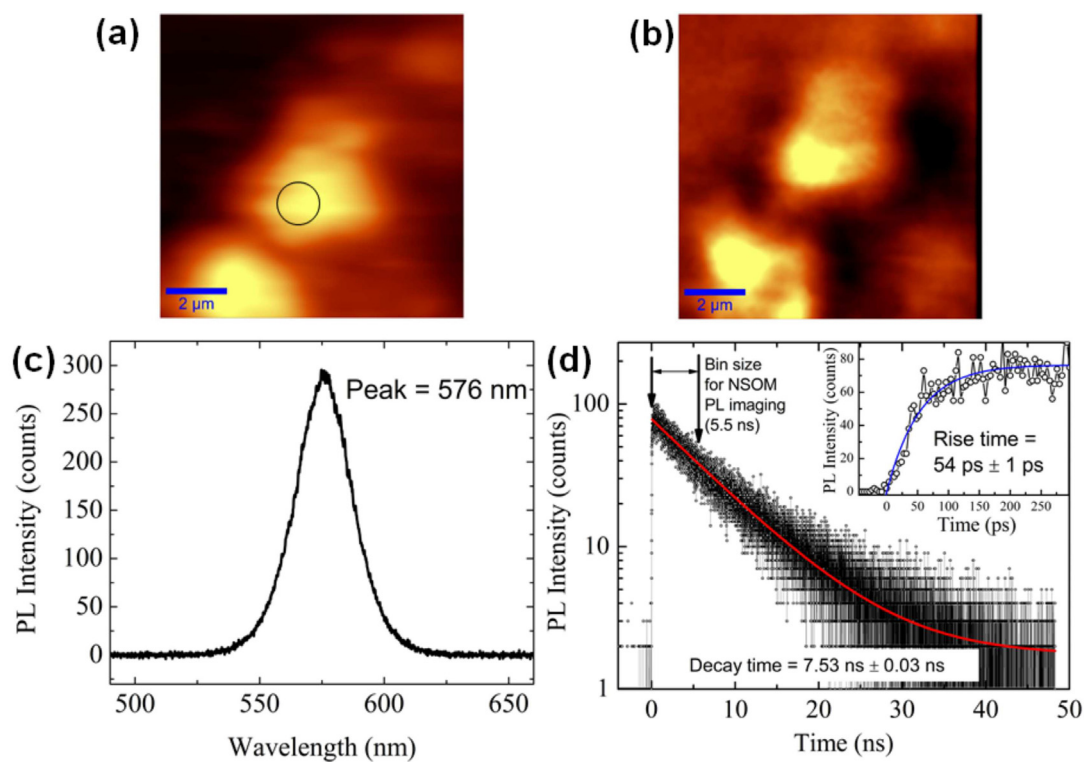


Figure 8.7: (a) Topography of the CdSe/ZnS core-shell nanocrystals cluster drop coated on fused silica glass. (b) Ultrafast NSOM temporally-resolved PL image corresponding to the initial 5.5 ns PL lifetime. (c) Two-photon TIPL spectrum taken at the location marked by a circle on the topography image and (d) the corresponding PL lifetime decay measured at 570 nm. Inset: rise-time of the PL signal is 54 ps, which corresponds to the time resolution of the ultrafast NSOM PL set-up and TCSPC system.

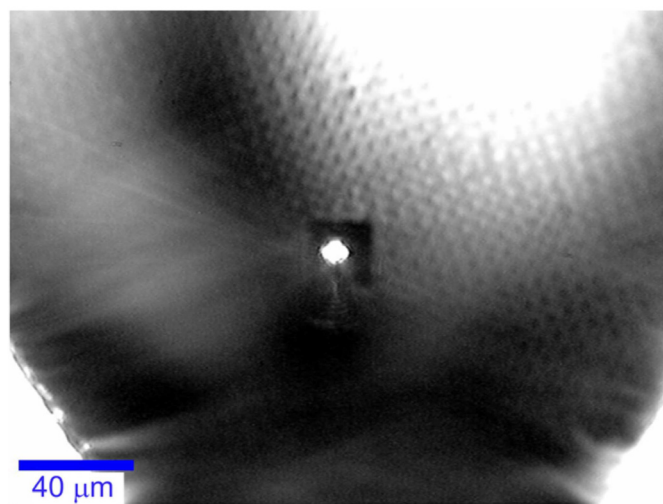


Figure 8.8: Image of the cantilever probe taken after the time-resolved PL microscopy. Before coupling the excitation pulses to the NSOM, the cantilever aperture is 100 nm in diameter (Fig. 8.3(a)), but after the first scan, was damaged by the excitation pulses.

8.2.3 Ultrafast NSOM pump-probe transient absorption set-up

The capability of the ultrafast NSOM system was initially planned to accommodate all optical pump-probe transient absorption experiments. The initial design included a 400-nm pump pulses that would be used to excite the carriers in the sample and 800 nm probe pulses that would monitor the pump-induced changes in transmission. The 400 nm pump pulses were generated by second-harmonic generation (SHG) of 800 nm laser pulses from a beta barium borate (BBO) crystal. The original 800 nm pulses from the Ti:Sapphire laser were split by a 95%/5% beam splitter. The 800 nm pulses that have 95% power were used to excite the BBO crystal while the one with the 5% power was used as the probe pulse. Both pump and probe pulses were coupled to the NSOM using single mode fiber.

Several strategies were attempted to generate 400 nm pulses from the BBO crystal, all of which used free-space coupling of the 800 nm excitation pulses to the fiber, similar to the 800 nm probe pulses. The initial compressor setting of 1 ps, which corresponds to a fiber output pulse width

of 200 fs was used. In the first configuration, the BBO crystal was placed inside a fiber coupler with the BBO crystal having no direct contact with the fiber tip. This configuration was unsuccessful in generating a SHG signal from the BBO crystal even at the maximum excitation power of 60.1 mW. In the second configuration, the BBO crystal was mounted on a sample holder, with the fiber tip placed in very close proximity to the crystal. This configuration yielded a low power 400 nm pulse with less than 100 μW (excitation power of 60.1 mW). The power was successfully increased to 900 μW by increasing the compressor setting from 1 ps to 3.4 ps. However, this amount of power may still not be enough to excite a sufficient number of carriers in the sample (throughput of the 20x objective is only 35% and the throughput of the cantilever aperture is much less than 10%) (Minh *et al.* 2000). In addition, adjusting the compressor setting to 3.4 ps resulted in a fiber output pulse width of 1.5 ps. Since in a pump-probe set-up, the time resolution is limited by the pulse width of the pump and probe pulses, the time resolution will be 1.5 ps at best. This resolution is below the desired time resolution for a pump-probe set-up which typically probes photoexcited carrier dynamics in sub-ps time scales. Due to these difficulties, the ultrafast NSOM pump-probe transient absorption set-up was not successfully realized. This aspect of the project was later discontinued due to time limitations and the difficulties encountered.

CHAPTER 9

Summary and Recommendations

9.1 Summary

In this work, ultrafast spectroscopy was applied to study the optical properties of silicon nanocrystals (Si NCs). Particularly, time-integrated photoluminescence (TIPL), time-resolved photoluminescence (TRPL) and optical pump-probe transient absorption spectroscopies were utilized to study the emission dynamics of functionalized Si NCs and Si NC films.

Dodecyl functionalized Si NCs prepared using two related techniques, thermal and photochemical hydrosilylation, exhibit different emission properties as observed in the TIPL and TRPL spectra. Photochemically-functionalized Si NCs exhibit higher emission energies than the thermally-functionalized equivalent. While microsecond lifetime emission attributed to carrier recombination within the NC core was observed from all dodecyl functionalized si NCs, much faster, size-independent nanosecond lifetime components were only observed in samples prepared using photochemical hydrosilylation that possessed substantial surface oxidation. In addition, photochemically modified Si NCs exhibit higher absolute photoluminescent quantum yields (AQY) consistent with radiative recombination processes occurring at the oxygen-based defects. Correlating spectrally- and time-resolved PL measurements and XPS-derived relative surface oxidation for NCs prepared using different photo-assisted hydrosilylation reaction times provides evidence that the PL blue-shift as

well as the short-lived PL emission observed for photochemically functionalized Si NCs are related to the relative concentration of oxygen surface defects.

The effects of surface passivation on the emission dynamics of colloidal Si NCs were also studied. The PL emission in functionalized Si NCs can be tuned across the visible spectrum without changing the size of the NCs. The origins of the size-independent PL emission were identified and associated to the type of surface functionalization. A quantum confined core state emission characterized by microsecond-PL lifetime was observed in oxygen-free dodecyl functionalized Si NCs. On the other hand, oxide-based defect emission is observed in oxidized dodecyl functionalized Si NCs and TOPO functionalized Si NCs. PL emission from oxide-based defects are significantly blue shifted compared to quantum confinement prediction and exhibit fast recombination in less than 10 ns. Lastly, charge transfer state emission characterized by a solvent-polarity-dependent PL is observed from dodecylamine and acetal functionalized Si NCs. Similar to oxide-based defect emission, the observed charge transfer state emission is significantly blue shifted compared to quantum confinement predictions and exhibits sub-10 ns PL decay.

The carrier dynamics of blue emission from dodecylamine and ammonia functionalized Si NCs with average diameters of ~ 3 nm and ~ 6 nm was explored using TRPL spectroscopy. The measured TIPL spectra for these functionalized Si NCs are size-independent and characterized by sub-10 ns PL decay, inconsistent with core state emission. Spectrally-resolved PL lifetime indicate that the emission dynamics is uniform across the emission spectrum with a radiative recombine rate of $\sim 5 \times 10^7 \text{ s}^{-1}$. The NC-size-independent blue emission is attributed to charge transfer states at the Si/SiO_xN_y interface. Absorption measurements of the sample reveal that absorption occurs within the Si core, but the absence of μs -PL from all of our samples suggests a very efficient electron transfer from the Si NC core excited states to the charge transfer (CT) state.

The effect of silicon filling fraction on the PL emission dynamics of Si NC films embedded in a SiO₂ matrix was studied using optical pump-probe transient absorption and TRPL spectroscopy. Si NCs films that have filling fractions below the percolation threshold of 38% exhibit strong luminescence in the infrared region. SSPL reveals that the PL peak emission blue shifts as the silicon filling fraction decreases (as the silicon volume filling fraction decreases, nanocrystals size also decreases),

attributed to quantum confinement effect. PL blue-shift was also observed in silicon nanocrystal films with $x = 1.4$ ($\rho_{Si}=16\%$) as the excitation fluence increased which was attributed to state filling effect/absorption bleaching of the Si core excited state. The blue-shift in PL emission is assigned to oxygen-related defects. Detailed studies of the carrier dynamics reveal the coexistence of microsecond, sub-100 ps and sub-ps lifetime decays. The sub-ps lifetime decay observed in the transient PA measurements is attributed to carrier trapping at the nearby traps or surface-related states while the sub-100 ps component observed in ns-TRPL and transient PA measurements is assigned to recombination of the trapped carriers. The size-dependent microsecond lifetime component is attributed to recombination of excited carriers in the quantum confined core states.

An ultrafast near-field scanning optical microscopy (NSOM) was developed to probe the PL dynamics of individual nanocrystals. The 800 nm pulses were successfully coupled to a commercially available NSOM system using a single mode fiber. The ultrafast NSOM system was also integrated to the time-resolved PL setup with time-correlated single photon counting unit for carrier dynamics measurements. The capability of the ultrafast NSOM was initially tested using CdSe/ZnS core-shell quantum dots drop coated on a fused silica glass. A good correlation between the temporally-resolved NSOM transmission image and the topography of the sample was observed. This result indicates that the newly developed system can be used for ultrafast NSOM spectroscopy.

9.2 Recommendations

This work presented the characterization of the optical properties of functionalized Si NCs and Si NC films using different time-resolved techniques. All measurements were done at room temperature. However, literature accounts show that the emission dynamics of Si NCs, in general, behaves differently at low temperature (Dovrat *et al.* 2004) It is therefore recommended to study the effect of temperature on the emission dynamics of the said Si NCs studied here. By doing so, it is possible to see the splitting of energy in quantum confined Si NCs as previously reported by Dovrat *et al.* (2004). In addition, using the temperature-dependent PL and PL lifetime data, it is possible to probe any quasi-direct transition from Si NCs regardless of functionalization.

While detailed ns-TRPL was performed in all samples, the carrier dynamics immediately after photoexcitation is unknown. It is then recommended to do pump-probe transient absorption measurements in the functionalized Si NCs. It is probably best to use probing energies that are within the emission spectrum of the sample in order to elucidate the dynamics of the states responsible for the observed emission.

Another experiment that can help elucidate the exact nature of the emitting states in functionalized Si NCs that do not follow the quantum confinement prediction is scanning tunneling spectroscopy. Using this technique, the actual bandgap of the emissive state can be obtained as well as the associated density of states (Eisele, Cocker *et al.* 2014).

It was shown that the newly-developed ultrafast NSOM system can be used for time-resolved NSOM measurements. However, it was observed that the 800 nm ultrafast laser pulses with a repetition rate of 250 kHz burned the cantilever tip during the scan. One way to possibly avoid this is to use a laser pulse that have higher repetition rate. Extending the ultrafast NSOM design to accommodate optical pump-probe transient absorption measurements encountered a lot of difficulties. Using single mode fibers to couple the pump and probe pulses to the NSOM system is not ideal due to very low 400 nm signal generated from the BBO crystal and too much pulse spreading in the fiber. One way to solve this issue is to use the output of the optical parametric amplifier (OPA), which has both 400 nm and 800 nm pulses and then free-space couple them to the NSOM system. Since transient absorption measurements require that the intensity of the probe pulses must be much smaller than the pump pulses, then coupling the 800 m pulses will probably not damage the cantilever tip.

Bibliography

- Ajayi, O. A.; Anderson, N. C.; Cotlet, M.; Petrone, N.; Gu, T.; Wolcott, A.; Hone, F. J.; Owen, J. S.; Wong, C. W. *Appl. Phys. Lett.* **2014**, *104*, 17101-5.
- Alex, V.; Finkbeiner, S.; Weber, J. *J. Appl. Phys.* **1996**, *79*, 6943.
- Al Harthy, R. 2008. *Supercontinuum probe of ultrafast carrier dynamics in nanostructured silicon thin films*. (Masteral Thesis, University of Alberta)
- Alivisatos, A. P. *Science* **1996**, *271*, 933-937.
- Alsharif, N. H.; Berger, C. E. M.; Varanasi, S. S.; Chao, Y.; Horrocks, B. R.; Datta, H. K. *Small* **2009**, *5*, 221.
- Anedda, A.; Bongiovanni, G.; Cannas, M.; Congiu, F.; Mura, A.; Martini, M. *J. Appl. Phys.* **1993**, *74*, 6993.
- Arndt, A. P.; Gerhard, M.; Quintilla, A.; Howard, I. A.; Koch, M.; Lemmer, U. *J. Phys. Chem. C* **2015**, *119*, 13516-13523.
- Ashmore, A. D.; Finley, J. J.; Oulton, R.; Fry, P. W.; Lemaitre, A.; Mowbray, D. J.; Skolnick, M. S.; Hopkinson, M.; Buckle, P. D.; Maksym, P. A. *Physica E* **2002**, *13*, 127-130.
- Augustine, B. H.; Irene, E. A.; He, Y. J.; Price, K. J.; McNeil, L. E.; Christensen, K. N.; Maher, D. *M. J. Appl. Phys.* **1995**, *78*, 4020.
- Ball, P. *Nat. Mater.* **2005**, *4*, 119.

- Bansal, A.; Li, X.; Lauermann, I.; Lewis, N. S.; Yi, S. I.; Weinberg, W. H. *J. Am. Chem. Soc.* **1996**, *118*, 7225.
- Bawendi, M. C.; Steigerwald, M. L.; Brus, L. E. *Annual Review of Physical Chemistry* **1990**, *41*, 477.
- Barbaggiovanni, E. G.; Lockwood, D. J.; Simpson, P. J.; Goncharova, L. V. *Applied Physics Reviews* **2014**, *1*.
- Beard, M. C.; Knutsen, K. P.; Yu, P.; Luther, J. M.; Song, Q.; Metzger, W. K.; Ellingson, R. J.; Nozik, A. J.; *Nano Lett.* **2007**, *7(8)*, 2506-2512.
- Benson, S. W. *Thermodynamical Kinetics*, Wiley: New York, 1976.
- Berera, R.; Grondelle, R.; Kennis, J. T. M. *Photosynth Res.* **2009**, *101(2-3)*, 105-118.
- Betzig E.; Chichester R. J. *Science* **1993**, *262*, 1422.
- Betzig, E.; Trautman, J. K.; Harris, T. D.; Weiner, J. S.; Kostelak, R. L. *Science* **1991**, *251*, 1468.
- Betzig, E.; Lewis, A.; Harootunian, A.; Isaacson, M.; Kratschmer, E. *Biophys. J.* **1986**, *49*, 269.
- Biteen, J. S.; Lewis, N. S.; Atwater, H. A.; Polman, A. *Appl. Phys. Lett.* **2004**, *84*, 5389.
- Bouhelier, A.; Beversluis, M.; Hartschuh, A.; Novotny, L. *Phys. Rev. Lett.* **2003**, *90*, 013903.
- Boukherroub, R.; Wayner, D. D. M.; Lockwood D. J. *Appl. Phys. Lett.*, **2002**, *81*, 601.
- Boukherroub, R.; Morin, S.; Wayner, D. D. M.; Bensebaa, F.; Sproule, G. I.; Baribeau, J. M.; Lockwood, D. J. *Chem. Mater.* **2001**, *13*, 2002.
- Brus, L. *Nature* **1991**, *353*, 301.
- Brus, L. E. *J. Chem. Phys.* **1984**, *80*, 4403.
- Brus, L. E. *J. Chem. Phys.* **1983**, *79*, 5566.
- Buschmann, V.; Hempel, H.; Knigge, A.; Kraft, C.; Roczen, M.; Weyers, M.; Siebert, T.; Koberling, F. *Journal of Applied Spectroscopy* **2013**, *80(3)*, 449-457.
- Canham, L. T. *Nature* **2000**, *408*, 411-412.

- Canham, L. T. *Appl. Phys. Lett.* **1990**, *57*, 1046.
- Casey, H. C. Jr.; Sell, D. D.; Wecht, K. W. *Journal of Applied Physics* **1975**, *46*, 250.
- Cava, R. J. *Nature* **2006**, *444*, 427-428.
- Cheng, K. Y.; Anthony, R.; Kortshagen, U. R.; Holmes, R. J. *Nano Lett.* **2010**, *10*, 1154-1157.
- Cicero, R. L.; Linford, M. R.; Chidsey, C. E. D. *Langmuir* **2000**, *16*, 5688.
- Cocker, T. L.; Jelic, V.; Gupta, M.; Molesky, S. J.; Burgess, J. A. J.; De Los Reyes, G.; Titova, L. V.; Tsui, Y. Y.; Freeman, M. R.; Hegmann, F. A. *Nature Photonics* **2013**, *7*, 620-625.
- Collins, C.B.; Carlson R. O.; Gallagher, C. J. *Phys. Rev.* **1957**, *105*, 1168.
- Conibeer, G.; Green, M.; Corkish, R.; Cho, Y.; Cho, E. C.; Jiang, C. W.; Fangsuwannarak, T.; Pink, E.; Huang, Y.; Puzzer, T. *Thin Solid Films* **2006**, *511*, 654-662.
- Cooke, D. G.; MacDonald, A. N.; Hryciw, A.; Wang, J.; Meldrum, A.; Hegmann, F. A. *Phys. Rev. B* **2006**, *73*, 193311.
- Cooke, D. G.; Hegmann, F. A.; Young, E. C.; Tiedje, T. *Appl. Phys. Lett.* **2006**, *89*, 122103.
- Creazzo, T.; Redding, B.; Marchena, E.; Murakowski, J.; Prather, D. W. *J. Lumin.* **2010**, *130*, 631-636.
- Credo, G. M.; Mason, M. D.; Buratto, S. K. *Appl. Phys. Lett.* **1978**, *74*, 1999.
- Cullis, A. G.; Canham, L. T. *Nature* **1991**, *353*, 335-338.
- Dabbousi, B. O.; Rodriguez-Viejo, J.; Mikulec, F. V.; Heine, J. R.; Mattoussi, H.; Ober, R.; Jensen, K. F. Bawendi, M. G. *J. Phys. Chem. B* **1997**, *101*, 9463-9475.
- Dal Negro, L.; Yi, J. H.; Kimerling, K. *Appl. Phys. Lett.* **2006**, *88*, 183103.
- Dal Negro, L.; Cazzanelli, M.; Pavesi, L.; Ossicini, S.; Pacifici, D.; Franzo, G.; Priolo, F.; Iacona, F. *Appl. Phys. Lett.* **2003**, *82*, 4636.
- Danckwerts, M.; Novotny, L. *Phys. Rev. Lett.* **2007**, *98*, 026104.

- Dasog, M.; De los Reyes, G. B.; Titova, L. V.; Hegmann, F. A.; Veinot, J. G. C. *ACS Nano* **2014**, *8*(9), 9636.
- Dasog, M.; Yang, Z.; Regli, S.; Atkins, T. M.; Faramus, A.; Singh, M. P.; Muthuswamy, E.; Kaularich, S. M.; Tilley, R. D.; Veinot, J. G. C. *ACS Nano* **2013**, *7*, 2676-2685.
- de Boer, W. D. A. M.; Timmerman D.; Dohnalova K.; Yassievich, I. N.; Zhang H.; Buma, W. J.; Gregorkiewicz, T. *Nat. Nanotech.* **2010**, *5*, 878.
- Deibel, C.; Strobel, T.; Dyakonov, V. *Adv. Mater.* **2010**, *22*, 4097-4111.
- Delerue, C.; Allan, G.; Lannoo, M. *Phys. Rev. B* **1993**, *48*, 11024.
- de Mello Donega, C.; Hickey, S. G.; Wuister, S. F.; Vanmaekelbergh, D.; Meijerink, A. *J. Phys. Chem. B* **2003**, *107*, 489-496.
- Diamare, D.; Wojdak, M.; Lettieri, S.; Kenyon, A. J. *J. Lumin.* **2013**, *136*, 57-62.
- Dohnalová, K.; Gregorkiewicz, T.; Kůsová, K. *J. Phys.: Condens. Matter* **2014**, *26*, 173201.
- Dohnalová, K.; Poddubny, A. N.; Prokofiev, A. A.; de Boer, W. D. A. M.; Umesh, C. P.; Paulusse, J. M. J.; Zuilhof, H.; Gregorkiewicz, T. *Light. Sci. Appl.* **2013**, *2*, e47.
- Dohnalová, K.; Ondič, L.; Kůsová, K.; Pelant, I.; Rehspringer, J. L.; Mafouana, R.-R. *J. Appl. Phys.* **2010**, *107*, 053102.
- Dohnalová, K.; Kůsová, K.; Cibulka, O.; Ondič, L.; Pelant, I. *Physica Scripta* **2010**, *2010*, 014011.
- Dohnalová, K.; Židek, K.; Ondič, L.; Kůsová, K.; Cibulka, O.; Pelant, I. *J. Phys. D: Appl. Phys.* **2009**, *42*, 135102.
- Dokland, T.; Huttmacher, D. W.; Ng, M. M. L.; Schantz, J.-T. *Techniques in Microscopy for Biomedical Applications*. World Scientific publishing, Singapore, pp. 18.
- Dovrat, M.; Goshen, Y.; Jedrewski, J.; Balberg, I.; Sa'ar, A. *Phys. Rev. B* **2004**, *69*, 155311.
- Effenberger, F.; Götz, G.; Bidlingmaier, B.; Wezstein, M. *Angew. Chem. Int. Ed.* **1998**, *37*, 2462.
- Eisele, M.; Cocker, T. L.; Huber, M. A.; Plankl, M.; Viti, L.; Ercolani, D.; Sorba, L.; Vitiello, M. S.; Huber, R. *Nature Photonics* **2014**, *8*, 841-845.

- Ekimov, A. I.; Onushchenko, A. A. *JETP Lett.* **1981**, *34*, 345-349.
- English, D. S.; Pell, L. E.; Yu, Z.; Barbara, P. F.; Korgel, B. A. *Nano Lett.* **2002**, *2(7)*, 681-685.
- Erogbogbo, F.; Yong, K.-T.; Roy, I.; Xu, G.; Prasad, P. N.; Swihart, M. T. *ACS Nano* **2008**, *2*, 873-878.
- Fan, J. C.; Chen, C. H.; Chen, Y. F. *Appl. Phys. Lett.* **1998**, *72*, 1605.
- Fauchet, P. M. *J. Lumin.* **1996**, *70*, 294.
- Fisher, D. L.; Gamboa, A.; Harper, J.; Lauerhaas, J. M.; Sailor, M. J. *MRS Proceedings* **1994**, *358*, 507.
- Fleischhaker, R.; Krauß, N.; Schättiger, F.; Dekorsy, T. *Opt. Express* **2013**, *21(6)*, 6764-6776.
- Foreman, J.; Li, J.; Peng, H.; Choi, S.; Everitt, H.; Liu, J. *Nano Lett.* **2006**, *6*, 1126-1130.
- Fox, M. 2004. *Optical properties of solids*. Oxford University Press, New York.
- Franceschetti, A. and Zunger, A. *Phys. Rev. B.* **2000**, *62(4)*, 2614-2623.
- Francoeur, S.; Seong, M.-J.; Mascarenhas, A.; Tixier, S.; Adamcyk, M.; Tiedje, T. *Appl. Phys. Lett.* **2003**, *82*, 3874.
- Fujii, M.; Mimura, A.; Hayashi, S.; Yamamoto, Y.; Murakami, K. *Phys. Rev. Lett.* **2002**, *89*, 206805.
- Fujita S.; Sugiyama, N. *Appl. Phys. Lett.* **1999**, *74*, 308.
- Fukuda, M. 1999. *Optical Semiconductor Devices*. John Wiley and Sons, Canada.
- Fuzell, J.; Thibert, A.; Atkins, T. M.; Dasog, M.; Busby, E.; Veinot, J. G. C.; Kauzlarich, S. M.; Larsen, D. S. *J. Phys. Chem. Lett.* **2013**, *4*, 3806.
- Garcia, C.; Garrido, B.; Pellegrino, P.; Ferre, R.; Moreno, J. A.; Morante, J. R.; Pavesi, L.; Cazzanelli, M. *Appl. Phys. Lett.* **2003**, *82*, 1595.
- Gaponenko, S. V. 2003. *Optical Properties of Semiconductor Nanocrystals*. Cambridge University Press, p. 31.

- Garcia, C.; Garrido, B.; Pellegrino, P.; Ferre, R.; Moreno, J. A.; Pavesi, L.; Cazzanelli, M.; Morante J. R. *Physica E* **2003**, *16*, 429-433.
- Gfoerer, T. H.; Meyers, R. E. ed. 2000. *Photoluminescence in Analysis of Surfaces and Interfaces*. Encyclopedia of Analytical Chemistry, John Wiley and Sons Ltd., Chichester, pp. 9209-9231.
- Gole, J. L.; Dudel, F. P.; Grantier, D.; Dixon, D. A. *Phys. Rev. B* **1997**, *56*, 2137.
- Goller, B.; Polisski, S.; Wiggers, H.; Kovalev, D. *Appl. Phys. Lett.* **2010**, *97*, 041110.
- Gregor, M. J.; Blome, P. G.; Ulbrich, R. G.; Grossmann, P.; Grosse, S.; Feldmann, J.; Stolz, W.; Gobel, E. O.; Arent, D. J.; Bode, M.; Bertness, K. A.; Olson, J. M. *Appl. Phys. Lett.* **1995**, *67*, 3572.
- Gritsenko V. A. 1998. *Silicon Nitride in Electronic*. Elsevier: New York, pp 138-187.
- Grober, R. D.; Harris, T. D.; Trautman, J. K.; Betzig, E.; Wegscheider, W.; Pfeiffer, L. N.; West, K. W. *Appl. Phys. Lett.* **1994**, *64*, 1421.
- Grundmann, M. 2010. *The Physics of Semiconductors: An introduction including nanophysics and applications*. Springer Heidelberg Dordrecht, London, pp.33.
- Hall, R. N. *Phys. Rev.* **1952**, *87*, 387.
- Hamman, H. F.; Gallagher, A.; Nesbit, D. *J. Appl. Phys. Lett.* **2000**, *76*, 1953-1955.
- Hannah, D. C.; Yang, J.; Kramer, N. J.; Schatz, G. C.; Kortshagen, U. R.; Schaller, R. D. Reply to "Comment on 'Ultrafast Photoluminescence in Quantum-Confined Silicon Nanocrystals Arises from an Amorphous Surface Layer'". *ACS Photonics* **2015**, *2(3)*, 456-458.
- Hannah, D. C.; Yang, J.; Kramer, N. J.; Schatz, G. C.; Kortshagen, U. R.; Schaller, R. D. *ACS Photonics* **2014**, *1*, 960.
- Hao, J.-J.; Zhou, J.; Zhang, C.-Y. *Chem. Commun.* **2013**, *49*, 6346-6348.
- Hao, X. J.; Podhorodecki, A. P.; Shen, Y. S.; Zatoryb, G.; Misiewicz, J.; Green, M. A. *Nanotechnology* **2009**, *20*, 485703.

- Hao, X. J.; Cho, E.-C.; Flynn, C.; Shen, Y. S.; Conibeer, G.; Green, M. A. *Nanotechnology* **2008**, *19*, 424019.
- Hell, S. W. and Wichmann, J. *Optics Letters* **1994** *19*(11), 780-782.
- Harris, D. K.; Bawendi, M. G. *J. Am. Chem. Soc.* **2012**, *134*, 20211-20213.
- Hartschuh, A. *Angew. Chem. Int. Ed.* **2008**, *47*, 8178-8191.
- He, G. S.; Zheng, Q.; Yong, K.-T.; Erogbogbo, F.; Swihart, M. T.; Prasad, P. N. *Nano Lett.* **2008**, *8*, 2688.
- Hecht, B.; Sick, B.; Wild, U. P.; Deckert, V.; Zenobi, R.; Martin, O. J. F.; Pohl, D. W. *J. Appl. Phys.* **2000**, *112*(2), 7761-7774.
- Heitmann, J. J.; Müller, F.; Zacharias, M., Gösele, U. *Adv. Mater.* **2005**, *17*, 795-803.
- Hessel, C. M.; Reid, D.; Panthani, M. G.; Rasch, M. R.; Goodfellow, B. W.; Wei, J.; Fujii, H.; Akhavan, V.; Korgel, B. A. *Chem. Mater.* **2012**, *24*, 393-401.
- Hessel, C. M.; Reid, D.; Panthani, M. G.; Rasch, M. R.; Goodfellow, B. W.; Wei, J.; Fujii, H.; Akhavan, V.; Korgel, B. A. *Chem. Mater.* **2011**, *24*, 393.
- Hessel, C. M.; Henderson, E. J.; Kelly, J. A.; Cavell, R. G.; Sham, T.-K.; Veinot, J. G. C. *J. Phys. Chem. C.* **2008**, *112*, 14247.
- Hessel, C. M.; Henderson, E. J.; Veinot, J. G. C. *Chem. Mater.* **2006**, *18*, 6139-6146.
- Hiller, D.; Goetze, S.; Munnik, F.; Jivanescu, M.; Gerlach, J. W.; Vogt, J.; Pippel, E.; Zakharov, N.; Stesmans, A.; Zacharias, M. *Phys. Rev. B* **2010**, *82*, 195401.
- Hirschman, K. D.; Tsybeskov, L.; Duttagupta, S. P.; Fauchet, P. M. *Nature* **1996**, *384*, 338-341.
- Holman, Z. C.; Liu, C.-Y.; Kortshagen, U. R. *Nano Lett.* **2010**, *10*, 2661.
- Holmes, J. D.; Ziegler, K. J.; Doty, R. C.; Pell, L. E.; Johnston, K. P.; Korgel, B. A. *J. Am. Chem. Soc.* **2001**, *123*, 3743-3748.
- Hryciw, A.; Laforge, J.; Blois, C.; Glover, M.; Meldrum, A. *Adv. Mater.* **2005**, *17*(7), 845-849.

- Huang, R.; Lin, Z.; Guo, Y.; Song, C.; Wang, X.; Lin, H.; Xu, L.; Song, J.; Li, H. *Opt. Mater. Express* **2014**, *4*, 205.
- Huang, R.; Chen, K.; Qian, B.; Chen, S.; Li, W.; Xu, J.; Ma, Z.; Huang, X. *Appl. Phys. Lett.* **2006**, *89*, 221120.
- Iacona, F.; Pacifici, D.; Irrera, A.; Miritello, M.; Franzo, G.; Priolo, F.; Sanfilippo, D.; Di Stefano, G.; Fallica, P. G. *Appl. Phys. Lett.* **2002**, *81*, 3242.
- Irrera, A.; Pacifici, D.; Miritello, M.; Franzo, G.; Priolo, F.; Iacona, F.; Sanfilippo, D.; Di Stefano, G.; Fallica, P. G. *Appl. Phys. Lett.* **2002**, *81*, 1866.
- Jasinski, J. M.; Becerra, R.; Walsh, R. *Chem. Rev.* **1995**, *95*, 1203.
- Jung, S. W.; Park, W. I.; Cheong, H. D.; Yi, G.-C.; Jang, H. M. *Appl. Phys. Lett.* **2002**, *80*(11), 1924-1926.
- Jurbergs, D.; Rogojina, E.; Mangolini, L.; Kortshagen, U. *Appl. Phys. Lett.* **2006**, *88*, 233116.
- Kakalios, J.; Street, R. A.; Jackson, W. B. *Phys. Rev. Lett.* **1987**, *59*, 1037.
- Kanemitsu, Y. *J. Lumin.* **2002**, *100*, 209-217.
- Kanemitsu, Y. *Phys. Rev. B* **1994**, *49*, 16845.
- Kang, Z.; Liu, Y.; Tsang, C. H. A.; Ma, D. D. D.; Fan, X.; Wong, N.-B.; Lee, S.-T. *Adv. Mater.* **2009**, *21*, 661-664.
- Kagan, C. R.; Murray, C. B.; Nirmal, M.; Bawendi, M. G. *Phys. Rev. Lett.* **1996**, *76*, 1517-1520.
- Kaupp, G.; Herrmann, A. *J. Phys. Org. Chem.* **1997**, *10*, 675-679.
- Kelly, J. A.; Shukaliak, A. M.; Fleischauer, M. D.; Veinot, J. G. C. *J. Am. Chem. Soc.* **2011**, *133*, 9564.
- Kern, D. P.; Kuech, T. F.; Oprysko, M. M.; Wagner, A.; Eastman, D. E. *Science* **1988**, *241*, 936-944.
- Khriachtchev, L.; Rasanen, M.; Novikov, S.; Sinkkonen, J. *Appl. Phys. Lett.* **2001**, *79*, 1249.
- Kim, H.; Shin, D.-S.; Ryu, Y.; Shim, J. *Jpn. J. Appl. Phys.* **2010**, *49*, 112402.

- Kim, S.; Shin, D. H.; Choi, S.-H. *Appl. Phys. Lett.* **2012**, *100*, 253103.
- Kim, S.; Park, T. M.; Choi, S.-H.; Kim, K. J.; Choi, D. H. *J. Phys. D: Appl. Phys.* **2007**, *40*, 1339-1342.
- Kim, T.-Y.; Park, N.-M.; Kim, K.-H.; Sung, G. Y.; Ok, Y.-W.; Seong, T.-Y.; Choi, C.-J. *Appl. Phys. Lett.* **2004**, *85(22)*, 5355.
- Kittel, C. 2005. *Introduction to solid to physics*. John Wiley and Sons, U.S.A.
- Klimov, V. I.; Schwarz, Ch. J.; McBranch, D. W.; White, C. W. *Appl. Phys. Lett.* **1998**, *73*, 2603.
- Kocevski, V.; Eriksson, O.; Ruzs, J. *Phys. Rev. B* **2013**, *87*, 245401.
- Kontkiewicz, A. J.; Kontkiewicz, A. M.; Siejka, J.; Sen, S.; Nowak, G.; Hoff, A. M.; Sakthivel, P.; Ahmed, K.; Mukherjee, P.; Witanachchi, S.; Lagowski, J. *Appl. Phys. Lett.* **1994**, *65*, 1436.
- Korinek, M.; Kozak, M.; Trojanek, F.; Hiller, D.; Hartel, A.; Gutsch, S.; Zacharias, M. *Physics E* **2014**, *56*, 177-182.
- Koyama, H.; Matsushita Y.; Koshida, N. *J. Appl. Phys.* **1998**, *83*, 1776.
- Kovalev, D. I.; Yaroshetzki, I. D.; Muschik, T.; Petrova-Koch, V.; Koch, F. *Appl. Phys. Lett.* **1994**, *64*, 214.
- Kůsová, K.; Ondič, L.; Pelant, I. Comment on “Ultrafast Photoluminescence in Quantum-Confined Silicon Nanocrystals Arises from an Amorphous Surface Layer”. *ACS Photonics* **2015**, *2(3)*, 454-455.
- Kůsová, K.; Cibulka, O.; Dohnalová, K.; Pelant, I.; Valenta, J.; Fučíková, A.; Žídek, K.; Lang, J.; English, J.; Matějka, P.; Štěpánek, P.; Bakardjieva, S. *ACS Nano* **2010**, *4*, 4495.
- Kupchak, I. M.; Korbutyak, D. V.; Kryuchenko, Y. V.; Sachenko, A. V.; Sokolovskik, I. O.; Sreseli, O. M. *Semiconductor* **2006**, *40*, 94.
- Kutner, M. L. 2003. *Astronomy: A new perspective*. Cambridge University Press, New York, pp. 16.

- Laguitton-Pasquier, H.; Pansu, R.; Chauvet, J.-P.; Collet, A.; Faure, J.; Lapouyade, R. *Chemical Physics* **1996**, *212*, 437-455.
- La Rosa, A. H.; Yakobson, B. I.; Hallen, H. H. *Appl. Phys. Lett.* **1997**, *70*, 1656.
- Lauerhaas, J. M.; Credo, G. M.; Heinrich, J. L.; Sailor, M. J. *J. Am. Chem. Soc.* **1992**, *114*, 1911.
- Lechner, R.; Stegner, A. R.; Pereira, R. N.; Dietmueller, R.; Brandt, M. S.; Ebbers, A.; Trocha, M.; Wiggers, H.; Stutzmann, M. *J. Appl. Phys.* **2008**, *104*, 053701.
- Ledoux, G.; Gong, J.; Huisken, F.; Guillois, O.; Reynaud, C. *Appl. Phys. Lett.* **2002**, *80*, 4834.
- Ledoux, G.; Guillois, O.; Porterat, D.; Reynaud, C.; Huisken, F.; Kohn, B.; Paillard, V. *Phys. Rev. B* **2000**, *6*, 15942.
- Lee, M. K. and Peng, K. R. *Appl. Phys. Lett.* *1993*, *62*, 3159.
- Leong, J. K.; McMurray, J.; Williams, C. C.; Stringfellow, G. B. *J. Vac. Sci. Technol. B* **1996**, *14*, 3113.
- Levy, J.; Nikitin, V.; Kikkawa, J. M.; Awschalom, D. D.; Samarth, N. *J. Appl. Phys.* **1996**, *79*, 6095.
- Lewis, M. K.; Wolanin, P.; Gafni, A.; Steel, D. G. *Opt. Lett.* **1998**, *23(14)*, 1111-1114.
- Link, S.; and El-Sayed, M. A. *Annu. Rev. Phys. Chem.* **2003** *54*, 331.
- Link, S.; Burda, C.; Nikoobakht, B.; El-Sayed, M. A. *Chem. Phys. Lett.* **1999**, *315*, 12-18.
- Linnros, J.; Galeckas, A.; Lalic, N.; Grivickas, V. *Thin Solid Films* **1997**, *297*, 167-170.
- Lioudakis, E.; Othonos, A.; Nassiopoulou, A. G. *Appl. Phys. Lett.* **2007**, *90*, 171103.
- Lipson, M. *Journal of Lightwave Technology* **2005**, *23(12)*, 4222-4238.
- Littau, K. A.; Szajowski, P. J.; Muller, A. J.; Kortan, A. R.; Brus, L. E. *J. Phys. Chem.* **1993**, *97*, 1224.
- Liu, C.-Y.; Holman, Z. C.; Kortshagen, U. R. *Nano Lett.* **2008**, *9*, 449.
- Lockwood, R.; Meldrum, A. *Physica status solidi (a)* **2009**, *206*, 965.

- Lockwood, R.; Heyciw, A.; Meldrum, A. *Appl. Phys. Lett.* **2006**, *89*, 263112.
- Lockwood, D. J. *Solid State Commun.* **1994** *92*, 101.
- Loi, M. A.; Toffanin, S.; Muccini, M.; Forster, M.; Scherf, U.; Scharber, M. *Adv. Funct. Mater.* **2007**, *17*, 2111.
- López, J. A. L.; Román, A. G.; Barojas, E. G.; Gracia, J. F. F.; Juárez, J. M.; López, J. C. *Nanoscale Research Letters* **2014**, *9*, 571.
- Lu, X.; Beaton, D. A.; Lewis, R. B.; Tiedje, T.; Zhang, Y. *Appl. Phys. Lett.* **2009**, *95*, 041903.
- Luterova, K.; Pelant, I.; Mikulskas, I.; Tomasiunas, R.; Muller, D.; Grob, J.-J.; Rehspringer, J.-L.; Honerlage, B. *J. Appl. Phys.* **2002**, *91*, 2896.
- Ma, Y.; Chen, X.; Pi, X.; Yang, D. *J. Nanopart. Res.* **2012**, *14*, 802.
- Maier-Flaig, F.; Rinck, J.; Stephan, M.; Bocksrocker, T.; Bruns, M.; Kübel, C.; Powell, A. K.; Ozin, G. A.; Lemmer, U. *Nano Lett.* **2013**, *13*, 475-480.
- Mashford, B. S.; Stevenson, M.; Popovic, Z.; Hamilton, C.; Zhou, Z.; Breen, C.; Steckel, J.; Bulovic, V.; Bawendi, M.; Coe-Sullivan, S. *Nat. Photon.* **2013**, *7*, 407-412.
- Mason, M. D.; Credo, G. M.; Weston, K. D.; Buratto, S. K. *Phys. Rev. Lett.* **1998**, *80*, 5405.
- Mastronardi, M. L.; Maier-Flaig, F.; Faulkner, D.; Henderson, E. J.; Kübel, C.; Lemmer, U.; Ozin, G. A. *Nano Lett.* **2011**, *12*, 337-342.
- McNeill, C. R.; Frohne, H.; Holdsworth, J. L.; Furst, J. E.; King, B. V.; Dastoor, P. C. *Nano Lett.* **2004**, *4(2)*, 219-223.
- Meldrum, A.; Hryciw, A.; Macdonald, A. N.; Blois, C.; Marsh, K.; Wang, J.; Quan, L. *J. Vac. Sci. Technol. A* **2006**, *24*, 713.
- Meldrum, A.; Buchanan, K. S.; Hryciw, A.; White, C. W. *Adv. Mater.* **2004**, *16(1)*, 31-34.
- Metzger, W. K.; Ahrenkiel, R. K.; Dippo, P.; Geisz, J.; Wanlass, M. W.; Kurtz, S. **2006** Conference Paper NREL/CP-52037028.

- Mi, Z.; Chang, Y. -L. *J. Nanophoton.* **2009**, *3*, 031602.
- Miller, J. B.; Van Sickle, A. R.; Anthony, R. J.; Kroll, D. M.; Kortshagen, U. R.; Hobbie E. K. *ACS Nano* **2012**, *6(8)*, 7389-7396.
- Mimura, A.; Fujii, M.; Hayashi, S.; Kovalev, D.; Koch, F. *Phys. Rev. B: Condens. Matter Mater. Phys.* **2000**, *62*, 12625.
- Minh, P. N.; Ono, T.; Esashi, M. *Rev. Sci. Ins.* **2000**, *71(8)*, 3111-3117.
- Mizuno, H.; Koyama, H.; Koshida, N. *Appl. Phys. Lett.* **1996**, *69*, 3779.
- Moskalenko, A.; Berakdar, J.; Prokofiev, A.; Yassievich, I. *Phys. Rev. B* **2007**, *76*, 085427.
- Muraoka, T.; Abe, K.; Haga, Y.; Nakamura, T.; Ueno, K. *J. Am. Chem. Soc.* **2011**, *133*, 15365.
- Nayfeh, M. H.; Barry, N.; Therrien, J.; Akcakir, O.; Gratton, E.; Belomoin, G. *Appl. Phys. Lett.* **2001**, *78*, 1131.
- Nechay, B.; Siegner, U.; Achermann, M.; Biedefelt, H.; Keller, U. *Rev. of Sci. Instru.* **1999**, *70*, 2758.
- Nejo, H. ed. 2003. *Nanoelectrodynamics: Electrons and Electromagnetic Fields in Nanometer-scale structures*. Springer Verlag Berlin Heidelberg.
- Nemanick, E. J.; Hurley, P. T.; Brunshwig, B. S.; Lewis, N. S. *J. Phys. Chem. B* **2006**, *110*, 14800.
- Nguyen, A. Q. *Adv. Nat. Sci.: Nanosci. Nanotechnol.* **2010**, *1*, 025004.
- Niquet, Y. M.; Delerue, C.; Allan, G.; Lanoo, M. *Phys. Rev. B.* **2000**, *62*, 5109.
- Ostraat, M. L.; De Blauwe, J. W.; Green, M. L.; Bell, L. D., Brongersma, M. L.; Casperson, J.; Flagan, R. C.; Atwater, H. A. *Appl. Phys. Lett.* **2001**, *79*, 433.
- Othonos, A.; Lioudakis, E.; Nasiopoulou, A. G. *Nano Res. Lett.* **2008**, *3*, 315-320.
- Park, J.-H.; Gu, L.; von Maltzahn, G.; Ruoslahti, E.; Bhatia, S. N.; Sailor, M. J. *Nat. Mater.* **2009**, *8*, 331.
- Pavesi, L.; Gaponenko, S.; Dal Negro, L. eds. 2012. *Towards the First Silicon Laser*. Springer Science & Business Media.

- Pavesi, L.; Lockwood, D. J. eds. 2004. *Silicon Photonics. Vol. 1*, Springer-Verlag Berlin Heidelberg, p. 177.
- Pavesi, L. *J. Phys.: Condens. Matter* **2003**, *15*, R1169-R1196.
- Pavesi, L.; Dal Negro, L.; Mazzoleni, C.; Franzo, G.; Priolo, F. *Nature (London)* **2000**, *408*, 440.
- Peng, X. S.; Wang, X. F.; Zhang, J. Y.; Wang, W.; Sun, S. H.; Meng, G. W.; Zhang, L. D. *Appl. Phys. A* **2002**, *74*, 1-3.
- Photopoulos P.; Nassiopoulou, A. G. *Appl. Phys. Lett.* **2000**, *77*, 1816.
- Pi, X. *J. Nanomater.* **2012**, *2012*, 912903.
- Pi, X.; Chen, X.; Ma, Y.; Yang, D. *Nanoscale* **2011**, *3*, 4584-4588.
- Pi, X. D.; Liptak, R. W.; Nowak, J. D.; Wells, N. P.; Carter, C. B.; Campbell, S. A.; Kortshagen, U. *Nanotechnology* **2008**, *19*, 245603.
- PicoHarp 300: Manual Ver. 2.3. *Time-Correlated Single Photon counting systems with USB interface*. PicoQuant, Unternehmen für optoelektronische Forschung und Entwicklung.
- Pola, J.; Galíková, A.; Bastl, Z.; Šubrt, J.; Vacek, K.; Brus, J.; Ouchi, A. *Appl. Organometal. Chem.* **2006**, *20*, 648-655.
- Pradhan, S.; Chen, S.; Zou, J.; Kauzlarich, S. M. *J. Phys. Chem. C* **2008**, *112*, 13292-13298.
- Prasankumar, R. P. and Taylor, A. J. ed. 2012. *Optical techniques for solid-state materials characterization*. CRC Press, Boca Raton.
- Puzder, A.; Williamson, A. J.; Grossman, J. C.; Galli, G. *J. Chem. Phys.* **2002**, *117*, 6721.
- Qin, G. G.; Liu, X. S.; Ma, S. Y.; Lin, J.; Yao, G. Q.; Lin, X. Y.; Lin, K. X. *Phys. Rev. B* **1997**, *55(19)*, 12867.
- Qiu, T.; Wu, X. L.; Xie, Y. T.; Mei, Y. F.; Siu, G. G. Chu, P. K. *Nanotechnology* **2005**, *16*, 2222-2226.
- Ramakrishna, G.; Ghosh, H. N. *J. Phys. Chem. B* **2001**, *105*, 7000-7008.

- Raymond, J. E.; Goodson, T. *J. Phys. Chem. Lett.* **2011**, *2*, 329-333.
- Redfield, D.; Bube, R. H. 1996. *Photoinduced Defects in Semiconductors*. Cambridge University Press, Cambridge.
- Reimann, S. M.; Manninen, M. *Reviews of Modern Physics* **2002**, *74*(4), 1283.
- Rittweger, E.; Han, K. Y.; Irvine, S. E.; Eggeling, C.; Hell, S. W. *Nature Photonics* **2009**, *3*, 144-147.
- Rodriguez, R.; Gau, D.; Troadec, T.; Saffon-Merceron, N.; Branchadell, V.; Baceiredo, A.; Kato, T. *Angewandte Chemie* **2013**, *125*, 9150.
- Rodríguez-Núñez, J. R.; Kelly, J. A.; Henderson, E. J.; Veinot, J. G. C. *Chem. Mater.* **2012**, *24*, 346-52.
- Robertson, J. *Phys. Rev. B* **1996**, *53*, 16302.
- Rosso-Vasic, M.; Spruijt, E.; Popovic, Z.; Overgaag, K.; van Lagen, B.; Grandidier, B.; Vanmaekelbergh, D.; Dominguez-Gutierrez, D.; De Cola, L.; Zuillhof, H. *J. Mater. Chem.* **2009**, *19*, 5926.
- Sa'ar, A.; Reichman, Y.; Dovrat, M.; Krapf, D.; Jedrzejewski, J.; Balberg, I. *Nano Lett.* **2005**, *5*, 2443.
- Sailor, M. J.; Lee, E. J. *Adv. Mater.* **1997**, *9*, 783.
- Sankaran, R. M.; Holunga, D.; Flagan, R. C.; Giapis, K. P. *Nano Lett.* **2005**, *5*, 537.
- Sato, K.; Niino, K.; Fukata, N.; Hirakuri, K.; Yamauchi, Y. *Nanotechnology* **2009**, *20*, 365207.
- Schaller, R. D.; Sykora, M.; Jeong, S.; Klimov, V. I. *J. Phys. Chem B* **2006**, *110*, 25332-25338.
- Schols, S. 2011. *Device Architecture and Materials for Organic light emitting devices: Targeting High current densities and control of the Triplet concentration*. Springer Dordrecht Heidelberg London New York.
- Schonbrun, E.; Tinker, M.; Park, W.; Lee, J.-B. *IEEE Photonics Technology Letters* **2005**, *17*(6), 1196-1198.

- Seo, J.; Kim, S.; Park, S. Y. *J. Am. Chem. Soc.* **2004**, *126*, 11154-11155.
- Sevik, C.; Bulutay, C. *Phys. Rev. B* **2008**, *77*, 125414.
- Sham, T. K. ; Jiang, D. T.; Coulthard, I.; Lorimer, J. W.; Feng, X. H.; Tan, K. H.; Frigo S. P.; Rosenberg, R. A.; Houghton, D. C.; Bryskiewicz, B. *Nature* **1993**, *363*, 331-334.
- Shiohara, A.; Prabakar, S.; Faramus, A.; Hsu, C.-Y.; Lai, P.-S.; Northcote; P.T.; Tilley, R. D. *Nanoscale* **2011**, *3*, 3364-3370.
- Shiohara, A.; Hanada, S.; Prabakar, S.; Fujioka, K.; Lim, T. H.; Yamamoto, K.; Northcote, P. T.; Tilley, R. D. *J. Am. Chem. Soc.* **2010** *132*, 248-253.
- Shockley, W. and Read, W. T. Jr. *Phys. Rev.* **1952** *87*, 835.
- Sieval, A. B.; van den Hout, B.; Zuilhof, H.; Sudhölter, E. J. R. *Langmuir* **2001**, *17*, 2172.
- Sieval, A. B.; van den Hout, B.; Zuilhof, H.; Sudhölter, E. J. R. *Langmuir* **2000**, *16*, 2987.
- Spencer, M. 1982. *Fundamentals of Light Microscopy*. Cambridge University Press, Oxford, pp. 21.
- Stradling, R. A., Klippstein, P. C. 1990. *Growth and characterization of semiconductors*. Bristol, p. 135.
- Sun, Q.-Y.; de Smet, L. C. P. M.; van Lagen, B.; Giesbers, M.; Thüne, P. C.; van Engelenburg, J.; de Wolf, F. A.; Zuilhof, H.; Sudhölter, E. J. R. *J. Am. Chem. Soc.* **2005**, *127*, 2514.
- Sung, K.; Yong Min, P.; Suk-Ho, C.; Kyung Joong, K.; Dong Hoon, C. *J. Phys. D: Appl. Phys.* **2007**, *40*, 1339.
- Sychugov, I.; Fucikova, A.; Pevere, F.; Yang, Z.; Veinot, J. G. C.; Linnros, J. *ACS Photonics* **2014**, *1*, 998.
- Sychugov, I.; Valenta, J.; Mitsuishi, K.; Fujii, M.; Linnros, J. *Phys. Rev. B* **2011**, *84*, 125326.
- Sykora, M.; Mangolini, L.; Schaller, R. D.; Kortshagen, U.; Jurbergs, D.; Klimov, V. I. *Phys. Rev. Lett.* **2008**, *100*, 067401.
- Synge, E. H. *Philosophical Magazine* **1928**, *6*, 356-362.

- Szymanski, C.; Wu, C.; Hooper, J.; Salazar, M. A.; Perdomo, A.; Dukes, A.; McNeill, J. *J. Phys. Chem. B* **2005**, *109*, 8543-8546.
- Tessler, L. R.; Alvarez, F.; Teschke, O. *Appl. Phys. Lett.* **1993**, *62*, 2381.
- Tewary, A.; Kekatpure, D.; Brongersma, M. L. *Appl. Phys. Lett.* **2006**, *88*, 093114.
- Timmerman, D.; Gregorkiewicz, T. *Nanoscale Research Letters* **2012**, *7*, 389.
- Titova, L.V.; Cocker, T.L.; Wang, X.; Meldrum, A.; Hegmann, F. A. *ECS Transactions* **2012**, *45(5)*, 21-29.
- Titova, L.V.; Cocker, T.L.; Cooke, D.G.; Wang, X.; Meldrum, A.; Hegmann, F. A. *Phys. Rev. B* **2011**, *83*, 085403.
- Trinh, M. T.; Limpens, R.; de Boer, W.D.A.M.; Schins, J. M.; Siebbeles, L. D. A.; Gregorkiewicz, T. *Nature Photon.* **2012**, *6*, 316-321.
- Trojaneck, F.; Neudert, K.; Maly, P.; Dohnalova, K.; Pelant, I. *J. Appl. Phys.* **2006**, *99*, 116108.
- Trojaneck, F.; Neudert, K.; Bittner, M.; Maly, P. *Phys. Rev. B* **2005**, *72*, 075365.
- Tsybeskov, L.; Vandyshev, J. V.; Fauchet, P. M. *Phys. Rev. B* **1994**, *49*, 7821-7824.
- Valenta, J.; Fucikova, A.; Vácha, F.; Adamec, F.; Humpolíčková, J.; Hof, M.; Pelant, I.; Kůsová, K.; Dohnalová, K.; Linnros, J. *Adv. Funct. Mater.* **2008**, *18*, 2666.
- Valenta, J.; Fucikova, A.; Pelant, I.; Kůsová, K.; Dohnalová, K.; Aleknavičius, A.; Cibulka, O.; Fojtík, A.; Kada, G. *New J. Phys.* **2008**, *10*, 073022.
- Veldman, D.; Ipek, Ö.; Meskers, S. C. J.; Sweelssen, J.; Koetse, M. M.; Veenstra, S. C.; Kron, J. M.; van Bavel, S. S.; Loos, J.; Janssen, R. A. J. *J. Am. Chem. Soc.* **2008**, *130*, 7721.
- Vinciguerra, V.; Franzò, G.; Priolo, F.; Iacona, F.; Spinella, C. *J. Appl. Phys.* **2000**, *87*, 8165.
- Vivien, L. and Pavesi, L. 2013. *Handbook of Silicon Photonics*, Taylor & Francis.
- Von Behren, J.; Wolkin-Vakrat, M.; Jomé, J. *Journal of Porous Materials* **2000**, *7(1-3)*, 81-84.
- Voos, M.; Uzan, P.; Delalande, C.; Bastard, G.; Halimaoui, A. *Appl. Phys. Lett.* **1992**, *61*, 1213.

- Wagner, P.; Brohl, M.; Gräf, D.; Lambert, U. *MRS Proceedings* **1995**, 378.
- Wallart, X.; Henry de Villeneuve, C.; Allongue, P. *J. Am. Chem. Soc.* **2005**, 127, 7871.
- Walters, R. J. 2007. *Silicon nanocrystals for silicon photonics*. (Dissertation (Ph.D.), California Institute of Technology),
- Wang, L.; Li, Q.; Wang, H.-Y.; Huang, J.-C.; Zhang, R.; Chen, Q.-D.; Xu, H.-L.; Han, W.; Shao, Z.-Z.; sun, H.-B. *Light Science and Applications* **2014**, 4, e245.
- Wang, M.; Anopchenko, A.; Marconi, A.; Moser, E.; Prezioso, S.; Pavese, L.; Pucker, G.; Bellutti, P.; Vanzetti, L. *Physica E* **2009**, 41, 912.
- Wang, J.; Wang, X. F.; Li, Q.; Hryciw, A.; Meldrum, A. (2007) *Philosophical Magazine*, 87, 11.
- Warner, J. H.; Rubinsztein-Dunlop, H.; Tilley, R. D. *J. Phys. Chem. B* **2005**, 109, 19064.
- Wen, X.; Dao, L. P.; Hannaford P.; Cho, E.-C.; Cho, Y. H.; Green, M. A. *New Journal of Physics* **2007**, 9, 337.
- Wilcoxon, J. P.; Samara, G. A.; Provencio, P. N. *Phys. Rev. B* **1999**, 60, 2704.
- Wilcoxon, J. P.; Samara, G. A. *Appl. Phys. Lett.* **1999**, 74, 3164.
- Willig, K. I.; Rizzoli, S. O.; Westphal, V.; Jahn, R.; Hell, S. W. *Nature* **2006**, 440, 935-939.
- Wolf, O.; Dasog, M.; Yang, Z.; Balberg, I.; Veinot, J. G. C.; Millo, O. *Nano Lett.* **2013**, 13, 2516-2521.
- Wolkin, M. V.; Jorne, J.; Fauchet, P. M.; Allan, G.; Delerue, C. *Phys. Rev. Lett.* **1999**, 82, 197-200.
- Wu, X. L.; Siu, G. G.; Tong, S.; Liu, X. N.; Yan, F.; Jiang, S. S.; Zhang, X. K.; Feng, D. *Appl. Phys. Lett.* **1996**, 69, 523.
- Xiong, Y.; Yao, S.; Müller, R.; Kaupp, M.; Driess, M. *Nat Chem* **2010**, 2, 577.
- Xiong, Y.; Yao, S.; Driess, M. *J. Am. Chem. Soc.* **2009**, 131, 7562.
- Xu, S. J. and Chua, S. J. *Appl. Phys. Lett.* **1998**, 73(4), 478.

- Yang, Z.; de los Reyes, G. B.; Titova, L. V.; Sychugov, I.; Dasog, M.; Linnros, J.; Hegmann, F. A.; Veinot, J. G. C. *ACS Photonics* **2015**, *2*(5), 595-605.
- Yang, Z.; Iqbal, M.; Dobbie, A. R.; Veinot, J. G. C. *J. Am. Chem. Soc.* **2013**, *135*, 17595.
- Yang, S.; Li, W.; Cao, B.; Zeng, H.; Cai, W. *J. Phys. Chem. C* **2011**, *115*, 21056-21062.
- Yarotski, D.; Taylor, A. *Annu. Rev. Biomed. Eng.* **2000**, *2*, 399-429.
- Yates, J. T. Jr. *Science* **1998**, *279*, 335-336.
- Yoffe, A. D. *Advances in Physics* **2001**, *50*(1), 1.
- Zacharias, M.; Heitmann, J.; Scholz, R.; Kahler, U.; Schmidt, M.; Bläsing, J. *Appl. Phys. Lett.* **2002**, *80*, 661.
- Zayats, A. V.; Smolyaninov, I. I. *Philos. Trans. R. Soc. London Ser. A* **2004**, *362*, 843-860.
- Zhang, Q.; Bayliss, S. C.; Hutt, D. A. *Applied Physics Letters* **1995**, *66*, 1977.
- Žídek, K.; Pelant, I.; Trojánek, F.; Malý, P.; Gilliot, P.; Hönerlage, B.; Oberlé, J.; Šiller, L.; Little, R.; Horrocks, B. R. *Phys. Rev. B* **2011**, *84*, 085321.
- Žídek, K.; Trojánek, F.; Malý, P.; Ondič, L.; Pelant, I.; Dohnalová, K.; Šiller, L.; Little, R.; Horrocks, B. R. *Opt. Exp.* **2010**, *18*, 25241.
- Zhou, Z.; Brus, L.; Friesner, R. *Nano Lett.* **2003**, *3*, 163.

APPENDIX A

Microsecond-photoluminescence lifetime of dodecyl functionalized silicon nanocrystals

This appendix provides details of the spectrally-resolved μs -PL lifetime components of dodecyl functionalized Si NCs prepared using thermal and photochemical hydrosilylation.

Figures A1 and A2 show the spectrally-resolved μs -PL lifetime components of dodecyl functionalized Si NCs prepared using thermal and photochemical hydrosilylation, respectively. The emission wavelength was chosen using bandpass filters with 10 nm bandwidth. For both hydrosilylation methods, the PL lifetime and the dispersion factor β do not follow a clear trend. However, for the same emission wavelength, the 5-nm samples exhibit higher μs -PL lifetime component than their corresponding 3-nm samples. The origin of this behavior is still unclear but might be associated with the stress induced by ligand passivation and/or surface oxidation.

Photochemically-functionalized Si NCs exhibit an initial resolution-limited fast decay that is strongly wavelength-dependent, as shown in Fig. A.2. Significant contribution of this fast PL is observed in the PL lifetime for 780 nm. This observation supports the hypothesis that oxygen-induced-defect quenching is more likely observed in larger Si NCs. This observation is discussed in detail in Chapter 4. In the case of the 3-nm photochemically-functionalized Si NCs, the fast component is not observed probably because a fast oxygen-defect related emission is only significant

at wavelengths closer to the peak emission which is 638 nm.

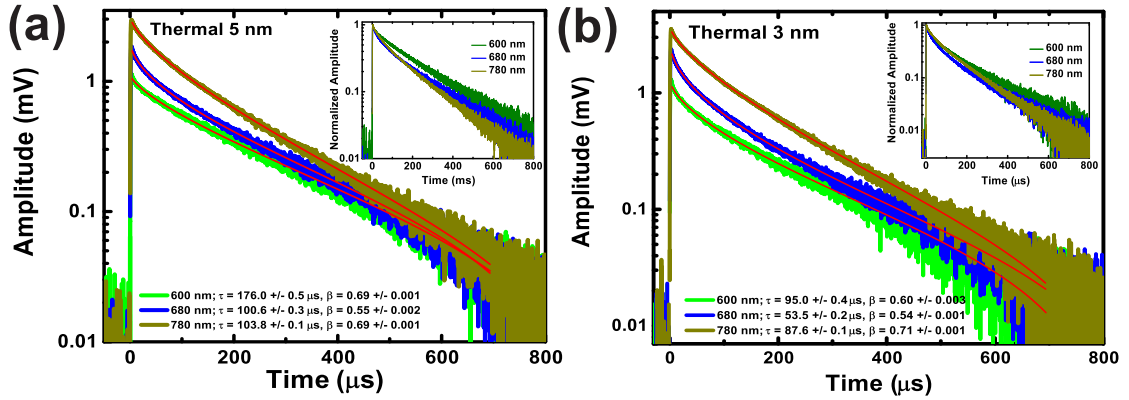


Figure A.1: Spectrally-resolved μ s-PL lifetimes of (a) 5 nm and (b) 3 nm thermally-functionalized Si NCs. The red lines are the stretched exponential fit to the data. Inset figures are the normalized PL lifetimes.

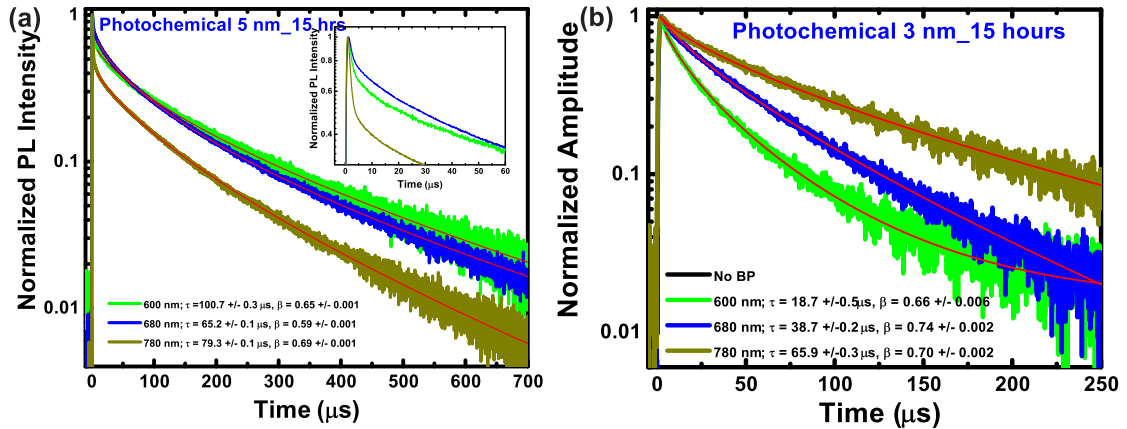


Figure A.2: Spectrally-resolved μ s-PL lifetimes of (a) 5 nm and (b) 3 nm photochemically-functionalized Si NCs. The red lines are the stretched exponential fit to the data. Inset figures are the normalized PL lifetimes.

APPENDIX B

Time-resolved photoluminescence of functionalized silicon nanocrystal films

This appendix provides the initial results of the comparison of the dynamics of colloidal Si NCs in solution and in films. Two types of films were made from the original solution. The first film was simply dropcast on a quartz glass slide and was allowed to dry at room temperature. The second film was made by continuously irradiating the solution of the acetal functionalized Si NCs in a 1-cm quartz vial using 267 nm pulsed laser. A yellowish film was deposited on the inside of the vial that was in front of the incident beam. The 267 nm pulsed laser was not focused on the inside of the vial to avoid any possible damage on the vial. During the characterization of the UV deposited films, the solution was removed to make sure that the measured PL originated from the films.

B.1 Acetal functionalized Si NCs

Figure B.1 shows the comparison of the emission properties of acetal functionalized Si NCs in solution and in films. The acetal functionalized Si NC films exhibit red-shifted PL emission (peak emission is ~ 518 nm for the dropcast film and ~ 560 nm for the UV deposited film) compared to the original solution (peak emission is ~ 478 nm), as shown in Fig. B.1(a). The UV deposited films exhibit the lowest PL peak emission of 560 nm. In addition, the FWHM of the PL spectrum from the films are

much wider than the solution. The observed PL red-shift in the dropcast films is possibly due to surface oxidation as it was allowed to dry in air environment. In the case of the UV deposited films, the PL red-shift is possibly due to the breaking of the Si-C surface bonds which has a dissociation energy of ~ 370 kJ/mol (Pola *et al.* 2006, Jasinski *et al.* 1995, Benson 1976) during the UV irradiation which led to a possible formation of Si-O bond. The Si-O forms a stronger bond (dissociation energy of 809 KJ/mol) (Pola *et al.* 2006, Jasinski *et al.* 1995, Benson 1976) which is much higher than the corresponding 267 nm irradiation energy (~ 448 kJ/mol).

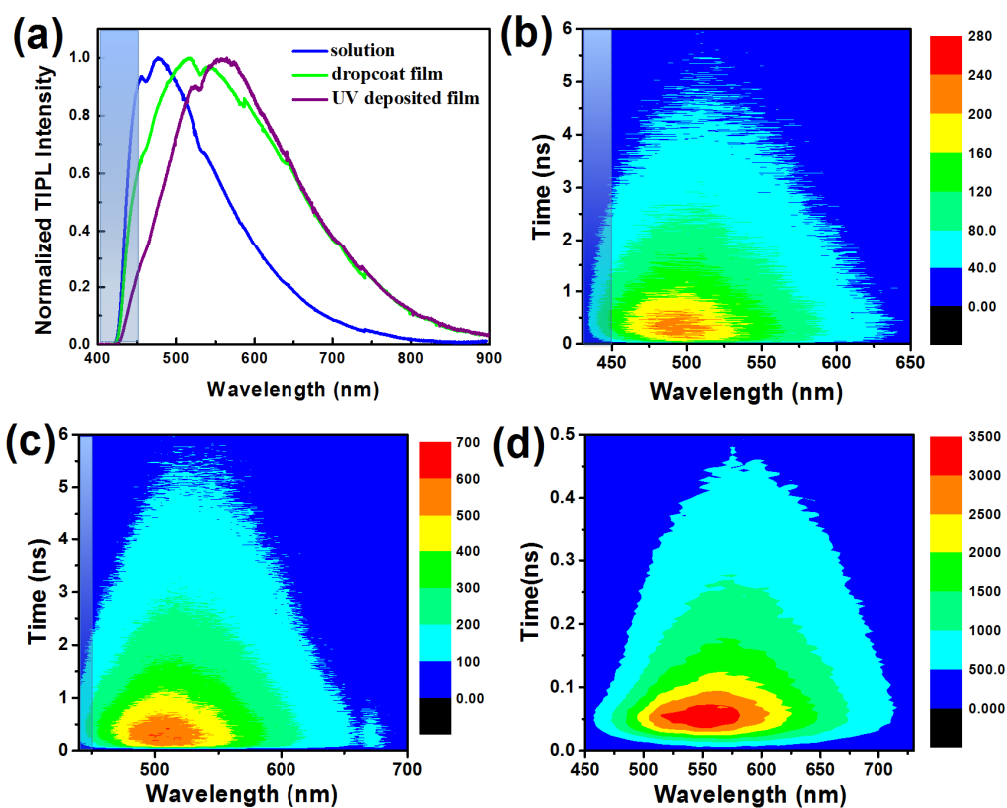


Figure B.1: Comparison of the emission properties of acetal functionalized Si NCs in solution and in films. (a) Time-integrated PL and (b-d) time-resolved PL of acetal functionalized Si NCs in solution (b), in films dropcoated on a quartz glass slide (c), and deposited by UV irradiation using 267 nm pulsed laser (d).

B.2 Dodecylamine functionalized Si NCs

Figure B.1 shows the comparison of the PL properties of dodecylamine functionalized Si NCs in solution and in films. The TIPL measurements of the samples show that the UV deposited dodecylamine functionalized Si NC films exhibit red-shifted PL spectrum compared to the dropcast film and Si NCs in solution. Detailed TRPL studies in ns time scale of the dodecylamine functionalized Si NCs in solution and in films also indicate a significant change in the PL emission dynamics, as shown in Fig. B.1(b), B.1(c), and B.1(d). From the contour plots of the PL intensity as a function of wavelength and time after photoexcitation, the UV deposited films exhibit the fastest radiative recombination process of less than 1 ns. On the other hand, the recombination time of the dropcast film is slightly longer than the solution. These results support the hypothesis of the possible change in the surface bonds of the deposited films.

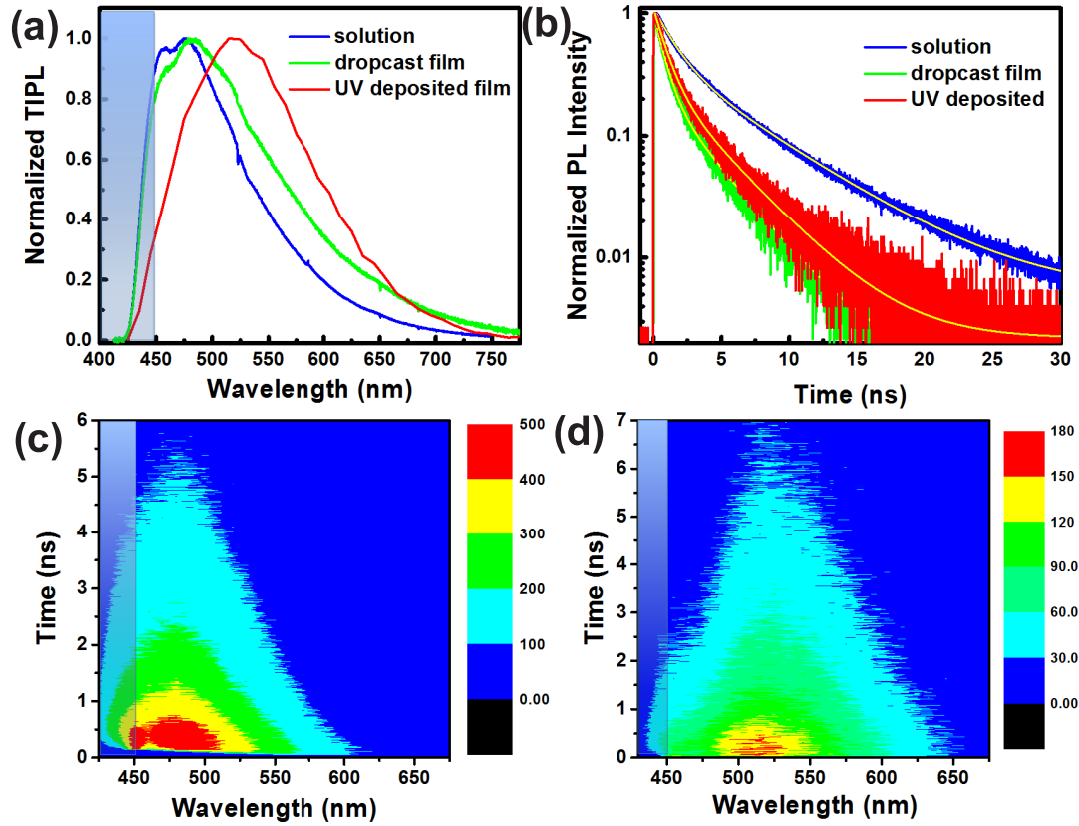


Figure B.2: Comparison of the emission properties of dodecylamine functionalized Si NCs in solution and in films. (a) Time-integrated PL, (b) PL lifetime measured at 505 nm, and detailed TRPL of (c) solution and (d) film deposited by UV irradiation using 267 nm pulsed laser. The red curves in (b) is the bi-exponential fit to the data.

APPENDIX C

Thickness dependence transient absorption measurements of Si NC films with different filling fractions

This appendix provides details of the effect of the film thickness on the transient photoinduced absorption (TPA) dynamics of Si NC films with Si volume filling fraction of $\rho = 16\%$ and (b) 51% .

The TPA dynamics of Si NC films with Si volume filling fraction of $\rho = 16\%$ and (b) 51% are shown in Figs. C1(a) and C1(b), respectively. The thickness was varied from 100 nm to 1000 nm. Figure C1(a) shows that for $\rho = 16\%$, the lifetime and the dispersion factor β increases as the thickness increases. On the other hand, due to the poor quality of the signal for 100-nm film, fitting cannot be done. However, it is clear from the plot that it has the fast lifetime decay.

The TPA dynamics for Si NC films with Si filling fraction of $\rho = 51\%$ is shown in Fig. C1(b). The TPA signals exhibit a weird decay profile for film thickness of 100 nm and 1000 nm while the decays go beyond zero (negative) for 200 nm and 500 nm. This observed behavior is possibly due to multiple beam interference of the 800 nm probe in this Si NC films. This hypothesis is supported by the UV-VIS absorption of the Si NC films, shown in Fig. C2.

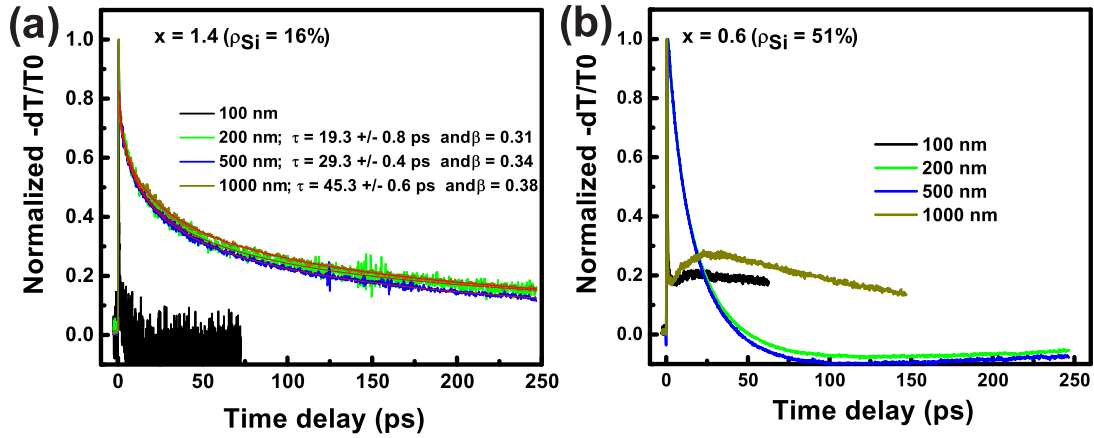


Figure C.1: Thickness dependence transient photoinduced absorption of Si NC films with filling fractions of $\rho = 16\%$ and (b) 51% . The red curves in (a) are the stretched exponential fit to the data.

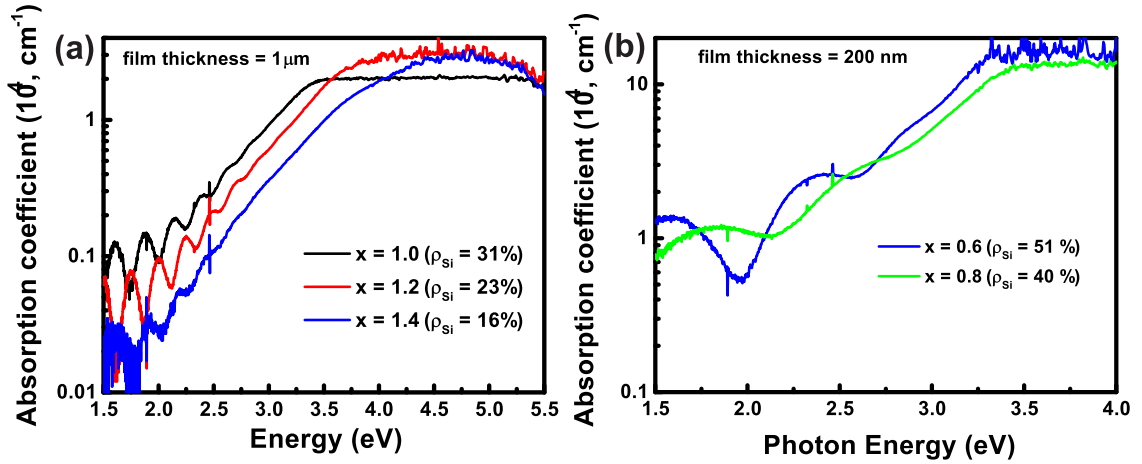


Figure C.2: UV-Vis absorption of Si NC films with different Si volume filling fractions and thicknesses. (a) has a film thickness of $1 \mu\text{m}$ and (b) 200 nm . The oscillations observed at lower energy is due to multiple beam interference.

APPENDIX D

Comparison of the different fitting functions

This appendix provides detail analysis of the different fitting functions that were tested in describing the PL lifetimes of the functionalized Si NCs. Three different functions were tested for describing the μ s- and ns-PL lifetime components of the Si NCs, namely, single exponential, bi-exponential, and stretched exponential.

Figure D1(a) shows the PL lifetime of the 5 nm photochemically-functionalized Si NCs together with the stretched exponential, bi-exponential and single exponential fits. As shown in the plot, the stretched and bi-exponential fits both accurately describe the behavior of the lifetime while the single exponential results in a poor fitting on the data. In addition, there is no significant difference in the reduced R^2 and χ^2 values for the stretched and bi-exponential fits. However, comparing the residual plots, the stretched exponential fit describes the behavior of the plot more accurate than the bi-exponential.

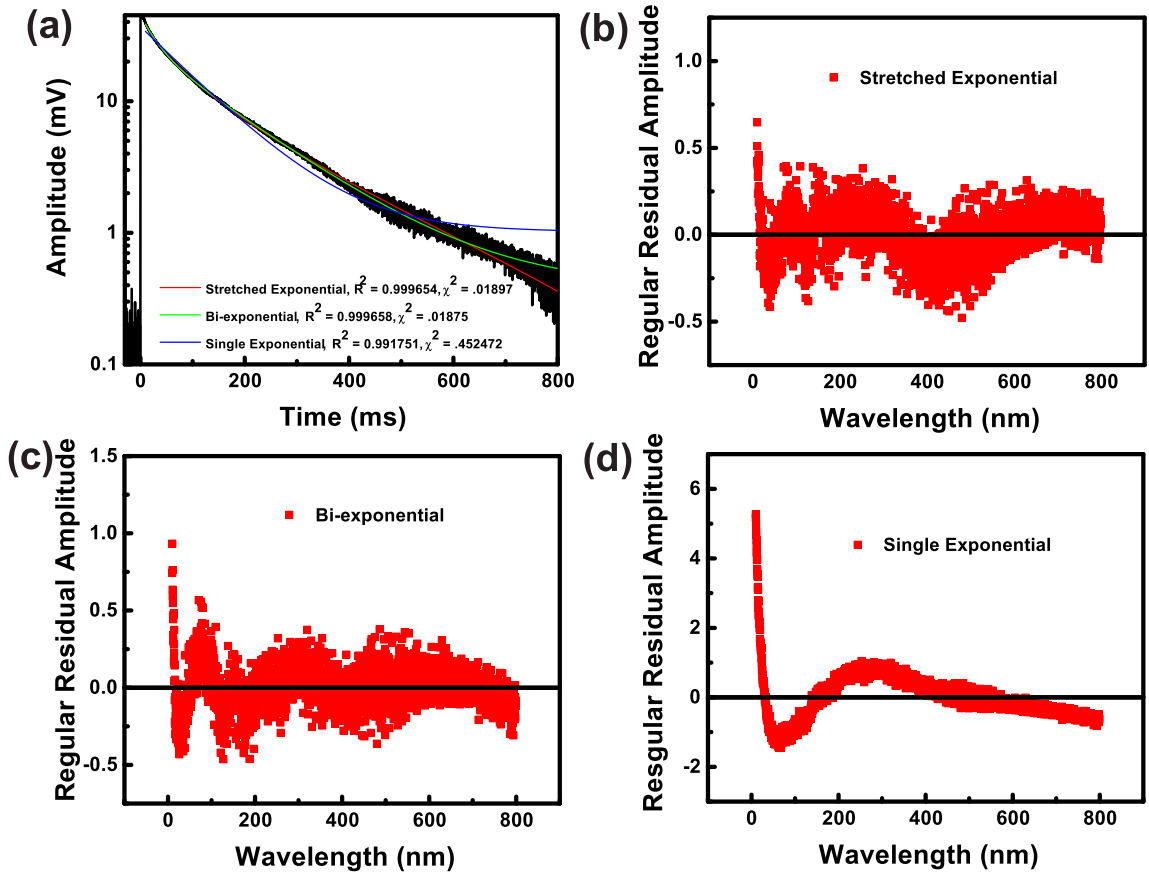


Figure D.1: Comparison of the different fitting functions that were tested to describe the μ s-PL lifetime behavior functionalized Si NCs. (a) shows the stretched exponential, bi-exponential, and single exponential fits to the data. Also shown are the values for reduced R^2 and χ^2 . Residual plots of the (b) stretched exponential fit, (c) bi-exponential fit, and (d) single exponential fit.

APPENDIX E

p-type GaAsBi : photoluminescence spectroscopy and AFM measurements summary

E.1 Photoluminescence Spectroscopy

We have also performed room temperature photoluminescence measurements on the GaAsBi film using two different excitation regimes: CW 400 nm excitation with average power of ~ 30 mW and excitation spot size $\sim 50 \mu\text{m}$, and pulsed 800 nm excitation with average power of 3.1 mW, and fluence of $\sim 6 \mu\text{J}/\text{cm}^2$. While the 400 nm light is absorbed entirely in the 250 \AA 300 nm GaAsBi layer, 800 nm light penetrates well into the substrate and is able to excite GaAs buffer layer as well. Normalized PL spectra of four of the samples excited with both 400 nm and 800 nm lasers are shown in Figure 5. In case of 800 nm excitation, two peaks are visible - GaAs peak at ~ 1.43 eV, and GaAsBi peak at lower energy. Note that a long-pass optical filter with 850 nm (1.46 eV) cut-off was used to block the excitation laser, resulting in distorted shape of the GaAs peak.

In case of 400 nm excitation, only the GaAsBi peak appears, and it is red-shifted relative to the peak observed under 800 nm excitation. In both 400 nm and 800 nm excitation cases, the GaAsBi peak position is significantly blue-shifted relative to the expected value according to the $-88 \text{ meV}/\%$ Bi formula (Francoeur *et al.* 2003). This is likely an effect of high excitation intensity, particularly

in the case of the pulsed 800 nm excitation. As was suggested by Lu *et al.* (2009), increase of the PL emission energy with the excitation intensity is related to the presence of the Bi localized states which dominate the emission at low excitation intensities.

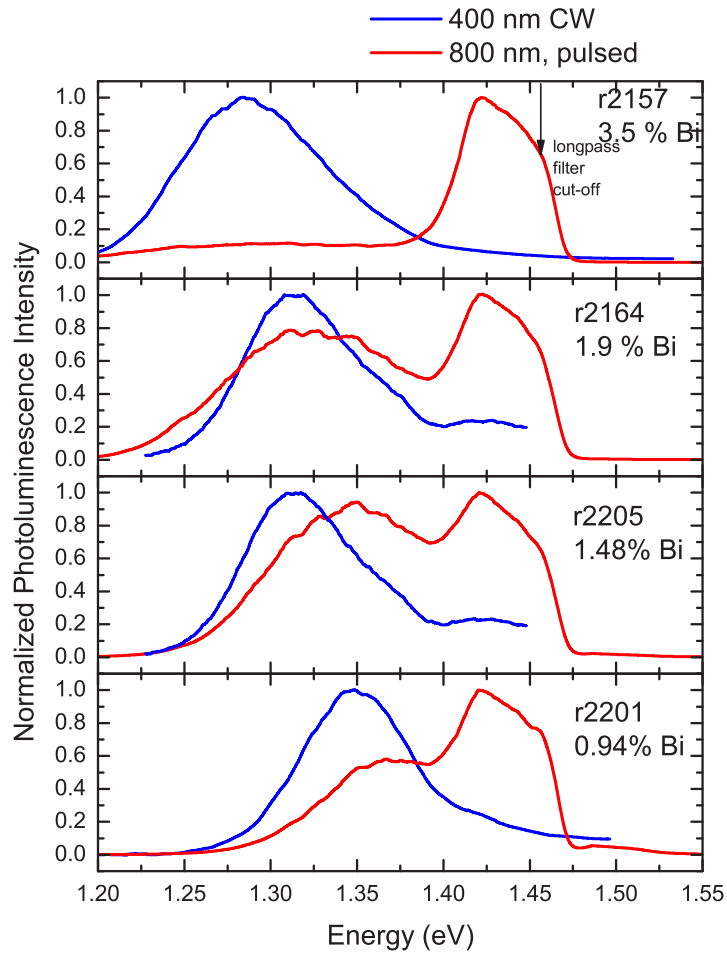


Figure E.1: Normalized PL spectra of GaAsBi films under 400 nm and 800 nm excitation.

PL spectra for the entire series of GaAsBi samples with Bi content up to 5.5% under 800 nm excitation is shown in Fig. G2. GaAsBi peak red-shifts with increasing Bi concentration, and its intensity peaks at 1.4-1.9% Bi.

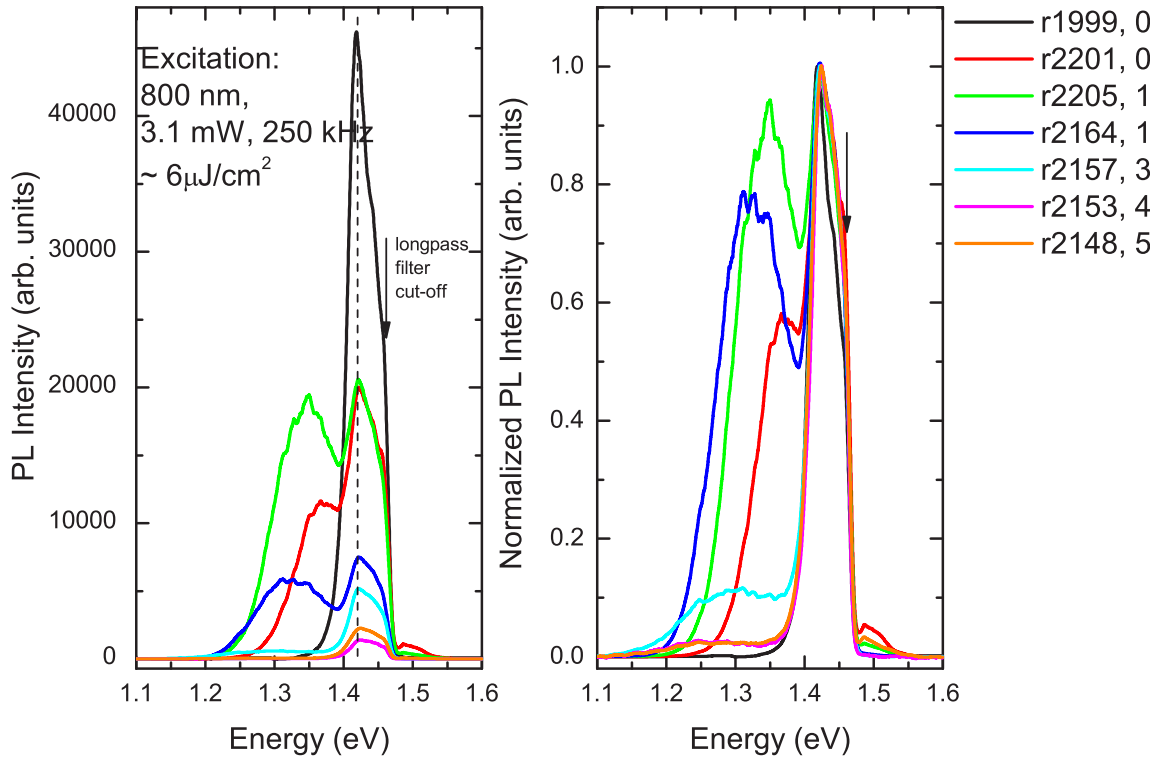


Figure E.2: PL spectra under 800 nm excitation.

The summary of the PL emission energy, peak FWHM as well as the ratio of the GaAsBi and GaAs emission intensities is shown in Fig. G3. In the bottom panel, the ratio of the GaAsBi and GaAs emission intensities was determined as the ratio of the peak areas with GaAs peak intensity normalized to 1.

We observe that the integrated PL intensity of GaAsBi and the slow decay component of the THz photoconductivity have the same dependence on Bi concentration. Both parameters are plotted together in Fig. G4. Both of these parameters exhibit a clear peak at 1.4 - 1.9% Bi, and decrease dramatically at higher concentration. As the slow decay component of the THz photoconductivity is believed to be governed by carrier loss to the trap states distributed within the volume of the GaAsBi film (Cooke *et al.* 2006), it is likely that the peak composition range (1.4 - 1.9% Bi)

corresponds to the lowest number of trap states, resulting in longer lifetimes of mobile carriers and improved radiative recombination rates. This hypothesis needs to be verified with time-resolved PL measurements.

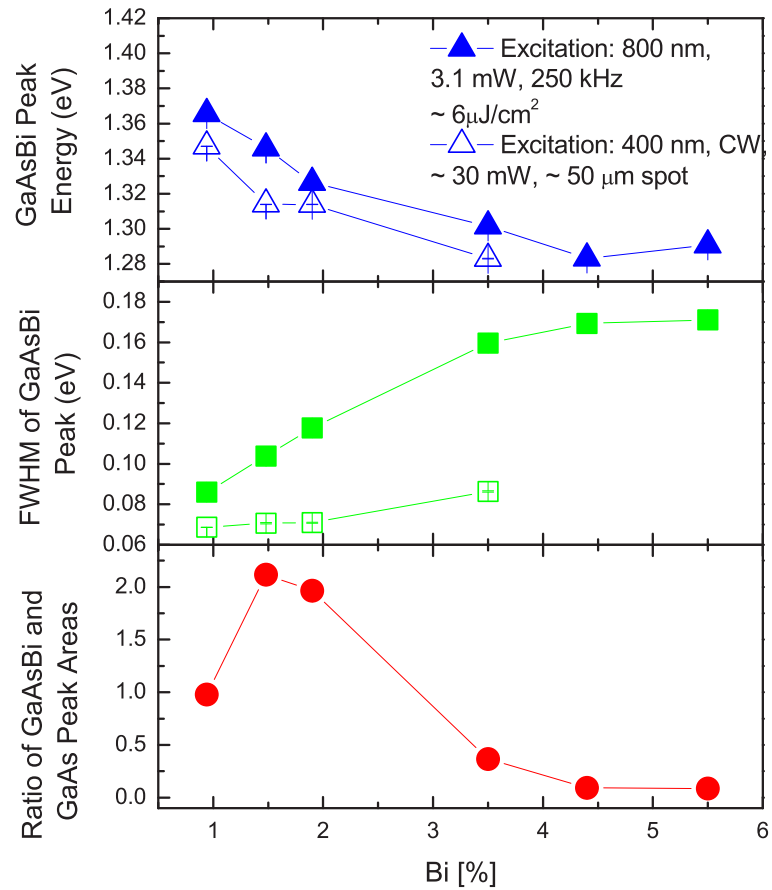


Figure E.3: Summary of PL peak parameters for 800 nm (filled symbols) and 400 nm (open symbols) excitation.

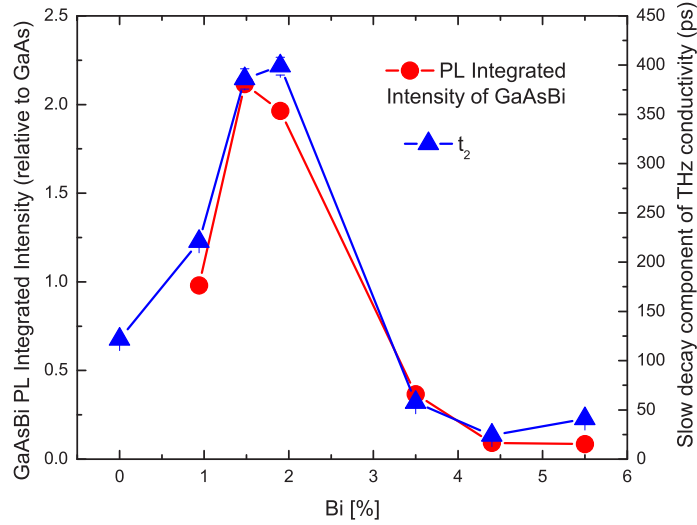


Figure E.4: Integrated PL intensity and slow decay component of THz photoconductivity decay of GaAsBi.

E.2 Atomic Force Microscopy and Confocal Microscopy

As the photoexcited carriers in GaAsBi are generated in within the thin layer (~ 20 nm) close to the surface, both the optical emission and photoconductivity of GaAsBi are expected to be strongly influenced by the surface morphology. In order to investigate the relation between the surface properties and optical properties, we have performed AFM and confocal microscopy imaging of the series of p-type GaAs and GaAsBi samples. Confocal PL imaging measurements are now under way.

Most of the samples exhibit various pronounced sub-micron features on their surface that are visible in the conventional optical microscope with $100\times$ magnification. The sizes of the structures increase, and their density seems to decrease with increasing Bi concentration. They also show great variation in shaped from sample to sample. However, within one sample, the distribution of feature shapes and sized is quite narrow. Figures E5-E11 show AFM and confocal optical micrographs of four of the studied samples.

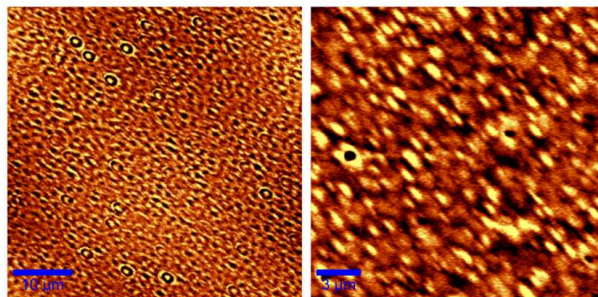


Figure E.5: r2208, p-type GaAs, confocal microscopy image (left) and AFM image (right).

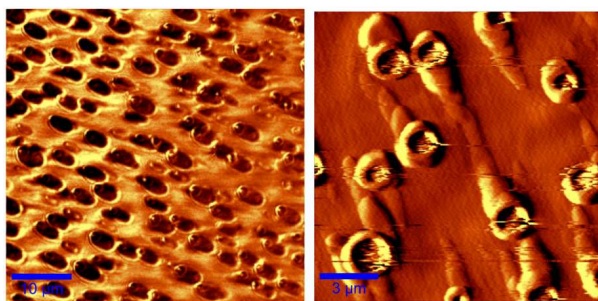


Figure E.6: r2201, GaAsBi, 0.91% Bi, confocal microscopy image (left) and AFM image (right).

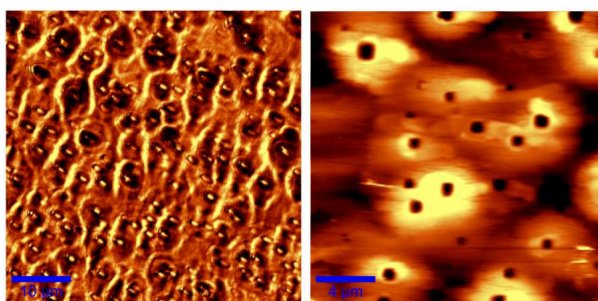


Figure E.7: r2205, GaAsBi, 1.4% Bi, confocal microscopy image (left) and AFM image (right).

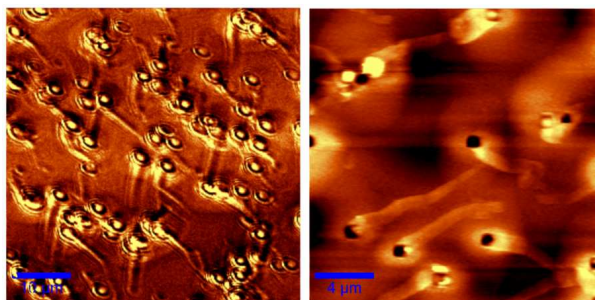


Figure E.8: r2164, GaAsBi, 1.9% Bi, confocal microscopy image (left) and AFM image (right).

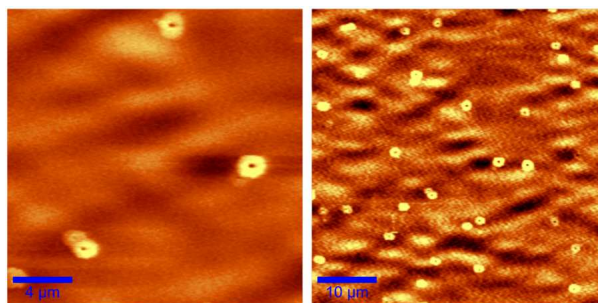


Figure E.9: r2157, GaAsBi, 3.5% Bi, AFM images.

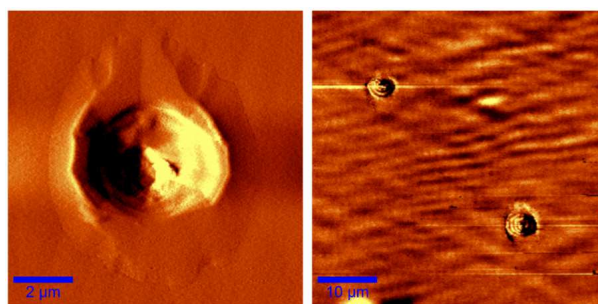


Figure E.10: r2153, GaAsBi, 4.4% Bi, AFM images

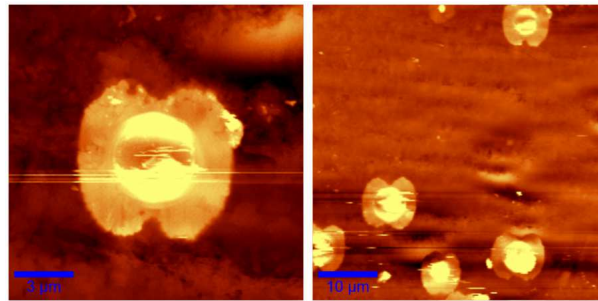


Figure E.11: r2148, GaAsBi, 5.5% Bi, AFM images

APPENDIX F

A walk-through in using the TIPL and TRPL set-up

This appendix provides a brief description on calibrating and using the CCD of the confocal set-up used in the time-integrated PL and time-resolved PL measurements in the Ultrafast Nanotools Laboratory in the Department of Physics at the University of the Alberta.

F.1 Calibrating the CCD and gratings

To perform the calibration of CCD and gratings:

1. Open SpectraSense, click the Hardware Config. Click the CCD icon on the diagram to direct the light to the CCD.

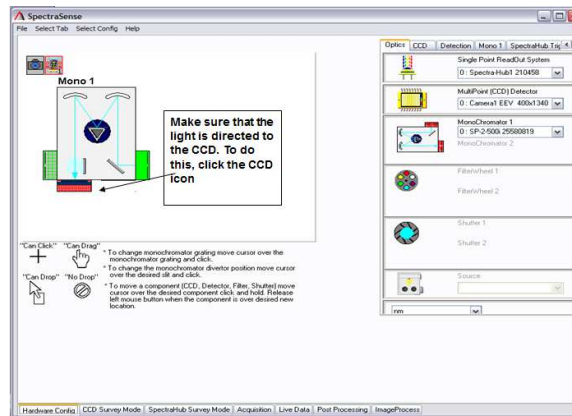


Figure F.1: Configuring the Hardware Config tab of the SpectraSense software

2. Select the gratings that you want to calibrate.

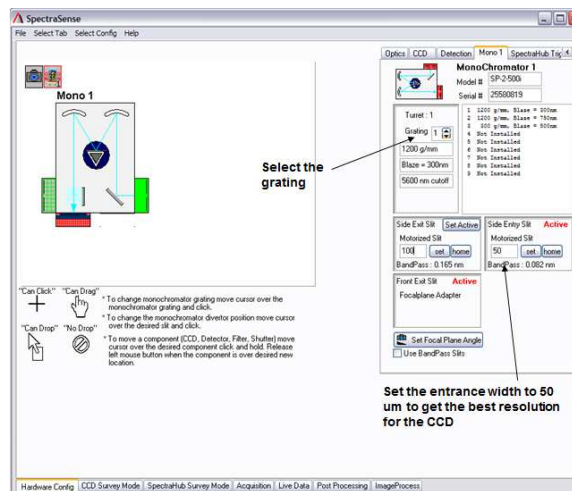


Figure F.2: Selecting the grating to calibrate.

3. Go to Detection tab. Set the Channel 1 to 'None'.
4. Using the Acquisition tab, set the range of wavelength from 500 to 600 nm if using the room light for calibration. Click the 'acquire' button to get the room light spectrum.

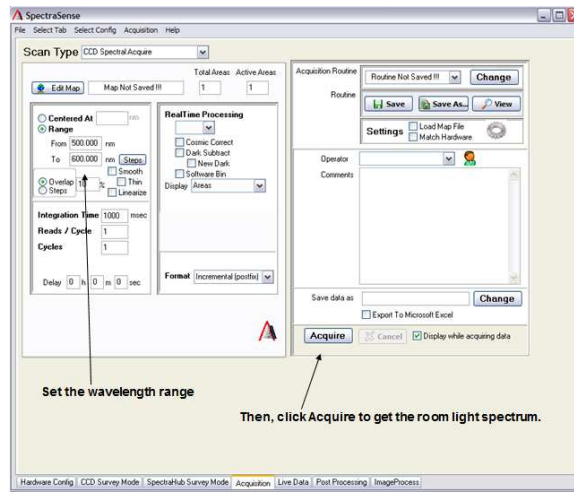


Figure F.3: Acquiring the room lights spectrum.

5. Go to CCD Survey mode tab, click Spectral, then click Go to get the spectrum of the room light. If the spectrum does not show the mercury lines between 535 to 555 nm, click Step backwards. Then click the Calibrate button to start the calibration of the grating.

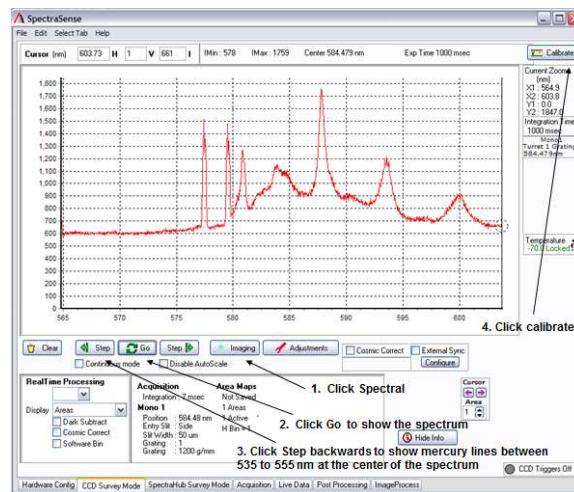


Figure F.4: Performing the calibration at the CCD Survey mode tab.

6. The area plot should show the mercury lines between 535 to 555 nm. Click OK.
7. Move the cursor until you get wavelength position with the maximum intensity. This corre-

sponds to the measured position. Using the known mercury line, set the reference position to 546.07 nm, then click OK.

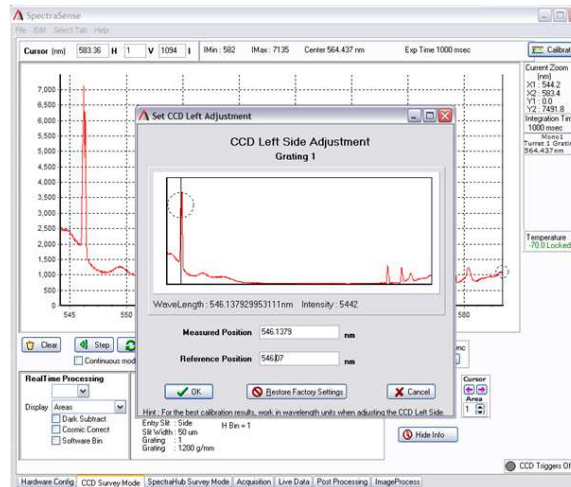


Figure F.5: Setting the center wavelength for the calibration.

8. Move the spectrum by clicking the Step forward to place the 'measured position' as close as possible to the left edge of the spectrum. Then click calibrate to move to Step 2.
9. Repeat Step 6.
10. Move the spectrum by clicking the Step backward to place the 'measured position' as close as possible to the right left edge of the spectrum. Then click calibrate to move to Step 3.
11. Repeat Step 6.
12. Make a quick check if the location of the 546 peak is close to the theoretical mercury line, 546.07 nm. If not, repeat Steps 2 to 12.
13. Open the WinSpec/32 program. Click the spectrograph to get the calibration parameters then click "calibrate" to see the calibration parameters. Chose the grating then click the "offset", "adjust", and "dispersion" button to see the calibration parameters.

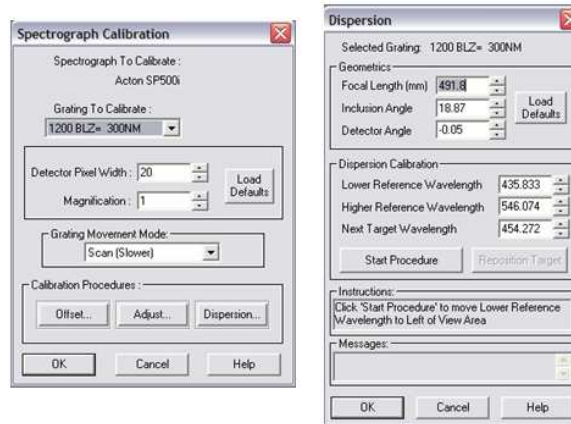


Figure F.6: Extracting the calibration parameters.

14. Copy those parameters to the CCD only and Picoharp.vi program. Then, click “calibrate grating” to update the calibration parameters. The gratings are calibrated now similar to that in the Spectrasence software.

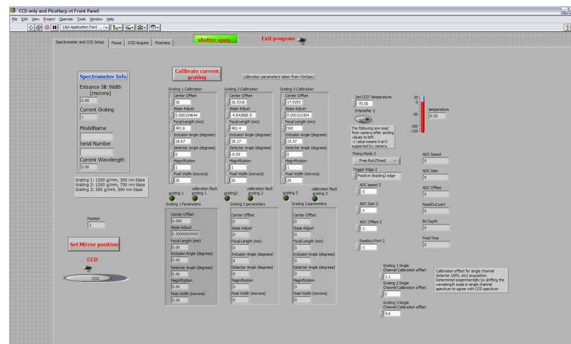


Figure F.7: Placing the calibration parameters of the grating for the TIPL and TRPL measurements.

F.2 Performing TIPL spectroscopy using the CCD

To perform time-integrated photoluminescence (TIPL) spectroscopy using the CCD:

1. Open the program “CCD only and Picoharp.vi” labview program.

2. Click the “run” button. Check if the CCD temperature reaches -70°C , if not, try closing the program and then run it again. The CCD temperature should always be at -70°C .
3. For TIPL measurements, choose the CCD by pressing the “toggle” switch. Then click the “mirror” button to adjust the mirror position such that the light will be directed to the CCD. Mirror position 1 means the light is pointing to the CCD and mirror position 2 means the light is directed to the (single photon avalanche photodiode) SPAD.
4. Press the “Focus” tab and set the entrance slit width. The best resolution can be obtained by setting it to 50 microns (~ 0.8 nm) but the signal is normally low. Using 200 microns slit width still has a decent spectral resolution (~ 1.0 nm) with a significantly large signal.
5. The grating can also be changed by simply typing the grating number then click “change grating”.
6. The “current wavelength” is the center of the spectrum that will be displayed on the window. Setting it to zero means a diffraction order of $m=0$, so the zeroth diffraction order will be shown. Setting it to a certain wavelength means that that wavelength will be at the center of the spectrum displayed in the window.
7. “Accumulations” is the number of spectra that will be taken before the final spectra will be shown (the average). Setting this to 3-5 is advisable if the signal is weak.
8. Set the integration time. Don’t set it lower than 1 s because it might damage the shutter. It is advisable to use 1 s when still aligning the set-up to get the optimum signal.
9. Change the toggle switch to “full” to get the entire spectrum in the CCD. Click the “start data collection” button. Once a picture of the signal is observed at the lower panel, click the “stop” button.
10. Using the “User defined area processing”, set the strips 1 and 3 as the regions in the CCD image where the background noise is located. Strip 1 should be the height in pixel (y-axis) before the signal and strip 3 should be the region in y-axis after the signal. Strip 2 should contain the signal. The height of strip 2 should also be defined such that only the signal is within strip 2.

11. Optimize the signal by adjusting the mirrors and lenses in the set-up.
12. Set the “user bin processing” to ‘2’ to obtain the signal alone. Then change the toggle switch to “user-defined”. You are now ready to get the PL spectrum.
13. Change the window to “CCD Acquire”. Copy the parameters used in the “Focus” window.
14. Set the toggle switch to “user-defined”, set the center wavelength, the step size, number of spectra, averages, exposures at each step, exposure time. The center wavelength will be the center of the first spectrum if there are several spectra to be taken. The step size is normally set such that the consecutive spectra will have enough overlap. This is done only if the spectrum is broad and beyond the maximum scan range of the grating. The number of averages can be set to 3-5 to improve the signal. The “exposure time” should not be below 1 s to avoid possible damage with the shutter, but setting it too long will also damage the shutter. Normally 120-240s is used.
15. Click the “apply spectral correction” so that the TIPL is corrected to the spectral response of the system.
16. Make sure that the “save” button is enabled. Then click the “Start” button.

F.3 Performing TRPL spectroscopy using the TCSPC

To perform time-resolved photoluminescence spectroscopy (TRPL) using the time-correlated single photon counting (TCSPC) module:

The time-correlated single photon counting (TCSPC) can be used for spectrally-resolved photoluminescence (PL) lifetime and a more detailed time-resolved photoluminescence spectroscopy (TRPL) where both the spectrally-resolved PL lifetime and the temporal evolution of the spectral profile can both be obtained. Before doing any of these procedures, make sure that the count rate in the detectors is not more than 10% of the laser excitation repetition rate to ensure single photon statistics (single carrier excitation/per pulse or single photon arrival at the single photon avalanche

photodiode (SPAD)). Ideally, the count rate is equal to 5% of the repetition rate of the laser. This can easily be achieved by reducing the excitation power.

After getting the TIPL spectra, go back to the “spectrometer and CCD set-up” tab. Click the toggle switch and the “set mirror position” to direct the light to the SPAD detector attached at the exit slit window. The mirror position should be at '2' and the toggle switch is at “single channel” position. Go to “picoHarp” tab then change the entrance and exit slit widths, as illustrated in the Fig. below. It is advisable that both slit widths will not be more than 200 μm to have a reasonable spectral width (1 nm) and to make sure that the light is not illuminating the entire SPAD detector (50 μm). The best time resolution can be achieved when the light is directed at the center of the SPAD. Next, change the “Discriminator Settings”. The Ch0 level determines the repetition rate of the sync pulse, which is the excitation pulse. For 250 kHz system, the Ch0 level is set to 120 which correspond to $\sim 250,000$ reading in the “SyncRate” (repetition rate of the laser). The Ch1 level is the actual counts of the signal. By default this is set to 50. The “Ch0 ZeroX” and “Ch1 ZeroX” are set to 10 mV which corresponds to the noise level of ~ 100 counts, which is the normal noise level of the detector. If the noise level is higher than 100 counts, try to cover completely the entrance and exit of the monochromator. If this doesn't solve the problem, try turning off the room lights.

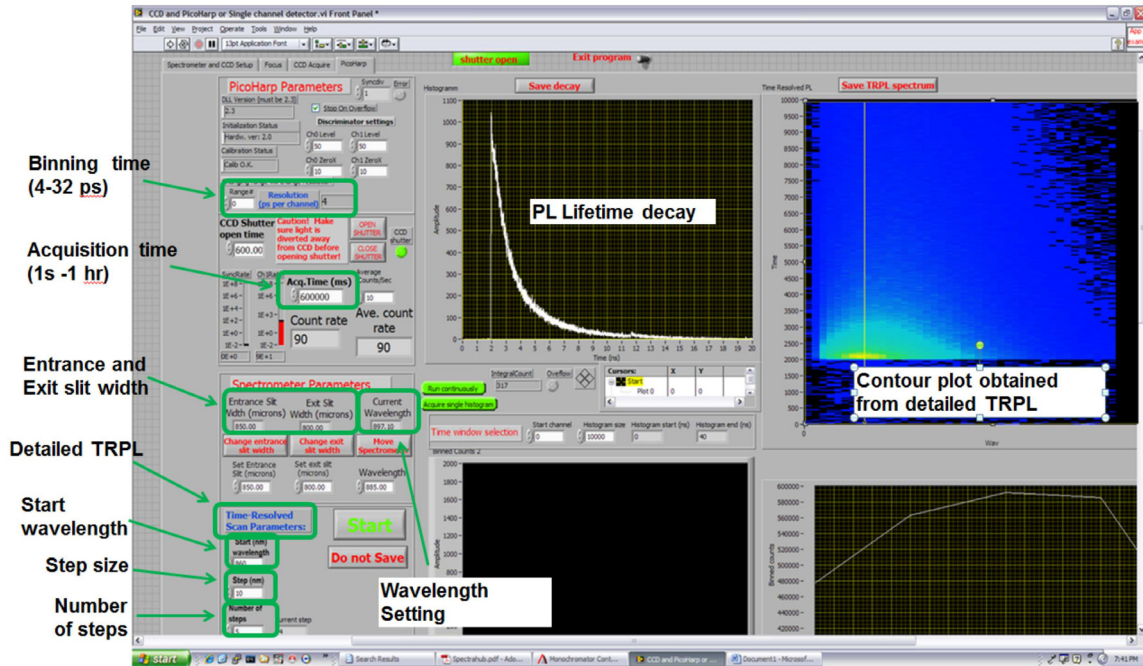


Figure F.8: An image of the acquisition labview program, CCD only and PicoHarp.vi, for the spectrally-resolved PL lifetime and detailed TRPL measurements.

APPENDIX G

A walk-through in using the near-field scanning optical microscope

This appendix outlines the steps in performing near field scanning optical microscopy (NSOM) using a standard sample for new users. Please refer to the user manual of the Alpha300S for the schematic diagrams of the scanning probe microscope Alpha300S and the complete procedures of performing NSOM with the use of the Witec software. The following procedures entails four modes of scanning; (1) Confocal transmission, (2) Confocal reflection, (3) AFM contact, and (4) NSOM transmission.

For the microscope control and data acquisition, the remote control interfaced to the computer and the Witec Control software is used. In the following measurements, Al deposits onto a glass slide is used as a sample.

G.1 Confocal transmission mode

1. The CW 532 nm laser should be turned on but the shutter should remain closed until the scanning processes.
2. Adjust the focal and aperture knobs of the microscope to the maximum level.
3. Switch the reflector into the bright field (BF) mode.

4. Use the Nikon objective in the upper microscope.
5. Open the Witec Control software and set the configuration to the Confocal APD transmission mode.
6. Set the illumination to about 20, which is enough to see the image of the Al deposits.
7. Using the remote control, lower the upper objective (microscope Z direction) at a speed of $500 \mu\text{m/s}$. When the objective is about $500 \mu\text{m}$ away from the sample, lower the speed to about $200 \mu\text{m/s}$ and switch from video camera to reflection camera. The reflection camera allows you to view the objective as it approaches the sample.
8. Decrease the speed until about $0.5 \mu\text{m/s}$ as the objective gets nearer to the sample. Switch to video camera to see the pattern of Al deposits that will slowly appear. Make fine adjustments to see a clearer image.

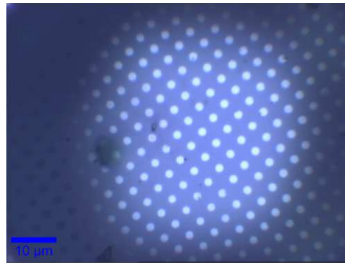


Figure G.1: Sample image taken from the upper objective.

9. Change to inverted microscope to control the lower objective. The lower objective can also be manually lifted up and down using the knob below the microscope stage.
10. Change the illumination to ~ 0.1 to decrease the brightness.
11. Increase the height of the lower objective to approach the sample. As the objective approaches the sample, you may notice the brightness changes from dark to bright and then dark to bright, due to the fringes of the diffracted light. Eventually, a shadow of the upper objective will be seen before the clear patterns of the Al deposits appear. At this time, decrease the speed to about $1 \mu\text{m/s}$.

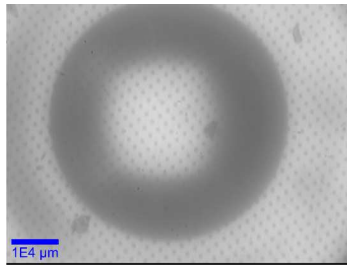


Figure G.2: Sample image taken from the lower objective.

12. The next steps are for focusing the upper and lower objectives into the image of the Al deposits. Turn off the illumination and then switch the reflector from BF to dark field (DF) mode. Switch to the upper objective and fine adjust the microscope Z to have very clear image of the Al deposits. Open the shutter of the laser.
13. By adjusting the collimating lens (using the micrometer near the fiber optic coupler into the microscope), focus the laser beam into the sample.
14. 'Set zero' the height of microscope Z.
15. Switch to the inverted microscope and decrease the intensity of the laser (slowly adjust the intensity knob clockwise).
16. At a speed of $\sim 0.3 \mu\text{m/s}$ speed, fine adjust the microscope Z of the lower objective to have a very clear image of the Al deposits. Refocus the laser by re-adjusting the collimator (see step 11).
17. Maintain the laser intensity at 500 kHz.
18. Click for the APD icon (the icon with gray waves). This will show a window of the APD counts.
19. Switch to the lower objective and adjust the X,Y,Z direction to get maximum CPS (counts per second). If it reached saturation, reset APD at the Detection section. Then increase the laser intensity to about 2500 kHz. 'Set zero' the X,Y,Z of the Inverted Microscope.

20. For a quick scan, use 256×256 image with a dimension of $25 \times 25 \mu\text{m}^2$ ($5 \mu\text{m}$ resolution). Click the Image scan button (the one with red waves), which will show an image as seen below.

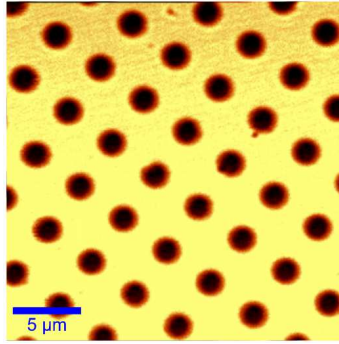


Figure G.3: Confocal transmission image of Al deposits.

G.2 Confocal reflection mode

1. For this mode, the inverted objective is not used, thus it should be lowered (by manually using the knob below the stage).
2. The optical fiber line inside the box below the microscope should be disconnected from the transmission mode and re-connected for the reflection mode. Here, the fiber outside the black box below the stage is connected to another camera at the right eyepiece of the microscope.
3. Pull out the camera switch to use the reflection mode camera.
4. Using the Nikon upper objective, follow the procedures from the Confocal transmission mode to obtain an image of the sample.
5. When the laser is already focused onto the sample, turn on the APD oscilloscope.
6. The initial laser intensity should be around 500 kHz and then adjust the filter holder to get maximum CPS. These are the two knobs near the optical fiber coupler for reflection mode.
7. Increase the laser intensity to 1000 kHz and set the image parameters (same with the Confocal transmission mode) to start the scan.

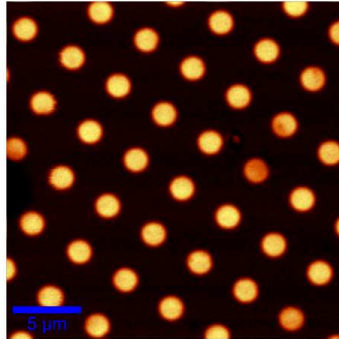


Figure G.4: Confocal reflection image of Al deposits.

G.3 AFM Contact mode

1. Change to AFM contact configuration and use the SPM objective at the upper microscope.
2. Make sure that the inverted objective should be far below the sample stage.
3. Let the upper objective approach the sample. Similar to the confocal mode procedures, use the reflection camera as the objective approach the sample then switch to the SNOM/AFM video to get the pattern of the sample. You may see that the image will eventually appear after passing through the glass surface image.
4. 'Set zero' the Microscope Z after making fine adjustments in getting a clear image.
5. Raise back the upper objective and to attach the magnetic cantilever arm. The cantilever arm holds the AFM tip that was glued via a washer. Adjust the position of the cantilever arm such that the laser beam is reflected from the AFM tip.
6. Using the remote control, adjust the position of the cantilever until the image of the AFM tip is clearly shown at the center of the screen through the video camera.
7. Refer to the quadrant window with a small red circle. This is used for the alignment of the laser beam into the AFM tip. The red circle represents the deflected beam. Use the T-P and L-R knobs to align this circle at the center of the quadrant window.

8. Lower the SPM objective (see steps in the Confocal reflection mode) to about $200\ \mu\text{m}$ distance from the sample and always make sure that beam is aligned by referring to the quadrant window.
9. Click 'tip approach' button (the one with cantilever icon going down). If 'tip approach' is not successful, the tip is either damaged or not glued properly onto the cantilever arm. In this case, ensure that a pristine AFM tip is placed properly and repeat the processes from steps 5.
10. Set the parameters for scanning the image (as used in the confocal mode). Set the suggested parameters of $V=0.5\ \text{V}$, $P=5\%$, $I=5\%$ from the manual.
11. Start the topography scan. There will be four images shown and at least two of the images should be clear, as shown in the images below. You may change the image parameters to get better results.
12. When scanning is finished, click 'tip retract' button (the one with cantilever icon going up) before making new scans.

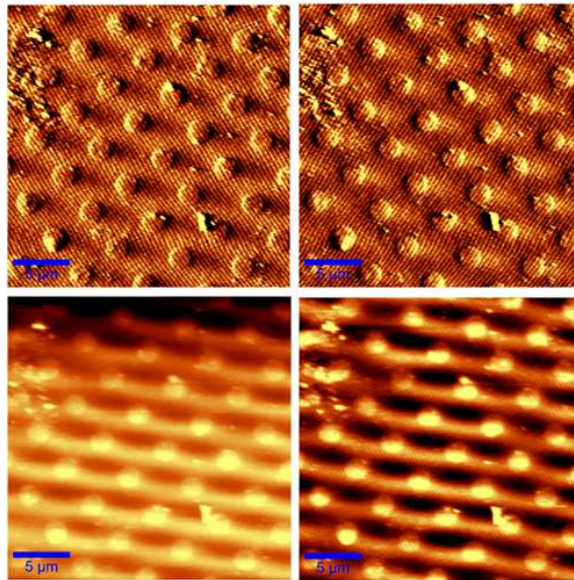


Figure G.5: Topography of the Al deposits obtained from the AFM contact mode scan.

G.4 NSOM transmission mode

1. Using the procedures in the confocal transmission mode, get the pattern of the sample using the SPM objective at the upper microscope.
2. Using the procedures in the confocal transmission mode, get pattern of the sample using the inverted objective.

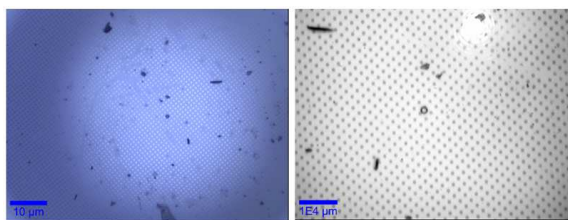


Figure G.6: The image of the Al deposits taken from the upper objective (left) and lower objective (right) at bright field.

3. At dark field, focus the laser onto the top of the sample by adjusting the collimator. Redo this using the inverted objective. (Note: Do not focus the laser into the sample by moving the objective. Use the collimator to focus the laser into the sample.)

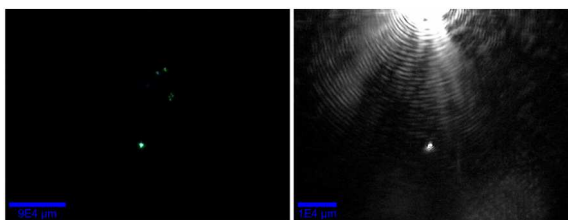


Figure G.7: Focused laser on the image of the Al deposits taken from the upper objective (left) and lower objective (right) at dark field.

4. Following the AFM mode procedures, place the cantilever arm, but this time, an NSOM tip is attached instead of an AFM tip. It has a hole in the tip to allow laser to pass through. In this measurement, an NSOM tip with 50 μm was used.

5. Decrease the illumination to about 0.1 and then turn on the laser. Direct the laser beam into the hole of the SNOM tip and at the center of its hole flaps.

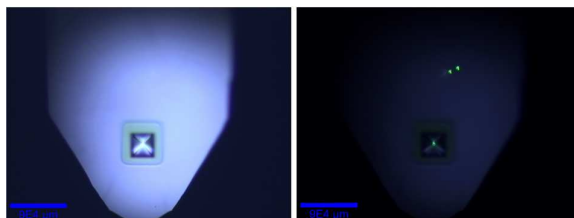


Figure G.8: Image of the NSOM tip at bright field (left) with the focused laser centered at its hole (right).

6. Similar to AFM contact mode procedures, let the tip approach the sample.
7. Check the image through the inverted microscope. You should see the shadow of the tip and the square hole.
8. Turn off the illumination and switch to DF mode using the reflector. Increase the intensity of the laser which will allow you to see a white dot at the center of the hole. If the dot is not visible, the beam is not aligned through the SNOM tip hole. In this case, re-align the laser beam as you 'tip retract' at about 50 μm distance from the sample. Repeat this process until the laser beam passes through the hole when the 'tip approach' is done.

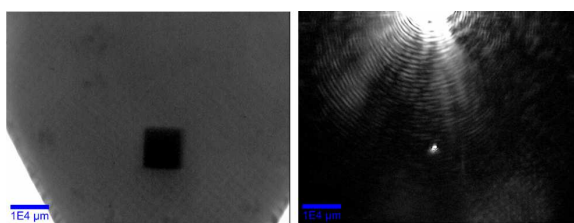


Figure G.9: Image taken from the lower objective at dark field (left) with increased intensity of laser beam (right).

9. You will notice that the microscope Z of the upper objective is no longer set to 'zero' when the tip approached the sample. Compensate this distance by exactly moving the objective of the inverted microscope further downwards.

10. Looking through the inverted microscope, refocus the laser into the sample by adjusting the collimator.
11. Click the 'APD icon' and adjust the X and Y axis of the inverted objective to obtain maximum CPS. Then gradually adjust the Z-axis as well. This means that the laser, the upper objective and the lower objective are vertically aligned. Set the intensity to about 2000 kHz.
12. Set the parameters for the image scan. This time use suggested settings of $V=1.0$, $P=2\%$, $I=4\%$.
13. Scan the image. The images are a combination of the topography and confocal transmission image of the sample. Adjust the image parameters to get better results.

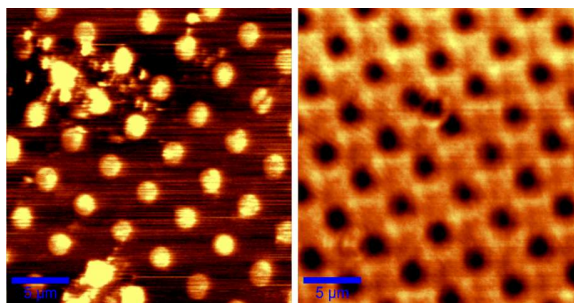


Figure G.10: NSOM images of the Al deposits. The image on the left is the topography while the one on the right is the transmitted image.

14. When scanning is finished, click 'tip retract' button before making new scans.

The Witec edit software can be used to edit and analyze the images.